Towards safe & soft robotic perception & interaction via situated morphological control

Shiva, Ali

Awarding institution:
King's College London

Towards Safe & Soft Robotic Perception & Interaction Via Situated Morphological Control

Ali Shiva

Supervisor: Dr. Thrishantha Nanayakkara

Department of Engineering, Faculty of Natural and Mathematical Science

King's College London

This dissertation is submitted for the degree of

Doctor of Philosophy

King's College London June 2019

To

The Awaited

"And He has disposed for you whatever is in the heavens and whatever is on the earth; all is from Him. There are indeed signs in that for a people who reflect."

(45:13)

"A year spent in robotics and artificial intelligence is enough to make one believe in God."

Alan Perlis (1922-1990)

"Out beyond the realm of wrongdoing and rightdoing, there is a field. I'll meet you there."

Rumi

Declaration

I hereby declare that except where specific reference is made to the work of others, the contents of this dissertation are original and have not been submitted in whole or in part for consideration for any other degree or qualification in this, or any other university. This dissertation is my own work and contains nothing which is the outcome of work done in collaboration with others, except as specified in the text and Acknowledgments.

Ali Shiva

June 2019

Acknowledgements

Special thanks to my supervisors, Thrish Nanayakkara & Kaspar Althoefer. My thanks to Jamie Paik & Andrew Conn for being my examiners, concluding a story of 5 years of my life. “Final moments”, as said, unfold a torrent of memories. Things have changed; I’m past 40, with 2 little daughters.

All started with my father’s encouragement, leading to an early-morning notification from King’s at work & sharing the joy by waking up my mum. I remember lying down in the small prayer room around 9 pm to meet the delegation at the hotel, towards the end of the year; tired, yet cherishing my last days at office. Followed was the 1st week with my father by arriving on a Thursday afternoon & rushing for registration at Guy’s Campus; the “Happy” cologne; induction at Franklin Wilkins Bldg.; Westfield with my brother & father; watching Silence of Lambs while minding my final calm moments.

I was first greeted by Kaspar outside his office, with a warm smile which pervaded through our many adventures with STIFF-FLOP, 4x3, & QMUL with Ataka on NCNR. He supported me morally & financially. I still remember my first group meeting on an Oct. 2014 evening in the submarine room S1.12, sitting on the 1st chair with Kaspar walking in with a test apparatus from Imperial. Scary.

Thrish opened my eyes to the world of impedance and morphological computation. My first encounter with Thrish was in Sept. 2014, where he walked me from his office to the embankment area to where I first met Helge. He continued the same assistance all the way through our time at Imperial.

Maughan Library, my little cubicle & the long working hours, the modelling, the Mechatronics lab & my test setup, STIFF FLOP project & partners from Surrey & PIAP & ... the ROS codes, group meetings, Silicone casting, the Khapera robots & Angela’s help, the long corridors, the IEEE plaque, the showers, the 5th floor common room, the canteen (where I once had sandwiches with my dad & daughter), the prayer room, the Quad, the desolated underground passages to the exit ... it was fun.

The 4x3 project swept through Saarbrucken, Augsburg, Magdeburg, Milan, Bilbao, and Eibar: from our first trip to Saarbrucken, driving the highways in Germany and Spain, to audio conf.’s which lasted for 3 years every other week; from the Adrenaline rush for first presentation (no idea what we were talking about), to the last presentation at Tekniker in front of EU officers and the final farewell.

Waking up to the tune of Mr. Tumble, TreeFu Tom, Chuggington, Balamory, & Katie Morag; silent walks through Woodstock lane towards Turnham Green; enjoying the view from Ravenscourt tube station into Flora Gardens; Stamford brook; Temple; Spong Book; the entrance through Macadam Building; Ladybird nursery & Ark Byron, walking through beautiful Acton Park ...

... The vacations at my in-laws'; Christmas trip to Switzerland; watching "Rogue One" with my brother; long bus rides with the pram on cold nights to the Islamic centre for Muharram; our outings with the car; ... from No. 10 Prince's Garden, to my desk at Imperial & the newly designated lab at the refurbished post office building - where I spend a lot of hours in the basement alone working on the setup, to the remote hallways and small lab at St. Thomas's hospital for the code on the final weekends with Yohan ...

... Gradually saying goodbye to fellow PhD students as they left one by one ... two months of solitude in the UK without my family; four months of intense writing up in Iran; and finally, back to the embankment building at KCL, were it all started: the final hours of vigorous lonely work; my evening seclusion in the same vacant room on the last days of May 2019; ... as if coming back to the beginning of the story ... and the relief of submission ... binge-watching the Mentalist while I was alone ... all will be remembered. With a special mention to those who were 1) on the verge of graduation: Anuradha, Evangelos, Joao, Liza - 2) ahead of me: Angela, Agostino, Ali Shafti, Chen, Peng, Udeme, Shan, Nantachai, Max, Brenden, Jungwan – 3) more or less with me: Ataka, Hadi, Lukas, Sara, Ashraf, Hasitha – 4) the postdocs: Sina, Helge, Yohan, and Nicolas. Most notably, Ataka: for sharing a lot of my PhD life with him; Yohan: for his constant and kind help; Hadi: For our long collaboration on many topics; and last but not least, Helge; an acquaintance which started by a quick tour about the labs & 3D printers & corridors, and carried on through STIFF-FLOP & group meetings, up to my viva. He helped me, supported me, and guided my journey.

What a sense of relief after the viva in the newly refurbished 1.05 classroom of Bush house with my parents. The soothing nightly stroll with my father after dinner at "Mehdi Restaurant", walking towards home from Chiswick and through Woodstock road ... special thanks to my family: my father, mother and brothers. Their support, encouragement, and love, made this possible. Many thanks to my parents for believing in me. My wife endured all the hard work of making things work; with the kids, with the home, and every other sacrifice. She stood steadfast by my side. Her presence, support, and partnership was and continues to be a warmth in my life. My sincerest gratitudes to her.

P.S.: I had promised myself to a treat of a little cup of coffee upon the submission of my thesis from the little mobile stall at the entrance of KCL building I passed every morning. The stall was there no more on the day I submitted.

Abstract

This thesis investigates active and/or passive utilization of robot morphology to achieve effective and safe interaction with its environment. The proposed approach is based on replicating certain morphological features observed in nature to enhance robotic performance during contact. The term morphology herein refers not only to the shape, but also physical properties such as stiffness, as well as actuator and sensor distribution [1].

Within the context of "Soft Robotics", two paradigms entailing contact are considered: a soft continuum manipulator for soft interaction and haptic perception; and a rigid-link arm with internal actuator compliance for potential industrial collaborative tasks.

Firstly, A fluid-actuated intrinsically-soft continuum robot is proposed as a bioinspired finger-like appendage. A novel analytical model is presented to solve the continuum kinematics based on the Cosserat Beam Theory and the Principle of Virtual Work, yielding complete pose and force data across the backbone hence attaining embodied sensory information. In addition, elasticity versus hyperelasticity considerations are discussed, showing the validity of elastic assumptions within its operational range.

Secondly, for the first time, the soft robotic appendage is used for haptic perception in soft tissue palpation for anomaly detection. Using Silicone as a tissue phantom, different actuation pressures are applied to the robot for mapping the tissue surface and detecting a hard nodule embedded in the phantom while estimating the tip force of the robotic appendage.

Thirdly, an innovative design is introduced to generate variable impedance for the soft robotic appendage. Inspired by muscular movement in nature, a hybrid actuation scheme is proposed by introducing embedded tendons inside the manipulator's wall to enable stiffness adjustment, which also improves manoeuvrability. Experiments are carried out by applying

an external force in different configurations while changing the stiffness by the two actuation mechanisms, demonstrating that dual antagonistic actuation increases load bearing capacities in this class of manipulators.

Subsequently, the tendon-augmented robotic appendage is enhanced by multiplying the tendons to produce a more uniform longitudinal tension distribution. Sweeping tests of a Silicone phantom with an embedded nodule are again carried out with different actuation pressures and tendon tensions. Utilising force sensors placed at the tip and at the base (representing tactile and proprioceptive cues, respectively), the behaviour of selected sensing modalities are investigated and compared. This novel setting delivers insights into the role of internal impedance regulation in perceptive exploration and how the tactile and proprioceptive sensory cues evolve by alteration in the morphology of the appendage. The final outcome of this stage presents a soft robotic appendage which emulates some biological morphology in being intrinsically soft and safe by its passive conformity, benefiting from embodied action-perception coupling, while enabling antagonistic actuation for actively adjusting internal impedance to arbitrate information gain.

Finally, the concept of exploiting variable impedance for safe interaction is extended to a rigid link robotic arm. A novel active approach is presented by employing a fuzzy inference mechanism to generate a decision for actively adjusting the overall stiffness of the robotic arm in the task-space direction(s) along the trajectory that is assumed to lead to a collision between the human and the robot, while not affecting the stiffness in other direction(s). It is shown that the torque experienced by the actuators in the joints have the potential to be used as a "stiffness" index for the arm in a coupled action/perception setting.

Table of contents

List of figures

List of tables

Chapter 1

Introduction

Abstract—*A research trend has emerged recently which investigates how to transfer certain morphological features observed in nature to robots, aiming to produce a more "natural" robotic behaviour for close interaction with humans which not only would be versatile but also safe. One of the key elements to this end has been identified as "softness"; whether incorporated in the robot's body (i.e. hardware) or in the robot's behaviour (i.e. software). This underlying concept has evolved in two domains: A) To employ compliant material in the robot's physical assembly; and, B) To implement compliant dynamical algorithms. The outcome has given birth to a field known as "Soft Robotics" which takes both concepts under its umbrella. This research explores and exploits certain morphological features in this regard and demonstrates the potential advantages of attaining variable impedance by introducing novel methods and mechanisms in both domains to achieve safe and effective contact with humans. This chapter describes the outline of this thesis by presenting the problem statement, the proposed approach and the basis of its inspiration, the contributions, and the relevant background studies.*

1.1 Introduction

The behaviour of biological entities is directly correlated to their morphological qualities, enabling their effective performance within the uncertainties and dynamic nature of their surroundings [2]. These characteristics encompass the ability to regulate internal impedance which contributes to safe interaction, active sensing, and co-emergence of action and perception in embodied intelligence [3]. From a behavioural aspect, transferring various degrees of this concept [4] to robotic systems has opened a new research field known as "Soft Robotics" [5], which aims to extend robotic assistance by facilitating safe and effective interaction with humans. Such a vision has potential applications in many areas ranging from medical interventions [6, 7], elderly care [8], disaster response, industrial tasks [9], and so on. The field of soft robotics has flourished in two sub-domains:

1. Accommodating compliant elements in the structure of robots; whether in localized joints in a rigid-link robotic assembly [10, 11], or constituting the overall body of the robot [12].
2. Implementing control algorithms to exhibit variable impedance entailing hard components [13].

This thesis investigates certain morphological features in the concept of soft robots to promote interaction with humans. With respect to the first category, a soft continuum manipulator is investigated and proposed for safe operation and active haptic perception. For the second category, a novel approach is presented to generate variable impedance in a rigid-link robot for close collaborative tasks. Safe manipulation is achieved by the passive intrinsic softness in the former case, while accomplished via active arbitration in the latter. Exploiting active or passive morphological adaptations - whether through inherent material softness or via active impedance regulation - herein is referred to as "morphological control" [14]. The term "situated" denotes "taking place in the context of task-relevant inputs and outputs" [15].

1.2 Problem Statement

Traditional robots are neither safe nor effective for delicate contact.

The recent growth of robotics has risen expectations for extending robotic operation to more uncertain situations than before [16]: not only in industry, but also where physical/bio hazards or logistic remoteness compel tele-operation, entailing physical contact within irregular surroundings. One such emerging demand is working in close proximity with delicate and/or living tissues, specifically humans [17, 18]. This, in turn, necessitates developing robotic platforms which not only are capable of effective performance, but would also ensure physical safety in interaction. Robots with safe and effective collaborative abilities are claimed to have a transformative effect on our lifestyle with a wide range of applications from home to healthcare, rehabilitation, and disaster rescue [8]. Even in factories which typically utilize precision-based automation, there is a growing demand to utilize robots in close proximity of human workers [19] in various scenarios involving irregular patterns of motion and contact, whilst preserving the human's safety.

Traditional robotic systems have mainly been inspired by nature [20]. However, amid all progress in modelling and control, these robots in general fall short to operate safely and successfully in unstructured environments [21, 22], namely in close contact with living organisms [23, 24]. "Contact", nonetheless, is a fundamental form of interaction [25] and one of the principal means of attaining information [26]. Hence, for robots to extend their operation beyond the bounds of controlled scenarios, the sense of touch [27] along with the ability to cope with the changes in real world scenarios [2] is essential. Therefore, it seems that promoting intelligent and effective robotic behaviour should be sought in conceptual paradigms [28, 29], rather than solely furthering rigorous mathematical depth along traditional methods.

"Robotics has been defined as the science which studies the intelligent connection between perception and action" [30]. A robot's perception and behaviour is formed by the dynamic interaction between its body, sensory-motor coupling, and the environment [2, 31]. Until recently, robots were mainly developed for environments intended for well-defined (and often repetitious) tasks where qualities such as rapid production and precision are key. In these settings, robots in general appear as rigid-link mechanisms governed by centralized controllers which actively set the precise actions for stiff actuators where elastic behaviour

is considered undesirable [32]. Their sensors' abilities are determined by accommodating sensing elements in defined locations, with modalities corresponding to specific and recognized sensing tasks [16].

Two main outcomes of such an approach fall in the scope of interest of this thesis:

1. Favoring maximum rigidity has led to robots being regarded as harmful for operation in conjunction with delicate environments. For example, a metallic gripper would damage most fruits and vegetables in automated harvest [24]; or, humans and robots are segregated in factories due to potential danger of collision [33].

2. Despite being highly capable and robust in precision-oriented tasks, the sensory-motor arrangement in such robots are sensitive to alterations in the dynamic parameters of the setting, therefore intrinsically limited [11, 34, 35]. This results in lack of adaptability for tasks involving interaction with irregular geometries/surroundings [36] such as grasping, where the arising control and sensing problems have often deemed to be too complex [31, 37].

On the other hand, humans ubiquitously engage in activities entailing contact on a daily basis, which - for example - involves adjusting the pose or the pressure/relaxation in fingers to distinguish stiffness of objects, stroke a surface to identify its texture, grasp a fruit, hold a hamster, or palpate a patient's abdomen to locate anomalies. A simple observation discloses several features in these actions, which are quite contrary to those listed earlier for current robotic systems:

1. Geometries and motions are not well-defined and are mathematically unpredictable;

2. The precise contact point(s) is (are) not decided a priori. Humans naturally tend to simplify manipulation tasks; a factor which is often waived when designing a robot.

3. The sensory-motor coupling is modulated by changing the sensors' morphology [16, 37], which is highly coupled with forming the desired response to a physical stimuli induced by the surroundings to produce useful sensory information [37].

These characteristics pose a challenge for employing robotic assistance in activities comprising delicate contact. Within such a context inundated with nonlinear and/or metastable dynamics [23], simply transferring the same conventional methods from industrial settings to our daily routine has not been effectual [2], as new situations or conflicting constraints will always arise for which robots have not received instructions, rendering traditional control strategies inadequate [29].

1.3 Inspiration

Nature is safe and effective for delicate contact.

Animals operate very differently from rigid robots with respect to their surroundings. The co-evolving of body and brain in their tight interplay has made biological species efficient for continuous, compliant and robust engagement in a world full of fast changes, low predictable information and high uncertainty, while preserving safety [2]. Notably, abilities such as gripping, grasping, and sensing as prominent attributes have played a key role for survival.

As opposed to traditional robots where controllers enforce a prescribed behaviour in a fully actuated space, animals are capable of manipulating their body with remarkable efficiency despite the high under-actuation of neuro-muscle-skeletal system [38]. Their appropriate adaptation of sensor morphology and active sensing capability enables managing diverse tasks with distinct requirements [16].

Amongst the animal kingdom, appendages like the octopus's arm or the chameleon's tongue display fascinating features. The octopus is a biological case of embodied intelligence, demonstrating how effective behaviour is closely associated with the body's morphology and its interaction with the surroundings. The motor capabilities of its arms facilitate dexterous manipulation for conforming to the task at hand not only through its shape and geometry, but also by regulating the stiffness [36]. These enhanced manoeuvres and motor control are mostly ascribed to the special morphological features of the body [39] and not by alteration in the brain control strategy [36], as the brain of the octopus is relatively small and contains

as many neurons as in the dog brain (around half a billion) in its central nervous system (CNS) [40, 41].

Yet, with the current state of technology, an attempt to explicitly duplicate a biological system does not seem viable. Not only is a single neuron - comprising all intricate details - too complex to be synthesized artificially, but also may not be of much relevance. Rather, the focus is to figure out the underpinning principles of biological systems and transfer those to robots [2]. Some of these principals which stem from the morphological properties could be summarized as follows:

1. **Softness:** Contrary to rigid-link conventional manipulators were elasticity is deemed unfavorable and works adversely against prescribed tasks, softness at contact point(s) for biological species has proven beneficial [35] especially in highly unstructured tasks. This prevalence of tissue softness along with body compliance in nature is extensively exploited for effective and adaptable interaction with the surroundings [8] and simplifying actions [5]. Compliance not only enables safety for both the agent and the environment, but also allows coping with the object's irregularities in shape and stiffness through passive adaptability.

2. **Dexterity:** Biological contact appendages are usually seen to be capable of dexterous motion with relatively high degrees of freedom (DoF). Species such as the octopus display tremendous dexterity and manoeuvrability in performing tasks, thanks to the continuum structures with no rigid components which allows stretching, shortening and bending in all directions hence providing an infinite number of DoF; as the structure is able to undergo excessive deformations which allows adapting to physical constraints [42].

3. **Variable impedance:** According to Hogan [43], ensuring mechanical coupling between the agent and its environment requires the agent adopting the behaviour of an impedance. In biological species, this function is realized by physical changes in the agent (or its relevant extremities) [44], usually at an internal level. Regulating internal impedance facilitates harmonious contact dynamics as the agent arbitrates between contact locations to select the optimum points of contact or grasp [23]. Controlled stiffness in limbs is extensively

used to manage different levels of force received from or exerted to the environment. Additionally, internal impedance is one of the main factors determining the quality of perception [3].

4. **Coupled action-perception:** Motor cognition conceptualizes the idea that perception is embodied in action. "Action" is defined as generating movements to satisfy a specific motor purpose, or as a response to the environment's physical stimulation. Action and perception are inherently coupled in a shared embodiment in humans and animals [45], as opposed to conventional robots where we commonly witness distinct apparatus for action (e.g. motors) and perception (e.g. sensors of various types). "Embodiment" has been described as processing the exchange of information between the environment and the agent as a result of their structural coupling through adaptive morphology [3, 15]. We perceive to act, and we act to perceive [46]; preserving a circular relation at a hardware level as actuators and sensors are not decoupled [47]. The combination and coordination of sensing and motor functions act to optimize sensory information gain and the quality of perception [2, 3]. Information is the principal currency of cognitive tasks and when information is computationally expensive [48] and nonetheless vital for survival, embodiment matters. In embodied perception, levels of computation are delegated from the brain to the musculoskeletal structure to reduce the computational burden of the brain for faster action and reaction. Thus, control, in part, is actually performed by the morphology of the body via its mechanical circuits [39]. Numerous examples show how the body's morphological properties can significantly reduce the burden of the brain, such as grasping and tactile exploration [49]. According to the principle of embodiment, intelligent behaviour requires a body with the capability of interacting with the environment [39].

5. **Adaptive sensor morphology:** Species in nature extract their information via sensors embedded in their body. Many studies in biology refer to the role of sensor morphology in performing sensing tasks within different kinds of environments, such as modulating the mechanoreceptors in the hand by physical changes of the body [50]. Cognition

processing, though, comes at a high price. Every signalling event in neural activity uses energy, partaking in the high metabolic rate of the brain. About 50% of the total metabolic energy consumption in a mammalian brain is associated with signalling. This rate inhibits excessive synaptic activity [48]. Therefore, optimum functionally requires capturing not all the information, but all the information you can "afford" to acquire. Sensing components need to comply interactively with the external stimuli through a dynamic sensor morphology, influencing the sensorimotor coupling network which in turn results in changes in behaviour [3, 51]. As a result, the way the sensory receptor detects the stimuli is very much influenced by how the muscle is actuated, hence affected by the internal impedance of the body [4]. Such a behaviour is referred to as active sensing, which is purposeful information seeking [16] and has evolved with the evolution of biological species, enhancing internal information processing [2]. The morphological variation of embodied sensors is one of the most important features in biological systems for improving the interpretation of the perceived information by regulating their own behavioural variables with respect to the environment [3].

1.4 Proposed Approach

Soft Robotics show promise for safe and effective delicate contact.

As mentioned above, exploiting the mechanically intelligent arrangement of the body's morphology to deliver dexterous and safe manipulation has motivated researchers explore novel robotic paradigms [42, 52, 53]. The outcome has given birth to an emerging field called "Soft Robotics"; with the promise of safe and effectual robotic assistance in close contact with delicate environments, whether at home or hospital or remotely accessed locations [24].

This term "Soft Robotics" has been used in a generic sense covering all types of active and reactive compliant systems, encompassing soft actuators in artificial muscles, soft stretchable sensors and soft electronics [24, 54]. The underlying concept is based on diverging from the common wisdom in manipulation research, which could be mainly summarized in two aspects:

1- Contact with anything else than the manipulated object or the designated points of contact was considered a "collision" and to be avoided. In contrast, soft robots in general handle contact-rich interactions either via variable impedance in localized joints, or through soft-bodied underactuated designs, departing from the conventional notion of many individually-actuated degrees of freedom.

2- Compliance was considered as a defect in manufacturing and design [35]. Yet in the sphere of soft manipulation, compliance (whether inherently available or artificially generated) is an imperative ingredient, enabling the robot to adapt with the surroundings during contact and grasping.

This paradigm shift results in many differences in design, modelling and control. Encompassing new and exciting set of technologies, soft robotics has been highly envisioned as a potential solution to traditional problems in contact with living organisms due to notable advantages [55]. The classical method to alleviate the innate danger to humans from conventional robots was either by segregation or by considerable increase in sensorization along with adding layers of control. The concept of "Soft Robotics" puts forward an alternative approach by introducing compliance, as inspired by nature. This elastic behavior has been manifested in two forms [56]:

1- Active compliance; by implementing algorithms in the controller to exhibit elastic and compliant dynamics [57], thus achieving behavioural softness through hard materials.

2- Passive compliance; by incorporating compliant elements in the robot's structure, either in joints assembled with rigid-link elements (as inspired by vertebrate animals) [11], or by composing the entire structure from soft materials (as inspired by the invertebrate world) with the outcome of soft continuum appendages as grippers, actuators and manipulators. Here, motion is partially achieved through deformation [58] resulting from intrinsic compliance; i.e., the capability of undergoing large deformations without failure [59]. The body itself serves as an additional safety layer to cope with unpredictable behaviour of humans [24], endowing safety and adaptability via gentle and passive conformity with the environment [60] at potentially low cost [61]. A broad categorization of soft robotic paradigm is shown in Figure 1.1.

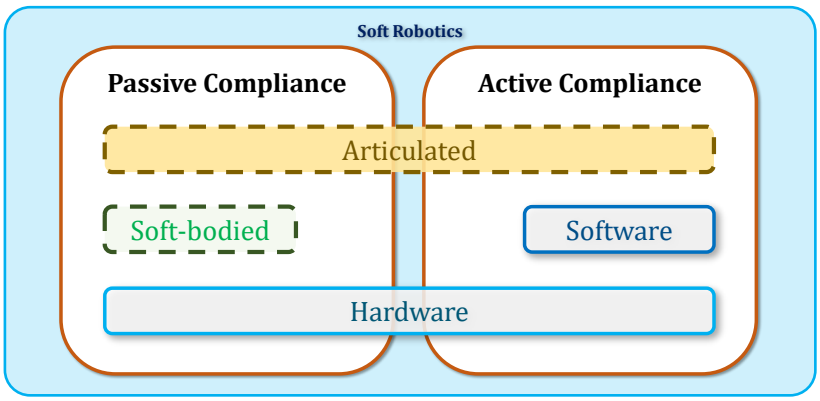

Fig. 1.1 *Soft Robotic Paradigm*

As mentioned earlier, Hogan's theory states that for maintaining a stable dynamic coupling with the environment, a body should be able to regulate its internal impedance accordingly [43]. In general, the term "impedance" refers to the combined effect of mass, damper, and spring properties. Although in literature, impedance has also been used as a generalization or extension of stiffness [3, 33, 44, 47, 62, 63], in this thesis, the term is used to encompass the passive mechanical response and/or the active modulation of the robot, during contact or else. As with the soft continuum manipulator considered in this study, the overall shape undergoes evident changes during contact/palpation to comply with the interaction forces. Additionally, the intrinsic properties of the constructive material contribute to damping effects in quasi-static motions; and finally, stiffness is directly tuned via tendons as discussed in related chapters. Hence, the term "impedance" has been employed to raise awareness of not being solely constricted to stiffness while neglecting other effects.

This quality is vastly exploited in biological entities. Humans regulate the posture and stiffness of their fingers and arms through flexing/relaxing their muscles and tendons (i.e., varying internal impedance) to compensate for their slow response time in manipulation [64]. When biological agents enter a coupled dynamic interaction, the number of DoF instantly increase to even as much as a double. This drastic change poses a major challenge to robotic controller stability, as they are usually designed to compensate for small changes in the unmodelled dynamics [65]. Adjustable impedance assists in preserving the stability of

artificial and biological agents in interaction with a large class of stable environments [65] and reduces the burden of feedback because of reactively curbing disturbances [66].

Physical human-robot interaction has emerged as an important subject to extend robotic assistance for close collaboration and sharing tasks and/or workspaces with industrial robots, which traditionally are assembled from hard material [24]. The utmost principle to be observed in such settings is the safety of the human [67]. Regulating impedance in a rigid link robot enables reducing contact forces when colliding with the environment, giving rise to the concept of impedance control which looks into coordinating force and displacement in rigid robots by feeding back torque sensory information to the control loop, generating a desired elastic behaviour resembling a mass–spring–damper system [68, 69]. However, there is a risk of instability in strictly controlling the impedance due to drastic changes in an uncertain environment, as these methods need to measure interaction forces and a fixed target impedance model [70]. In addition, selection of suitable impedance parameters for a satisfactory behavior is claimed to be non-trivial [30].

An alternate approach for realizing safe interaction in rigid systems has been developing variable-impedance/stiffness actuators (VI/SA) by attaining compliant behavior through mechanical elements in the actuators [10, 11, 71]. A main difficulty with the control of the impedance parameters of VSA robots is the dynamics introduced by the separation of motor and link side and the nonlinear elasticity [13].

The notion of morphological computation is subject to controversy as the community is still striving to categorize and unravel this subject [72]. In general, it is claimed that conducting intelligent behaviour with respect to the environment is - to an extent - carried out by active or passive utilization of the mechanical circuits of the body, and not exclusively by the neural circuits [26]. The body adapts to the surroundings and in turn regulates the sensory-motor coupling. Although the intricate details of this is not entirely clear for both robotic and organic motor control [45], yet it has been shown that exploiting embodiment could reduce sensory burden [73]. In this sense, layers of computation are “offloaded” to the body from the brain [26, 72] to facilitate effective performance, and is believed to be dominant in biological manipulation. Such a belief requires appreciating the control system

within the context of the body, and not independent of it; quite contrary to the traditional approach which designs the physical structure and the controller in separate contexts [20].

Morphological computation in haptics could be defined as active and/or passive utilization of the embodiment to facilitate information exchange during contact between the probe (as part of the body) and the sensed object. This utilization involves geometrical or mechanical adaptation or regulation to serve a higher sensory information gain. In this manner, part of the computation is delegated to the body. An artificial counterpart to biological systems with this capability are soft-bodied agents. Firstly, their continuous deformability relaxes the need for constant force/position monitoring. In the absence of a traditional controller, the body itself compensates for the complex nature of interaction without the need to allocate time, energy, and computational power to a centralized controller. Secondly, the amount and nature of their deformation could be used for estimating contact forces [74] since it directly causes the severity of this deflection. Removing the sensing element(s) from the proximity of the end effector and utilizing information from joints or proximity of the base is referred to as intrinsic sensing [75] and an appealing capacity in continuum manipulation [76].

Soft continuum manipulators are a subdomain of soft robots where the constitutive soft material forms concatenating curves with continuous tangent vectors [60], usually designed for large-scale flexibility and adaptability [54]. In addition to safety, a main benefit of the inherent compliance in soft continuum robots is the faculty of embodied intelligence (e.g. preflexes[1]) that can potentially reduce the mechanical complexity and/or computational burden in ways not possible with rigid-link robots [53]. The continuum distribution of the actuation medium provides a suitable platform for coupled action-perception in a shared embodiment, with the potential to reduce sensory hardware [80]. Such a quality would be desirable especially in sensor-deprived scenarios or facing limited energy supply. Embodiment design in these robots requires co-designing the control and mechanics to optimize the performance and increase the efficiency [36]. Within this class, soft braided designs demonstrate a more linear behaviour and homogeneous deformation which are desirable for control purposes, compared

[1]Preflexes are the latent capacities in the musculoskeletal system that auto-stabilize movements through the use of the nonlinear viscoelastic properties [77–79].

to non-braided systems where radial expansion could restrict their applicability in confined zones [81].

Another important issue in soft continuum systems is underactuation. Continuum structures possess relatively high DoF, yet only a limited number of these DoF's are directly accessible through actuation. Most are usually governed by the inherent elasticity of the structure in response to actuation and external loading [60].

A soft continuum robotic surrogate could potentially benefit a wide range of applications such as tele-operated medical interventions, whether as a sensory device or as an operative device or both. In [82], the authors demonstrate that how the complexities of soft systems can be harnessed and used to for information processing of nonlinear dynamical systems. Minimally Invasive Surgery (MIS) is a prime example where most regular instruments are rigid, incapable of adapting their morphological properties to suit the task at hand, and suffer from insufficient number of DoF [6]. In open surgery, the surgeon heavily relies on haptic sensation [83]. Yet this feature is lost in MIS as contact takes place via surgical tools. Soft continuum manipulators have the potential to enhance manoeuvrability while minimizing tissue damage due to inherent softness [84–86], while utilizing their embodiment for sensing contact forces [87]. Disease outbreaks (e.g. the 2014-2016 Ebola crisis) is another case demonstrating the necessity to provide access to professionally trained staff for examining patients in remote situations that can even pose a threat to healthcare providers. Tele-operated soft robots could enable a future prospect which a clinician located off-site could examine and "feel" a patient via haptic feedback utilizing a soft continuum robot as an interface [88], benefiting from their adaptive morphology. Delivering assistance to the elderly care in their own households is another domain where application of soft robots has been proposed [89, 90].

1.5 Motivation

The prime motivation driving this research was to emulate certain morphological attributes of biological species in robotic systems to move closer to exhibiting bioinspired behaviour.

The intention is enhancing robot performance in unstructured scenarios especially in close contact with living organisms, and also to address some of the challenges that have hindered full grasp of soft robotic traits in practical applications.

1.5.1 Morphological Control in Soft Continuum Robot for Safe Interaction and Perception

Although soft continuum manipulators enable safe interaction in unstructured surroundings via their inherent passive compliance and high dexterity, yet their successful implementation in practical scenarios rests on developing real-time models that facilitate reliable, accurate, and energy-efficient control. Traditional approaches entailing fully actuated control, detailed modelling of the environment, and identified contact locations with pre-computed exchange forces are incapable of handling the complexities in the highly-fluctuating contact states that occur in soft manipulation. The continuous deformability with high DoF in this class of robots continues to pose a challenge for modeling [91] and real-time simulations [92]. As a result, difficulties in forming control strategies and comprehensive system integration continue to persist [53, 81, 93].

On the other hand, load bearing capacity in these robots are influenced by the compliance which basically reduces the endurable level of force exchange with the environment [26], also limiting intrinsic actuator-based force sensing abilities due to reduced backdrivability [60]. Lack of adjustable levels of stiffness/resilience can undermine efficient performance in tasks such as active haptic exploration, which relies on adaptive morphological embodiment. Conversely, facilitating active internal variable impedance in this class of robots could broaden applicability by ameliorating the continual tendency to deform in contact. Hence developing methods to realize stiffness control has gained a lot of attention recently, such as jamming or incorporating smart materials [84]. Moreover, the ability to regulate stiffness is also shown to empower haptic information gain [83] with numerous applications listed before.

In line with the above-mentioned concerns, this research looks into a soft continuum manipulator, reminiscent of a biological haptic appendage such as a human finger, comprising braided extensors to accommodate fluid actuation pressure. The first step taken here is

to provide a comprehensive model which can take into account basic overall deformations of extension/compression, twisting, and bending; aiming to provide a real-time simulation platform. To this end, a descritization method is adopted to benefit from the transfer of data which enables internal force monitoring in real-time. Additionally, extensive literature review unveiled that assuming hyperelastic behaviour is a widespread notion proposed in many models. Considering the extent of strain witnessed in the operational range of the soft robot, this researched studies the validity of elastic assumptions compared to several hyperelastic models.

In the next step, this thesis investigates the possibility of increasing the load bearing capacity of the afore-mentioned manipulator. Inspired by antagonistic muscle activation in living organisms which enable stiffening of a limb, it is hypothesized that transferring such a feature to the soft robot under study can elevate structural resilience when needed. This task is carried out by accommodating longitudinal tendons in the body of the manipulator.

This thesis also investigates the applicability of the soft continuum appendage as a haptic interface. Haptic sense is one of the most complex yet capable means of sensing [94] which is often underrated [3], in spite of being the only perception system distributed throughout the human body. Acquiring haptic information in irregular surroundings continues to be an open problem in robotics, which could be addressed by the geometrical adaptability and soft structure in these robots. Also, since sensory information in haptics is imparted by the local deformation field induced by the object in the probe due to contact [94, 95], this class of manipulators appear to be a suitable candidate for haptic sensing due to their ability to deform while safely interacting with delicate objects and living tissue.

Haptic sensing incorporates information processing for both tactile and proprioceptive cues [96, 97]. It has been suggested that haptic perception in human is not solely reliant on tactile feedback, but also incorporates proprioceptive modalities [98]. Although there have been many studies on tactile sensing in artificial systems [96, 99], yet the role of proprioception especially within the context of variable impedance has not received much attention [3]. Variation in impedance directly affects the behaviour of the agent as it constitutes the mechanical circuitry of the embodiment. Therefore, awareness of its role is of

high significance for robot design. For this purpose, the tendon-augmented soft manipulator is utilized as a haptic mechanism for sweeping a soft Silicone tissue which contains an embedded hard nodule. The underlying hypothesis driving this section is that not only the soft manipulator could benefit from embodiment in acquiring force data, but also different levels of induced tension could sharpen the haptic perception of the stiffness anomaly. Hence, two industrial force sensors are employed, one at the tip and another at the base, for ground truth force acquisition; as the soft tissue is probed with the manipulator and the capability of conveying meaningful sensory information via the morphology of the soft appendage is explored. Different initial indentations of the manipulator's tip are considered to investigate any significance in this aspect.

It has been shown that humans employ modulation strategies for localizing a hard nodule in a soft tissue using their finger [100]. In this regard, an artificial agent emulating a biological appendage (such as a finger) capable of antagonistic actuation and internal variable impedance provides an interesting basis for studying the not only the efficacy of probing strategies, but also investigating the correlation between distinctive tactile and proprioceptive sensing modalities in haptic perception. As many aspects of haptics are still not well understood [83, 97], results from the proposed notion could offer insights to hidden layers of human behaviour regarding their morphological adaptations in similar contexts, in addition to foster innovative guidelines in designing soft robots with perceptive functionalities.

1.5.2 Morphological Control to Develop Soft Behaviour in Rigid-link Robot for Safe Interaction

Rigid-link manipulators, although versatile in task-oriented settings, fall short on safe human interaction. Yet, as intuitively witnessed in our daily endeavours, humans utilize a qualitative strategy to adjust their bodily compliance when manoeuvring through surroundings which dictate delicate contact. This thesis puts forward the notion of qualitative decision-making strategies inspired by humans to mitigate collision by adjusting their internal impedance accordingly, and transferring this idea to a robotic arm. Taking a rigid-link robot

as the test platform, a Fuzzy algorithm based on considering distance and velocity with a potential collision is investigated to promote safety while cooperating with humans. The proposed method does not rely on measuring the interaction forces, yet utilizes the distance and velocity between the human and the robot. With a straightforward and easy-to-implement framework, the invoked soft behaviour could enable safe collaboration with human workers in a shared workspace.

Figure 1.2 demonstrates the rationale motivating this thesis.

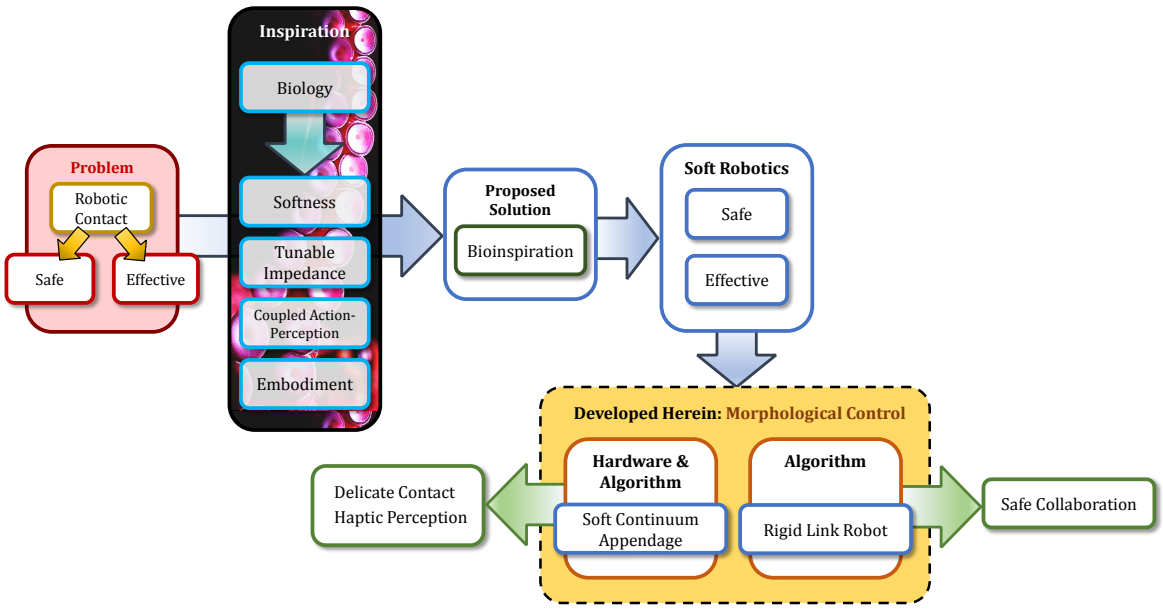

Fig. 1.2 *Thesis Rationale*

1.6 Contributions

- A novel variable curvature model for fluidic soft continuum manipulator comprising braided extensors was proposed and validated. This approach accounts for shear, torsion, bending and extension; and not restricted to training data. The model is spatial (3D) and computationally efficient for real-time simulation of position and deformation. Position and force information propagate toward the proximal base and are retrievable at any selected point along the backbone via discretization (based on a number of sections definable by the user). Structural inhomogeneity such as rigid inter-segment connective elements can be included in the model.

In line with facilitating contact-force sensing, the external force can be applied at any point on the body and not only at the tip; thus practically extending the force sensing and perception capabilities which are especially beneficial for sensor-deprived environments.

- With respect to the above-mentioned model, this thesis compared the results of elastic versus hyperelastic assumptions which are commonly postulated in similar platforms. Experiments demonstrated that within the operational range of the studied soft continuum manipulator, Hookean assumptions yield accurate results notwithstanding the fact that the structure is composed of hyperelastic material. The elongation for the braided extensors as a function of stress were derived for the hyperelastic models and can be applied for structural design in analogous cases. In addition, the sensitivity to proper selection of Young's modulus (E) for the model was investigated, revealing that the inaccuracy in results increases at a higher rate when lower Young's Moduli are designated for simulation.

- An innovative design was presented to combine fluidic actuation with tendon stiffening mechanism in the soft continuum robot under study. This feature not only enables dual actuation, but also increased the load bearing capacity.

- The soft continuum robotic appendage was employed for the first time in active haptic perception for anomaly detection of a soft phantom, benefiting from variable impedance which enables mediation of sensory information. This thesis also investigated the role of internal impedance on how the morphological properties of a soft continuum robot regulate the tactile and proprioceptive cues and their interplay.

- An innovative framework was presented for safe robotic interaction by taking inspiration from qualitative decision-making strategies in humans' interaction. A novel Fuzzy inferencing for variable impedance in a rigid-link robots was introduced which enables directional stiffness adjustment, with the potential of conducting collaborative tasks in industrial environments by adjusting the reactionary torque in the joints generating compliance to preserve safety.

1.7 Publications

Several publications emerged during working on this thesis which are either a direct output of this research or have resulted from works which were in close conjunction with this thesis.

- **Journal Papers**

1. **A.Shiva**, A.Stilli, Y.Noh, A.Faragasso, I.De Falco, G.Gerboni, M.Cianchetti, A.Menciassi, K.Althoefer, and H.A.Würdemann, "Tendon-Based Stiffening for a Pneumatically Actuated Soft Manipulator", *IEEE Robotics and Automation Letters (RA-L)*, vol. 1, pp. 632–637, July 2016.
2. **A.Shiva**, S.M.H.Sadati, Y.Noh, J.Fraś, A.Ataka, H.A.Würdemann, H.Hauser, I.D.Walker, T.Nanayakkara, and K.Althoefer, "Elasticity versus hyperelasticity considerations in quasistatic modeling of a soft finger-like robotic appendage for real-time position and force estimation", *Soft Robotics*, vol. 6, no. 2, 2019. PMID: 30702390.
3. S.M.H.Sadati, S.E.Naghibi, **A.Shiva**, Y.Noh, A.Gupta, I.D.Walker, K.Althoefer, and T.Nanayakkara, "A Geometry Deformation Model for Braided Continuum Manipulators", *Frontiers in Robotics and AI*, vol. 4, no. June, pp. 1–25, 2017.

- **Conference Proceedings**

1. S.M.H.Sadati, S.E.Naghibi, **A.Shiva**, I.D.Walker, K.Althoefer, and T.Nanayakkara, "Mechanics of Continuum Manipulators, a Comparative Study of Five Methods with Experiments," in *Towards Autonomous Robotic Systems (TAROS)*, vol. 10454, (Surrey, UK), pp. 686–702, Springer International Publishing, 2017.
2. S.M.H.Sadati, **A.Shiva**, A.Ataka, S.E.Naghibi, I.D.Walker, K.Althoefer, T.Nanayakkara, "A Geometry Deformation Model for Compound Continuum Manipulators with External Loading", in *IEEE International Conference on Robotics and Automation (ICRA)*, 2016.
3. A.Ataka, P.Qi, **A.Shiva**, A.Shafti, H.A.Würdemann, P.Dasgupta, K.Althoefer, "Towards Safer Obstacle Avoidance for Continuum-Style Manipulator in Dynamic

Environments", in *IEEE RAS/EMBS International Conference on Biomedical Robotics and Biomechatronics (BioRob)*, 2016.

4. A.Ataka, P.Qi, **A.Shiva**, A.Shafti, H.A.Würdemann, H.Liu, K. Althoefer, "Real-Time Pose Estimation and Obstacle Avoidance for Multi-Segment Continuum Manipulator in Dynamic Environments", in *IEEE/RSJ International Conference on Intelligent Robots and Systems (IROS)*, 2016.
5. A.Shafti, A.Ataka, B.Urbistondo Lazpita, **A.Shiva**, H.A.Würdemann, K.Althoefer, "Real-time Robot-assisted Ergonomics", in *IEEE International Conference on Robotics and Automation (ICRA)*, 2019.
6. S.M.H.Sadati, **A.Shiva**, S.E.Naghibi, D.C.Rucker, L.Renson, C.Bergeles, K.Althoefer, T.Nanayakkara, H.Hauser, I.D. Walker, "Reduced Order vs. Discretized Lumped System Models with Absolute and Relative States for Continuum Manipulators", in *Robotics Science and Systems (RSS)*, 2019.

- **Book**

1. J.Konstantinova, H.A.Würdemann, A.Shafti, **A.Shiva**, and K.Althoefer, eds., "Soft and Stiffness-controllable Robotics Solutions for Minimally Invasive Surgery: The STIFF-FLOP Approach." Gistrup, Denmark: River Publishers, 1st ed., 2018.

1.8 Thesis Structure

The structure of the thesis is depicted in the flowchart in Figure 1.3.

• Chapter 1 lays the groundwork for this thesis by introducing the main topic and its associated premises. The motivation and primary objectives are discussed and the proposed approach is explained. The background study follows, encompassing relevant research works and concluding with an outline of the thesis structure.

• Chapter 2 describes the soft continuum robotic appendage utilized in this research. A novel analytical model for forward kinematics is presented in detail, taking into account all main deformations (stretch, bending, torsion, and shear). Assumption of elasticity is compared

with neo-Hookean and Gent hyperelastic models. Tests are carried out in both cases of no load and in the presence of external load, validating the proposed model for real-time contact force estimation along with delivering total pose information.

- Chapter 3 investigates using the soft robotic appendage for the first time in haptic perception for anomaly detection. The soft robot is swept across a silicone phantom representing a soft tissue containing an embedded nodule.
- Chapter 4 presents an innovative design by combining fluidic actuation with embedded tendons in the soft continuum robot under study. This feature enables dual actuation and active variable impedance, as experiments reveal increased load bearing capacity via tendon stiffening.
- Chapter 5 explores utilizing the tendon-augmented soft continuum appendage in active haptic perception of a soft tissue with an embedded nodule. Building on the tendon-augmented robotic appendage described in the previous chapter, the tendons are multiplied to gain a

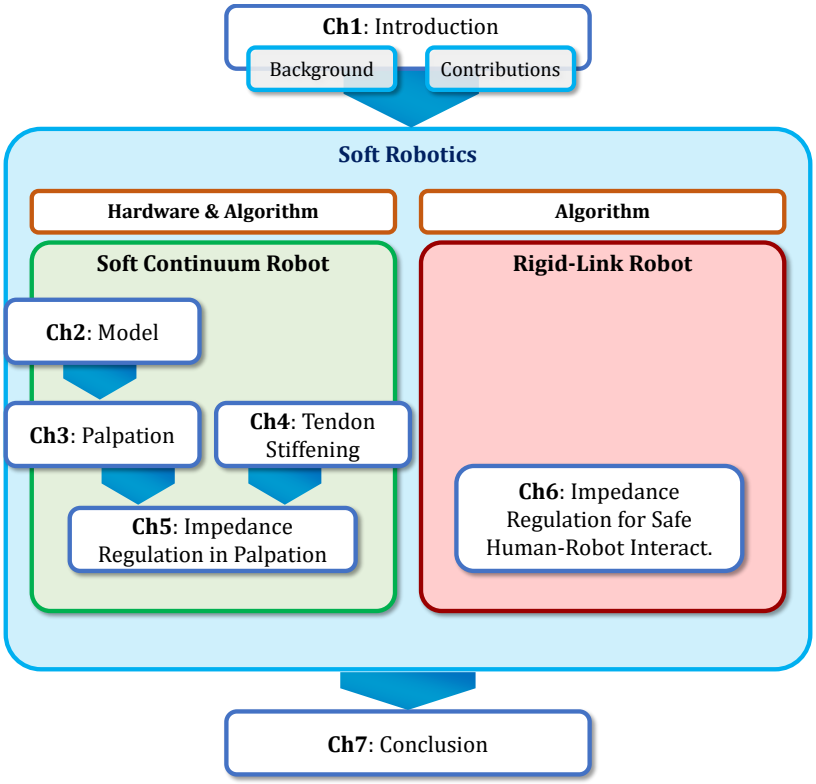

Fig. 1.3 *Thesis Flow Chart*

more uniform longitudinal tension distribution, as an abstraction of a biological finger such as a human's. Tests entailing sweeping a soft Silicone phantom with an embedded anomaly are again carried out with different actuation pressures and tendon tensions, resulting in an improvement in the quality of perception, while removing the need for a tip force sensor due to embodiment sensing. Aspects of correlation between tactile and proprioceptive sensing in using the soft continuum appendage are discussed.

- Chapter 6 extends the concept of variable impedance to a rigid-link manipulator by developing a novel stiffness adjustment strategy in a close proximity of human worker. Theoretical background is laid out and a fuzzy inference mechanism is used to achieve directional variable stiffness, both in simulation and experiments.
- Chapter 7 summarizes the findings of this thesis, and concludes with a prospect on potential research directions for further studies based on the framework outlined herein.

Chapter 2

A Model for Real-time Position & Force Estimation of a Soft Finger-like Continuum Robotic Appendage

Abstract— *Recently, various methods based have been presented to address the mathematical complexities of modelling motion and deformation of continuum manipulators. Here, a novel quasi-static approach is proposed for 3D modelling and real-time simulation of a pneumatically actuated soft continuum robotic appendage to estimate the contact forces and the overall pose. The developed model can incorporate external load at any arbitrary point on the body and deliver positional and force propagation information along the entire backbone. In line with the proposed model, the effectiveness of elasticity versus hyperelasticity assumptions (Neo-Hookean and Gent) are investigated and compared. Experiments are carried out with and without external load, and simulations are validated across a range of Young's moduli. Results show best conformity with Hooke's model for limited strains with about 6% average normalized error of position; and a mean absolute error of less than* $0.08\,\mathrm{N}$ *for force applied at the tip and on the body; demonstrating high accuracy in estimating the position and the contact forces.*

2.1 Introduction

Qualities such as dexterity and high deformability in biological appendages like the octopus arm have sparked a research trend which aims to replicate these features using intrinsically soft materials in continuum robotic platforms; with the promise of safely performing delicate tasks [6, 101], improving manoeuvrability in confined or unstructured environments [86], achieving higher dexterity for grasping [102, 103] or for motion in dynamic biomimetic systems [104, 105] such as submerged locomotion [5, 42]. These robots are also appealing for investigating morphological computation [106] and embodied intelligence [5], providing a framework for bodily force sensing without the need for additional sensory hardware, in contrast to rigid-link robots [107].

Yet, the inherent structural flexibility results in modelling and/or control [108] challenges. Several approaches have been investigated for modelling this class of manipulators. Beyond the distinction between planar (2D) [102, 107, 21, 109–111] or spatial (3D) [112–116] operation, it seems plausible to identify two key stages which determine the modelling strategy:

I. The "Priori" stage; to consider:

   - Taking external loading into account versus no external loads; and,
   - Inertial (dynamic) versus non-inertial (static/quasi-static, or kinematic) modelling.

II. The "Approach" stage; to consider a mechanistic solution versus shape function estimation (or a combination). While the former might entail some experimental identification, yet is based on analytical derivation and solving of the mechanistic equations, with the potential to be more comprehensive. The latter, on the contrary, is entirely structure-specific in implementation, with the unknown coefficients to be determined from the manipulator's behaviour.

The constant curvature (CC) formulation has widely been used [21, 112, 117–121] for mapping the actuation space to the configuration space by formulating the backbone deformation as a planar curve with constant radius. In this regard, Webster and Jones [122] demonstrated two separate sub-mappings: a robot-specific map relating the mechanical actuation to the

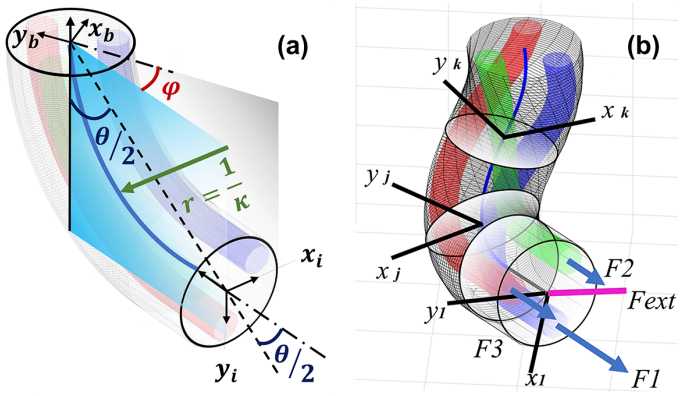

Fig. 2.1 *(a) Three arc parameters: total arc length, bending angle θ (or curvature κ), and out of plane angle ϕ, (b) Three-dimensional simulation with actuation and external load causing bend, shear, torsion, and extension. Discretization and transfer of frames are selectively displayed. F1,2,3 are internal forces due to pressurization.*

three arc parameters (Figure 2.1.a), and a robot-agnostic map relating the arc parameters to the spatial kinematic configuration of the manipulator. The first mapping usually involves some identification of the system from experiments; for example, as in Chen et al. [117] where a CC model is developed to control the manipulator's shape via tip position control.

However, the validity of CC depends on the mechanical and geometrical properties of the structure and/or the magnitude of loads. For example, torsional effects are reported to be capable of significant effects on the behaviour and deformation of soft manipulators [60] which CC falls short of incorporating [123]; in addition to shear or internal forces [124] when resulting in deformations not conforming to a constant-radius curve.

Conversely, variable curvature (VC) methods offer more viable solutions in the presence of external loads, in addition to providing singularity-free kinematic maps [125–127]. Many research works achieve VC from CC by modifications, such as deviations added as uncertainty [128], piecewise CC (PCC) [114, 122, 129], (where the infinite dimensionality of the configuration is resolved by assuming the overall shape as a composition of consecutive CC segments, linked such that the resulting curve is continuously differentiable [130]) such as a serial chain of subsegment arcs [131], PCC along with compensating free parameters (identified experimentally) [132], PCC combined with general 3D paths described by B-spline

curves [115], PCC with internal friction forces [133], or piecewise constant strain modelling based on screw theory [129].

As an alternative approach to VC methods, approximate identification based on polynomial solutions for estimating the shape function has been proposed [134–136], where the coefficients are identified using experimental results to derive a structure-specific model. For instance, Godage et al. [134] used a horizontally fixed orientation to train the coefficient matrices to derive a solution-based model for the kinematic map and implement the identified solution in the Lagrange equations of motion; however, this is achieved without considering external loads, Their model is singularity free and accurate, with regard to the training data sets, and the final solution is faster than beam modelling and lumped parameter methods.

Although identification-based models are relatively accurate, computationally efficient, and appropriate for real-time control [137], their validity is limited to their experimentally-derived conditions, presence and/or magnitude of external loads, input values, and training data sets, and do not account for the structural characteristics. Results are not guaranteed when dealing with unknown conditions and are not intuitive for shape interpretation [126].

In this regard, beam theory [86, 21, 112, 138–140] (such as Euler-Bernoulli (EB) models with small deflections in the absence of shear [109, 132, 140, 141]) and Cosserat rods [113, 115, 116, 123, 125, 142] have been considered. Beam modelling has also been applied as infinitesimal elements along the body [143] similar to the infinitesimal CC elements to attain VC kinematics. For a tendon-driven catheter, Rucker and Webster [116] coupled the Cosserat string and Cosserat rod models for the tendons and backbone, respectively, by deriving the distributed loads on the backbone from the tendons and solving via numerical integration. Shear and extension are considered negligible and hence omitted. Their model was adopted by Neumann and Burgner-Kahrs [115] in a 3D follow-the-leader scenario with distributed loads from self-weight, and applied to their tendon-driven setup (assumed to be frictionless) for beam statics and dynamics. After predicting a CC path, the true response is optimized, yielding a solution incorporating bending, shear, and extension, resulting in a VC solution with a robot-specific mechanical map that is free from singularity. Godage et al. [127] implemented the Cosserat rod model for a multi-section continuum arm, resulting in a

boundary value problem (BVP) with a system of nonlinear equations to be solved using recursive numerical optimization; however, in the absence of external loads. As a drawback, Sadati et al. noted in a comparative study [137] that Cosserat rod models entail relatively cumbersome calculations, which could be a hindrance.

In the modelling approach presented in here, we take three key elements into consideration:

I. *Discrete Kinematics*

Various structures for continuum manipulators have been designed to emulate continuum articulation along the entire body. Thus, many of the continuum manipulators are developed as serially concatenated multi-segment [6, 5, 112, 125, 144, 145] or as multisection robots [121, 134, 142, 146, 147]. This type of design makes discrete modelling appealing [110, 127, 143, 148]. A well-known method to this end is the lumped parameter approach, which approximates the continuum embodiment with a series of rigid-link segments interconnected via compliant joints [110, 124, 146, 149, 150], or in a network of spring/mass/damper [144], or in conjunction with other methods such as virtual power [131]. For example, Godage et al. [150] implemented Lagrangian dynamics for a lumped model to achieve VC kinematics, yet assuming that the robot always deforms in a circular arc without twisting, Tatlicioglu et al. [110] used lumped modelling to capture the planar behaviour of the three-section OctArm where the total kinetic energy is computed for an infinite number of rigid sections, and the summation over the Lagrangian terms is replaced with an integral over the backbone handing continuum Lagrange dynamics, although without torsion, However, while lumped parameter models reduce complexity of analysis, they are considered less accurate [150] and usually suffer from extensive calculations [126].

Alternatively, discretized differential equation describing VC kinematics can be used for forward integration of a model with finite number of elements (FEM) [151–153]. This approach eliminates spatial integration by considering a finite number of kinematic states associated with each element that result in a large and computationally expensive system of equations, usually expressed in vector format. FEM models, however,

are overwhelmingly restricted to off-line structural analysis and optimization rather than system modelling for control purposes [151]. Real-time FEM-based solutions for continuum manipulator mechanics and control have been extensively studied by Duriez et al., by utilizing mass matrix sparsity in the resulting system of equations [151, 152]. This sparsity is not achievable with a series-link rigid body kinematic approach, where relative states (e.g., joint angular and transnational position) are usually considered the modelling states rather than element absolute states (e.g., element orientation and position with regard to the reference frame). Moreover, current reports on real-time implementation of this method mention execution cycles slower than 40 Hz [154].

II. *Quasistatic versus dynamic modelling*

While many dynamic models have been proposed [104, 116, 125, 127, 146, 155], nonetheless, with most continuum manipulators, inertial effects due to motion could be neglected by assuming static equilibrium and slow transitions in the system states [126], as they are not operated close to dynamic boundaries [146]. Besides, silicone-based continuum manipulators present under-damped nonlinear dynamic modes with relatively large-value nonlinear damping and short transition time [93] which is insignificant and fast in most applications. In addition, capturing this exact behaviour requires extensive analytical and computational efforts [136]. Hence, static [113, 128, 132, 139], quasistatic [107, 111, 140, 141, 156] and kinematic analyses [120, 128, 133] are deemed reasonable assumptions for kinematic modelling and force sensing. Such circumstances are frequently witnessed in medical interventions [101, 5, 75] such as minimally invasive surgery [6, 60, 84, 157], catheterization [21, 112, 118], bladder surveillance [158], colonoscopy [117], endoscopic surgery [133], or other areas in medical training [8]. The same is true for most proposed assistive tasks [114, 159, 89], for example, using bionic hands [121]. This assumption has also been used in motion control [118, 160], navigation [148, 161], path following [147], leader following [115], manipulation [142, 148, 162], grasping [120, 148], or realizing biomimetic systems [8]. Even when developing a lumped model for a catheter, Jung et al. [124] claim that the dynamics of the system is not a

significant factor and is only considered to incorporate nonlinear friction, as solving for the quasistatic solution. Shapiro et al. [140] implemented a quasistatic kinematic model using an iterative solver for a simple EB beam model using CC for kinematic maps in a bi-bellows manipulator. The STIFF-FLOP manipulator [6, 52] was modelled by Fras et al. [143] in a quasistatic approach but without shear. Tunay [163] developed a spatial model using quaternions for the configurational variables of the Cosserat rod model incorporating bending, twisting, extension, and shear via approximate series solution for static modelling for the weak form integral equations in a finite element discretized form. This approach is accurate and comprehensive, but with complex shape function and limitations related to the finite element method. Xu and Simaan [164] analysed static equilibrium using elliptic integrals in a multi-backbone robot to investigate 2 degrees of freedom (DoF) bending. A quasistatic EB beam analysis was employed by Alici et al. [141] to formulate the 2D bending behaviour of an arm of a silicone gripper.

Moreover, not only shape sensing, but also force sensing is considered as one of the grand challenges that has hindered complete transfer of soft robotics to practical applications, such as medical robotics [60]. In general, force measurement and control play a crucial role in human robot interaction, and many inertia-less models have been used for force sensing [107, 60, 128, 165]; for example, Bajo and Simaan [160] developed a motion/force control algorithm assuming interaction forces (applied specifically at the tip) do not deform the continuum manipulator beyond circular bending for the segments. A deflection-based force sensing algorithm presented by Alici et al. [141] utilized Kalman filtering in a probabilistic approach to estimate forces applied at the tip. An intrinsic force sensing method was proposed by Xu and Simaan [75] to sense the wrench applied at the tip of continuum robot with 2 DoF bending motion.

III. *Elasticity versus hyperelasticity*

Low-modulus materials are favourable candidates for the core structure as they enable reduction of actuation forces; which, in addition to bio-compatibility [166] and safety [167], have made elastomers such as silicone a popular choice for the body. In this

regard, silicone has been used not only with tendons (as actuators) [104, 109, 139, 7] but also extensively in manipulators that entail actuators operating on the principle of fluidic expansion in chambers reinforced with inextensible fibres [168], constituting braided extensors [6, 117, 60, 84, 162, 169] or fibre-reinforced bending actuators [111] or hybrid actuation [144, 170]. Hence, hyperelastic modelling, using neo-Hookean (NH) [107, 111, 125, 126] or Yeoh [107] formulation, has received attention for soft component modelling, for example, in braided fluidic actuators. Trivedi et al. [125] applied the principle of virtual work to derive elongation for the braided extensor assuming neo-Hookean behaviour and used a Cosserat rod model resulting in a BVP, solving nonlinear equations via numerical methods to achieve VC kinematics for the planar 2D motion assuming infinite shear. Sadati et al. [125] proposed a geometry deformation model using PCC, where the bending of a braided pneumatic actuator is studied along with the effect of cross-section deformation and is compared with experimental results, entailing a method that is mathematically intensive.

2.2 Objectives & Contributions

For a soft continuum robotic appendage comprising braided extensors, we propose a forward kinematic, quasistatic, discrete VC model for real-time contact force sensing. This approach accounts for shear, torsion, bending, and extension, with its validity not restricted to training data. The model is spatial (3D) and computationally efficient for real-time simulation of position and deformation. In line with facilitating contact force sensing, external force can be applied theoretically at any arbitrary point on the body and not only at the tip (contrary to many models such as [107, 126, 142, 160, 165]), thus being practically beneficial for sensor-deprived environments and soft tactile sensing. In compliant robotic systems, the trend is to attach rigid force sensors at the end-effector [80]. Departing from such an approach, the proposed model demonstrates the intrinsic force sensing capability by comparing sensor data retrieved at the base with the calculated values. Position and force information propagate toward the proximal base and are retrievable at any selected point along the backbone via

discretization (based on a number of sections definable by the user). Structural inhomogeneity such as rigid inter-segment connective elements can be included. This approach is capable of reporting back on the pressure values from actuation, which is desirable for control strategies.

The real-time discretized approach allows us to include and exploit local information, in the form of internal constraints on the physical structure via the infinitesimal segments. Basically, rather than having "clean" equations via a closed-form approach, we "open up" the system to calculate the internal effects-but still get the same basic shapes and movements as generated by alternative approaches such as those obtained from beam theory. This proposed approach inherently computes internal forces/strains that, in cancelling out between the segments, do not directly cause motion, but do contribute to the mechanical stress imposed on the structure, enabling real-time monitoring of the health of the system.

The main contributions of this work are summarized as follows:

1. Developing a model for real-time pose and contact force estimation, based on discrete VC that benefits from simple forward spatial integration, capable of handling external and body loads, and estimating contact force at the tip or on any arbitrary point on the body.

2. Investigating the validity of elasticity compared with the conventionally used hyperelastic methods, and analysing whether the added complexity due to hyperelastic assumptions would assist the accuracy of continuum actuator models comprising braided extensors in such robotic platforms where only limited strains are produced.

2.3 Materials & Methods

2.3.1 Physical Structure

The soft robotic appendage developed in the EU FP7 project STIFF-FLOP is a cylinder of silicone made of Ecoflex® $00-50$ (Smooth-on, Inc.) with material properties shown in Table 2.1; with an overall length of 47 mm, outer diameter of 25 mm, and inner diameter of 9 mm. Embedded in the cylinder wall are three pairs of braided extensors (fibre-reinforced pressure chambers); aligned with the cylinder's longitudinal axis and mutually oriented at

Table 2.1 Technical properties of Ecoflex® 00 − 50 Supersoft Silicone[1]

Shore Hardness	Tensile Strength	Elongation at Break
00 − 50	315 psi	980%

120° from each other (Figure 2.3). Each pair of braided extensors is pneumatically actuated via a 2 mm outer diameter inlet air pipe; independent of the other two chamber pairs and therefore enabling the manipulator to bend by varying the air pressure in one chamber pair relative to the other two. A schematic procedure of casting the soft continuum appendage is depicted in Figure 2.2. Simultaneous pressurization of all chamber pairs elongates the manipulator. The central lumen enables the passing through of necessary actuation tubes in case of serially assembling multiple segments. A rigid hollow attachment of 3D-printed material is affixed at the tip for sensor connection. A more detailed description of the STIFF-FLOP manipulator is given in [6, 52].

2.3.2 Modelling Framework

The following assumptions are made throughout this approach:

1. Manipulator cross sections remain circular [21, 150].

2. Gravitational forces are ignored (verified in millimeter-sized continuum manipulators [107, 124, 75]) with no noticeable effect on the results for the given setup and experiments.

[1]Smooth-On, Inc. *Ecoflex® Series* Available on https://www.smooth-on.com/tb/files/ECOFLEX_SERIES_TB.pdf, Accessed on Feb. 2019.

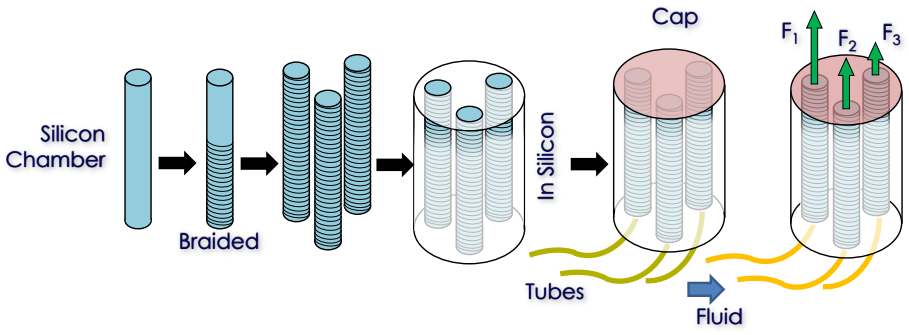

Fig. 2.2 *Schematic diagram of casting procedure of the braided soft continuum manipulator.*

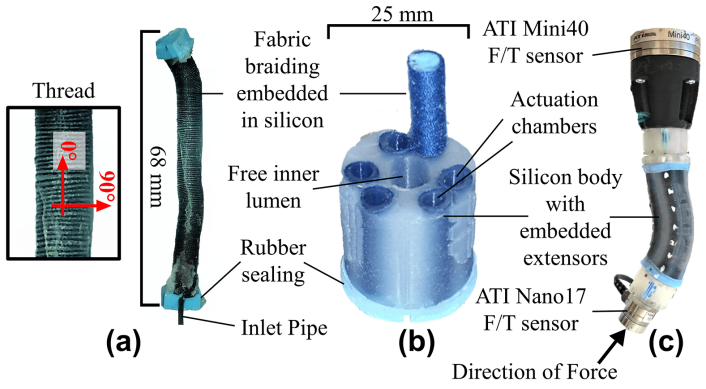

Fig. 2.3 *(a) A single braided extensor elongated due to pressurization via inlet air pipe, with the thread angle shown. (b) Cutaway of the body with one of the braided extensors (fluidic elastomer actuators) kept intact. (c) STIFF-FLOP manipulator, with ATI Nano17 and ATI Mini40 force sensors at the tip and base, respectively, and pressurized while applying force at the tip sensor.*

3. The chamber shell volume is constrained by the fiber braiding during its deformation [126].

4. PCC assumption is used only to calculate the incremental bending component between each pair of neighboring infinitesimally-distanced frames.

Pneumatic Braided Extensors. The intrinsic actuation of the robotic appendage is achieved via the braided extensors, which consist of silicone walls reinforced with fibre threads (Figure 2.3.a). Poisson's ratio (denoted by ν) is 0.499 for elastomers [171], which, given the relationship between Young's modulus (E) and the shear modulus (G) as $E = 2G(1+\nu)$, results in $E = 3G$, indicating incompressible isotropic material. Hence, the principal engineering stresses for each braided extensor are calculated as [111]:

$$\sigma_j = \frac{\partial u}{\partial \lambda_j} - p\lambda_j^{-1}; \qquad j = 1, 2, 3 \tag{2.1}$$

where u is the deformation energy density, p is the Lagrange multiplier, and the λ_j 's are the Cauchy-Green principal stretches constituting the first invariant of the right Cauchy-Green deformation tensor as $I_1 = \sum_{i=1}^{3} \lambda_j^2$. Incompressibility yields $\lambda_1\lambda_2\lambda_3 = 1$. Alternatively, the longitudinal stress in each braided extensor can be expressed as a function of internal

pressure P and axial forces as follows:

$$\sigma = Pr_n^2/(r_o^2 - r_n^2) + f_z \tag{2.2}$$

denoting the outer and inner radii as r_o and r_n, respectively, and the resultant boundary axial force as f_z (setting local z axis in chamber's axial direction). The volume of the chamber wall is $V_t = \pi(r_o^2 - r_n^2)l_1$, and volume of the area pressurized by air is $V_{ch} = \pi {r_n}^2 \lambda_2^2 l_1 \lambda_1$, where $l_2 = \lambda_1 l_1$and $r_2 = \lambda_2 r_{o,n}$ are the deformed length and radii (outer or inner), respectively. For utilizing the principle of virtual work, it is noted that the total deformation action is calculated by: $U = u.V_t$ and the total action of the actuation medium (air) is $W = P.V_{ch}$. For a 3D-distributed energy field in equilibrium, we can write the following:

$$\delta W = \delta U \tag{2.3}$$

Solving this equation results in the expression of stress as a function of the elongation, depending on the deformation energy density function as well as the chosen constraint for the Lagrange multiplier. We comparatively investigate three modelling frameworks:

1. **Hookean (H):** Each extensor is assumed to elongate according to Hooke's law,

$$\lambda_1 = (\sigma/E) + 1 \tag{2.4}$$

2. **Neo-Hookean (NH):** One of the most representative strain energy density mechanistic functions in this class [172] which is derived based on the underlying material structure,

$$u = E(I_1 - 3)/6 \tag{2.5}$$

3. **Gent (G):** A hybrid empirical/mechanistic yet mathematically simple model that captures the strain stiffening at large strains observed experimentally [173],

$$u = -\left(\frac{G}{2}\right) J_m \ln[1 - (I_1 - 3)/J_m] \tag{2.6}$$

where J_m is the constant value for limiting polymeric chain extensibility [173] such that $J_m + 3 = \lambda_m^2 + (2/\lambda_m)$ [171]. For Ecoflex-00 − 50, $\lambda_m = 9.8$ results in $J_m = 93.2$.

For the two hyperelastic models (NH and G), we investigate three types of constraints to solve Equation 2.1:

A. Uniaxial Extension (UNI), where $\lambda_1 = \lambda, \lambda_2 = \lambda_3 = 1/\sqrt{\lambda}$.

B. Inextensible Fiber (INF), where $\lambda_1 = \lambda$, $\lambda_1^2 C_\gamma^2 + \lambda_2^2 S_\gamma^2 = 1$ and $\gamma \in (0, \pi/2)$ is the braiding angle [168] (C_γ and S_γ represent $\cos\gamma$ and $\sin\gamma$, respectively), and $\lambda_3 = 1/\lambda_1\lambda_2$.

C. No Radial Deformation (NR), where $\lambda_1 = \lambda, \lambda_2 = 1, \lambda_3 = 1/\lambda$. It should be noted that this case is the simplified version of the previous case where the braiding angle is 90°, which is valid for a dense braiding [111, 126, 137].

A schematic display of the three constraints are shown in 2.4, where subfigure (a) depicts an isometric view of a braided extensor along with the direction of the three principal stretches; i.e longitudinal, radial, and circumferential. The uniaxial extension constraint (subfigure b) allows stretch in all three directions, governed by the relation mentioned in part A above . Inextensible fibre (subfigure c) constraint also permits stretch in all three directions, albeit with different magnitudes than the uniaxial extension constraint, formulated in part B. The constraint on no radial deformation (subfigure d) allows stretches in the longitudinal and circumferential directions yet restricts the radial deformation, as described in part C.

The NH model with constraints

A. Uniaxial Extension (NH-UNI): The engineering stress is calculated as $\sigma = G(\lambda - 1/\lambda^2)$. The relationship is rearranged to $\lambda^3 - (\sigma/G)\lambda^2 - 1 = 0$ and solved for λ using the cubic equation as follows:

$$\begin{aligned}\lambda = &\left[\frac{\sigma^3}{27G^3} - \left(\left(\frac{\sigma^3}{27G^3} + \frac{1}{2}\right)^2 - \frac{\sigma^6}{729G^6}\right)^{\frac{1}{2}} + \frac{1}{2}\right]^{\frac{1}{3}} \\ &+ \left[\frac{\sigma^3}{27G^3} + \left(\left(\frac{\sigma^3}{27G^3} + \frac{1}{2}\right)^2 - \frac{\sigma^6}{729G^6}\right)^{\frac{1}{2}} + \frac{1}{2}\right]^{\frac{1}{3}} + \frac{\sigma}{3G}\end{aligned} \tag{2.7}$$

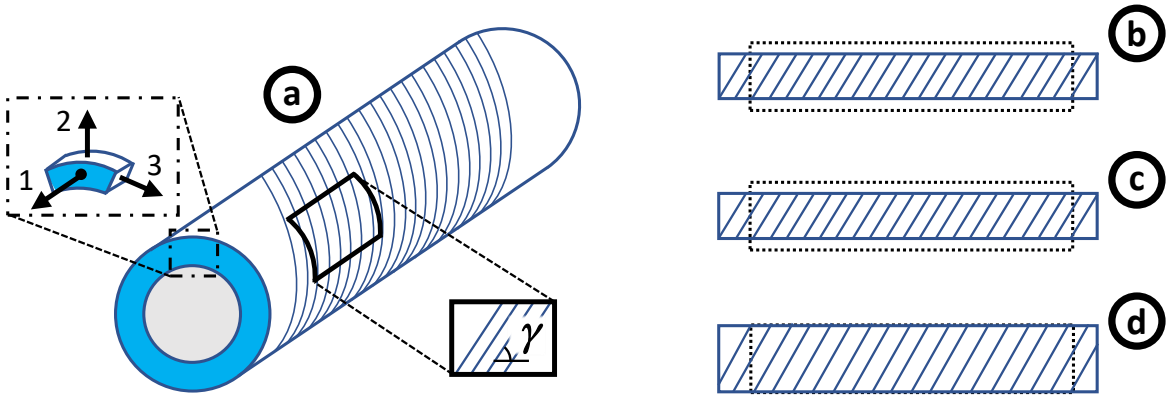

Fig. 2.4 *Braided Extensors Constraints: a) Isometric schematic view of a braided extensor with γ denoting the thread angle, and the directions of the 3 principal stretches. b,c,d) Schematic side view of undeformed (dotted) and deformed braided extensor w.r.t the 3 types of constraints; with b) uniaxial extension where stretches in the 3 principal directions are possible. c) inextensible fibre extension where stretches in the 3 principal directions are possible. d) no-radial extension, where longitudinal and circumferential stretches are possible and the radial stretch is restricted.*

B. Inextensible Fiber (NH-INF): The engineering stress is calculated as:

$$\sigma = 2G(1-\lambda^2)\Big[\Big(1-2S_\gamma^6+5S_\gamma^4-4S_\gamma^2\Big)\lambda^6+\Big(7S_\gamma^6-16S_\gamma^4+11S_\gamma^2-2\Big)\lambda^4 + \Big(7S_\gamma^6-4S_\gamma^4-3S_\gamma^2+1\Big)\lambda^2+3S_\gamma^4\Big]/\lambda^4\Big(\lambda^2C_\gamma^2-1\Big)^3 \tag{2.8}$$

C. No Radial Deformation (NH-NR): The engineering stress is calculated as $\sigma = G(\lambda^2 - 1)(\lambda^2+3)/2\lambda^4$. The relationship is rearranged to $(2\sigma/G-1)\lambda^4 - 2\lambda^2 + 3 = 0$ and solved for λ using the bi-quartic equation as follows:

$$\lambda = \Big[-\Big(\sqrt{(4-6\sigma/G)}-1\Big)/(2\sigma/G-1)\Big]^{0.5} \tag{2.9}$$

The Gent model with constraints

A. Uniaxial Extension (G-UNI): The engineering stress is calculated as follows:

$$\sigma = GJ_m(\lambda^3-1)/\Big[\lambda(-\lambda^3+\lambda J_m+3\lambda-2)\Big] \tag{2.10}$$

This equation is numerically solved for λ (up to the range of $\lambda = 2$) as follows:

$$\lambda = -0.015(\frac{\sigma}{G})^3 + 0.17(\frac{\sigma}{G})^2 + 0.31(\frac{\sigma}{G}) + 1 \tag{2.11}$$

B. Inextensible Fiber (G-INF): The engineering stress as a function of elongation and the braiding angle is expressed in the addendum 2.8 at the end of this chapter.

C. No Radial Deformation (G-NR): The engineering stress is calculated as follows:

$$\begin{aligned}\sigma = GJ_m\Bigg[&(\lambda^4 - 1)/(J_m\lambda^4 - \lambda^6 + 2\lambda^4 - \lambda^2) \\ &+ (1/2\lambda^2)\left(\ln\left(1 - \left(\lambda - \frac{1}{\lambda}\right)^2/J_m\right)\right)\Bigg]\end{aligned} \tag{2.12}$$

This equation is numerically solved for λ (up to the range of λ= 1.8) as follows:

$$\lambda = 0.9549e^{0.5157(\sigma/G)} + (7.16 \times 10^{-11})e^{32.98(\sigma/G)} + (4.5 \times 10^{-2}) \tag{2.13}$$

Continuum Manipulator Model. Considering the entire body, the manipulator model is discretized into serially connected infinitesimal sections to generate a small-deflection beam [174] between each section. We denote the initial element length as ξ_0. Starting from the distal tip to the proximal base, a Cosserat rod model can be used to formulate the Newtonian force equilibrium on each infinitesimal element, where each of these local deflections contributes to the final configuration as a whole by integrating over volume for the quasistatic case, eventually leading to an overall VC behaviour.

The incremental elongated length of the backbone in each section is calculated as the summation of all chambers' new lengths divided by three:

$$\delta s_b = \frac{\sum_{i=1}^{3}[\xi_{0,i}(1 + \lambda_i)]}{3} \tag{2.14}$$

The local bending moment vector due to internal actuation at each section, with regard to the backbone of the manipulator, is calculated by the cross product of the distance to the

centre: $\boldsymbol{M}_i = \boldsymbol{d} \times \sum \boldsymbol{F}_i$, where $\boldsymbol{F}_i$ is the force due to intrinsic actuation. The local bending moment vector due to external load at each section is calculated by the following:

$$\boldsymbol{M}_e = \delta s_b [0, 0, -1]^T \times \boldsymbol{F}_e \tag{2.15}$$

where $\boldsymbol{F}_e$ is the total boundary load at each incremental section, being transferred from the previous section. Therefore, the total local moment is calculated as $\boldsymbol{M}_{tot} = \boldsymbol{M}_e + \boldsymbol{M}_i$. Projecting this moment vector onto its local Cartesian components delivers curvature/torsion in the local frame, $\boldsymbol{k}_{\xi_i}$, along the backbone. The local strain caused by internal and external load is denoted as $\boldsymbol{\varepsilon}_{\xi_i}$. To derive the system differential mechanics, the curvilinear path can be considered a concatenation of infinitesimal elements. The VC kinematics is expressed with the following two differential equations for the Cartesian position vector $\boldsymbol{\rho}(s)$ and rotation matrix $\mathbf{R}(s)$ of each point along the backbone with regard to $\boldsymbol{\varepsilon}$ and $\boldsymbol{k}$ (the dependency of the terms on s are omitted hereafter for brevity). Hence,

$$\begin{aligned} \boldsymbol{\rho}_{,s} &= \mathbf{R}(\boldsymbol{\varepsilon} + [0, 0, 1]^\top) ds \\ \mathbf{R}_{,s} &= \mathbf{R}\ [\boldsymbol{k}]_\times \end{aligned} \tag{2.16}$$

where $y_{,x} = \partial y / \partial x$ and $[\boldsymbol{x}]_\times = \mathbf{X}$, an operator creating a skew-symmetric matrix $\mathbf{X}$ from a vector $\boldsymbol{x}$. The set of differential equations in 2.16 is to be numerically integrated over the spatial domain. For such equations, optimization-based methods, approximate continuous solutions, and FEM are conventionally used. Alternatively, by considering a fixed number of elements n_s with length $\delta s = s_{total}/n_s$, we can rewrite equation 2.16 in the discrete form as follows:

$$\begin{aligned} \boldsymbol{\rho}_{(i+1)} &= \boldsymbol{\rho}_{(i)} + \mathbf{R}_i(\boldsymbol{\varepsilon}_i + [0, 0, 1]^\top) \delta s \\ \mathbf{R}_{(i+1)} &= \mathbf{R}_i + \mathbf{R}_i\ [\boldsymbol{k}_i]_\times \delta s \end{aligned} \tag{2.17}$$

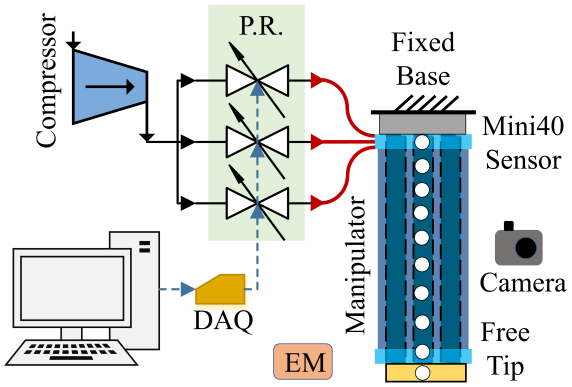

Fig. 2.5 *The setup consists of an air compressor, three P.R., DAQ board, camera, visual markers, EM tracking system, and the manipulator, interconnected with necessary tubing and wiring. DAQ, data acquisition; P.R., pressure regulators*

The transformation matrix from one section to the other is composed as follows:

$$\mathbf{T}_{i+1} = \begin{bmatrix} \mathbf{R}_{(i+1)} & \boldsymbol{\rho}_{(i+1)} \\ \mathbf{0}^T & 1 \end{bmatrix} \tag{2.18}$$

where $\mathbf{0}$ denotes the 3×1 zero vector. Finally, the overall transformation matrix from the tip to the base is formed as a multiplication of all transformations:

$$\mathbf{T}_n^0 = \left(\prod_{n-1}^{0} \mathbf{T}_{tot} \right) \mathbf{T}_n^{n-1} \tag{2.19}$$

where $\prod$ is the post-multiplication operator. The inverse of the final product, $(\mathbf{T}_n^0)^{-1}$, multiplied by the previously stored $3 \times n$ matrix of coordinates would transform all coordinates to the base-frame representation; that is, the first frame becomes the base, and the last frame becomes the distal tip. An alternative method for forming the transformation matrices in this discretized setup is provided in the addendum 2.9 at the end of this chapter.

2.3.3 Setup

The effectiveness of the above modelling strategy is demonstrated via experiments. The schematic interconnection of the setup's main components is depicted in Figure 2.5.

Pressurized air from the compressor (BAMBI MD Range Model 150/500) is supplied to three individual pressure regulators (SMC ITV0030-3BS-Q), with their outlet each separately connected to one of the dual chambers in the manipulator for adjusting the pressure to achieve manipulator operation in a feedforward approach, according to the command received from the computer (64-bit Windows 10; Intel Core i7 CPU@ 3.4 GHz; 64GB RAM) through a data acquisition board (NI USB-6211). One Aurora sensor (NDI) is placed at the fixed base and the other at the tip for tracking the spatial tip position. Monitoring the overall pose is made possible by marking an additional 8 points on the body, which are recorded via two cameras (Canon EOS D60) facing the manipulator from two directions perpendicular to each other, and the progression of the marked points are monitored via the open source program Tracker 4.96 (www.opensourcephysics.org). The diameter of the marked points averaged at 1.5 mm and tracked with ≈ 0.5 mm tolerance. An ATI Mini40 force sensor reads the resultant forces at the fixed base (Figure 2.3.c). The data acquisition software is coded in C#.

Initially, we consider the deformation, both in the absence and in the presence of external loads. We characterize E considering the different modelling assumptions discussed earlier. Thereafter, the manipulator is used for contact force estimation based on the obtained results from the previous stage. For tip force sensing, external force is applied at an ATI Nano17 force sensor affixed to the tip (Figure 2.3.c). For sensing forces applied on the body, the ATI Nano17 force sensor is mounted on an external indenter to exert force on the body of the manipulator (Figures 2.12, 2.13, 2.14, 2.15). In both cases, the manipulator is actuated in various configurations and is deformed further by applying external force. We record the applied force in addition to the force measured at the base (via ATI Mini40 force sensor) while tracking the body deformation. Both force sensors are connected to the computer via NI PCIe-6320 I/O cards.

2.4 Experiments & Analysis

In the following, we empirically discretized the length of 47 mm of the robotic appendage to 100 sections for all simulations. It was observed that decreasing the number of sections to

less than 30 tends to demonstrate more deviations, while above 50 sections, the results are tangentially closer to 100 sections and deliver benign results.

2.4.1 Elasticity versus hyperelasticity in braided extensor model

A closer look into the hyperelastic models reveals that as the thread angle is increased, the INF constraint demonstrates closer resemblance to the NR constraint in both the neo-Hookean and Gent models, ultimately becoming the same in its limit at 90° (depicted in Figure 2.6 for the Gent model, setting E as a free parameter varying from 60 to 180 kPa). Decreasing the thread angle less than $\approx 70°$ in a single-braid configuration is usually not practised, as it also undermines the primary role of reinforcement against radial expansion. As seen, 100% elongation ($\lambda = 2$) is achieved at a higher internal pressure when the thread angle is smaller, compared with thread angles closer to 90°. Inspection of the thread on the braided extensor in Figure 2.3.a demonstrates dense braiding where the assumption of 90° for the thread angle is reasonable. Hence, we only examine UNI and NR constraints in both hyperelastic models. Moreover, the asymptotic progression in Figure 2.6.f (thread angle 90°) shows that

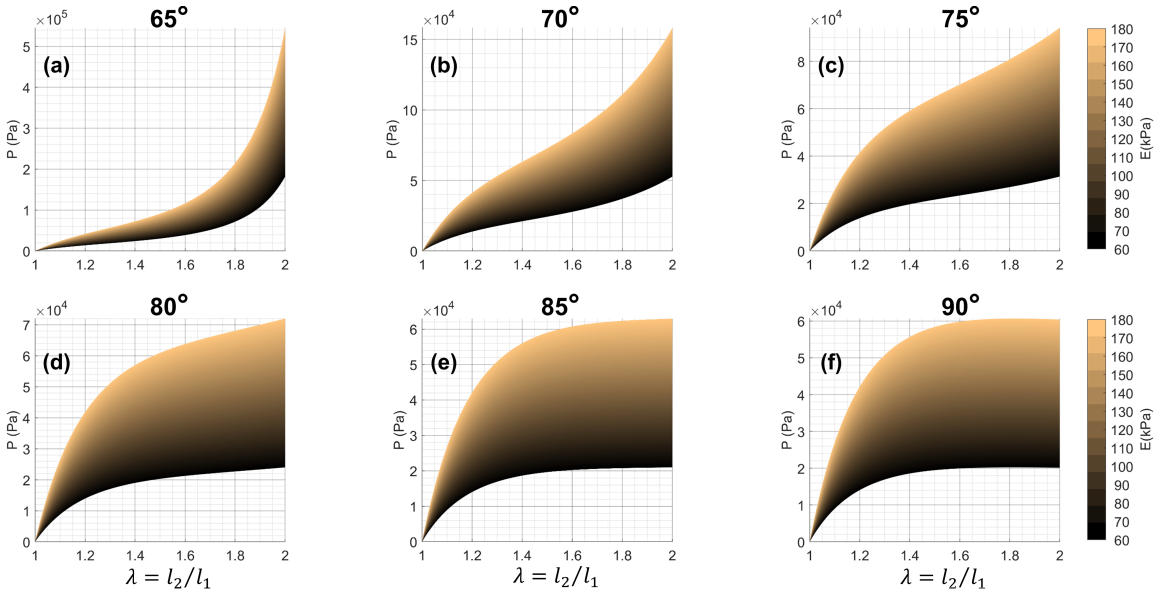

Fig. 2.6 *Gent model with INF constraint-plotting internal pressure (Pa) versus stretch (λ), showing progression of the enveloped area (range of $E = 60 - 180$ kPa) as the braiding angle is increased from 65° (a) to 90° (f). l_1 and l_2 are the initial and extended length, respectively. Thread angle is shown in Figure 2.3a. INF, inextensible fibre.*

depending on the value of E, there exists a threshold internal pressure where the stretch (λ) perpetually increases, demonstrating how the model predicts continuous unwinding of the chain polymers when the radial deformation of the chamber is fully constrained. Hence, using the hyperelastic models requires caution when dealing with the NR constraint.

2.4.2 Elasticity versus hyperelasticity in soft manipulator model

No external load. The robotic appendage is actuated in nine stages by giving an input voltage of 1 V to each pressure regulator in turn, then increasing to 2 V, and finally to 3 V. The average pressure outlets corresponding to these voltages are tabulated in Table 2.2. The excitation input voltages versus time are shown in Figure 2.7.

The tip spatial coordinates and the bending angle are recorded. To determine how well the observed results are replicated by the model, the coefficient of determination (R^2) for the

Table 2.2 Air Pressure ($Pa \times 10^5$) Outlet From Each Pressure Regulator Resulting From The Corresponding Input Signal (V)

Input Signal (V)	*Air pressure outlet ($Pa \times 10^5$) from each P.R.*		
	PR1	**PR2**	**PR3**
1	0.45	0.35	0.45
2	0.92	0.87	0.91
3	1.33	1.38	1.38

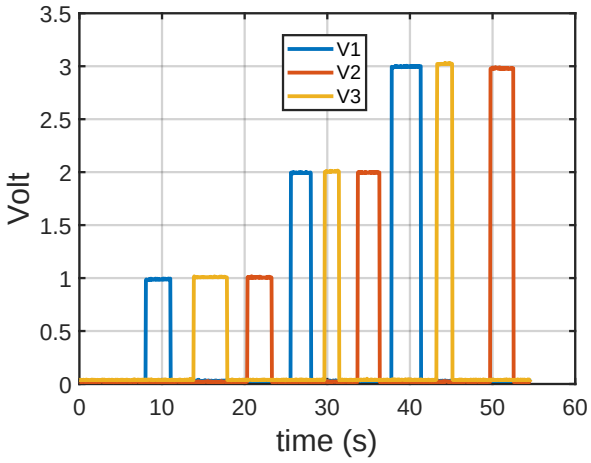

Fig. 2.7 *Excitation voltage of the three pressure regulators. The corresponding pressure values are tabulated in Table 2.2*

coordinates and the bending angle between the simulations and experiments are depicted in Figure 2.8, in which we set E as a free parameter varying from 60 to 180 kPa.

In all cases, the highest values of R^2 (close to 1) correspond to an E in the range of $100 - 140$ kPa. As it can be seen, the z coordinate displays sharper changes compared with the x, y coordinates especially at lower E values as opposed to higher values where the R^2 conformity degenerates at a slower rate, indicating higher sensitivity at lower values of Young's modulus. This could be attributed to the material constructing the robotic appendage body being more distributed along the z axis compared with x and y, which holds true even in a bent configuration on average. Selecting $E = 130$ kPa, we plot the test results of measured tip coordinates against the simulation using the Hooke relationship.

The absolute displacements are depicted in Figure 2.9a for each of the coordinates. The initial offset in the coordinates is due to the placement of the Aurora tracker. The absolute error for each coordinate is shown in Figure 2.9(b-d). The coefficient of determination is calculated as $R_x^2 = 0.998$, $R_y^2 = 0.998$, $R_z^2 = 0.994$, and $R_\theta^2 = 0.995$, indicating very high conformity between experimental measurements and simulation results as the robotic

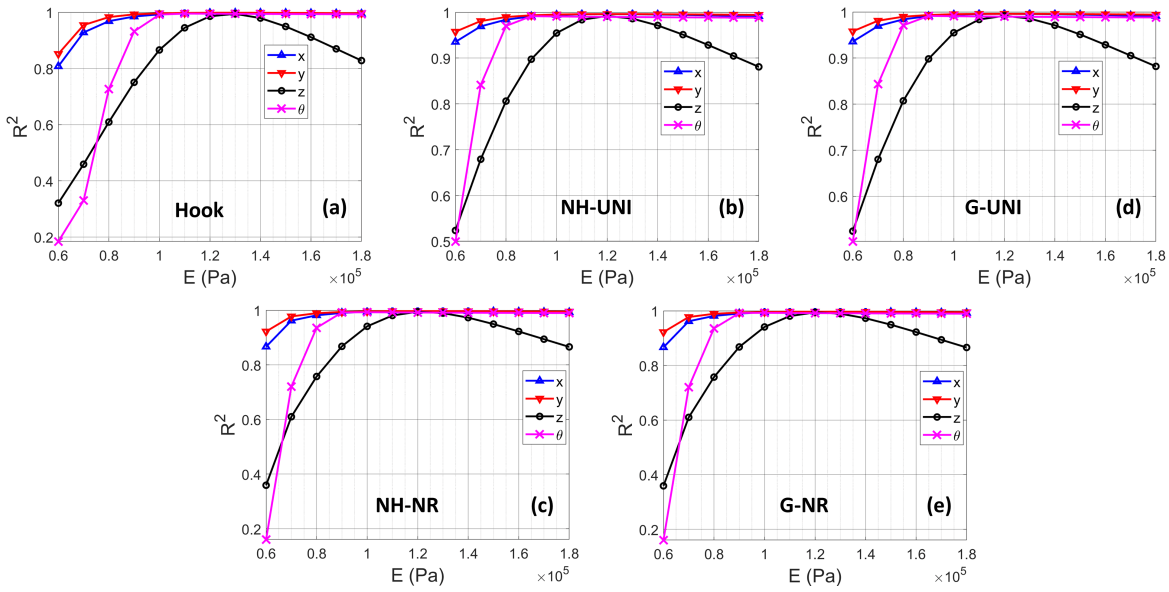

Fig. 2.8 *Experiments with no load, showing R^2 of tip coordinates between results from simulations and experiments across variations of E: (a) Hooke, (b) neo-Hookean uniaxial, (c) neo-Hookean no radial, (d) Gent uniaxial, (e) Gent no radial.*

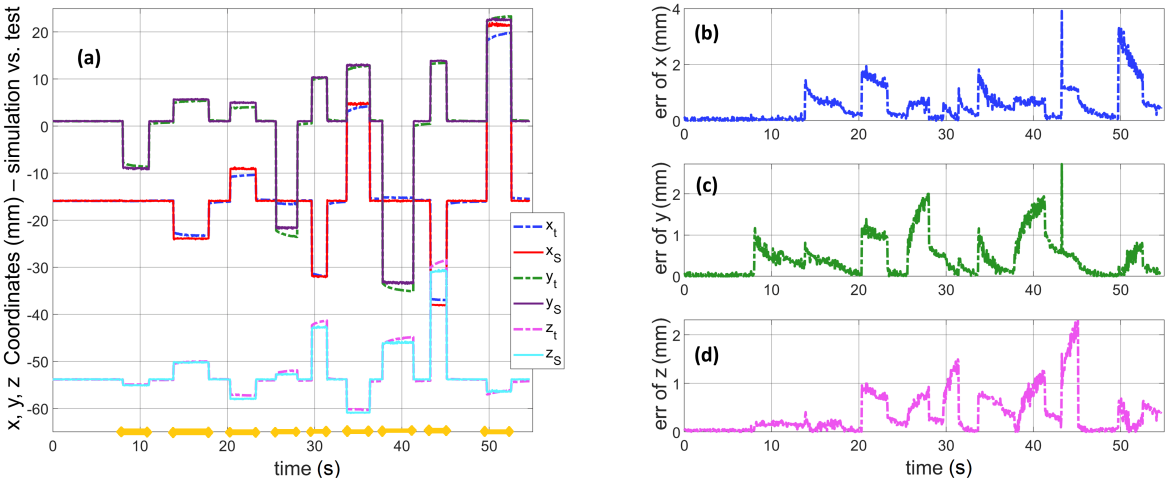

Fig. 2.9 *(a) Tip coordinates from test "t" compared against simulation "s". (b-d) The error in all three coordinates. Hooke model, setting* $E = 130\,\text{kPa}$. *No load; with nine stages of actuation marked on the horizontal axis of (a).*

appendage is actuated. With the manipulator discretized into 100 sections, the simulation operates at an execution rate of 170 Hz in MATLAB with no noticeable difference between the investigated methods.

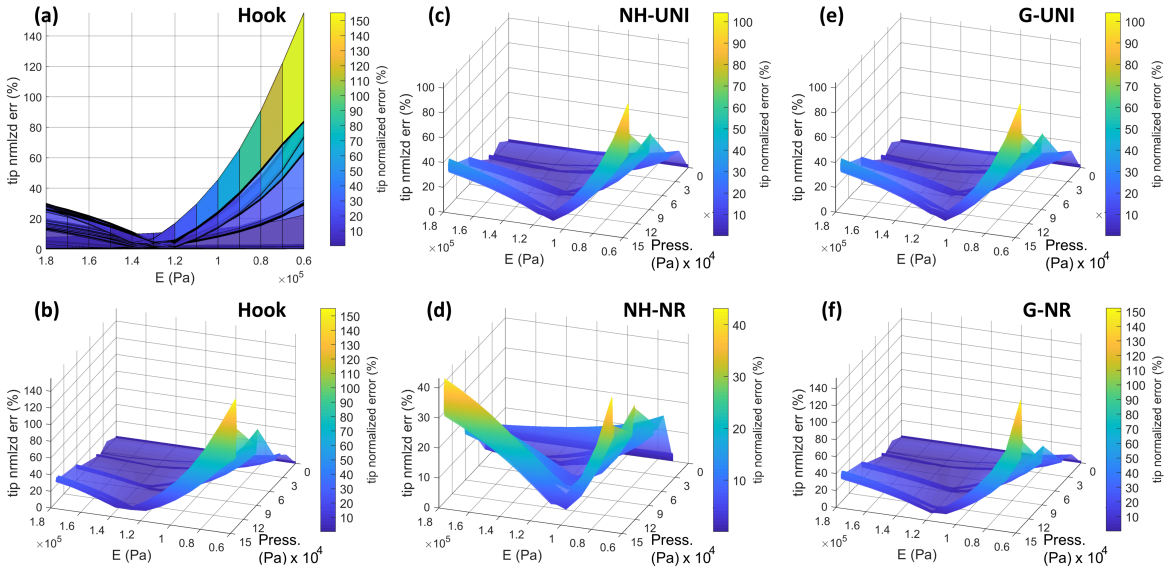

Fig. 2.10 *Normalized tip error versus pressure across variation of E: (a) Hooke (y − z view), (b) Hooke, (c) neo-Hookean uniaxial, (d) neo-Hookean no radial, (e) Gent uniaxial, (f) Gent no radial. No load.*

The normalized tip error is calculated by measuring the error vector divided by the manipulator's initial length [125, 126]. To create a unique pressure metric, the three pressure values are treated as components of a pseudo-vector, and the norm is calculated. Figure 2.10 demonstrates how the tip normalized error changes with the norm of the pressure vector (from 0 to 1.5 bar), across a variation of E from 60 to 180 kPa.

As pressurizing the soft appendage follows a similar sequence in all braided extensors (Figure 2.7), the sensitivity analysis to the variation of E is performed w.r.t one braided extensor with the pressurization profile of $P1$, as shown in Figure 2.11. The darker region in blue represents the Young's moduli which yielded the least error for each model; referring to its respective subfigure. These results do not demonstrate a noticeable difference than Figure 2.10 where the cumulative effect of internal pressure was considered using the magnitude of the pseudo pressure vector.

As expected, the error at the tip increases at higher pressures; however, where the value of E corresponds to the lowest error (in the range of $100 - 140$ kPa), a more uniform distribution of error with the increase of pressure is witnessed, forming a trough in the 3D surfaces in Figure 2.10. Taking the Hookean model as an example, a clearer demonstration is shown in

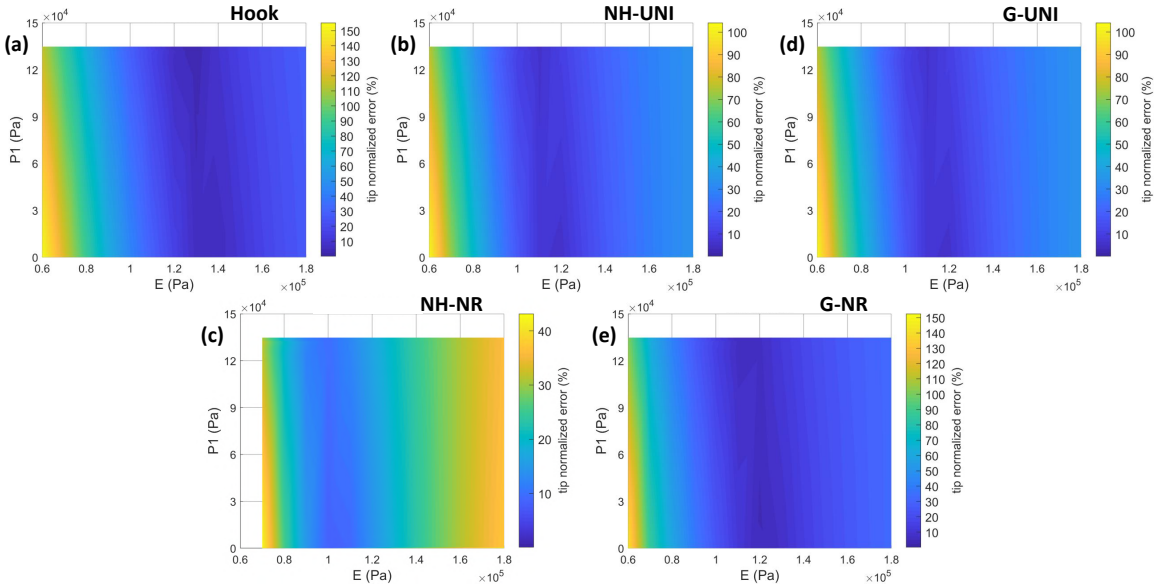

Fig. 2.11 *Normalized tip error versus pressure of one braided extensor across variation of E: (a) Hooke, (b) neo-Hookean uniaxial, (c) neo-Hookean no radial, (d) Gent uniaxial, (e) Gent no radial. No load.*

Figure 2.10a, which is a 2D view of the graph in Figure 2.10b, at $E \approx 130\,\text{kPa}$. These graphs also reaffirm that change of E at its lower levels affects the error more severely compared with at its higher values (above $\approx 130\,\text{kPa}$).

External load. Tests with external load were performed with load applied in various configurations; at the tip (Figure 2.3c), and on the body at the first, second, third, and fourth quarter of its length (Figures 2.12, 2.13, 2.14, 2.15). The ATI Nanol7 recorded the applied force and the ATI Mini40 recorded the forces measured at the base. The overall pose was observed by tracking 10 points on the body. The range of external load varied in different configurations from 0.46 N up to 1.79 N based on the contact point and deformation, with a more detailed report in the following section. The robotic appendage was initially activated via pressurization and the overall pose was recorded. Applying an external force caused additional deformation. In all cases of the elastic and hyperelastic assumptions detailed earlier, we calculated the normalized error of all 10 points on the body, which is averaged at each location over all tests and depicted in Figure 2.16 on the vertical axis ($0 - 30\%$), across the variation of E from 60 to 180 kPa and the initial distance from tip ($0 - 60\,\text{mm}$). At any chosen value for E, the error increases from base to tip (which is expected) in all graphs. The error variations at the tip across E lead to a convex profile. Closer inspection reveals

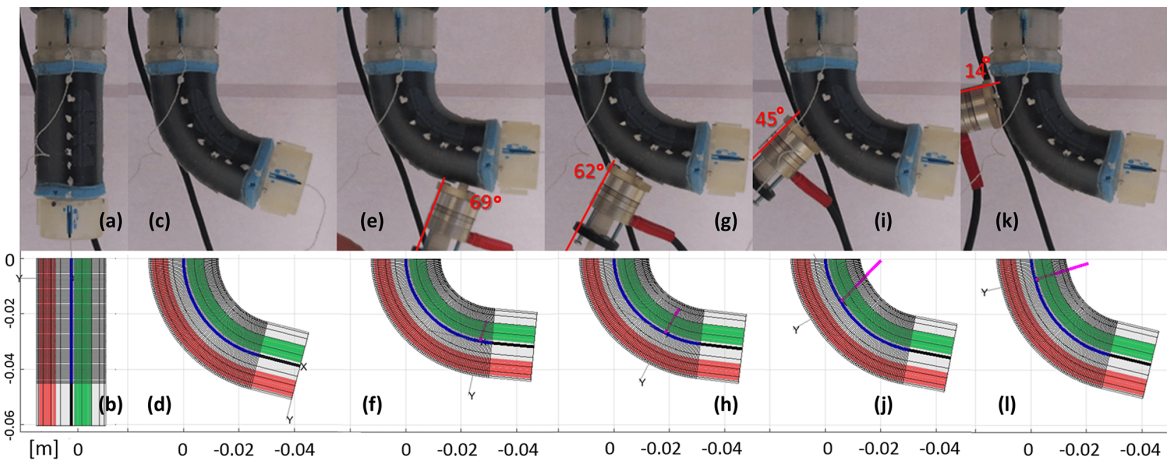

Fig. 2.12 *Applying an external load along the body in bent configuration on the first, second, third, and fourth quarters with the Nanol7 affixed to an external indenter, along with simulation results. Images (a, b) show the initial configuration, (c,d) show pressurized configuration w/o external load, (e-l) show pressurized configuration with external load.*

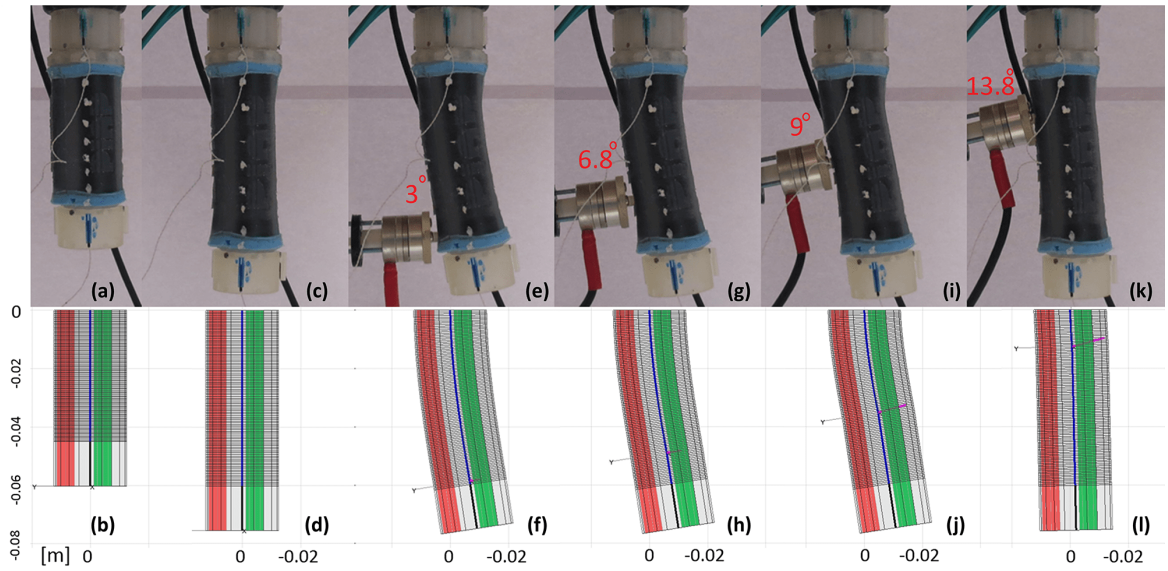

Fig. 2.13 *Applying an external load along the body on the first, second, third, and fourth quarters, in a straight elongated configuration, along with simulation results. Images (a, b) show the initial configuration, (c,d) show pressurized configuration w/o external load, (e-l) show pressurized configuration with external load.*

that the curve minimum not only indicates the E value yielding the least amount of error at the tip (in the range of $100 - 140$ kPa for the different cases) but also across the length of the manipulator, forming a trough in the corresponding 3D surface. Taking the Hooke approach as an example, this could be observed around an E of almost 130 kPa, shown in Figure 2.16a.

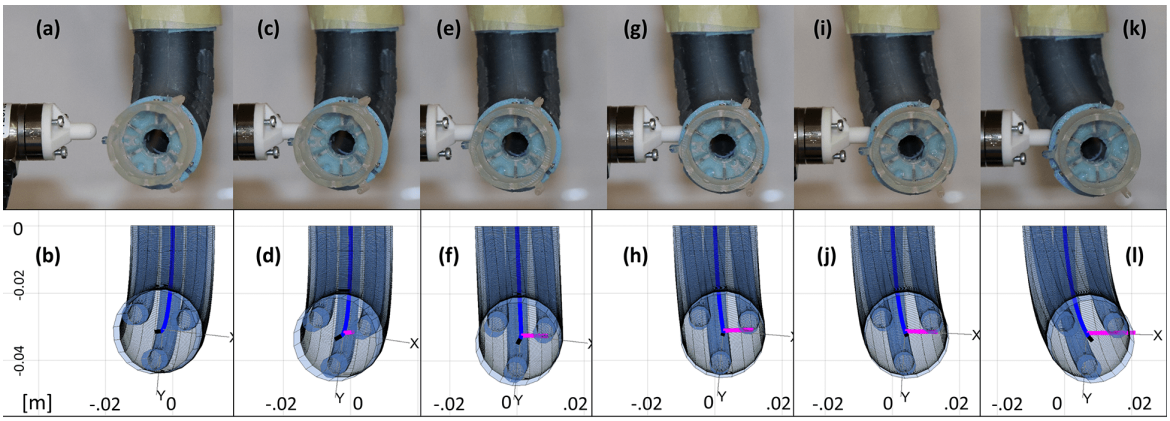

Fig. 2.14 *Applying an external load along the body on the first quarter of soft appendage length from the tip, in a bent configuration, along with simulation results. (a,b) Show initial pressurized configuration without external load, (c-l) show pressurized configuration with external load.*

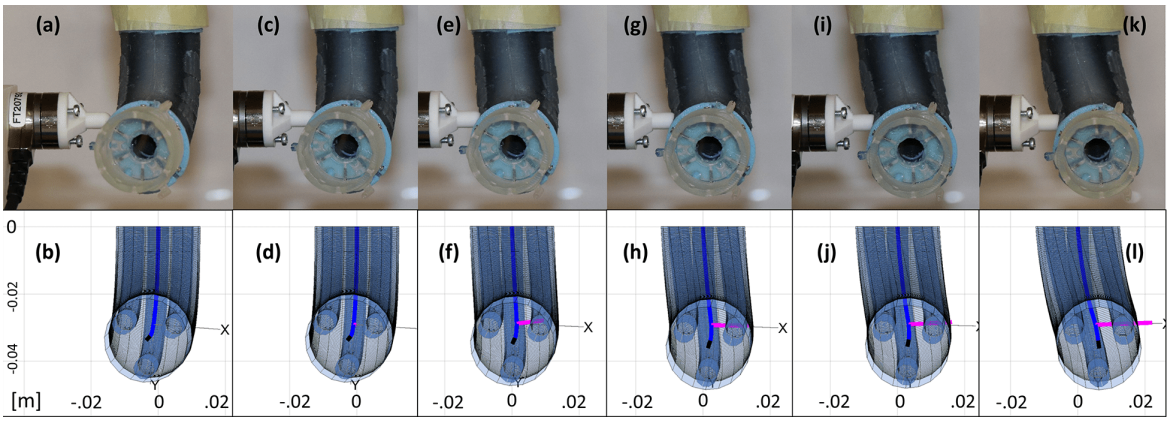

Fig. 2.15 *Applying an external load along the body on the second quarter of soft appendage length from the tip, in a bent configuration, along with simulation results. (a,b) show initial pressurized configuration without external load, (c-l) show pressurized configuration with external load.*

As seen before, variation of E at lower values (in the range of 60 to $\approx 100\,\text{kPa}$) affects the error more than at the higher E values, demonstrating higher sensitivity to lower Young's Moduli. Figure 2.17a, c, e, g, i summarizes the simulation results for all categories discussed earlier. The normalized error is plotted for the tip (considering three cases: no external load, external load at tip, and external load on body) on the vertical axis, and for all tracked points on the body (with force at the tip and force on the body). The standard deviation of the normalized error of all recorded points is shown in Figure 2.17b, d, f, h, j for tip load and body load cases, demonstrating lower values in the range of $100 - 140\,\text{kPa}$ for E, depending

Table 2.3 Young's Modulus Corresponding to The Least Normalized Errors and STD of Different Models.
[a] Average normalized error across body; [b] STD of normalized error across the body; [c] Average normalized tip error. NH, neo-Hookean; NR, no radial deformation; STD, standard deviation; UNI, uniaxial extension.

	External load at tip						*External load on the body*						*No external load*	
	%[a]	*E*	[b]	*E*	%[c]	*E*	%[a]	*E*	[b]	*E*	%[c]	*E*	%[c]	*E*
Hooke	5.3	140	2.2	130	6.3	130	2.7	130	1.0	130	4.3	130	1.8	130
NH														
UNI	6.6	120	2.6	120	7.8	110	4.1	110	1.5	110	5.6	110	2.6	110
NR	7.4	130	2.9	120	9.8	110	5.7	100	2.6	95	8.9	95	3.4	110
G														
UNI	6.6	120	2.6	120	7.8	110	4.1	110	1.5	110	5.7	110	2.6	110
NR	6.2	120	2.4	120	7.1	120	3.9	110	1.4	110	4.6	110	2.1	120

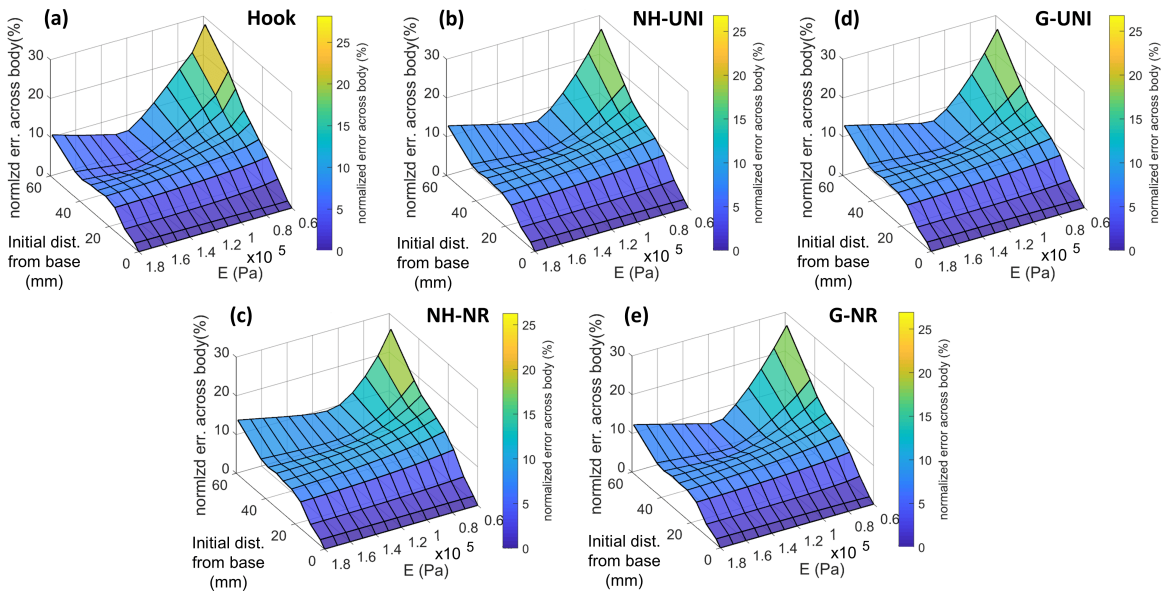

Fig. 2.16 *Experiments with external load on the robotic appendage. Variation of normalized error of 10 points along the body (from tip to base) along different Young's Moduli. (a) Hooke, (b) neo-Hookean uniaxial, (c) neo-Hookean no radial, (d) Gent uniaxial, (e) Gent no radial.*

on the model. As seen, loading applied to the body tends to result in a sharper sensitivity to the variation of E. The results are summarized in Table 2.3. In all columns, the Young's modulus which corresponded to the least error or least standard deviation, respectively, is presented.

In general, it can be seen that the Hooke formulation provides results with the least error compared with the neo-Hookean and Gent hyperelastic models.

2.4.3 Force estimation

Based on the results obtained, we select the Hooke formulation for contact force estimation. Four general cases were investigated as follows. In all cases, the simulation runs at an execution rate of about 170 Hz in MATLAB with the robotic appendage being discretized into 100 sections.

External load applied at the tip (Case 1). For this case, the robotic appendage was actuated via the three P.R., in turn according to the nine separate schemes in Figure 2.18a, and force was applied at the Nano17 force sensor affixed at the tip. The average of the maximum applied force across the nine schemes is 1.35 N, and the total average of the

Fig. 2.17 *Normalized error of tip and entire body for (a) Hooke, (c) neo-Hookean UNI, (e) neo-Hookean NR, (g) Gent UNI, (i) Gent NR; STD of tip and entire body for (b) Hooke, (d) neo-Hookean UNI, (f) neo-Hookean NR, (h) Gent UNI, (j) Gent NR. NR, no radial deformation; STD, standard deviation; UNI, uniaxial extension.*

(a)

Actuation Scheme No.	Input signal (v)	Pressure Regulator No. P.R.1	P.R.2	P.R.3
1		1	0	0
2		1	1	0
3		1	1	1
4		2	0	0
5		2	2	0
6		2	2	2
7		3	1	0
8		3	3	0
9		3	3	3

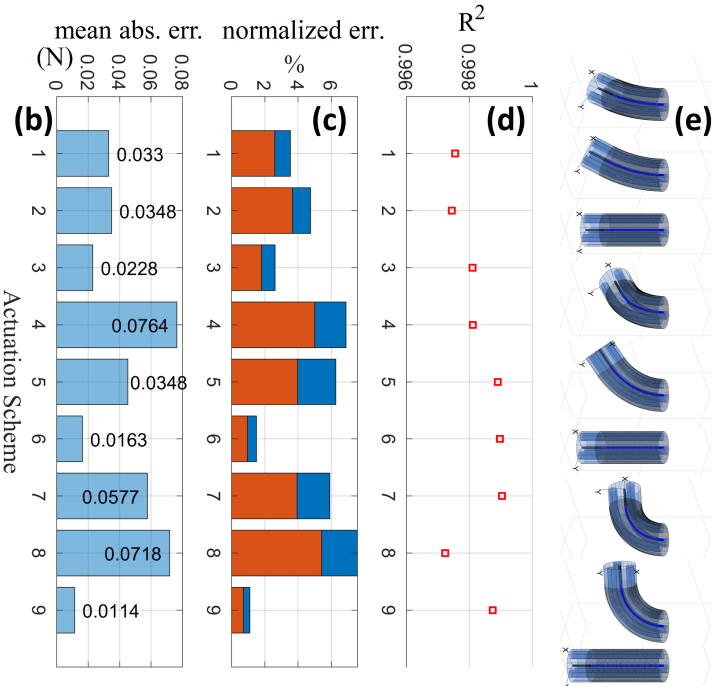

Fig. 2.18 *Load at the tip:(a) the three P.R. are activated according to the tabulated nine schemes. (b) Mean absolute error (MAE). (c) MAE/F_{max} (red), and MAE/F_{ave} (blue). (d) R^2 of model with regard to test. (e) Simulated activation schemes.*

applied force is 0.94 N. The mean absolute error (MAE) in each actuation scheme, plotted in Figure 2.18b, is calculated as follows:

$$MAE = \frac{\sum_{i=1}^{n} |e_i|}{n}$$

where e_i; is the error between sensor reading and model estimation at each sensor reading cycle i, during all n cycles. The normalized error in each scheme is calculated by two methods: with regard to the maximum force, according to (MAE/F_{max}); and with regard to the average amount of force, according to (MAE/F_{ave}), displayed in Figure 2.18c. The coefficient of determination, R^2, is depicted in Figure 2.18d.

External load applied to the body (Case 2). For this case, the P.R. were actuated to generate maximum bend, according to Figure 2.19a. Considering four quarters along the robotic appendage's length, an external load was applied on the body within each quarter of the length in tum, from the distal end toward the base (Figure 2.19e), constituting four force

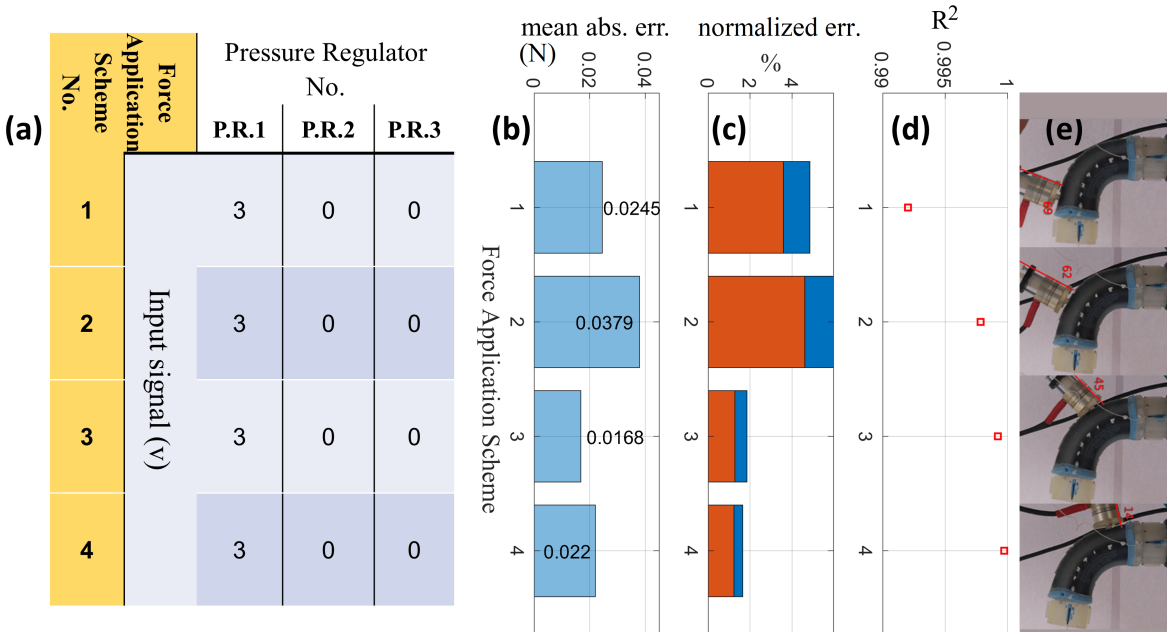

Fig. 2.19 *Load on the body:(a) in all four schemes of applying load, the three P.R. are activated according to the table for maximum bending. (b) Mean absolute error (MAE). (c)* MAE/F_{max} *(red), and* MAE/F_{ave} *(blue). (d)* R^2 *of model with regard to test. (e) Simulated activation schemes.*

application schemes. The average of the maximum applied force across the four schemes is 1.15 N, and the total average of the applied force is 0.85 N. Similar to the previous case, the mean absolute error, normalized errors, and R^2 are calculated, and displayed in Figure 2.19.

Stepwise lateral external load (Case 3). To demonstrate the effectiveness of the model prediction with regard to the out-of-plane applied load, the robotic appendage was actuated to maximum bending and an external load was laterally applied via an indenter, at the tip and on the body (in turn within the first and second quarters of the length from the tip). The magnitude of the load was increased during four steps. The average of the maximum applied force across the three schemes is 1.0 N, and the total average of the applied force is 0.51 N. The mean absolute error, normalized errors, and R^2 are calculated, and displayed in Figure 2.20. The results of all three cases (Case 1, Case 2, Case 3) are summarized in Table 2.4. Considering the three mentioned cases, the maximum normalized error with regard to the averaged applied force is less than 8% and we witness very high values of above 0.99 for R^2, demonstrating high accuracy of the model predicting the external load.

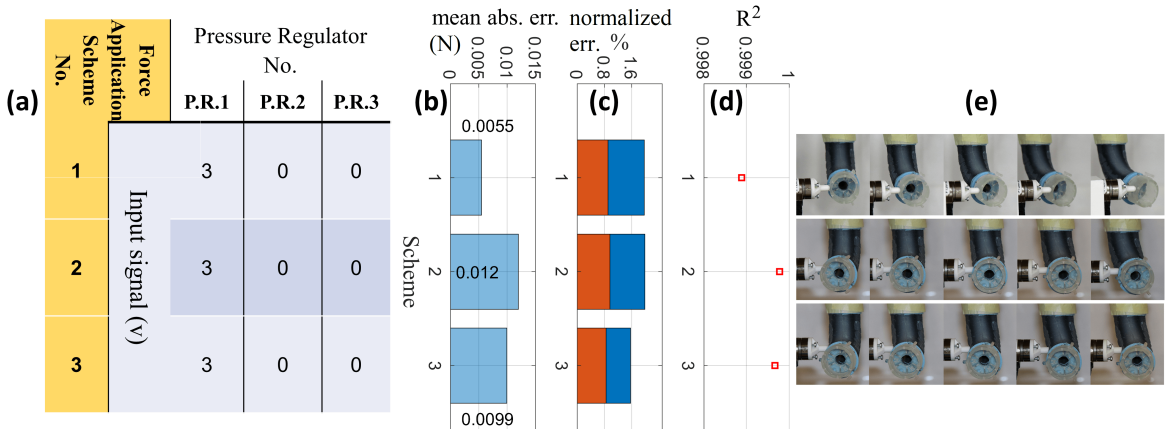

Fig. 2.20 *Stepwise load: (a) in all three schemes of applying load, the three P.R. are activated according to the table for maximum bending. (b) Mean absolute error (MAE). (c) MAE/F_{max} (red), and MAE/F_{ave} (blue). (d) R^2 of model with regard to test. (e) Simulated activation schemes.*

Cyclic external load (Case 4). For investigating the effect of cyclic load increase/decrease, the robotic appendage was actuated to maximum bending ($\approx 90°$), and a cyclic force was applied at the tip where the Nano17 was affixed while increasing and decreasing the loading in five cycles. The force components and the magnitude of force of the test and the simulation are plotted against each other in Figure 2.21. The average of the maximum applied force across is 0.46 N, and the total average of the applied force is 0.17 N across time.

Results show a mean absolute error of 0.015 N for the force magnitude and an R^2 of 0.99. The absolute errors are depicted in Figure 2.22.

Table 2.4 Summary of Mean Absolute Error, Normalized Mean Absolute Errors, and R^2 for The Three Cases of Case 1, Case 2, Case 3.
[a] See section "External load applied at the tip (Case1)." [b] See section "External load applied to the body (Case2)." [c] see section "Stepwise lateral external load (Case3)."
MAE, mean absolute error.

	MAE			MAE/F_{max}			MAE/F_{ave}			R^2
Case	*Max.*	*Ave.*	*Min.*	*Max.%*	*Ave.%*	*Min.%*	*Max.%*	*Ave.%*	*Min.%*	*Ave.*
Case1[a]	0.076	0.041	0.011	5.43	3.13	0.73	7.58	4.47	1.1	0.998
Case2[b]	0.038	0.025	0.0168	4.61	2.67	1.23	5.98	3.58	1.85	0.997
Case3[c]	0.012	0.009	0.005	0.96	0.91	0.85	1.98	1.84	1.57	0.999

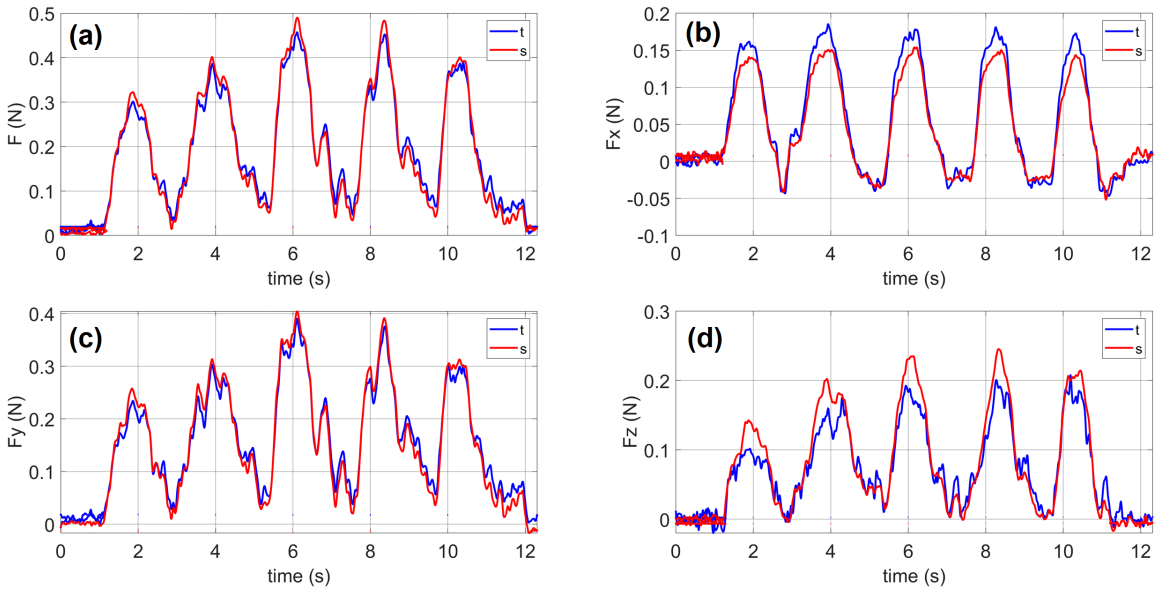

Fig. 2.21 *Comparison between force sensor readings "t", and model estimation "s": (a) total magnitude of forces, (b) Fx, (c) Fy, (d) Fz.*

2.5 Repeatability

Repeatability was investigated in three scenarios, by pressurizing the manipulator to its practical extreme configurations (bending and stretch) and applying external force at the tip to generate more deformation and internal stress compared with applying the force elsewhere; across three trials. The average of the force magnitude at the base along with the standard

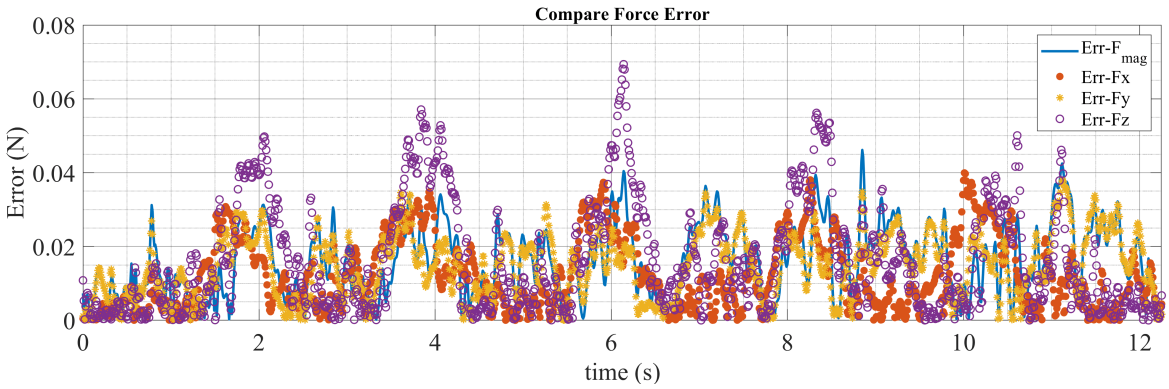

Fig. 2.22 *Absolute error between sensor reading and simulation for force magnitude, Fx, Fy, and Fz.*

deviation in each case is reported in Table 2.5. Due to limited strain, the soft appendage demonstrated good repeatability.

Table 2.5 Three scenarios: (A) maximum bending, external load applied at the tip, in line with the soft appendage's backbone; (B) maximum bending, external load at the tip laterally; (C) maximum stretch, external load at the tip laterally

		(A)		(B)		(C)
Average force magnitude at base (N)	2.5	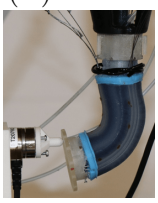	0.44	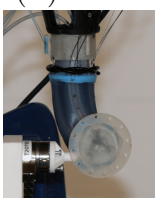	0.53	
STD of force	0.025		0.34		0.11	

2.6 Further Applications

The approach developed in the previous sections could be extended to other fluid-actuated manipulators comprising braided extensors with the same operational principles where the aforementioned assumptions are deemed valid. Figure 2.23 demonstrates the implementation on a 3-segment manipulator including rigid interconnecting elements in dexterous spatial quasi-static motions, with and without external forces.

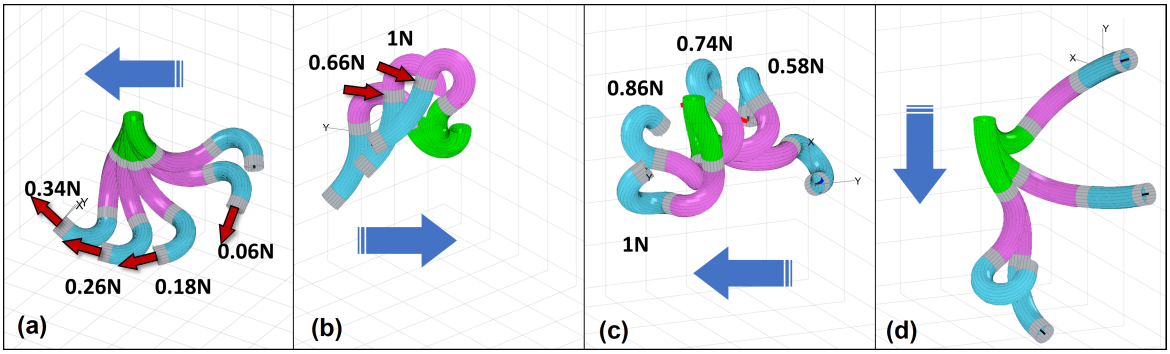

Fig. 2.23 *Three segment soft manipulator with rigid connective elements (gray). External force is applied at marked location and the kinematic progression is (selectively) displayed in MATLAB; omitting intermediate stages for clarity. (a) Force applied at tip; (b) Force applied on body; (c) Force applied at tip; (d) No force: displaying dexterous motion in a hypothetical grasping scenario. Blue arrows show direction of kinematic progression.*

2.7 Conclusions

In this chapter, we presented a mathematically straightforward yet comprehensive approach for modelling and real-time simulation of a silicone-based pneumatic soft continuum robotic appendage comprising braided extensors in quasistatic movements. The proposed model takes into account the effects of internal and external forces with regard to bending, shear, torsion, and extension, and transfers these effects along the entire backbone leading to a 3D kinematic deformation. We comparatively investigated three approaches (Hooke, neo-Hookean, and Gent) to determine the best conformity between the model and experiments (performed with the STIFF-FLOP manipulator). The latter two hyperelastic models were each separately considered with two different constraints: uniaxial deformation, and no-radial deformation. In each case, we derived the principal stretch as a function of stress for braided extensors.

Experiments were performed without load and with load, applied at the tip and along the body on multiple points. In all cases, we studied the response by setting the Young's modulus (E) as a free parameter ranging from 60 to 180 kPa, and we investigated the value with most conformity. It was seen that for this type of robotic appendage, which experiences only limited strains, the Hookean model provided a marginally better estimate for position/deformation and force analysis, with a higher predicted value for E, compared with the two hyperelastic models investigated. We also observed that variations of E at lower actuation pressure have a significantly less negative effect on the model prediction as opposed to higher pressures. Furthermore, the prediction from the model does not vary linearly with regard to E, as lower values for E result in sharper changes in error compared with higher values. Selecting 100 sections for the robotic appendage, the simulation is able to run at 170 Hz in MATLAB on the computer with the specifications mentioned in the Setup section, most likely to improve by implementing the modelling with a lower level language. This execution rate suffices for real-time applications, and as a result of the proposed approach, enables access to internal forces across (almost) the entire backbone, which is an important feature for monitoring the health of the system in addition to facilitating embodied force perception.

We conclude that the Hookean assumption is valid for silicone-based robotic appendages at small strains (about 50% in extension/compression [171]). This result indicates that research works with similar robotic platforms may not necessarily require hyperelastic analysis. The exact range of this validity with regard to dimensional and/or actuation limits is yet to be determined, and beyond the scope of this study. Further examination on this is included in the addendum 2.10 at the end of this chapter.

The proposed model's versatility in estimating external forces applied anywhere on the body and reporting the force values, empowers real-time force sensing and perception in this class of manipulators leading to a wider range of practical applications for safe human/robot interaction. The transfer of pose/force information from one section to the next in the discretized setting can be implemented for any similar platform consisting of multiple segments. In other words, the existing single segment can be treated as multiple virtual segments without loss of accuracy, with potential extension and application of the approach to multi-segment robots for future studies. The limitation depends on maintaining the assumptions in the Modelling Framework section. Another interesting area for additional investigation would be exploring the ability to predict the location of applied force.

Structural imperfections resulting from hand construction (especially in the braided extensors) cause some discrepancies in behaviour, which are not reflected in the model; for example, the extension of the fluidic chambers when subject to pressurization was observed to not be exactly homogeneous. In this regard, introducing compensating terms can improve the performance, however, at the cost of losing generality, and were not considered here. Finally, although the current implementation of the model could cope with multiple and/or distributed loads, however, it would require an iterative procedure with an impact on computational cost, with its feasibility for force estimation to be pursued in future work.

2.8 (Chapter 2) Addendum 1

Longitudinal engineering stress for a braided extensor as a function of elongation λ, and the braiding angle γ; for the Gent model with INF (inextensible fiber) constraint:

$$\begin{aligned}\sigma = &\frac{GJ_m \ln\left(\frac{\frac{\lambda^2 C_\gamma^2 - 1}{S_\gamma^2} + \frac{S_\gamma^2}{\lambda^2(\lambda^2 C_\gamma^2 - 1)} + 3 - \lambda^2}{J_m} + 1\right) C_\gamma^2 S_\gamma^2}{(1 - \lambda^2 C_\gamma^2)^2} \\ &+ \frac{GS_\gamma^2\left(2\lambda - \frac{2\lambda C_\gamma^2}{S_\gamma^2} + \frac{2S_\gamma^2}{\lambda^3(\lambda^2 C_\gamma^2 - 1)} + \frac{2S_\gamma^2 C_\gamma^2}{\lambda(\lambda^2 C_\gamma^2 - 1)^2}\right)}{2\lambda\left(\frac{\frac{\lambda^2 C_\gamma^2 - 1}{S_\gamma^2} + \frac{S_\gamma^2}{\lambda^2(\lambda^2 C_\gamma^2 - 1)} + 3 - \lambda^2}{J_m} + 1\right)(1 - \lambda^2 C_\gamma^2)} \\ &+ \frac{GJ_m \ln\left(\frac{\frac{\lambda^2 C_\gamma^2 - 1}{S_\gamma^2} + \frac{S_\gamma^2}{\lambda^2(\lambda^2 C_\gamma^2 - 1)} + 3 - \lambda^2}{J_m} + 1\right) S_\gamma^2}{2\lambda^2(1 - \lambda^2 C_\gamma^2)}\end{aligned} \tag{2.20}$$

2.9 (Chapter 2) Addendum 2

An alternate approach can be formulated for constructing the transformation matrices. As the total local moment is calculated as $\boldsymbol{M}_{tot} = \boldsymbol{M}_e + \boldsymbol{M}_i$, projecting this moment vector onto its local x and y components delivers curvature in the local frame as $\kappa_x = M_y/EI$ and $\kappa_y = M_x/EI$, with $\kappa = \sqrt{(\kappa_x^2 + \kappa_y^2)}$; and the out of plane bending angle as $\phi = atan2(\kappa_y/\kappa_x)$ [122]. Observing that $\boldsymbol{\rho} = [(1 - C_\theta), 0, S_\theta/\kappa]^T$ as the translational vector from the previous frame to next due to bending between two incrementally adjacent frames is derived as follows [122]:

$$\mathbf{T}_B = \begin{bmatrix} \mathbf{R}_z(\phi) & \mathbf{0} \\ \mathbf{0}^T & 1 \end{bmatrix} . \begin{bmatrix} \mathbf{R}_y(\theta) & \boldsymbol{\rho} \\ \mathbf{0}^T & 1 \end{bmatrix} . \begin{bmatrix} \mathbf{R}_z(-\phi) & \mathbf{0} \\ \mathbf{0}^T & 1 \end{bmatrix} \tag{2.21}$$

where $\mathbf{R}_{3\times3}$ is the rotational transformation matrix around the relevant local axis.

The torsion angle is computed as $\alpha = M_z\xi_0/GI_p$, where I_p is the polar moment of inertia. This can be represented by a local rotational transformation about the z axes by the angle a

in the following transformation matrix:

$$\mathbf{T}_{tor,z} = \begin{bmatrix} \mathbf{R}_z(\alpha) & \mathbf{0} \\ \mathbf{0}^T & 1 \end{bmatrix} \tag{2.22}$$

By considering each infinitesimal segment as a beam, the shear displacement in each local frame for both x and y directions are calculated as follows:

$$\delta_{x,y} = (f_{x,y}\xi_0/\beta AG) \tag{2.23}$$

where $f_{x,y}$ is the force projection of the resultant overall local force on the local x, y plane, and β is the form factor calculated $(A/I^2)\int_A (Q/t)dA$, which is 10/9 for circular cross sections. Therefore, the resulting shear translational vector in both the local x and y directions is $\boldsymbol{\psi} = [-\delta_x, -\delta_y, 0]^T$, forming the shear transformation matrix as follows:

$$\mathbf{T}_{sh,x,y} = \begin{bmatrix} \mathbf{I}_{3\times 3} & \boldsymbol{\psi}_{x,y} \\ \mathbf{0}^T & 1 \end{bmatrix} \tag{2.24}$$

where $\mathbf{I}_{3\times 3}$ is the identity matrix. The total homogeneous transformation matrix from one frame to the next is composed as a concatenation of all calculated homogeneous matrices:

$$\mathbf{T}_k^{k-1}{}_{tot} = \mathbf{T}_b \mathbf{T}_{sh} \mathbf{T}_{tor} \tag{2.25}$$

The relative coordinates of every following frame are the first three entries of the last column in each transformation matrix, which we stack successively in a separate 3×11 matrix. The overall transformation matrix from the tip to the base is formed as a multiplication of all transformations as mentioned in Equation 2.19.

By this approach, using an appropriate level of discretization, the system's nonlinear deformation is captured by geometrical nonlinearity as a result of a high number of segments, rather than the material nonlinearity, by considering more complex hyperelastic assumptions. Comparison with the results obtained from the method described in the text shows a minor

difference of about 2% between the two methods in the current robotic appendage, discretized in 100 sections.

2.10 (Chapter 2) Addendum 3

Although rubber is capable of experiencing large elastic deformations, in practice, rubber is often subjected only to relatively less than about 50% in extension or compression (small strains). The stress can then be approximated by common elastic analysis, assuming simple linear stress/strain relationships, since in small strains, rubber behaves as a linearly elastic material like all solids [171]. To further investigate the validity of Hooke linear relationship for the material used in the soft robot appendage, one chamber (braided extensor) was separated and pressurized to an elongation of almost over 87% more than its initial length. Results are depicted in Figure 2.24, showing elongation to follow a nearly linear trend.

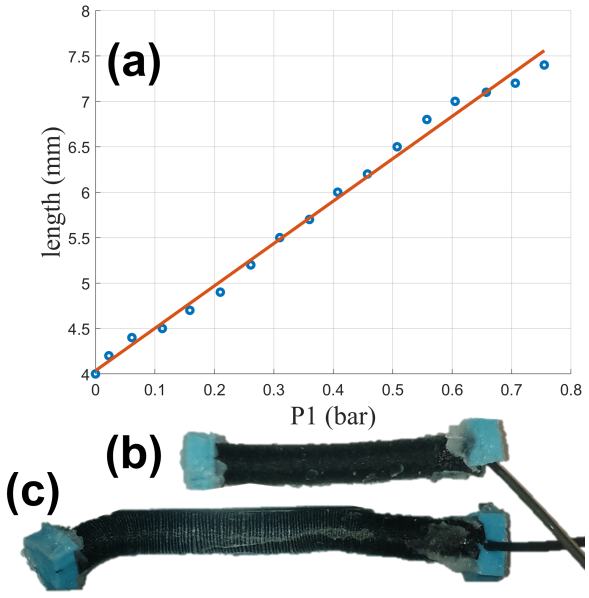

Fig. 2.24 *Pressurization of a braided extensor:(a) pressure versus length, (b) initial configuration, (c) elongated extensor.*

Chapter 3

Soft Tissue Probing with Continuum Robotic Appendage

Forward:

The content of this chapter is the output of a collaborative work between the author of this thesis, Mr. Ali Shiva; and Mr. S.M.Hadi Sadati. The contributions of the thesis author (Ali Shiva) consists of the main idea to sweep a soft tissue replica via a soft continuum fluidic manipulator for anomaly detection; preparation of the test setup (entailing - but not limited to - assembling the entire mechatronic circuitry, the hydraulic system, casting the silicone phantom, data acquisition interface, calibration); running all the tests; data gathering; initial post processing of the acquired data; and providing pictures.

The contribution of Mr. Sadati includes modeling the behavior of the system, data analysis, and generating most of the figures.

Abstract— *Herein, a novel approach is proposed for probing soft tissue to detect stiffness anomalies using a fluidic soft continuum appendage; which benefits from light-weight design and safe interaction due to the soft structure's intrinsic compliance. The shape and forces experienced at the tip of the continuum appendage are estimated based on real-time forward integration of Cosserat rod model that solely relies on load readings from a single 6-axis force sensor installed at the base, removing the need for position tracking sensors or a tip force sensor. Multiple probing runs with different actuation pressures are used for mapping the*

tissue surface shape and directional linear stiffness, as well as detecting non-homogeneous regions, e.g. a hard nodule embedded in a soft silicon tissue phantom. As a result, the appendage tip force is estimated with less than $0.35\,\mathrm{N}$ *mean error in the probing and less than* $0.1\,\mathrm{N}$ *in the indentation direction, and less than* $0.7\,\mathrm{mm}$ *mean error is achieved in estimating the surface profile between different trials of each experimental scenario. Further challenges with the tissue dynamic motion, palpation strategies, and benefits from a variable stiffness appendages are briefly discussed.*

3.1 Introduction

The unbalanced distribution of specialists in technology and medicine compared to the needs around the world is a key challenge in promoting global health. Advancements in telecommunication and relevant infrastructures in the past decades has helped the reachability of rural and hard-to-access places around the world. This, in turn, has sparked a research trend of designing novel diagnostic and examination techniques to connect patients and specialists globally. Such designs should be safe and easy-to-use, light-weight, mobile, affordable and at the same time robust and accurate. This study proposes the idea of using a hydraulic continuum appendage for probing soft tissue organs, e.g. a patient's abdomen in a remote-diagnosis scenario, benefiting from a simple yet accurate stiffness estimation method that solely relies on readings from a 6-axis force sensor for tissue probing and stiffness imaging.

Various probing devices, including tactile sensors, have been developed to minimize medical intervention damages for graspers, forceps, cutters, catheter tips, or to detect presence of abnormalities by evaluating tissue mechanical properties and providing tactile feedback [175].

While robust solutions for static single point stiffness measurements already exist, real-time accurate and stable stiffness mapping of a tissue surface is still challenging. Adapting to the variables of different soft tissues such as elasticity, texture, surface friction, shape, restitution dynamics, non-homogeneity and organ natural movements are the key requirements of a medical probing device. Additionally, there are medical requirements such as compliance with different procedures, fast operation, sensing accuracy and stability, small size design (to comply with incisions) easy sterilization, simplicity, affordability, and preferably, MRI (Magnetic Resonance Imaging) compatibility that must be satisfied before a device is approved for practical use [175, 73].

To this end, different concepts have been developed based on tissue indentation by direct contact, or non-contacting methods through visual or sonar feedback, sensor arrays for dynamic feedback during continuous probing [176], compliant and variable stiffness probes for maximizing sensory information gain to adopt to different tissue and palpation conditions [177, 73], and continuum probes for their dexterity, manoeuvrability, shape

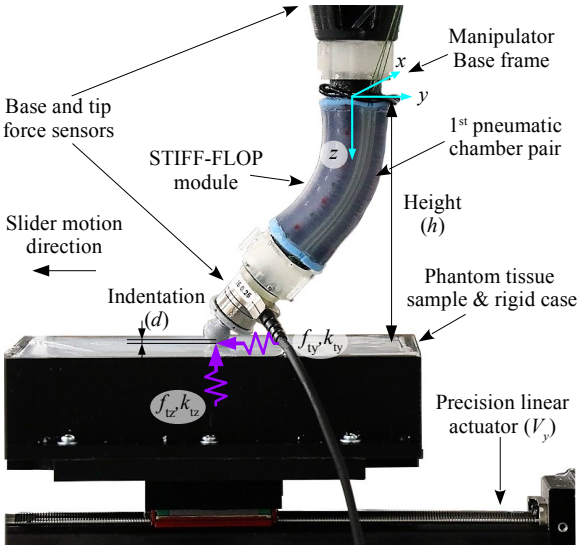

Fig. 3.1 *A hydraulically actuated continuum appendage (STIFF-FLOP) for soft tissue probing, stiffness imaging and anomaly (e.g. hard nodule) detection.*

adaptation and (to some extent) stiffness regulation properties [160]. In addition, task-specific probe designs and guidelines are necessary for different medical applications [175]. The tissue shape and stiffness estimation are possible by keeping a zero-force contact with the tissue surface, requiring a force/position control paradigm, [178, 128, 100, 160] and then comparing the indentation due to different applied force values from multiple palpation runs [179].

Among different solutions, soft continuum manipulators present unique features which have made this class of robots attractive. To name a few: robust fluidic or tendon actuation mechanisms, high dexterity and dexterous motion, along with inherent structural compliance. These features enable safe interaction with delicate surroundings, high manoeuvrability and large workspace for physical examination and rehabilitation, reaching complex confined anatomical paths in narrow port Minimally Invasive Surgeries (MIS), and providing intrinsic shape and force sensing through their body or actuation lines [60, 180]. Among different designs, braided fluidic continuum modules, such as STIFF-FLOP [85], perform better when robust, homogeneous and repeatable deformation and force control are needed, compared to the non-braided versions [181].

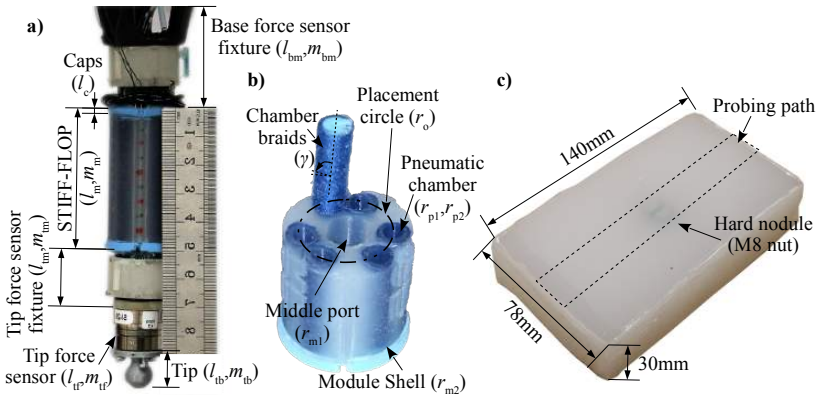

Sym.	Value
r_{m_1}[mm]	4.5
r_{m_2}[mm]	12.5
r_{p_1}[mm]	2.5
r_{p_2}[mm]	3.0
r_o[mm]	8.5
r_{tb}[mm]	2.5
l_m[mm]	50
l_c[mm]	3
l_{bm}[mm]	62
$l_{tm+tf+tb}$[mm]	42
m_{bm}[gr]	14.5
m_{tm+tf}[gr]	12.47
m_{tb}[gr]	1.45
γ[deg]	87
E[KPa]	205
σ[Kg/m^3]	1300
V_y[mm/s]	7

Fig. 3.2 *a) Schematic of the probing appendage consisting of a STIFF-FLOP actuator module, tip and base force sensors, and mountings. b) Cross section of a STIFF-FLOP module. c) A soft silicon phantom tissue with an embedded M8 nut to mimic a hard nodule in a soft tissue.*

However, real-time and accurate modelling of these manipulators, observation and control (especially in the dynamic environments of medical examination) remain a challenge [181, 126]. Numerous attempts have been made during the recent years to address these issues, such as hybrid force and position estimation and control methods based on combining force and position sensor readings to achieve the estimation and control tasks [130, 160]. Bajo and Siemann have recently proposed a hybrid position/force control method for a miniature tendon driven continuum manipulator and utilized it for stiffness imaging of a soft tissue. Relying on both force and position measurements, the authors compared the force/position data from two palpation rounds to estimate the shape and linear stiffness of an unknown soft environment [160].

Recent research has focused on body or tip (operation point) force estimation to remove the need to attach a force sensor on the manipulator. These methods rely on intrinsic force sensing, through the manipulator's actuation tendons [128, 160], pressure inlets [80], position tracking methods based on actuation tendon length [160], magnetic markers [80], or intraoperative methods using fluorescent, ultrasound or visual tracking markers, and fiber optic and fiber bragg grating sensors [165, 180]. Relying on simplifying assumptions about the manipulator geometry, e.g. the constant curvature assumption [126], the need for

expensive and bulky tracking devices with limited range and portability, occlusion problem, MRI interference, and noisy results [180] are the main disadvantages of these shape-based and indirect force estimation methods. However, the idea of benefiting from a variable stiffness continuum appendage for soft tissue probing has not been investigated yet.

To simplify the shape estimation of a continuum appendage, the idea of transforming the Boundary Value Problem (BVP) model of an elastic beam to an Initial Value problem in an Ordinary Differential Equation (ODE), by knowing the loading condition at a fixed-end has been utilized by Barbič for soft material graphical visualizing [182]. From a robotic point of view, Bretl and Mccarthy have shown that the reaction forces at one end of an elastic rod are global coordinate charts for estimating the rod's quasistatic configuration [183]. Further investigation of this concept has been carried out for modelling thin solids, e.g. flexible ribbons [184]; where the authors employed this idea for shape estimation of continuum rods with moving ends. They achieved real-time performance, small error (3-15%) and occlusion free tracking via simple forward integration, but limited accuracy due to discrete implementation of the Kirchhoff Elastic Rod method [184]. Rucker et al. have briefly investigated this idea as part of their actuation and deflection-based force sensing method for parallel continuum robots [185]. However, geometric constraint (their actuation port overlapped with base force sensor placement) and large sensitivity to noise in dynamic scenarios prevented them effective implementation.

Here, we propose the use of a hydraulically actuated STIFF-FLOP module, which is a 3-DoF braided continuum appendage, for probing and stiffness imaging of a soft silicon tissue phantom, as in Figure 3.1, with the aim of detecting anomalies in the form of a hard nodules in the tissue sample (section 3.2.1). A real-time shape and tip force estimation method is proposed based on forward numerical integration of Cosserat rod method that is made possible using 6-axis load readings from a force sensor fixed at the appendage base (section 3.2.2 & 3.2.3). As a result, no position tracking sensor is needed and the stiffness imaging algorithm is simple and efficient enough to be implemented in an affordable easy-to-use micro-controller. Numerical performance (accuracy and simulation time) of using rotation matrix and quaternions for the appendage kinematics are compared. Hyperelasticity and

braiding effects are taken into consideration in an intermediate numerical step as in [87, 136]. The results from multiple probing runs with different actuation pressures provide sufficient information to construct the surface profile and the linear stiffness map of the tissue with good accuracy compared to experimental results, showing the location and depth of the anomaly in the tissue. Suggestions for future research are provided in section 3.4 based the experimental and simulation results, advantages, possibilities and limitations of this method (section 3.3).

The main contributions of this study can be summarized as:

- Using a continuum actuator appendage for soft tissue palpation,
- Proposing real-time shape and tip force estimation via sensing the appendage base loads and hence enabling forward integration of a Cosserat rod model static case,
- Comparing the accuracy and real-time computational performance of different derivations of the continuum appendage mechanics using quaternions and rotation matrices,
- Suggestions for probing strategy and configuration based on actuation of the continuum appendage,
- Possible minimalistic implementation of the proposed stiffness imaging method, e.g. on a simple Arduino micro-controller for an affordable mobile device, for on-line surface stiffness and profile estimation of living moving tissue in an actual MIS task.

3.2 Materials and Methods

3.2.1 Experimental Setup and Procedure

A STIFF-FLOP module [85] employed here is a hydraulically-actuated continuum appendage for soft tissue probing (Figure 3.2.a). The manipulator is made of Silicone elastomer (Chapter 2). Independent actuation of three braided hydraulic chamber pairs (6 chambers in total) is via three separate plungers (10mL Terumo Syringe) moved back and/or forth by three 17HS5001-100D8 non-captive stepper motors, providing 3 DoF (one axial elongation

and two side-bending) of the appendage tip (Figure 3.2.b). The stepper motors are controlled via a C# program through a data acquisition board (DAQ) board (National Instruments Inc. NI-DAQmx USB-6411). Hydraulic pressure for each chamber pair is recorded via three separate pressure transmitters (WIKA model A-10). The first chamber pair is placed along the manipulator $+y$ axis (Figure 3.1) with 120° offset from the other pairs.

An ATI Mini40 F/T sensor is mounted at the appendage base as the single necessary sensor for the probing task. An ATI Nano17 F/T force sensor is connected at the manipulator tip to provide ground truth for validation. A 3D-printed spherical nob ($R = 5\,\text{mm}$) is affixed at the tip to avoid damaging sharp corners or blunt surfaces at the contact point, benefiting from the spherical geometry to generate the least friction during the slide [175, 186, 187].

The cubic soft tissue phantom ($140 \times 80 \times 30\,\text{mm}$) is made from soft silicon (Ecoflex-0010) and confined in a 3D printed rigid container (Figure 3.2.c). The Silicone phantom is wrapped with a cling film, and lubricated on the top surface to produce smoother transition [188]. An M8 nut (a hexagonal with $\approx 14.4\,\text{mm}$ circumferential circle diameter and $\approx 7.2\,\text{mm}$ thickness) is embedded vertically at the centre of the phantom and in 2 mm depth, as a hard nodule in a soft tissue. The measured and identified structural parameters of the experimental setup are presented in Figure 3.2. The phantom is fixed on a HIWIN KKA40 high precision linear actuator which is controlled with an Arduino UNO through a stepper motor.

The appendage is fixed at the target configuration, and the phantom is moved opposite the y axis ($-y$), as in Figure 3.1, with constant velocity ($V_y \approx 7\,\text{mm/s}$) using the linear actuator while in contact with the appendage tip. This configuration is used in the current study for simplicity; however, the results are similar to the case of a fixed phantom and a horizontally moving appendage. The phantom tissue is placed $h = 89\,\text{mm}$ away from the appendage base (2 mm less than the appendage overall height). Three actuation scenarios are tested, each three times, with different input pressure values ($p_{\text{I}} = [0.25, 0.42, 0.5]$ where the appendage bends against the slider motion, $p_{\text{II}} = [0.41, 0, 0]$ where it bends toward the slider motion and $p_{\text{III}} = [0, 0, 0]$ barg where it is not actuated at all, see Table 3.1) providing force measurements at different indention. Although the appendage in the third scenario slightly bends toward the slider motion passively. The mean (M) and Mean Standard Deviation

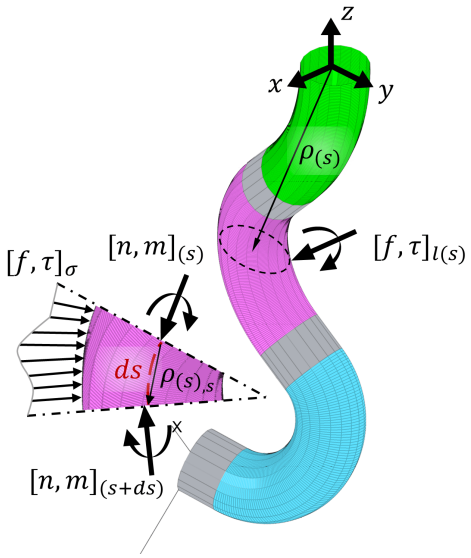

Fig. 3.3 *Variable curvature kinematics and the Cosserat rod method free body diagram for one differential element along the continuum backbone. Subscripts l, ρ and σ are for the external point loads at the tip or along the backbone, loads due to internal pressure, and distributed loads (e.g. gravity); respectively.*

(MSTD) values for the estimated tip force, based on simulations using the base force sensor readings, are compared with the actual measurements from the tip force sensor to evaluate absolute and percentage error (Err,%) for each actuation scenario. Note that the sensors' measurements are not equal despite the quasistatic assumption. The tip force sensor readings are measured w.r.t. the appendage tip local frame, since the force sensor is fixed to the tip, and we rely on our simulation results to estimated the tip orientation and its contacting point with and indentation in the phantom tissue. Besides, the mass for appendage body, filled hydraulic chambers, and all rigid connections should be taken into account. Result pairs from different actuation scenarios are compared to estimate the tissue stiffness and surface profile, and the mean value of the results based on the base and tip load readings are compared.

3.2.2 Continuum Appendage Static Model

Variable Curvature (VC) kinematics based on a quaternion representation of rotations, and Cosserat rod theory are used to model the static mechanics of the appendage [60]. The relation between the local physical curvilinear coordinates ($[\hat{d}_1,\ \hat{d}_2,\ \hat{d}_3]$, where $\hat{d}_3$ is tangent to the backbone, $\hat{d}_2$ is along the first pressure chamber pair, and $[\hat{d}_1,\ \hat{d}_2,\ \hat{d}_3]_{(s=0)} = [\hat{i},\ \hat{j},\ \hat{k}]$ at the appendage base (Figure 3.3). Note the orientation of the base reference frame in Figure 3.1. The backbone curve spatial configuration (ρ) and 1×4 rotation quaternion unit

vector (Q), expressed in inertial Cartesian coordinates ($[\hat{i},\ \hat{j},\ \hat{k}]$), are derived according to VC as in [189, 125]:

$$\begin{aligned} Q_{,s} &= Q \times [0, u]^\top / 2 \\ [0, \rho_{,s}]^\top &= \left(Q \times [0, (v + [0, 0, 1])]^\top \right) \times Q^{-1} \end{aligned} \tag{3.1}$$

where $Q = [q_0, q]$, $q_0 = \sqrt{1 - q.q^\top}$, q is the 1×3 quaternion vector, v is the curve local strain vector, u is the vector of curve local curvatures and torsion, s is the variable along the backbone with $s_{\text{tip}} = l$, where l is the manipulator length, $y_{,x} = \partial y / \partial x$, $Q^{-1} = \text{conj}(Q) = [q_0, -q]$, and $\times$ here denotes the quaternion product as [189]:

$$Q\times = \begin{bmatrix} q_0 & -q_1 & -q_2 & -q_3 \\ q_1 & q_0 & -q_3 & q_2 \\ q_2 & q_3 & q_0 & -q_1 \\ q_3 & -q_2 & q_1 & q_0 \end{bmatrix}. \tag{3.2}$$

which is equivalent to a matrix dot product. The curvilinear and Cartesian coordinates are aligned at the manipulator base ($s = 0$), where $[\hat{d_1},\ \hat{d_2},\ \hat{d_3}]_{(s=0)} = [\hat{i},\ \hat{j},\ \hat{k}]$, $\rho_0 = 0$ and $q = [0, 0, 0]$. Alternatively, using 3×3 rotation matrices (R), we obtain [60]

$$\begin{aligned} \rho_{,s} &= R(v + [0, 0, 1]^\top) \\ R_{,s} &= R\ [u]_\times \end{aligned} \tag{3.3}$$

where $[\ ]_\times$ is the skew-symmetric matrix denoting a standard mapping from $\mathbb{R}^3$ to SO(3) [60]

The simple implementation of quaternion rotation is more computationally expensive than using 3×3 rotation matrices; however, using quaternions improves numerical integration accuracy, and preserves frame orthonormality [125, 189]. A comparison between the results from both methods is presented in the next section.

The Cosserat rod theory exploits the conservation law to balance the total internal loads carried by the rod material (n, m) and the distributed external and body loads (f, τ_σ) - e.g. due to body weight (f_{g}). Here, $m, n_{(s)}$ is equal to the sum of the individual contributions of

the actuation chambers (f, τ_{p}) and the projected load on the rod cross-section due to external loads (f, τ_{m}) as $n = f_{\mathrm{p}} + f_{\mathrm{m}}$ and $m = \tau_{\mathrm{p}} + \tau_{\mathrm{m}}$. The resulting load from concentrated external loads $(f_{\mathrm{l}}, \tau_{\mathrm{l}})$ act as boundary conditions (e.g. of type shear load for an Euler-Bernoulli beam), expressed in the local frame, along the manipulator [190]. If the loads due to actuation pressure $(f_{\mathrm{p}}, \tau_{\mathrm{p}})$ are considered as concentrated external loads at the manipulator tip and handled as boundary conditions, similar to the case of external f, τ_{l} [125], complicated terms related to $f_{\mathrm{p}}\hat{d}_{3,s}$ and τ_{p} vectors appear in the derivations to compensate the accumulation of pressure loads as we integrate along the manipulator backbone. Instead, we sum up their contributions to the internal load carried by the rod material (n, m), where they act in parallel to the internal loads (f, τ_{m}) to deform the manipulator. This results in the same set of equations as in [125] but with a clearer and more physically relevant presentation which is less computationally expensive to integrate. For f, τ_{m} in static case, using the Cosserat rod method [60], we have:

$$f_{\mathrm{m},s} + f_{\sigma} = \mathbf{0},\ \tau_{\mathrm{m},s} + \rho_{,s} \times f_{\mathrm{m}} + \tau_{\sigma} = \mathbf{0} \tag{3.4}$$

where $f_{\sigma} = (\sigma_{\mathrm{m}} a_{\mathrm{m}} + 6\sigma_{\mathrm{p}} a_{\mathrm{p}})g$, σ is the material and water distributed weight, $a_{\mathrm{m}} = \pi(r^2_{\mathrm{m}_2} - r^2_{\mathrm{m}_1} - 6r^2_{\mathrm{p}_1})$ and $a_{\mathrm{p}} = \pi r^2_{\mathrm{p}_1}$ are the manipulator and hydraulic chamber cross-section area respectively, $g = [0\ 0\ -9.81]$ $[\mathrm{m/s^2}]$ is the gravity vector, r_{m_1} and r_{m_2} are the module cross-section inner and outer radii. As a standard approach in implementing Cosserat rod method, Hooke's law of linear stress-strain relation is used as the system constitutional law $(n = K_v.v, m = K_u.u)$. Transforming all the vectors in the local frame, we obtain:

$$\begin{aligned} [0, v]^{\top} &= K_v^{-1}.\left(Q^{-1} \times [0, f_{\mathrm{m}}]^{\top} + [0, f_{\mathrm{p}}]^{\top}\right), \\ [0, u]^{\top} &= K_u^{-1}.\left(Q^{-1} \times [0, \tau_{\mathrm{m}}]^{\top} + [0, \tau_{\mathrm{p}}]^{\top}\right) \end{aligned} \tag{3.5}$$

where hydraulic chambers are actuated in pairs ($p_{2i-1} = p_{2i}$ for $i = 1...3$), $f_{\mathrm{p}} = \Sigma_{i=1}^{6} p_i a_{\mathrm{p}}$ and $\tau_{\mathrm{p}} = \Sigma_{i=1}^{6} p_i a_{\mathrm{p}} r_{\mathrm{O}_i} \times [0, 0, 1]$, r_{p_1} and r_{p_2} are the hydraulic chamber inner area, inner and outer radius, $K_v = \mathrm{diag}(a_{\mathrm{m}}[G, G, E])$ and $K_u = \mathrm{diag}([E, E, G]).\mathrm{diag}(J)$ are diagonal stiffness matrices, associated with strains and curvatures/torsion respectively, in the $\hat{d}_i$ frame, E and

$G \approx E/3$ are the material elasticity and shear modulus, $J = \pi/4(r_{c_2}^4 - r_{c_1}^4 - 6r_p^4).[1,1,2] - a_p \text{diag}(r_O.r_O^\top)$ is a 1×3 vector consisting of the cross-section second moments of areas, r_O is a matrix of which rows are position vectors of the chambers in the manipulator cross-section plane

$$\begin{aligned} r_{O_i} &= r_o.\left[\cos(\psi_{o_i}), \sin(\psi_{o_i}), 0\right], \ i \in 1...6 \\ \psi_{o_{2j-1}} &= \pi/2 - 2(j-1)\pi/3 - \phi_o, \\ \psi_{o_{2j}} &= \pi/2 - 2(j-1)\pi/3 + \phi_o, \ j \in 1...3, \end{aligned} \tag{3.6}$$

and r_o is the radial offset of the chambers from the center. Using R, instead of Eq. (3.5), we obtain

$$v = K_v^{-1}(R^\top f_m + f_p), \ u = K_u^{-1}(R^\top \tau_m + \tau_p). \tag{3.7}$$

m, n can be used for stress analysis.

Eq. (3.1), (3.4), and (3.5) with Q (alternatively, (3.3), (3.4), and (3.7) with R) form a system of differential equations with states $[\rho, q, n, m]$ (alternatively, $[\rho, R, n, m]$). Benefiting from the load readings from 6-axis force sensor at the manipulator base ($[f, \tau]_{(s=0)} = [n, m]_{(s=0)}$), the system is reduced to an initial value ODE to be solved with forward numerical integration on $s \in [0, l]$ for the manipulator configuration (ρ, q) and tip load ($[f, \tau]_l = [n, m]_{(s=l)}$). In the case of known tip loads, a more computationally demanding BVP is formed with convergence and accuracy issues which is harder to solve. Note that reduced-order methods have been introduced recently to solve these systems in [191, 136]. The formed ODE is solved using MATLAB's "ode113" function. Simulation results for the tip position are used to estimate the indentation of and the contact point with the tissue to estimate the tissue profile and stiffness. The simulation results for the tip orientation are used to transform the tip force sensor readings to the base reference frame as the ground truth to be compared with the simulation results based on the base force sensor readings.

3.2.3 Appendage Shape and Tissue Stiffness Estimation

The actual tip contact position w.r.t. the tissue mean surface, at height offset h from the appendage base, and horizontal position of the appendage base in each time step t is $\rho_{\mathrm{t}} = [0, -V_y t, h] - \rho_{(s=l)}$. Then, the tissue linear stiffness can be estimated by comparing the appendage tip position and forces with different tissue indentations (d) due to different actuation pressures as $k_{\mathrm{t}y|z} = \Delta f_{y|z} / \Delta \rho_{\mathrm{t}y|z}$ [160], where k_{t} is the tissue linear stiffness w.r.t. d. $k_{\mathrm{t}y}$ is related to the surface friction (μ_{t}) as $k_{\mathrm{t}y} = k_{\mathrm{t}z}\mu_{\mathrm{t}} + k_{\mathrm{t}y_{\mathrm{real}}}$, where $k_{\mathrm{t}y_{\mathrm{real}}}$ is the tissue real stiffness, which is not considered in this study. While estimating the tissue surface profile is presented in [160] by zero force probing of the surface, here in this study, we use $f_{\mathrm{t}z}$ and the estimated $k_{\mathrm{t}z}$ to estimate the free surface as $z_{\mathrm{t}} = \rho_{\mathrm{t}z} - f_{\mathrm{t}z}/k_{\mathrm{t}z}$. This simple procedure does not require a complex force/position control design as in [160]. This way, the surface estimation will be less sensitive to moving tissue for real medical applications, which makes zero force probing a challenging task, and the estimation can be done online while the tip is performing another task, such as surgical tool attached to the tip in an MIS.

3.3 Results and Discussion

The results from 9 probing runs with 3 different pressure combinations are used to test the accuracy and computational performance of our method.

Fig. 3.4 shows raw data from a probing run with initial pressures $p_{\mathrm{III}} = [0, 0, 0]\,\mathrm{bar}$, changing to $p^*_{\mathrm{III}} = [-0.1, 0, 0.05]\,\mathrm{bar}$ upon tissue contact. The pressures can become negative due to induced suction in the chambers as a result of passive appendage deformation under its weight or other chamber elongation. The change in the pressure readings is used to detect the contact start time and transition period. The stabilized pressures after tissue contact for the other two sets of actuation scenarios are $p^*_{\mathrm{I}} = [0.1, 0.5, 0.7]\,\mathrm{bar}$ and $p^*_{\mathrm{II}} = [0.3, 0, 0]\,\mathrm{bar}$. $[f, \tau]_{\mathrm{base}}$ are used as $[n, m]_{(s=0)}$ and the estimated tip forces are compared with the actual tip force sensor readings. Using rotation matrices (R), Eq. (3.3) & (3.7), results in exactly the same results as in the case of quaternions (Q), Eq. (3.1) & (3.5), showing no accuracy improvements over the length and deformation range of our tests. While both approaches

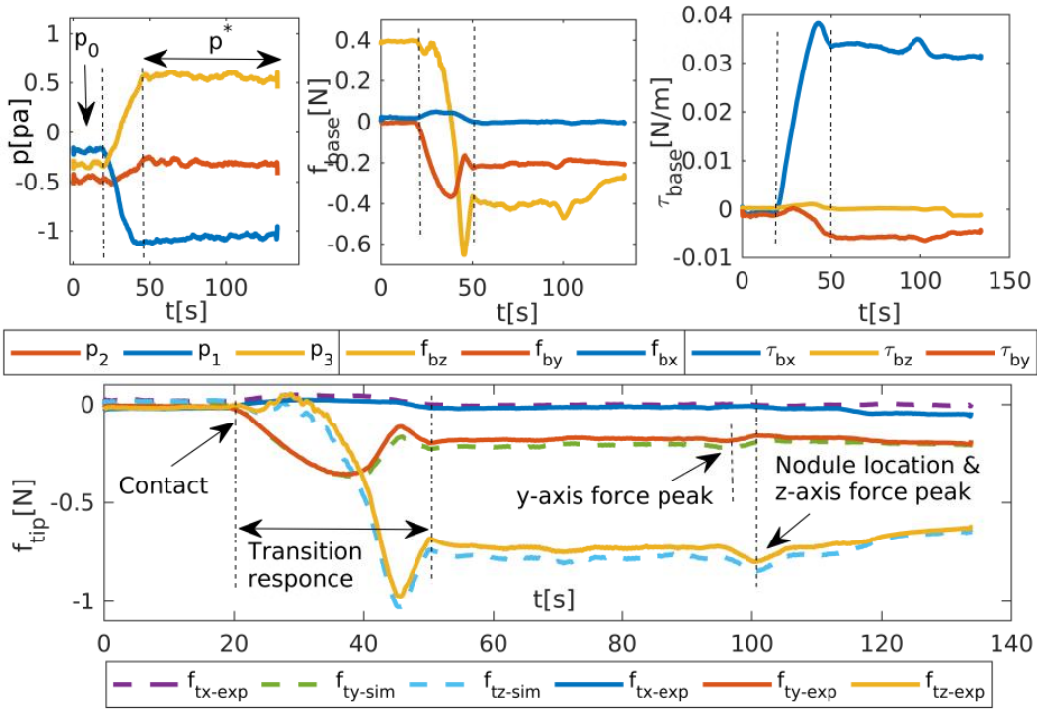

Fig. 3.4 *Sample raw data from a single probing run with initial pressures* $p_{\text{III}} = [0, 0, 0]$ bar *(experimental scenario III). The negative pressures (*p^**) are due to suction under appendage weight and phantom sliding force. The appendage contact with the phantom tissue is detected by monitoring sudden changes in the pressure readings and the transient behaviour after the contact (showed with vertical dash lines in all the plots). The nodule location (stiff region) is detected upon an increase in the force sensor* z*-axis readings.*

provide real-time performance, the mean execution time is about 18% faster in the case of using R (364 ms/s (millisecond of simulation time per each second of experiment) for R and 447 ms/s for Q, running on an Ubuntu 18.04.1 LTS operating system with Intel® Core™ M-5Y10c CPU (0.8-2.0 GHz × 4) and 8 Gb memory). A peak force value, at the appendage tip z-axis direction, occurs almost on top of the stiff region, e.g. hard nodule location, while this peak value for the y-axis (probing) direction occurs just before this point.

Table 3.1 presents the MSTD values for all experimental data points of the three probing runs in each of the actuation scenarios. MSTD values are less than 0.02 N and 0.05 N for both base and tip force readings in the y-axis (probing) and z-axis directions show good repeatability of the experiment results. The same is observed for the moment around the x-axis with MSTD less than 1 mNm. The first actuation scenario (appendage bends against

Table 3.1 *Mean Standard Deviation (MSTD), and simulation mean error value (Err) and percentage (%) for the three tested actuation scenarios. The slider moves from right to left.*

				
	Scenario	I (against)	II (toward)	III (neutral)
	p [atm]	$[0.25, 0.42, 0.5]$	$[0.41, 0, 0]$	$[0, 0, 0]$
	par.s	MSTD (Err,%)	MSTD (Err,%)	MSTD (Err,%)
exp.	f_{bx}[N]	0.005	0.009	0.019
	f_{by}[N]	0.0067	0.015	0.021
	f_{bz}[N]	0.051	0.016	0.035
	τ_{bx}[Nm]	0.0014	3.8e-4	0.001
	τ_{by}[Nm]	3e-4	7.5e-4	0.0011
	τ_{bz}[Nm]	3e-5	1.2e-4	2.5e-4
	f_{tx}[N]	0.0038	0.0011	0.02
	f_{ty}[N]	0.02	0.0093	0.014
	f_{tz}[N]	0.015	0.0045	0.018
sim.	f_{tx}[N]	0.005 (0.019)	0.009 (0.0067)	0.019 (0.009)
	f_{ty}[N]	0.0067 (0.015, 5.9%)	0.015 (0.0096, 8.7%)	0.021 (0.035, 19.6%)
	f_{tz}[N]	0.051 (0.091, 11.9%)	0.016 (0.012, 3.6%)	0.035 (0.045, 6.1%)

slider motion) poses the smallest variability of the base force readings in the y-axis direction, showing the best accuracy in measuring f_y, and the highest in the z-axis direction, showing the lest accuracy in measuring f_z. The second actuation scenario (appendage bends toward slider motion) shows the smallest variability of this reading in the z-axis direction, better for measuring f_z, and the third actuation scenario (inactive appendage) shows the highest variability in the y-axis direction, not desirable for force measurements in this direction. The lowest variability of base moment readings around x-axis occurred in the first actuation scenario. The tip force sensor readings show small MSTD values too (less than 0.02 N) but they are not considered in our argument about the advantages of each probing configuration, since their readings are in the tip local frame. f_x, and $\tau_{y|z}$ remain small and are not important here since our results are based on planar cases.

The variability of the estimated tip force readings from simulations (Table 3.1) relates directly to the base force reading variability. Results from comparing the simulation results with the actual readings from the tip force sensor are promising, showing less than 0.04 N and 0.9 N absolute error for f_y and f_z respectively. The accuracy of the estimation method is higher

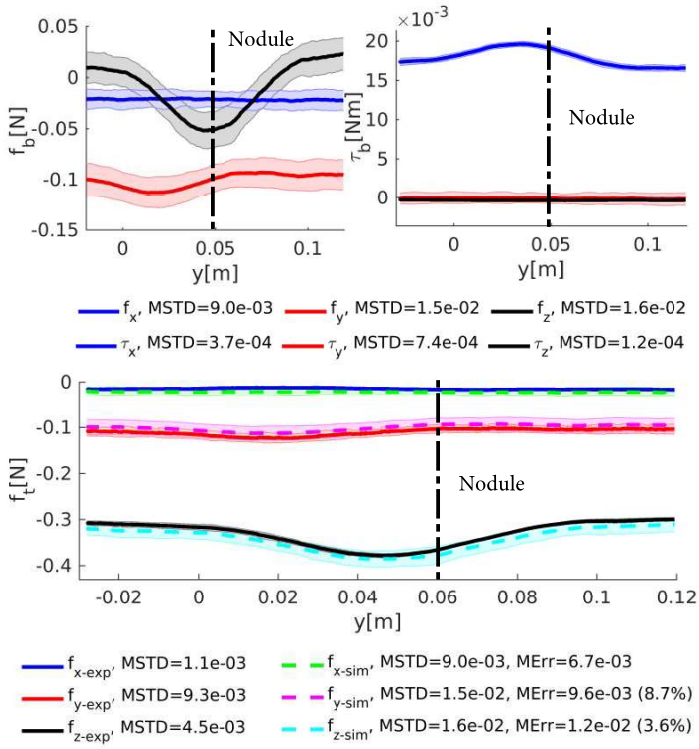

Fig. 3.5 *The statistical and error analysis of the experimental and simulations results for the second actuation scenario.*

for f_y in the first scenario (5.6%) and for f_z in the second scenario (3.6%), supporting our conclusion about the importance of bending direction on measurement axes. The statistical and error analysis of the experimental and simulations results for the second actuation scenario are presented in Figure 3.5, showing slightly higher variation in the results at the stiff region of the tissue (on top of the nodule), probably due to higher force absolute value at the point, but slightly less variation just before or after the stiff region, depending on the appendage bending direction. The plots are trimmed to remove the contact and transient phases, and to place the nodule location at the centre of the plots horizontal axis to be able to compare them with each other. Figure 3.6 shows the error analysis for the tip force estimation in the three actuation scenarios. The mean error values are higher around the stiff region ($y = 0.05\,\mathrm{m}$) and reduce after that. The first actuation scenario shows the smallest mean and variation in estimating f_y while these values are minimum for f_z in the second actuation scenario. The variation of f_z is higher around the stiff region but this becomes

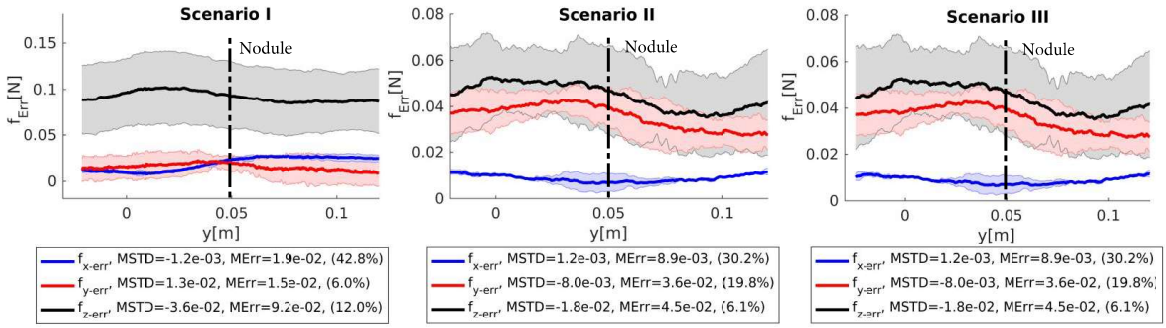

Fig. 3.6 *Error analysis for the tip force estimations in the three actuation scenarios, showing higher mean error values around the stiff region, where the variation of* f_z *increases but for* f_y *slightly decreases. Notice the different plot y-axis scales.*

smaller for f_y around this point. to explain this, we need to look into the surface stiffness and profile.

The appendage shape and tip position are estimated based on the base sensor force readings, showing higher apparent indentation, w.r.t. the mean height $h = 89\,\text{mm}$, in the first actuation scenario (bending opposing the probing direction), and smaller values for the second scenario (bending toward the slider motion), with a large difference between different actuation scenarios ($\approx 5.5\,\text{mm}$) but less overall variability (better accuracy) around the stiff region in each case (Fig. 3.7-top-left). The tissue stiffness is calculated, once based on the estimated tip force from the simulations, and once using tip force sensor readings, and compared with each other. In both cases, the estimated tip position from simulations is used. The large difference in the apparent indentation between the actuation scenarios results in high variation in the estimated tissue stiffness and surface profile around the stiff region (Fig. 3.7-top-right). The stiffness mean and MSTD values are smaller in the probing direction (y-axis) compared to the indentation direction (z-axis), with overall less variability (better accuracy) around the stiff region (Figure 3.7-top-middle). The mean and MSTD values of the calculated values for the tissue surface profile, estimated based on the base force sensor readings (z_b) or from the direct measurements by the tip force sensor (z_t), are very similar with $\approx 6.4\,\text{mm}$ mean difference and $< 1.2\,\text{mm}$ MSTD value, before and after the stiff region. However, the MSTD values are higher around the stiff region ($\approx 2.5\,\text{mm}$). This results in less accurate surface profile estimation around the stiff region but provides information that

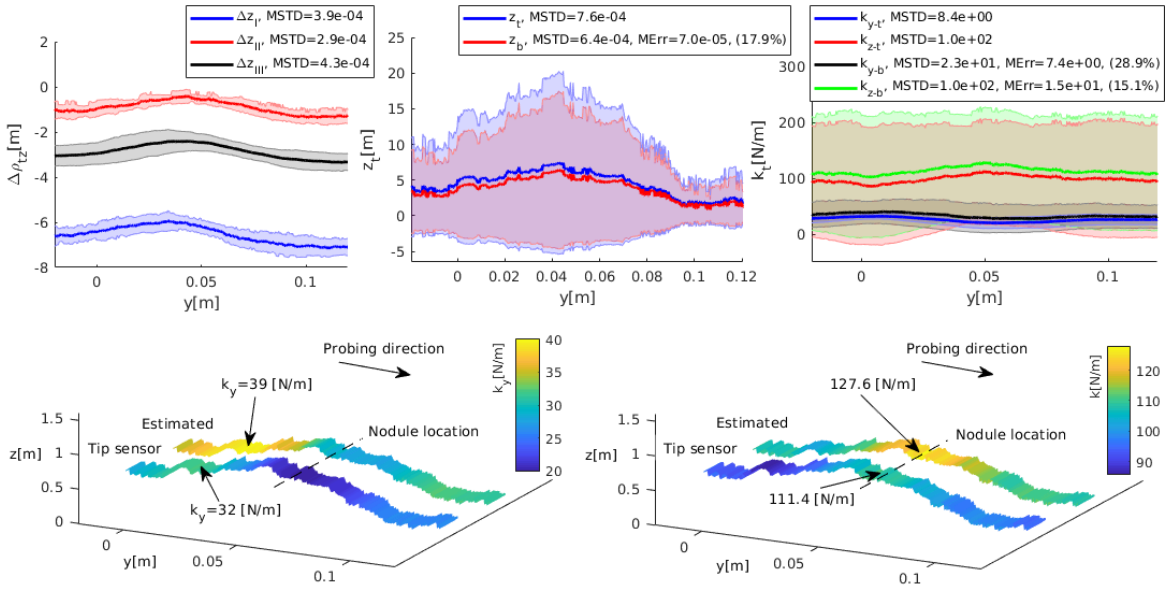

Fig. 3.7 *top) Error analysis for the tip indentation in the phantom tissue, tissue surface profile and directional stiffness values based on the estimated values from the simulations and the readings from the tip force sensor. bottom) the phantom tissue surface profile (in Cartesian coordinates) and directional stiffness colour map. The estimated and measured (based on tip force sensor) values for the same probing path (same x values) are shown side-by-side for comparison.*

eases the nodule detection [73, 100]. The estimated surface profile reveals irregularities in the tissue phantom surface which presents a small hump (≈ 0.4 mm) just on top of the embedded nodule, probably due to slightly less shrinking rate of this part of the phantom tissue during the curing process. This shows the feasibility of using base force sensor readings for surface profile estimation.

Finally, Figure 3.7-bottom shows 3D maps of the mean values for the surface profile and stiffness in the probing direction (k_y- left) and indention direction (k_z- right). The maximum value for k_y (≈30% increase w.r.t. the softer regions) occurs just before the stiff region (shown by dash line) providing predictive information about the nodule location. This value reaches its minimum almost on top of the nodule, due the small hump on top of the nodule and the fact that the nodule slightly slides back at this point. This suggests that the stiffness measurement along the probing direction (y-axis) provides a rich information signal for nodule detection tasks. The maximum value for k_z (≈17% increase w.r.t. the softer regions) occurs almost on top of the nodule, providing definite information about the nodule location. The

estimated value based on the base force readings is higher than the values based on direct tip force measurements (7.5 N/m (30%) for k_y and 15 N/m (15%) for k_y), showing the advantage of having direct tip force readings for accurate surface stiffness estimation. Smaller variation in measuring k_y strengthens the idea of using stiffness estimation in the probing direction as a more reliable means for hard nodule detection in a soft tissue sample [47].

Overall, the first actuation scenario, where the appendage bends against the slider motion, causes deeper indentation of the appendage tip into the tissue, since the surface friction and internal pressures act against each other. This scenario provides more repeatable/accurate force reading/estimation in the probing direction. The second actuation scenario, where the appendage bends toward the slider motion, results in more repeatable/accurate force reading/estimation along the indentation direction. This scenario is more suitable for accurate tissue stiffness estimation. An inactive appendage results in a mix of results with no obvious advantages for the considered aspects. Comparing estimated values from appendages with different initial bending directions results in large variability of the estimated value for the tissue stiffness. We suggest using measurements from actuation scenarios with similar bending direction for better stiffness estimation.

Compared to the similar efforts in the literature, the presented methods, does need a complex controller design [160], special considerations needed for guaranteeing convergence and accuracy of BVP numerical solvers [191], or suffer accuracy issues due to discretization consideration [184]. The appendage tip remains unoccupied with any force sensor and this space can be used for placement of any other required tool, with on-line real-time stiffness and surface profile estimations. There is no force sensor at the tip, exposed to direct contact with patients, meaning easier device sterilization and even the possibility of using a single-use probe. Finally, the fact that the presented shape and force estimation methods do not rely on any shape sensors [165], means they can be employed effectively as good basis models for Nonlinear Kalman Filter design if position measurements are not easily possible [180].

The proposed approach is tricky in the presence of external loads along arbitrary locations of the appendage backbone (f_l), hence, the appendage is not suitable for port-access surgeries. Using multiple force sensors to measure cross-section loads along the appendage would be a

feasible but hard to implement solution, due to size, cost and design complexity issues caused by adding multiple force sensors along a short appendage. An alternative is working toward fabrication of thin, light, accurate and affordable force sensors with this specific application in mind. Extension of this research could include investigating the effective palpation velocity and induced force, and comparing the results with the employed techniques by physicians, as in [47, 175]. Another possible avenue to look into is using a stiffness controllable appendage to increase the measurement accuracy and information gain [170, 47].

3.4 Conclusion

In this paper, for the first time, the use of a hydraulic-actuated braided continuum appendage is proposed for stiffness probing of soft tissues. Our method benefits from a robust light-weight easy-to-sterilize design featuring safe interaction due to the inherent compliance of the appendage soft structure. The appendage shape and tip force are estimated based on real-time forward integration of Cosserat rod theory that solely relies on load readings from a single base-fixed 6-axis force sensor. This approach removes the need for bulky and complex position tracking sensors or a tip force sensor. Multiple probing runs with different actuation pressures are used for mapping the tissue surface shape and directional linear stiffness along the probing direction and perpendicular to the tissue surface.

The results show that it is possible to detect non-homogeneous stiffness regions, i.e. a hard nodule embedded in the soft silicon phantom, in real-time. The accuracy and computational performance of using quaternions and rotation matrices for modelling the continuum appendage mechanics were compared, showing 18% faster execution time when using transformation matrices with exact similar results/accuracy. The appendage tip force is estimated with $< 0.35\,\mathrm{N}$ mean error in the probing and $< 0.1\,\mathrm{N}$ in the indentation direction, and $< 0.7\,\mathrm{mm}$ mean error is achieved in estimating the surface profile. However, $7.4 - 15\,\mathrm{N/m}$ (15-30%) mean error is observed in evaluating tissue directional stiffness, mainly due to comparing results from probing with appendages that are initially bent toward opposing directions. There are still many challenges to consider, e.g. tissue dynamic motion, palpation

strategies, etc, for which we propose using a variable stiffness appendage and a dynamic position/force modelling and control paradigm in future research.

Chapter 4

Tendon-Based Stiffening

Abstract— *As a result of the inherent property of soft robots being less rigid, the ability to control/obtain higher overall stiffness when required remains a challenge, to be further explored. Here, an innovative design is introduced which allows varying the stiffness of the continuum silicon-base soft robotic manipulator which has potential for applications involving close interaction with living tissue, as in Minimally Invasive Surgeries. Inspired by muscular structures in animals such as the octopus, a hybrid and inherently antagonistic actuation scheme is proposed. In particular, the octopus makes use of this principle activating two sets of muscles—longitudinal and transverse muscles—thus, being capable of controlling the stiffness of parts of its arm in an antagonistic fashion. Based on this concept, the designed manipulator presented here is pneumatically actuated employing chambers embedded within the robot's silicone structure. Tendons incorporated in the manipulator's wall complement the pneumatic actuation, to enable variation of overall stiffness. Experiments are carried out by applying an external force in different configurations while changing the stiffness by means of the two mechanisms. Test results show that dual, antagonistic actuation increases the load bearing capabilities for soft continuum manipulators with the potential to broaden their range of applications.*

4.1 Introduction

Taking inspiration from nature, researchers have created new robotic systems to overcome limitations of traditional robots composed of rigid joints and links [192]. In particular, animals' appendages such as the elephant trunk or the octopus arm have become the focus of studies creating soft, hyper-redundant robots, with capabilities similar to those of the biological role models [39, 193–195]. The application of these types of robots can result in significant improvements within a number of fields where traditional robots are currently deployed [161, 196, 197].

One of these areas is Minimally Invasive Surgery (MIS) - also called Laparoscopy or keyhole surgery [52, 85]. Most commonly, during minimally invasive procedures, rigid Laparoscopy instruments are inserted through so-called Trocar ports which are in turn inserted into a patient's abdomen through small incisions allowing surgeons to carry out surgical interventions inside the patient's body [6]. In particular during colo-rectal surgery, clinicians have observed considerable challenges when conducting keyhole procedures (such as the Total Mesorectal Excision (TME)) due to the limited manoeuvrability of the available surgical tools which are mostly rigid [6, 198]. It has been reported that soft robotics have great potential to overcome the aforementioned limitations [6, 92, 101]. A soft manipulator structure for MIS is beneficial because of increased dexterity and a more gentle interaction with soft tissue [60, 199] A decreased risk of injury to healthy tissue is another benefit to be noted. The large number of Degrees of Freedom (DoF) of a soft continuum robot provides enhancements when navigating around organs inside the patient's body towards the target, rather than "cutting through". A challenging task, however, when employing soft robots is how to exert/sustain effective forces against/from the environment and how to achieve an increased stiffness where required [101, 200].

An overview on stiffening techniques for continuum robots is presented in Section 4.2. Section 4.3 describes the proposed antagonistic actuation principle (see Figure 4.1) and summarizes the scientific contributions of this chapter. The mechanical design of the soft, stiffness-controllable robotic appendage is presented in Section 4.4 along with the overall

control architecture. Section 4.5 introduces the experimental methodology to validate the tunable stiffness mechanism and presents the main achievements. Conclusions and possible future works are discussed in Section 4.6.

4.2 Background

In the recent years researchers have investigated several solutions to the complex problem of changing and controlling the stiffness of soft manipulators [92]. A silicone-based, pneumatically actuated soft robot arm was developed as part of the EU-funded project STIFF-FLOP. STIFF-FLOP focuses on exploring some of the bio-mechanical characteristics of the octopus and attempts to extract relevant biological features to develop medical robotics systems for Minimally Invasive Surgery (MIS) [7, 60, 201] that are integrated with pose and force sensors [202]. Stiffness variation is realized with an embedded chamber within the silicone body filled with granules that can be jammed by applying a vacuum [200, 203]. Hence, the robot's configuration can be frozen once a desired pose is achieved.

The concept of polymeric artificial muscles described in [204] to actuate a robot manipulator was furthered in [205] by integrating granule-filled chambers which when exposed to varying degrees of vacuum could actuate, soften and stiffen the manipulator's joints. A similar concept is proposed in [206]. A hollow snake-like manipulator consists of multiple overlapping layers of thin Mylar film. By applying vacuum pressure, the friction between the film layers increases which results in a stiffening capability that is tunable. In [207], scale jamming is implemented on a set of curved scales which are 3D printed to form an overall helix, and jammed with two thin steel wires. The stiffness is controlled by changing the torsional stiffness and damping of the helical interface cross-section via the jagged contact surface. The structure, however entails external mounting on a (soft) continuum manipulator, adding to the total bulk and diameter of the system.

Researchers have further investigated smart materials to achieve different stiffness levels: A number of design parameters have been simulated and prototypes built/investigated in [208] in order to identify the impact of the overall structure on stiffness variation. In [209], the

authors report on a thermally tunable composite for mechanical structures - the used flexible open-cell foam coated in wax can change stiffness, strength, and volume. Altering between a stiff and soft state and vice versa introduces a time delay as the material does not instantly react to the heating-up or cooling down process. A similar approach has been chosen by [210]: a cPBE-PDMS composite has been created that can change its stiffness with in a duration of 6 s when exposed to an external voltage. Taking inspiration from sea cucumbers, a type of polymer nanocomposites has been explored in [211]. Being stimulated by a chemical regulator, a Young's modulus change was achieved and, hence, a variation in stiffness. A relatively comprehensive review on stiffening methods applied in MIS has been presented in [84].

In [212], a new mechanism inspired by the collaboration of longitudinal and transversal muscles in the tentacles of octopus has been presented. The developed manipulator combines a pneumatic activation and tendon-driven actuation mechanism in an entirely soft outer sleeve. The hybrid mechanism and design of the manipulator result in a new type of robotic manipulator that can collapse entirely, extend along its main axis, bend along the main axis and vary its stiffness. The proposed robot arm is inherently flexible, manufactured from segments that consist of an internal stretchable, air-tight balloon and an outer, non-stretchable sleeve preventing extension beyond a maximum volume. Tendons connected to the distal ends of the robot segments run along the outer sleeve enabling the manipulation of the manipulator by bending the sleeve when the corresponding tendon is pulled via 12 stepper motors.

However, Maghooa et. al. in [212] primarily use the antagonistic principle to "move" their robot, rather than an additional feature of "stiffening". The afore-mentioned manipulator in is not functional at all without the fluidic activation (being a one DoF inflating/deflating system), and the tendons are the sole means of controlled navigation. Maybe more precisely, Mahgooa et. al.'s manipulator is rather a fluidic "activated" and a tendon "actuated" system.

In this research, the hybridization principle has been transferred to a silicone-based soft robotic manipulator. The contributions of this study are as follows:

- The antagonistic actuation principle (pneumatic and tendon-driven actuation) is applied to a soft robotic segment made of a silicone structure, extending from the manipulator structure described in [212] which is composed of a fabric sleeve with an internal latex bladder and primarily utilizing the tendons for controlling the position and navigation, to an already-functional soft robotic platform.

- Fluidic actuation is used to bend and elongate the robotic arm (i.e. manoeuvring the robot's tip); tendon actuation is used to effectively lock the robot's configuration and, hence, increase its stiffness in the achieved pose. The work here shows the potential of "hybridizing" soft robots with a tendon-based actuation type, to achieve stiffening, similar to what can be achieved using granular jamming.

4.3 Bio-inspiration

Biological studies identify that the octopus arm is composed of longitudinal and transverse muscle groups acting antagonistically that are bonded by connective tissue [36, 41, 144, 213], rendering it capable of an extensive variety of movements in addition to controlling the arm's stiffness. On this basis, we propose an antagonistic actuation method combining the advantages of intrinsic, pneumatic and extrinsic, tendon-driven actuation. Tendon-based actuation is also beneficial for fine-tunning the tip position in miniaturized robotic systems. This is achievable due to the thin structure and high tensile strength of tendons. Fluidic actuation is suitable for driving compliant manipulators that operate in the vicinity of humans and, hence, need to be inherently safe. To summarize:

- Fluidic pressure is used for stretching out and controlling the motion and direction of the soft manipulator resulting in bending and elongation.

- The compliance of the manipulator is varied by changing the stiffness through the appropriate control of the two opposing actuation means; pneumatic and tendon-based actuation.

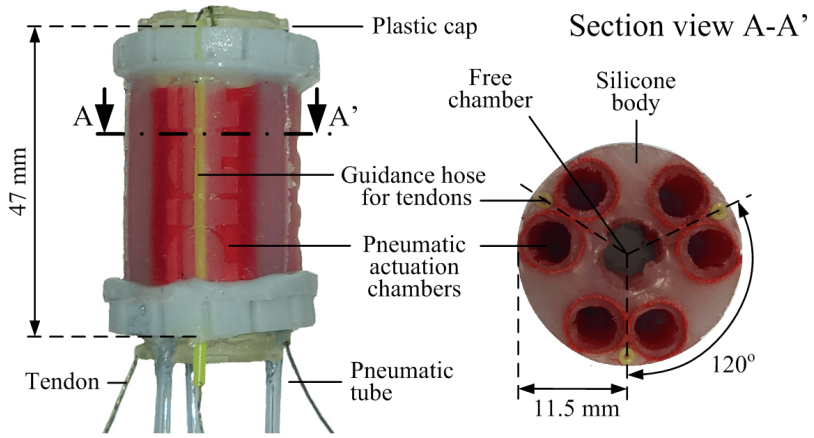

Fig. 4.1 *Side and cross-section view of a segment/module of the STIFF-FLOP manipulator with integrated stiffening mechanism based on the antagonistic principle: Three pairs of pneumatically actuated chambers are embedded into a silicone body. Between each set, a hose is integrated into the periphery of the manipulator to guide the tendons that are used to apply stiffening. The tendons are fixed to a plastic cap at the tip of the robot arm.*

4.4 Integration of the Antagonistic Stiffening Mechanism

As mentioned earlier, the work described here is the result of transferring the antagonistic actuation principle presented in [212] to a silicone-based soft continuum robot, such as the one developed in the EU FP7 project STIFF-FLOP: one segment of the STIFF-FLOP manipulator (Figure 4.2) is a cylinder of silicone made of Ecoflex® $00-50$ Supersoft Silicone with properties mentioned in Section 2.1 of this thesis.

The segment prototype utilized here has an overall length of 47 mm and an outer diameter of 23 mm. Along the wall of this cylinder, three pairs of fibre-reinforced pressure chambers (6 mm diameter) are implemented and actuated pneumatically. Each pair of chambers is connected to one inlet air pipe creating the ability to bend the segment by increasing the air pressure in one chamber pair relative to the other two chamber pairs. Simultaneous pressurization of the all dual chambers will result in an overall elongation of the segment. The created segment (Figure 4.2) has an inner free chamber of 9 mm diameter - this space is incorporated to pass through tubes from additional segments and wires when creating a manipulator with a series of multiple segments.

4.4.1 Embedding tendon-driven actuation into a STIFF-FLOP segment

The tendon-driven actuation mechanism is embedded into a single cylindrical silicone segment modelled after the STIFF-FLOP manipulator [85]. Figure 4.1 shows a side and cross-sectional view of the robot arm with the integrated antagonistic actuation principle. In this prototype, a stretchable, silicone-based tube (Cole-Parmer Instrument Co. Ltd.) with an outer diameter of 1.5 mm and an inner diameter of 0.8 mm is aligned in between each set of the fluidic chambers, parallel to the longitudinal axis of our robot. The three hoses are placed 120° from each other and housing the tendons for extrinsic actuation. This design will allow the tendons sliding within the tubes and avoiding any cuts into the silicone body. Due to the tube's material properties, the STIFF-FLOP segment keeps its key characteristics of being soft and squeezable; the silicone tubes move in a compliant way when intrinsically actuating the robotic appendage. The used tendons are braided microfilaments (PowerPro Super Line) of 0.15 mm diameter. The three tendons are fixed to a plastic cap at the tip of the robot arm to distribute forces onto the soft tip surface when under tension. The overall structure is shown in Figure 4.1.

4.4.2 Setup of the antagonistic actuation architecture

The overall actuation system consists of an air compressor, three pressure regulators, a data acquisition board (DAQ), three stepper motors, and a modified STIFF-FLOP segment as described in Section 4.4.1. Figure 4.2 illustrates the logical interconnection between the installed equipment.

As mentioned earlier, a hybrid actuation mechanism is employed here: On the pneumatic actuation side, an air compressor (BAMBI MD Range Model 150/500) supplies the required pressurized air of 5 bar to three independent pressure regulators (SMC ITV0030-3BS-Q). Their outputs, which connect to the three chamber pairs of the soft module, are varied via input signals proportionally controlling associated chamber pressures in a range between 0.001 to 0.5 MPa. Each pressure regulator adjusts the outlet pressure for each chamber pair according to the command received from the computer through a DAQ board (NI USB-6411).

On the tendon side, each tendon is connected to a stepper motor (Changzhou Songyang Machinery & Electronics Co. SY57ST56-0606B) which provides a maximum holding torque of 0.59 Nm. Each stepper motor has a pulley attached to its output shaft which the tendon is wound around to displace the length of each tendon, and are located outside the manipulator [214]. The pulley has a 6.4 mm radius, which results in a maximum of 92.6 N of tension. Since one STIFF-FLOP segment has three tendons, three stepper motors are used. Each stepper motor is driven via a driver (Big Easy Driver ROB-11876) which communicates with the computer via a DAQ board. The computer runs a Windows based operating system with a C# code interface.

4.5 Test Protocol, Experimental Results and Discussion

4.5.1 Methodology

Several stiffness experiments have been carried out mounting the module downwards and applying forces to the tip. In all scenarios, a motorized linear mechanism is programmed to

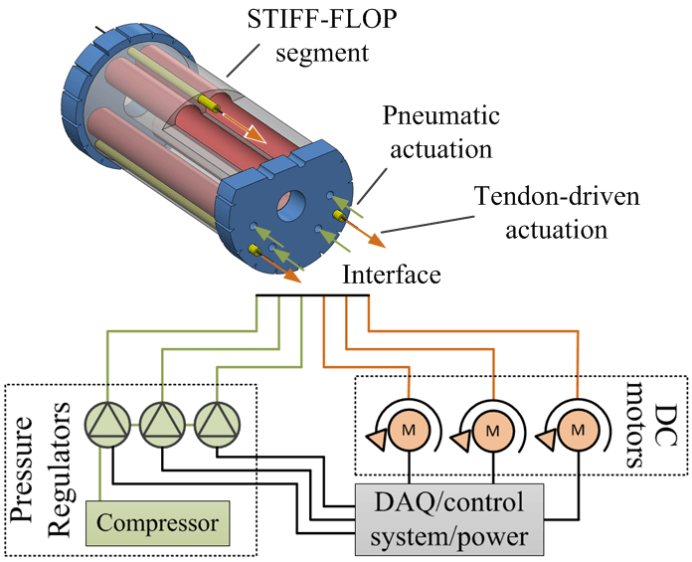

Fig. 4.2 *Schematic overview of the antagonistic actuation setup: The air chambers are connected to three pressure regulators. An air compressor supplies pressurized air to the regulators. Each tendon is wound around a pulley which is fixed to the shaft of a stepper motor. The analogue input for the three motors and three pressure regulator is controlled via a data acquisition board.*

create a displacement of 1 cm by sliding horizontally along its rails. Reaction forces created by the module to resist this displacement were recorded using a Nano17 Force/Torque sensor by ATI Industrial Automation. Three main scenarios were considered, equivalent to the investigations presented in [52, 215], (Hence, the obtained results will be comparable.):

Scenario 1:

The module is held vertically downwards. The force is applied laterally to the tip as shown in Figure 4.3a. In this scenario, four different sub-cases are investigated:

A No air pressure and no tendon tension.

B Equally air-pressurized chambers (i.e. elongation) with no tendon tension.

C No air pressure with initial equal tendon tension.

D Equally air-pressurized chambers with initial equal tension in tendons.

Scenario 2:

The module is held vertically and one of the dual chambers is pressurized to form a 90% curved shape, and the force is applied laterally as shown in Figure 4.3b. Two different sub-cases are investigated:

A One pressurized chamber and no tendon tension.

B One pressurized chamber and tension in tendons.

Scenario 3:

The module is pressurized to be configured as Scenario 2. This time, the force is applied opposing the tip as shown in Figure 4.3c. Also in this scenario, two different sub-cases are investigated:

A One pressurized chamber and no tendon tension.

B One pressurized chamber and tension in tendons.

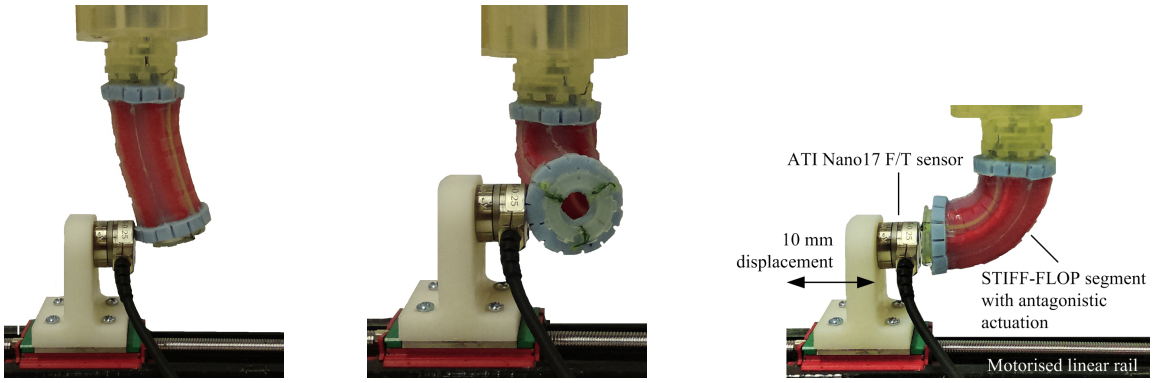

(a) (b) (c)

Fig. 4.3 *An ATI Nano17 Force/Torque sensor is mounted on a motorized linear mechanism displacing the manipulator's tip by* 1 cm*: The configurations in (a), (b) and (c) show Scenarios 1, 2 and 3, respectively.*

4.5.2 Experimental Results

Data from the ATI Nano17 F/T sensor and the corresponding displacement of the motorized linear rail were recorded at 1 kHz using a DAQ card (NI USB-6211). Four trials were performed for each sub-case. Experimental results of all four sub-cases of Scenario 1 are presented in Figure 4.4a. When the module is neither pressurized nor stiffened by tendons, the amount of its resistive force subjected to a 1 cm lateral displacement is about 1.32 N. This value is 0.55 N when all three chambers are pressurized. When subjected to tendon stiffening, the resistive forces displayed by the module reach values of 2.56 N and 0.93 N, respectively, showing a 94% and 69% increase compared to the first and second sub-case.

Results of the two sub-cases of Scenario 2 are shown Figure 4.4b. When the module is only pressurized, the value of the resistive force is 0.75 N. With tendon stiffening is added to the module, this resistive force increases to 0.98 N showing a 31% growth.

Results of the two sub-cases for Scenario 3 are presented in Figure 4.4c. It can be seen that in the presence of pressure only, the module generates a resistive force of 2.43 N. However, by introducing tendon stiffening, the resistive force due to 1 cm displacement intensifies to 3.02 N, displaying a 24% growth.

Table 4.1 summarizes the experimental results. For each sub-case, the maximum force, hysteresis and percentage of increase is calculated. Hysteresis was calculated by taking the

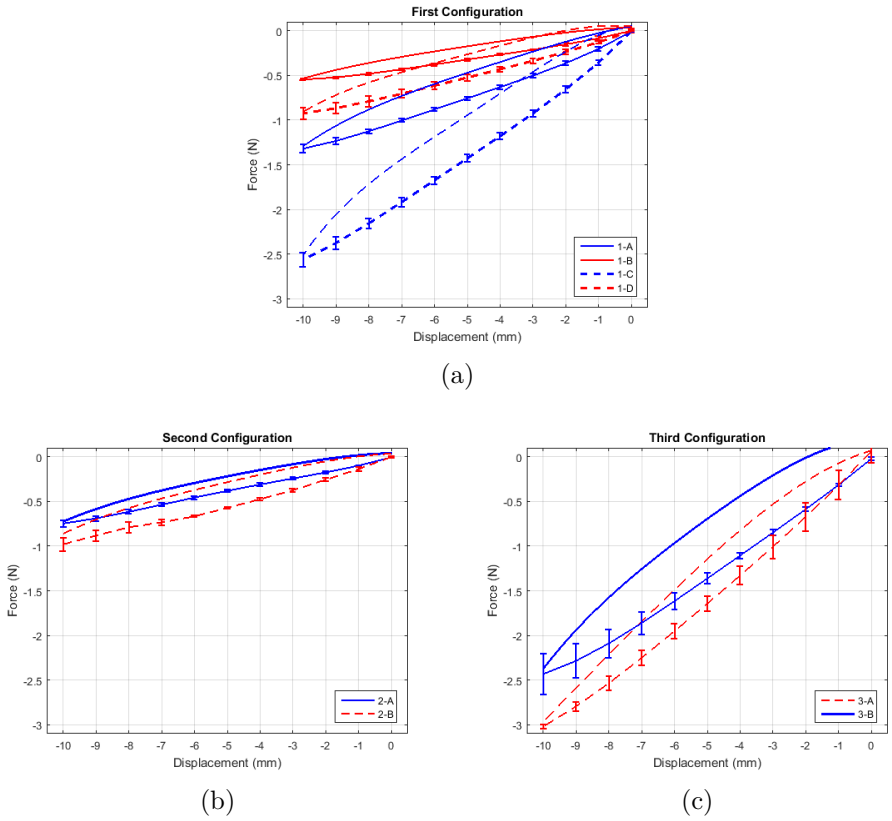

Fig. 4.4 *Experimental data for Scenarios 1, 2 and 3. Forces have been recorded for displacements of* 1 cm *of the manipulator's tip. Table 4.1 summarizes the data analysis.*

area between the loading and unloading curves, and normalizing by dividing it by the loading curve.

Table 4.1 Summarized results of stiffness tests for Scenarios 1, 2 & 3.

Scenarios					F_{max}	Hyst.	Increase
1-A	Tens.	No	Press.	No	1.32 N	21.6%	n/a
1-B	Tens.	No	Press.	Yes	0.55 N	27.2%	n/a
1-C	Tens.	Yes	Press.	No	2.56 N	18.9%	93.9%
1-D	Tens.	Yes	Press.	Yes	0.93 N	28.5%	69.1%
2-A	Tens.	No	Press.	Yes	0.75 N	21.8%	n/a
2-B	Tens.	Yes	Press.	Yes	0.98 N	33.46%	30.7%
3-A	Tens.	No	Press.	Yes	2.43 N	27.47%	n/a
3-B	Tens.	Yes	Press.	Yes	3.02 N	14.86%	24.3%

4.5.3 Discussion

Looking at the summary of the experimental results in Table 4.1 and Figure 4.3, using the antagonistic actuation principle allows us to increase the overall stiffness of the soft manipulator by almost 100%. Hence, the soft manipulator when tensioned using the tendons is more rigid and capable of performing tasks that require larger force exertions - as for example required at times in the tight environment inside a patient's body. This gives the surgeon the ability to move the manipulator, primarily with pressure actuation, and thereafter, use the tendon stiffening to acquire not only higher stiffness, but also fine-tune the final position of the end effector and more accurately manoeuvring the attached instrument to the desired target.

In [52], an 8 mm diameter channel of granular material (ground coffee) was embedded into a prototype of the silicone-based STIFF-FLOP segment; the length of this segment was 50 mm with the silicone structure having a diameter of 25 mm. The pneumatically actuated chambers were not reinforced; a crimped, braided sheath of a 35 mm covered the silicone structure and prevented a ballooning effect. Neglecting the outer cover, the STIFF-FLOP module has dimensions similar to the ones of the segment described in this chapter. The key experimental results for stiffness tests at a displacement of 10 mm are summarized in Table 4.2. The test configurations of three scenarios are equivalent to the ones described in Section 4.5.1, granular-jamming-based stiffening is achieved by applying a vacuum.

Table 4.2 Force results for granular jamming applying a 10 mm displacement as reported in [52].

Scenarios	Granular jamming	F_{max}	Increase
1-A	Off	2.2 N	n/a
1-A	On	3.1 N	40.9%
2-A	Off	2.3 N	n/a
2-A	On	2.7 N	17.4%
3-A	Off	2.8 N	n/a
3-A	On	3.3 N	17.9%

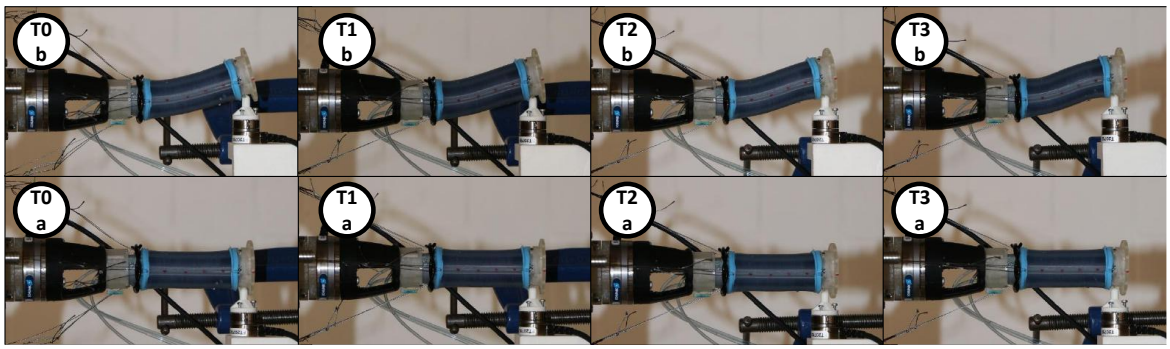

Fig. 4.5 *Change in overall posture at different tension levels: T0 to T3 indicate increasing tension levels, and subscripts "a" and "b" denote "no load" and "applied external load", respectively; without altering the initial internal pressure.*

Comparing Tables 4.1 and 4.2, the actual maximum forces F_{max} measured during the experimental tests of Scenarios 1 and 2 are larger using granular jamming. The presence of coffee granules (under atmospheric or vacuum pressure) integrated into the silicone-based robot results in a stiffer module. Looking, however, at the percentage increase caused by granular jamming on the one hand and the antagonistic mechanism on the other hand, the tendon-based stiffening principle is able to generate a larger increase.

As some final remarks; it is noted that altering the internal tension affects the overall pose of the soft manipulator. Figure 4.5 demonstrates the manipulator subject to an initial internal pressure ($P1 = 1.58$, $P2 = 1.64$, $P3 = 1.6$ bar) generating a uniform elongation, while increasing the overall tension in 3 stages ($T1$, $T2$, $T3$); with values tabulated in Table 4.3.

The lower row in Figure 4.5 shows the pressurized manipulator with no tension (sub-figure T0.a) up to maximum tension (subfigure T3.a), with no external load applied. The top row shows the corresponding level of tension from the lower row, while under 1 cm of lateral imposed displacement. Although stiffening the manipulator seems to have negligible effects on the tip position while no external load is applied in this case (lower row in Figure 4.5),

Table 4.3 Four levels of tension causing deformation of STIFF-FLOP under external loading (N)

T0	T1	T2	T3
0	1.63	8.12	10.04

comparing the shape of the deflected manipulator in subfigure T0.b (no tension) under external load, with the sequence of figures up to subfigure T3.b (maximum tension) depicts how the overall shape evolves with elevated levels of tension. A detailed discussion regarding the structural and geometrical effects of increased tension on the manipulator, however, digresses from the scope of the current study and is left for future investigations.

4.6 Conclusions

Here, we have transferred the antagonistic stiffening principle to a silicone-based robotic appendage initially comprising 3 DoF of fluid actuation, presenting a novel soft robot augmented by hybrid actuation. The mechanism is inspired by the longitudinal and transverse muscle fibres that the octopus uses to stiffen its tentacles. In this setting, air pressure is used for bending and elongating the soft manipulator. Tendons are used to act in an antagonistic way opposing the pneumatic actuation, providing the simultaneous ability to control the robot's pose and regulate its internal stiffness. The experimental results obtained using the antagonistic actuation principle are compared to a similar study where stiffening is achieved using granular jamming.

Tendon actuation could not only be used for structural stiffening, but potentially allows more accurate position control. Since the tendons are embedded inside the manipulator's wall, this ability is achieved without increasing the diameter of the manipulator.

Conclusively, this developed innovative hybrid soft system could potentially lead to invigorating topics stemming off from this concept. An interesting subject could be looking into the structural deformities and even buckling in different (and usually elevated) levels of antagonistic pressure-tension interplay (the buckling phenomenon was witnessed by increasing the tension above the values tabulated here, which was omitted from this report due to sever distortion of the manipulator beyond the point of designed operational posture). Also, the correlation between pressure and tension and their effect on tip positional displacement may yield in developing actuation strategies to compensate unintended drift due to internal

stiffening. Another possible future direction is exploring various forms of tendon/actuation routing within the manipulator, which falls beyond the scope of this study.

Chapter 5

Morphological Control in Haptic Perception Using a Soft Continuum Appendage

Abstract— *Tele-operation using soft robotic principals has attracted a lot of research interest for safe interaction with delicate and/or living tissue. In this regard, certain desirable morphological features such as structural compliance, safety, and embodied sensing are key. This chapter introduces a variant of the tendon-augmented soft appendage by adding tendons to the previous dual actuation soft continuum manipulator, in order to achieve a more uniform tension distribution along the body. The manipulator is hydraulically actuated and with the tendon stiffening mechanism, is used to probe a soft tissue with an embedded nodule in different pressure/tension scenarios. The antagonistic stiffening via dual actuation is a reminiscence of impedance regulation in biological appendages during haptic exploration. The manipulator is pressurized into various configurations along with different stiffness levels induced by the embedded tendons. As the morphological features of the soft appendage are altered, sensing modalities are monitored and the effects of perception is investigated across different poses and stiffness.*

5.1 Introduction

Developing a cognitive map between the real world and the agent for truthful perceptions and inferences about the environment is essential for successful action of the agent [216]. Although sensorial devices have advanced remarkably during the recent years, yet machine perception continues to be a challenging quest [37]. One of the most significant means of attaining sensory information is via "touch" or haptic perception [175], which facilitates extraction of mechanical properties that are visually concealed and accessible only upon physical interaction; such as weight, softness, texture and so on. Despite some vagueness and disagreements in definition and literature, haptic sensing can be roughly classified into two categories: A) surface sensing; i.e., tactile; and B) embodied sensing. The latter is subdivided into position (proprioception) and motion (kinaesthetic) sensing [217]. In a human hand, for example, mechanoreceptors at the tip of the finger are responsible for tactile information, while organs like Pacinian Corpuscles, muscle spindles, and Golgi tendon organs located in the muscles and ligaments contribute to embodied sensing. An artificial counterpart could be considered in a robotic finger were tactile signals are the force/pressure signals received from a tip-mounted sensor, while signals related to joint angles from encoders or actuator effort (e.g. motor force/torque) measured at the joints or the proximal base are considered as kinaesthetic or proprioceptive [26], depending on the context.

Research on modelling and understanding the function of the human hand has been underway since the mid 1980's, aiming to reproduce similar qualities for robotic grasping [218] and promoting research in robotic haptic sensation [219]. A prime example in this field is robotic palpation of soft tissue [186] and its applicability for medical procedures [217], due to the increasing demand to employ robotic surrogates in medical procedures such as Minimally Invasive Surgery (MIS) [160].

MIS or Laparoscopy promises many advantages over traditional open surgery, such as minimized tissue damage and reduced recovery time [83]. However, problems have been reported regarding tool manipulation and lack of intuition and dexterity during Laparoscopy procedures [217], as the clinicians lose both the sense of direct touch [220, 221] and direct

visualization [221]. One of the main drawbacks in MIS is the shortfall on haptic sensory feedback [203, 188]. In traditional procedures, the surgeon exploits haptic sensation via explicit contact with patient's tissues and organs, rendering it as of paramount importance [222] which yields valuable information for the surgeon [221]. The availability of haptic feeling enables exploration and health assessment of the organs as the fingers' natural sensations are available in applying pressure and/or feeling the texture [203]. Notably, it has been reported that tumours have significantly higher stiffness than the surrounding tissue [83, 187]. A surgeon often detects a tumour by palpating that region [221]. Palpation is abundantly used to locate anomalies concealed underneath the skin [217, 223] where the finger comes in direct contact with the compliant tissue resulting in both the finger and the tissue changing shape [83]. Hence, within this concept, practical and permanent utilization of any artificial agent designed for assistance in this field is heavily reliant on facilitating haptic sensation [224]. As of now, current tele-operated platforms do not provide haptic data for the medical practitioner [225].

Implementing robotic palpation is complicated due to uncertainties [224]. Many studies have attempted to understand human palpation strategies and compare them with results from robotic palpation, noting the importance of replicating the behavioral patterns in palpation in robotic devices [224] and the role of robotic assistance in MIS [226]. Most of these studies use a Silicone-based phantom to represent the soft tissue which accommodates artificial embedded hard elements. Gwilliam et. al. in [83] compared human tactile sensing with passive robotic tactile sensing on a Silicone phantom containing hard nodules buried from 1.5 mm to 3.5 mm of the surface. Their experimental results revealed that for robotic tactile detection of embedded anomalies, lower probing indentations and exerted pressures are required compared to humans. Their findings also supports the application of robotic devices in MIS where less applied pressure helps less tissue damage. Additionally, they stated that their robotic tactile perception outperformed the human subject in all cases. In [188], Ayvali et. al. implemented Bayesian optimization to explore the stiffness distribution of a Silicone phantom and an ex vivo liver using a rigid link robot with a force sensor at the base assuming that the stiffness distribution changes smoothly. The maximum applied force was 0.5 N and the experiments were carried out by discretized probing, which is claimed to be relatively

disadvantageous compared to continuous probing [220]. Chalasani e.t al. employed a Gaussian process to estimate stiffness and geometry at the same time, by palpating a Silicone phantom using sweeping movements and at different depths while maintaining quasistatic conditions using a rigid robotic link. In a comparative study [219], Konstantinova et. al. investigated human palpation behaviour of detecting a hard nodule embedded in Silicone in the depth of 5 mm compared to a rigid-link robot programmed to perform with the same behaviour. Their research continued in [186], by palpating a Silicone tissue with a rigid-link robot utilizing some of the human strategies autonomously, demonstrating increased efficiency in the robotic system. Liu et. al. in [221] developed a hard plastic wheeled device to probe a Silicone tissue with various embedded hard nodules embedded in depths from 5 to 13 mm and an indentation depths of 2 to 4 mm. In [187], a novel approach of stiffness measurement was proposed by Wanninayake et. al. using an air-float probe.

Apart from haptic perception, advancement in this subject also requires empowering other manipulation capabilities. For example, manoeuvrability is a necessary requirement for tools operating within confined environments such as MIS [75]. Particularly, one of the prominent issues in bringing robotic devices close to sensitive surroundings, is safety. Successful robotic interaction with their environment requires robots which safely and gently conform to the anatomical boundaries [60]. Force feedback is one of the means which not only enables detecting anomalies and tumours, but also has an important role in tissue safety [76]. However, the increase in the number of MRI procedures mandates utilizing tools which are material-wise compatible to the task and pose no signal interference. In addition, mounting a tip (end-effector) force sensor raises sterilization concerns [76]. These reasons urge investing in techniques which remove the need for force sensors placed on the end-effector.

All of the concerns mentioned above call for a robotic platform that is safe for interaction with sensitive tissue, easily sterilized, enables haptic perception without the need for a force sensor mounted at the tip, and is sufficiently dexterous. In this sense, soft continuum systems seem as a perfect candidate.

Inspiration from certain species in nature such as the octopus has sparked a new trend in robotics which aims to enhance artificial performance. The idea of soft-bodied robots

grasps the notion of intentionally integrating compliance right away at the mechanical design level, with the aim of getting closer to how nature exhibits compliant behaviour. Employing soft materials in robots produces certain morphological properties with unique advantages over conventional rigid link robots, such as inherent safe contact, variable passive stiffness, and highly dexterous manoeuvres. The emerging system benefits from embodied intelligence where coupled sensorimotor activity and body morphology facilitates regulation of the body to maximize sensory information gain [2], yet without exerting additional computational burden on a centralized controller. For example, Helps and Rossiter [227] employed a conductive liquid for both actuation as well as the sensing soft actuator.

Embodiment simplifies computation by "offloading" computational burden from a central controller and outsourcing it to the body. Studies in nature demonstrate such a trait amongst many biological entities [26]. In this regard, morphological control in haptics can be defined as utilizing the mechanical or geometrical properties of the body to enable and improve perception through contact.

Settings with soft continuum robots would also be appealing for tele-operated robotic activity operating on remote locations (with limited access to professionally trained staff) or where direct contact/exposure of professional staff with/to the subjects possesses potential biological or environmental hazard. Such scenarios are prone to experience scarcity of sensing hardware or limited sensory information. Hence, investing in techniques which reduce sensory hardware could be highly advantageous.

The ability to utilize artificial continuum appendages in real-time force estimation has been investigated in studies such as [87, 165], demonstrating the effectiveness of such devices in handing in force data via their intrinsic capabilities. In [3], Sornkran claims that an articulated soft probe is more efficient than a rigid mechanism in the task for localizing embedded nodules in soft phantoms.

A noteworthy and interesting topic in this regard is controlling the impedance of such robotic systems and its effect on amplifying a desired output in perceptual tasks which remains an open question and an ongoing research field [84]. As mentioned in Section 1.4, mechanical impedance is defined as the collective effect of inertia, damping, and spring

behaviour. Altering these properties in humans and animals usually occurs via manipulation of internal organs such as the muscles and tendons [3, 47], for example when a human bobs an object with his hand to estimate its weight, or when he palpates a surface with his finger to determine the texture or stiffness by modulating the finger's muscles.

In the realm of biological species, survival demands high information gain and fast data analysis. Hence affordance of sensory information becomes of prime importance. Tuning internal impedance [3, 44, 73] has proven to play a major role in refining environmental perception through contact in order to hand in beneficial results, and is one of the key factors in determining the quality of perception and action in both biological organisms and robots [3]. Regulating the internal impedance can be witnessed profusely in haptic perceptual tasks in nature. A prime example would be how the clinician adjusts the stiffness of his/her fingers to locate subsurface anomalies in patients [177]; a usual routine which is taught for medical examination [83]. Along these lines, Herzig et. al. developed a finger-like robot capable of internal impedance variation, which they used for hard nodule detection on Silicon phantom [177], albeit incorporating hard material.

In this research, the soft continuum appendage with dual actuation is used to palpate a soft tissue containing an embedded nodule, causing a concealed inhomogeneity in the stiffness of the tissue. We aim to explore whether: 1) A buried anomaly would affect the sensory readings conveyed via a soft robot in a haptic exploration, and whether the region with a different stiffness could be distinguished; 2) Augmenting this soft appendage with a variable stiffness mechanism would improve perception; and 3) Utilizing two sensors at different locations (tip and base) would unravel some of the aspects of correlation between tactile and proprioceptive sensing, and whether embodiment could be utilised to receive sensory information at the base, potentially removing the need for installing an additional sensor at the tip.

5.2 Objectives & Contributions

This study proposes a novel approach for active haptic perception by utilizing a bioinspired finger-like continuum soft appendage. The proposed robot not only benefits from intrinsically soft materials in its structure (hence ensuring inherently safe manipulation and contact), but also is equipped with a tendon stiffening mechanism to enable variable impedance to suit the task at hand and/or provide various perceptive readings on a task.

The variation in impedance - whether invoked actively (via pressure and tendon stiffening) and/or passively (via adaptive deformation) - is exploited to study the effects on tactile and proprioceptive modalities and to investigate how different sensing cues alter in the light of various combinations of pose, internal fluidic pressure, and elevated stiffness. This study does not address localizing the depth of nodule, but rather focuses on the role of morphology and its effect on sharpening the perception and the parameters involved in advancing information gain. Morphological control herein refers to the ability to control or vary physical structure of such an artificial agent, similar to how biological systems utilize their active and passive bodily features in order to adapt to the task or environment [47].

Findings form previous studies on human haptic perception claim that in processing information, a small number of tactile and proprioceptive sensory cues is preferable over a large number of the same type of sensory stimuli alone (e.g. only multiple channels of tactile signals) [47, 228]. Hence, contrary to most studies in the field which only look into either tactile or proprioception, we take both cues into account to construct a closer resemblance to natural agents. A tip force sensor provides tactile data of the soft manipulator probing the phantom while a base force sensor delivers the force readings transferred from the tip to the base via the manipulator's body. This setting is analogous to the human finger in the sense that complementary to the mechanoreceptors at the fingertip, forces are felt throughout the muscular structure and up to the distal joint, generating the proprioceptive cues [47]. Correlations between the recorded sensing modalities are derived with the aim to provide some insights not only for robotic probing strategies, but possibly explain some hidden layers of human behaviour in sweeping surfaces.

The work presented here, to the best of our knowledge, is the first time where a soft continuum manipulator has been used to emulate the human finger in palpating an artificial soft tissue. Additionally, it's the first time were a dual actuation soft robot is utilized for such a purpose, and it's also a pioneering study that incorporates two sensors (one placed at the tip and another mounted at the base) in a soft tunable impedance setting to the study the effects of morphological alteration not only on the quality of perception but also on the interplay between some of these sensory cues. The main contributions of this study are summarized as follows:

A. Introducing and utilizing a dual-actuation variable impedance soft continuum appendage for safe contact capable of active haptic perception,

B. Investigating the effect of tuning the internal impedance (via intrinsic fluidic or extrinsic tendon actuation) on haptic sensory information (both tactile and proprioceptive readings) in the context of soft continuum robots,

C. Studying aspects of the interplay between tactile perception and proprioception in a soft robotic platform; which may serve as a potential source of information for insights on biological behaviour in haptic exploration.

5.3 Materials & Methods

The experiments entail a soft continuum appendage sweeping the surface of a soft tissue containing an embedded hard nodule. The manipulator employed in this study is the STIFF-FLOP module described in previous chapters; comprising three independent channels for hydraulic actuation in addition to three other independent channels for tendon stiffening.

The phantom acting as a soft tissue is cast out of Ecoflex 00-10 soft Silicone with the dimensions of $140 \times 80 \times 30$ mm as shown in Figure 5.1. For casting, The A and B components of the chemical substance are mixed on a 1:1 ratio according to the manufacturer's data sheet. Initially, a bottom layer is cast into the mold and allowed to cure. Upon hardening, an M8 nut (used the hard embedded nodule) is placed on the center of bottom layer's surface, without submerging. Thereafter, the additional layer of the Silicone mixture is poured to

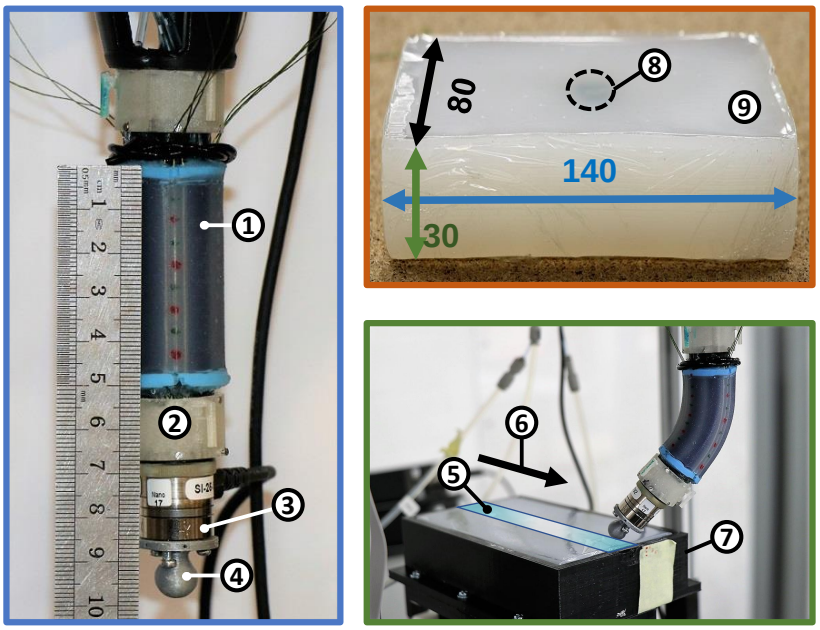

Fig. 5.1 *STIFF FLOP soft continuum appendage integrated with the Silicone phantom for probing. 1: The STIFF-FLOP, 2: 3D Printed place holder for attaching the Nano17 force sensor, 3: Nano17 force sensor, 4: 3D printed contact nob, 5: Probing path on the phantom, 6: Direction of relative motion, 7: The Silicone phantom in its container mounted on the linear guide rail, 8: M8 nut embedded as the hard nodule, 9: Silicone phantom with dimensions in mm.*

the amount designated to bury the nodule; i.e. 2 mm. A final resting time is subsequently required for the phantom to completely set. The size of the anomaly remains unaltered during the experiments, which is backed by the findings in [186] claiming that the behaviour of force modulation of humans is independent from the size of the nodule. The phantom is placed in a hard container and fixed on a HIWIN KKA40 high precision linear actuator which is controlled by an Arduino UNO through a stepper motor. The software interface is coded in C#.

An ATI Nano17 F/T sensor is attached to the tip for measuring direct contact forces, displayed in Figure 5.1 item 3 and Figure 5.2 item 6. As in Chapter 3, to facilitate a direct contact with the Silicone phantom without damaging effects, a 3D printed nob with a spherical tip ($R = 5$ mm) is affixed to the Nano17 tip. It is noted that for most accurate measurements in probing homogeneous material, minimum contact area is preferable. Hence a spherical shape was chosen for the contact interface which not only offers a small surface

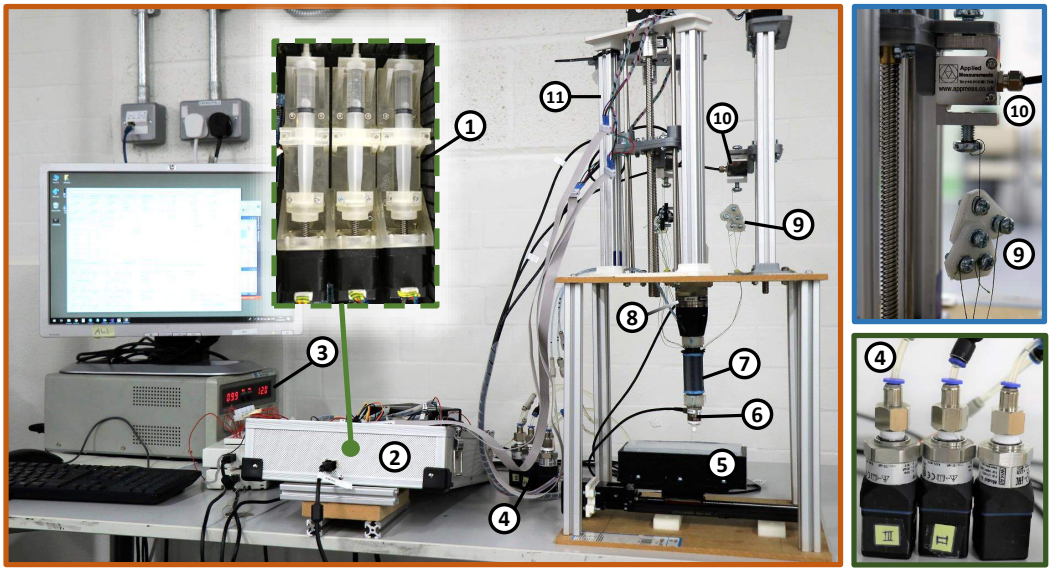

Fig. 5.2 *The complete setup, comprising 1: The hydraulic plungers, 2: Control box, 3: Power supply, 4: Hydraulic pressure transmitters, 5: Phantom encased in container mounted on linear guide, 6: Nano17 force sensor at tip, 7: STIFF-FLOP soft manipulator, 8: Mini40 force sensor at the base, 9: Whipplethree mechanism, 10: Tension sensor, 11: Custom-made linear guide for tendon-stiffening.*

but also would not damage the tissue [175, 186, 187]. For sensing the forces transmitted to via the body an ATI Mini40 F/T sensor is mounted at the base as shown in Figure 5.2 item 8.

The soft appendage comprises two actuation systems:

A. **Intrinsic Actuation:** In this hybrid setup, pneumatics (previously used in Chapter 4) have been replaced by hydraulics, aiming to reduce the working fluid compressing when the tendons are tightened and mitigate buckling effects at higher tensions. Hydraulic actuation is made possible via three independent syringes which act as plungers as shown in Figure 5.2 item 1; each pressurizing one set of dual chambers embedded in the soft manipulator (Figure 5.1 item 1) . Each syringe is driven back and forth using a 17HS5001-100D8 non-captive stepper motor with anti-rotation mechanism for the threaded shaft. The combination of the motor and the threaded shaft provides 8 mm linear displacement per revolution (0.04 mm per full step). The 200 steps per revolution is equivalent to 1.8° angle per full step. The motor is powered with 12 V and 0.4 A, therefore the maximum

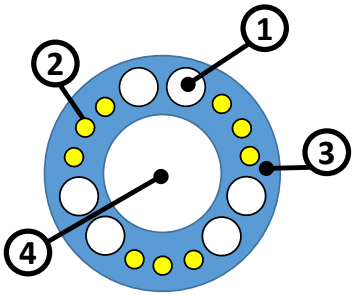

Fig. 5.3 *STIFF FLOP schematic cross section with multiplied tendons. 1: The dual pressure chambers, 2: Three tendons grouped together between pressure chambers, 3: Body of the manipulator, 4: Central lumen.*

speed can be calculated as:

$$MaxSpeed = \frac{Voltage}{2 \times (Induction) I_{max}} = \frac{12}{2 \times 0.045 \times 0.4 \times 200} \approx 1.67 \frac{rev}{s} \tag{5.1}$$

In order to determine the relationship between motor speed and the flow rate we need take into consideration the geometry of the syringe and the thread of the shaft. The diameter of the plunger of the 10 mL Terumo Syringe is 15.8 mm ($\approx 196\,\text{mm}^2$ surface area). The plunger has to move by ≈ 5.1 mm to inject 1mL. According to the motor specifications: 1 mL of Water = 127.5 Steps; The flow rate with 25 ms delay between the steps is ≈ 0.28 mL/s. The stepper motors are driven by StepStick A4988 motor driver controlled by an Arduino Mega micro-controller. The pressure from each pressure channel is monitored on-line via a WIKA A10 pressure transducer with $4-20$ mA output, connected to a NI-DAQmax USB 6211. The entire hydraulic system interconnected by tubes from SMC Hose Clear Polyurethane TUS Series with 4 mm OD and 2.5 mm ID and maximum operating pressure of 0.6 MPa.

B. **Extrinsic Actuation:** The concept of tendon stiffening from chapter 4 is utilized here to enable regulating the impedance at will, via tendons accommodated in the manipulator's wall. For a more uniform force distribution across the entire body, the number of tendons from chapter 4 are multiplied as the current design incorporates nine tendons, activated in groups of three. Each trio is placed between two pressure chambers (Figure 5.3).

To ensure simultaneous engagement and tension of all three tendons in a group, a Whippletree mechanism (Figure 5.2 item 9) is integrated and attached separately to the three grouped tendons. On the other end, The Whippletree is connected to a low range S-beam load cell DBBSMM-2kg-002-000 (Applied Measurements LTD) with 20 N capacity, supply voltage of $2 - 10$ Vdc and an output of 2 mV/V. The load cell is mounted on the moving component of a customized linear guide on the M8 thread. The three linear guides are placed vertically on top of the setup where the tendons are routed vertically (Figure 5.2 item 11), ultimately composing the stiffening mechanism.

5.4 Test Protocol & Experiments

This study focuses on exploiting the active and passive morphological attributes of a finger-like soft appendage for improving haptic perception, in addition to exploring the interplay between tactile and proprioceptive functionalities. Hence we aimed to utilize the soft appendage in various combinations of actuation and different postures, in the same manner that a human probes objects with different morphologies of the finger. The soft continuum appendage was hydraulically actuated to form 7 distinct initial configurations, with the respective hydraulic pressure values tabulated in Table 5.1.

Figure 5.4 demonstrates the 7 pressure configurations for sweeping the Silicone phantom, where the phantom is slided from right to left in each sub-figure. Cases (a), (c), (d), and (f), all start from a straight pose: with no applied pressure in case (a) up to the maximum

Table 5.1 Pressure values for the 7 different initial configurations for palpation (bar)

Config. Name	P1	P2	P3
(a) P000	0	0	0
(b) P300	0.89	0	0
(c) P333	0.97	0.94	0.98
(d) P666	1.18	1.42	1.50
(e) P966	1.84	1.42	1.63
(f) P999	1.77	1.55	1.72
(g) P066	0	1.44	1.63

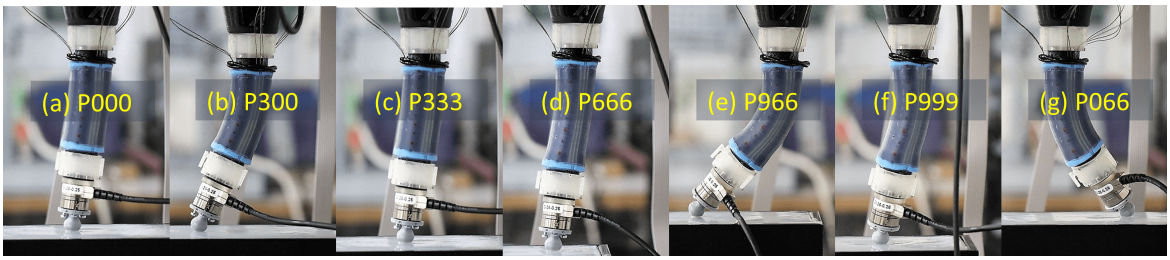

Fig. 5.4 *Seven different pressure configurations of the manipulator which were acquired by hydraulic pressurization, for sweeping the soft Silicone tissue. Pictures were taken while conducting the runs, as the Silicone phantom slides underneath the soft appendage tip. Phantom motion is from right to left in these figures.*

stretch in case (f). The straight poses are obtained by (almost) equal amount of hydraulic pressure applied to all three pressure chambers via equal travel of the plungers, designated by similar digits in the configuration names.

Cases (b) and (e) constitute a curved pose, concaving to the left in Figure 5.4 by applying a relatively higher pressure to chamber 1 than the other two chambers of the soft appendage. Contrarily, case (g) forms a curve opposed to cases (b) and (e) as a result of higher pressures in chambers 2 & 3 than chamber 1. (It is noteworthy that other pressure values forming an opposing curve as case (g) were also examined but without success, as the module tip pointing inwards to the phantom's top surface during the sweep would further deepen the penetration, resulting in a temporary undesirable adhesion of the module tip to the phantom surface and severely distorting the manipulator's pose, which would finally result in a sudden release of the tip and therefore disrupting a smooth sweeping trajectory.)

Each of these 7 cases was in turn subdivided into four schemes regarding tendon stiffening; from no tendon tension at all to the maximum stiffening in three increment, as tabulated in Table 5.2. The combination of 7 pressure levels and 4 tension levels in total yields 28 unique combination of intrinsic pressurization and extrinsic stiffening.

These 28 unique combinations were tested with two indentation depths (initial offset of the appendage tip pushing into phantom's surface) of 1mm and 3mm, separately; forming 56 scenarios of pressurization, stiffening, and indenting. Three trials were recorded for each scenario constituting 168 runs in total. It should be noted that the elevation of the Silicone soft phantom w.r.t the probing tip was manually adjusted after setting the relevant pressure

Table 5.2 Overall tension values for 4 tension levels across the seven different initial configurations for palpation (N)

Config. Name	T0	T1	T2	T3
(a) P000	0	0.26	4.63	6.85
(b) P300	0	1.02	4.47	9.52
(c) P333	0	0.48	5.65	8.46
(d) P666	0	1.42	3.62	6.91
(e) P966	0	2.38	4.33	6.12
(f) P999	0	2.64	8.38	11.74
(g) P066	0	1.19	5.05	8.46

and tension for each trial, to ensure the probing tip starts each sweep at the designated initial indentation regardless of the changes in the tip's initial position due to different pressures and/or tensions.

For generating relative motion between the phantom and the soft continuum appendage, the Silicone phantom was mounted on a linear guide rail and moved with constant velocity of 7 mm/s underneath the contact nob of the tip force sensor while brushing against it. Direction of motion and relative positioning of the phantom and the manipulator are shown in Figure 5.1. Force data from both the base and the tip force sensors were recorded online. As the manipulator sweeps the phantom, several factors influence the sensor readings. Apart from the internal pressure and the tendon tension, the overall shape of the soft appendage whether structurally opposing to the motion or curving in a compliant deformation along direction of motion plays a significant role.

The Silicone phantom was wrapped with cling film and mildly lubricated to reduce friction effects and produce smoother transition [188]. To avoid the complications of fast dynamics, this study looks into slow movements of probing [44] which is prevalent with humans. During the run, the tip and base sensors concurrently recorded the force data resulting from the interaction between the manipulator and the soft tissue. Four sensing modalities were taken into account, one at the tip and three at the base:

I. The total applied force at the tip, calculated as $F_{tot} = \sqrt{F_x^2 + F_y^2 + F_z^2}$, reminiscent of the tactile perception at the tip.

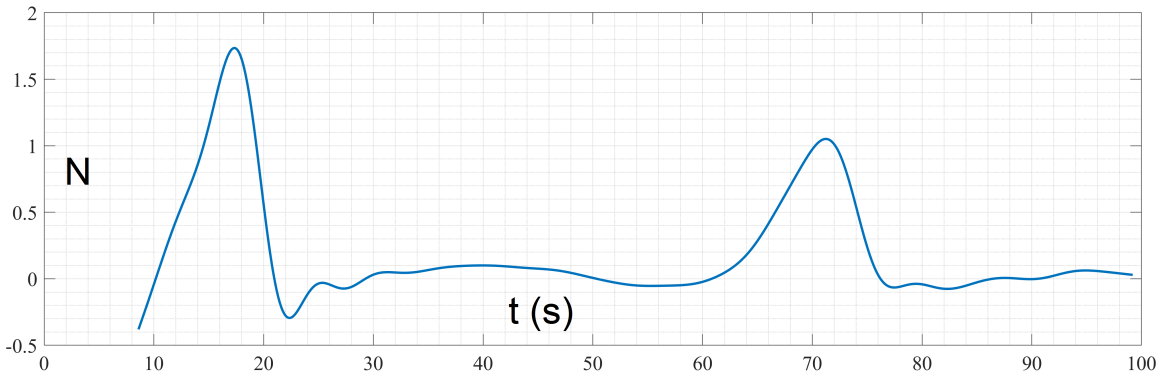

Fig. 5.5 *Example of a signal recorded by the base Mini40 sensor (F_z in this case). The first peak from the left indicates the contact with the phantom container. The second peak denotes the embedded nodule. Readings are from pressure level 1, tension level 4, indentation 2.*

II. Perpendicular force at the base, F_z, which would be the vertical component of the force directly sensing the perpendicular reaction to the uplift motion induced in the manipulator.

III. The base shear force, calculated as $F_{sh} = \sqrt{F_x^2 + F_y^2}$, as tangential forces are claimed to bear significance [27];

IV. The torque experienced at the base as $M_{xy} = \sqrt{M_x^2 + M_y^2}$ as a component frequently measured for robotic effort, whether during haptic exploration or in other manipulation tasks [45, 44].

An example of recorded sensory data during a run is depicted in Figure 5.5 . The initial peak shows the point where the tip of the soft appendage first comes into contact with the edge of the phantom and proceeds till the nodule is sensed where this stimulus is reflected in the second peak.

5.5 Discussion

The soft medium of the manipulator affects the reading of the sensors between the point of applying the external loading and the base sensor. It is noted that although pressurizing the manipulator would increase the internal liquid pressure and hence contribute to the stiffness,

yet the resulting elongation causes a more slender geometry and therefore exhibiting higher deflection when subjected to external loading.

5.5.1 Peak Values of Sensing Modalities

Referring to Figure 5.5, it is clearly observed that apart from the initial contact of the manipulator's tip with the container of the Silicone phantom (resulting in the peak on the left side of the figure), another peak in the readings occur which correspond to the location of the embedded nodule. Such a pattern was seen in all of the readings from different sensing modalities, yet with a variation in the amplitude of the occurring peak. Hence the graphs obtained from other sensing modalities are left out for brevity, and instead we focus on analysing the different features of these modalities w.r.t the buried nodule which has created the embedded stiffness anomaly in the phantom.

Figures 5.6, 5.7, 5.8, 5.9 show how the peak values of the sensing modalities change across different pressures and tension levels and indentations. In general, an increasing trend is seen in the peak value as the tension level increases. This rise, however varies in different pressure scenarios and in different sensing modalities. In all recorded signals, we witness that pressure scenario "g" (Figure 5.4) produces higher readings in the first indentation compared to the second indentation. This can be interpreted as a better sensation of an anomaly - both at the tactile level and the proprioceptive level - if the soft sensing appendage is pressed less against the surface of the soft tissue, when it is curved "against" the direction of sweeping. Also, visiting the graphs of the base torque values reveals that antagonistic stiffening of the soft continuum appendage does not significantly alter this sensation, as the height of the bars representing the peak values do not display a significant variation.

To hand in a comparative visualization of the peak values in each sensing modality for the 7 pressure scenarios, the 3D map in Figures 5.10, 5.11, 5.12, 5.13 were generated to demonstrate which postures mark higher force sensing values and how does regulating the tension affect the peak readings of the four sensing modalities separately. As seen, pressure scenarios 3 and 4 ("c" and "d" in Figure 5.4) exhibit the highest values for the peak, except for the base torque readings where pressure scenario 7 ("g" in Figure 5.4) is

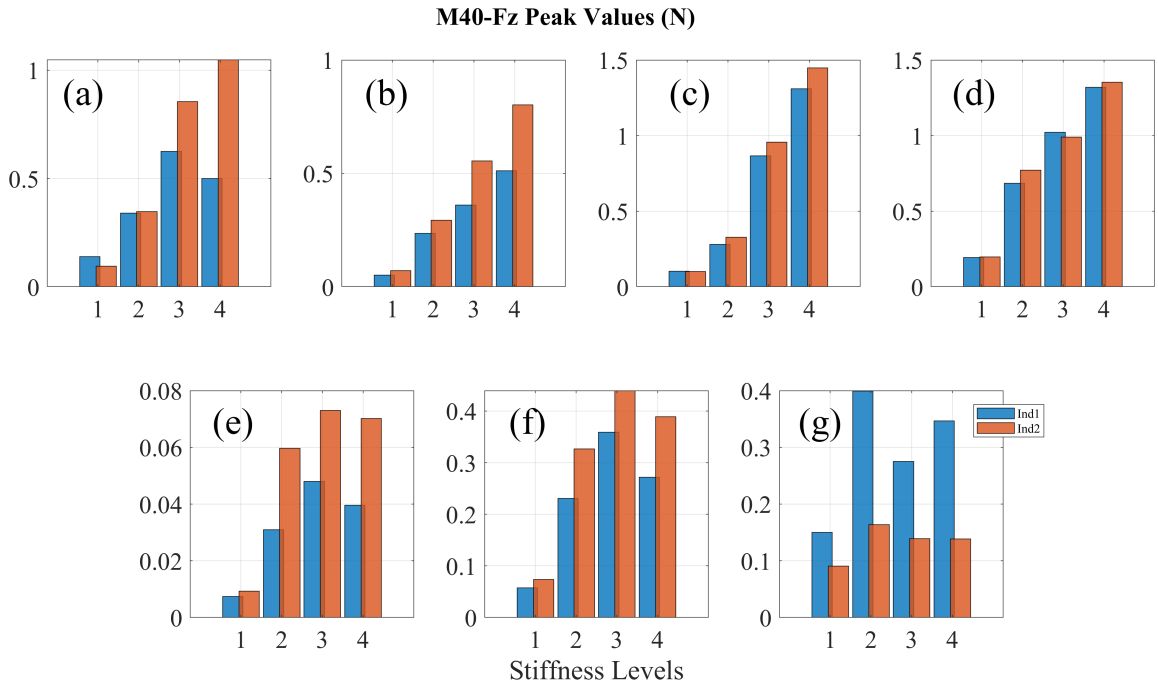

Fig. 5.6 *Peak Values of Mini40 F_z in different pressure schemes across four tension levels. Blue and red bars represent 1^{st} and 2^{nd} indentation, respectively.*

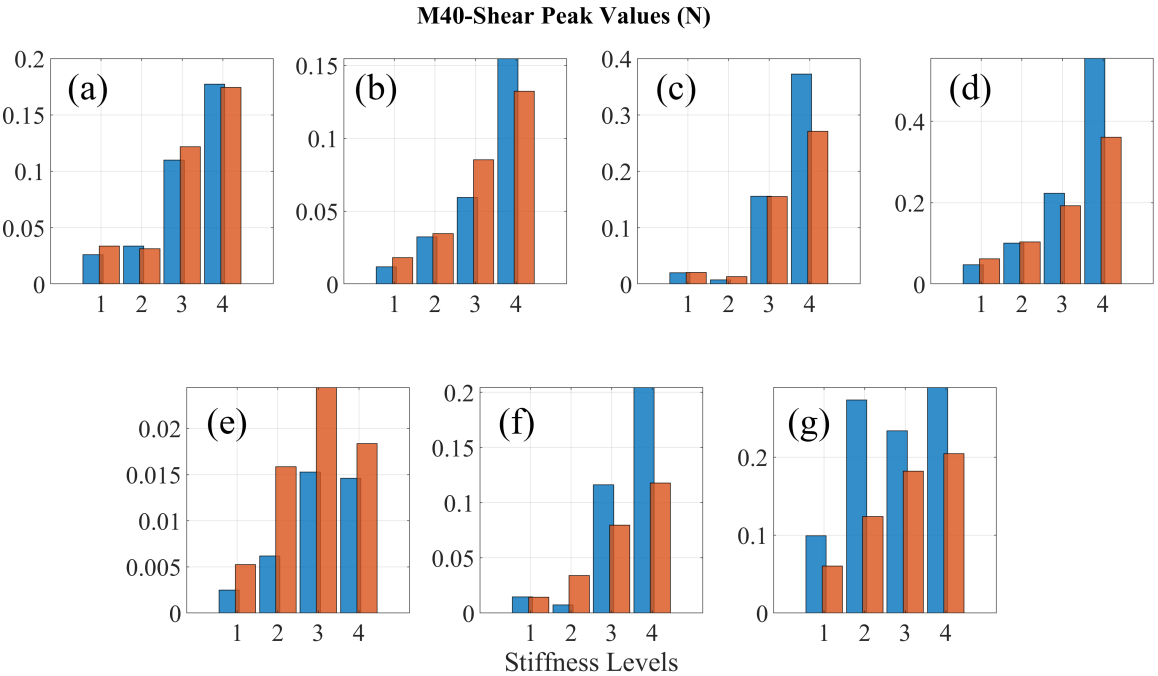

Fig. 5.7 *Peak Values of Mini40 F_{shear} in different pressure schemes across four tension levels. Blue and red bars represent 1^{st} and 2^{nd} indentation, respectively.*

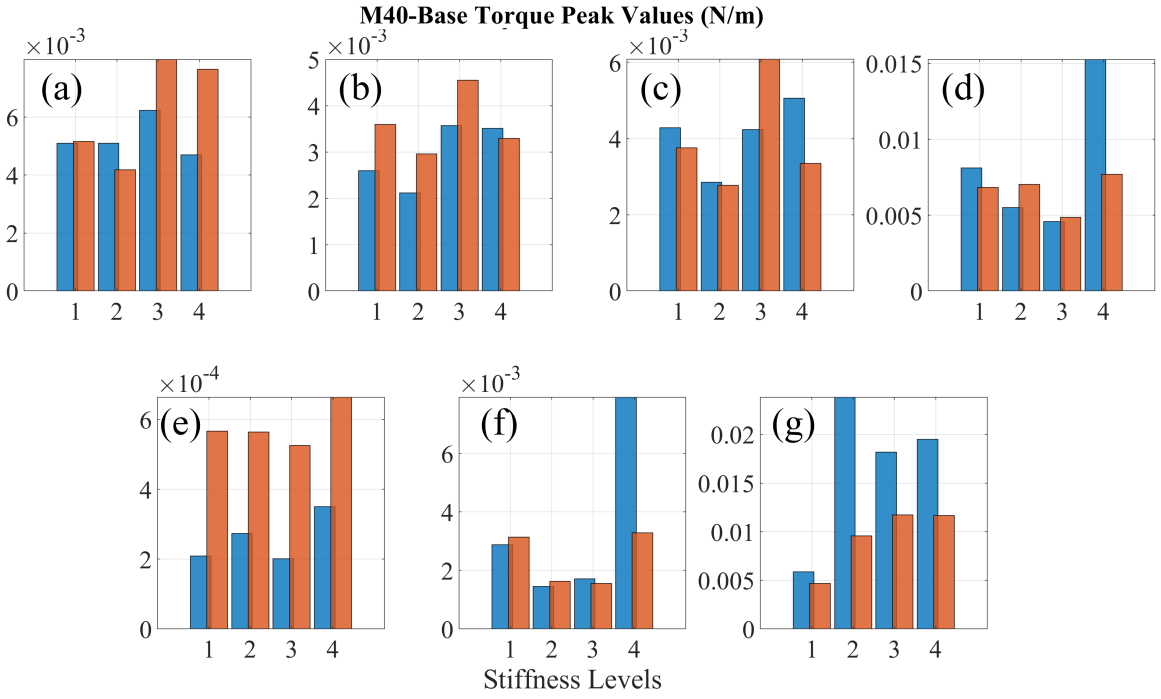

Fig. 5.8 *Peak Values of Mini40 torque in different pressure schemes across four tension levels. Blue and red bars represent* 1^{st} *and* 2^{nd} *indentation, respectively.*

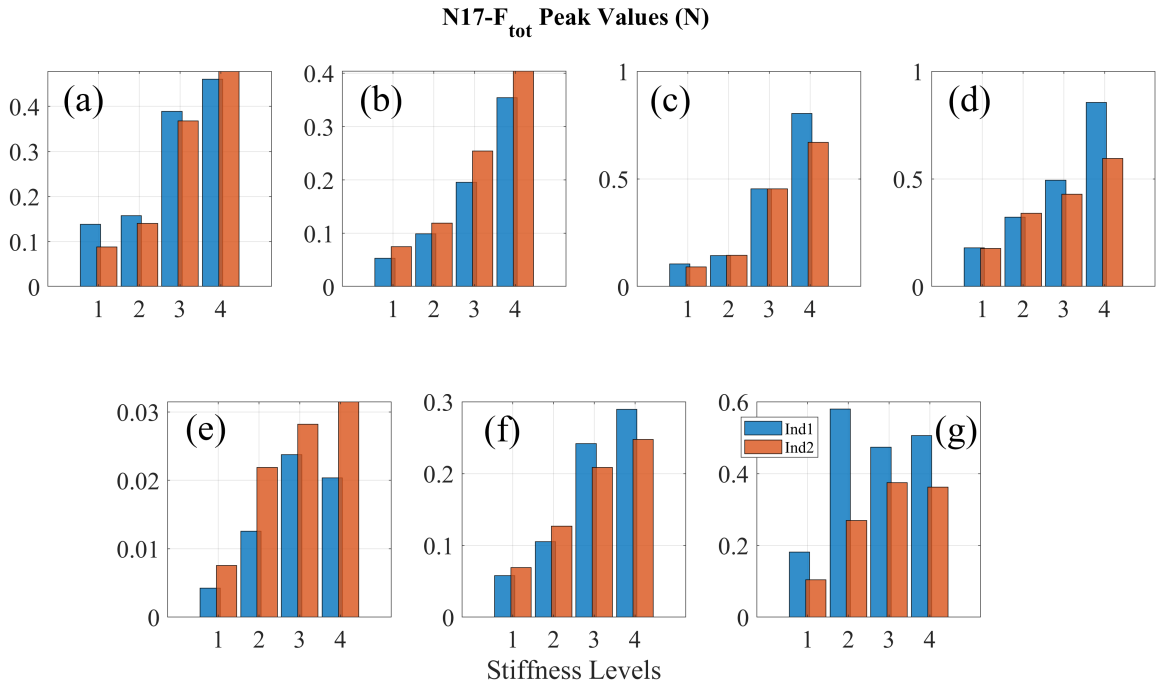

Fig. 5.9 *Peak Values of Nano17* F_{tot} *in different pressure schemes across four tension levels. Blue and red bars represent* 1^{st} *and* 2^{nd} *indentation, respectively.*

comparatively dominant; were the initial curvature of the soft module opposes the direction of the sweeping motion (like scraping a surface) contrary to other scenarios where the initial pose of the module is either vertically downwards, or with a curvature compliant with the motion (more towards gently stroking a surface). Cases 3 and 4 are postures were the pressure chambers have been equally pressurized to generate a uniform vertical elongation across the manipulator's body.

The case with notably lower peak values compared to other scenarios - across all sensing modalities - is scenario 5 ("e" in Figure 5.4). In this morphology, the soft appendage is in a curved posture facing the sweeping direction (same posture as "b" in Figure 5.4) yet pressurized higher thus experiencing a further extension compared to the similar scenario 2. This phenomenon indicates that despite the increased internal pressure, the added elongation has a detrimental effect on delivering readings with higher magnitudes in this posture, as the variation in tip force (tactile) is less transferred to the base (proprioception) due to a longer soft elastic medium between the two terminal points. This hypothesis is backed up by the behaviour demonstrated in scenario 6 ("f" in Figure 5.4). Although results from cases 3 and 4 – were the soft manipulator has been uniformly elongated to straight vertical postures - suggest a better performance in elevating the force readings, however case 6 implies a pressure/elongation limit to such a benign conduct. Here, though this posture delivers better than case 5, yet again it appears that the excessive extension has worked against higher readings.

The percentage of increase in the peak values of the sensor readings are depicted in Figure 5.14, 5.15. In general a rising trend is witnessed in modalities, with the base torque to express the least increase.

The obtained results demonstrate the possibility of increasing the force readings by regulating internal impedance to up to 14 times with the vertical forced sensed at the base in scenario 3 ("c" in Figure 5.4). The modalities experiencing the most drastic increase are the base vertical and shear forces. As witnessed before, scenario 7 ("g" in Figure 5.4) serves the base torque the most which can be seen in subfigure 7 for both indentations.

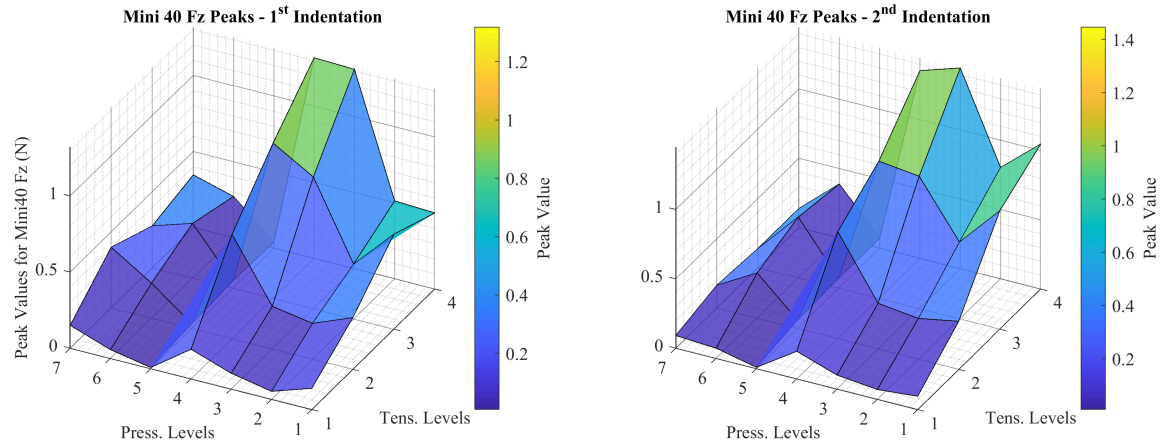

Fig. 5.10 *3D representation of peak values of Mini40 F_z in different pressure schemes across four tension levels.*

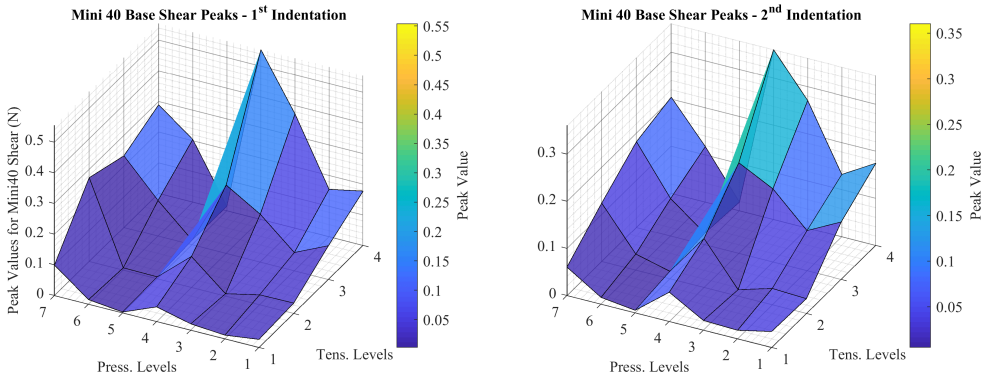

Fig. 5.11 *3D representation of peak values of Mini40 shear force in different pressure schemes across four tension levels.*

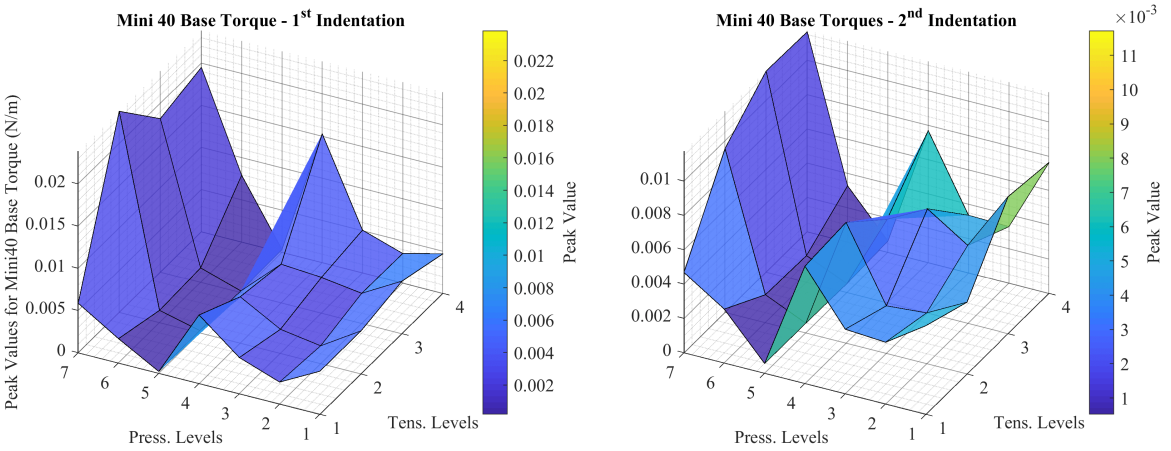

Fig. 5.12 *3D representation of peak values of Mini40 torque in different pressure schemes across four tension levels.*

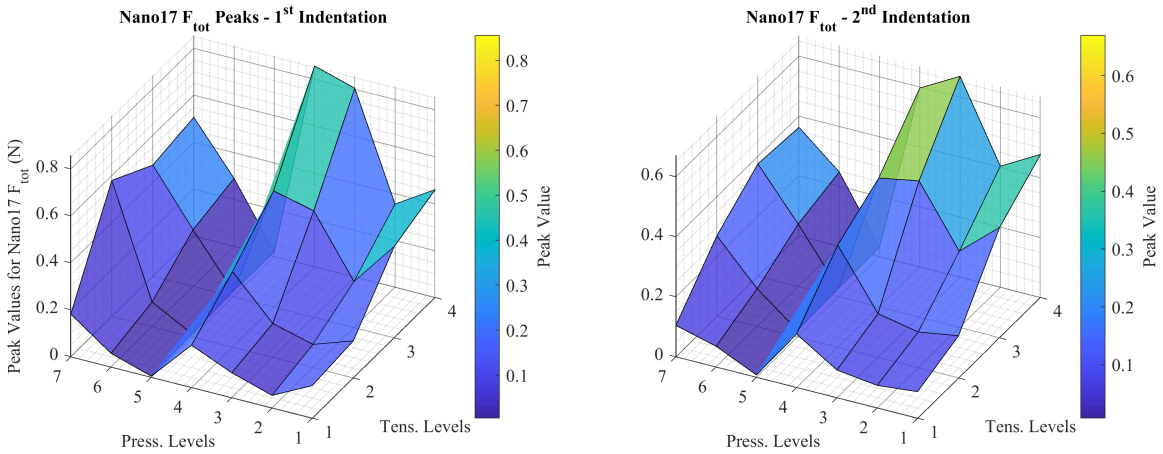

Fig. 5.13 *3D representation of peak values of Nano17 F_{tot} in different pressure schemes across four tension levels.*

The normalized peak values are calculated as dividing the peak value by the maximum value as:

$$peak_{normalized} = \frac{peak}{max(peak)} \tag{5.2}$$

The results are plotted in Figure 5.16, 5.17. These obtained graphs reveal the base torque to experience the least amount of increase compared to the other modalities.

A. RMS and Euclidean Distance Across Pressure Levels in Each of the Sensing Modalities

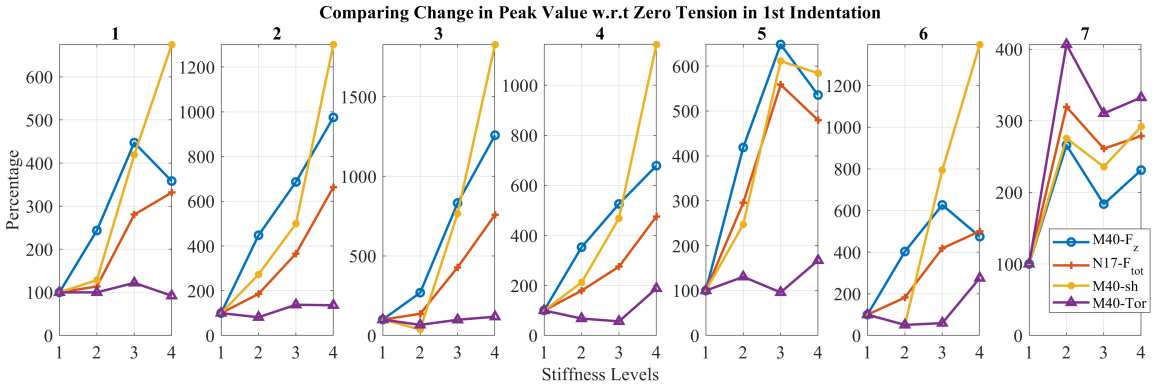

Fig. 5.14 *Percentage of increase peak values of all sensing modalities in different pressure schemes compared to no tension, across four tension levels; 1^{st} Indentation.*

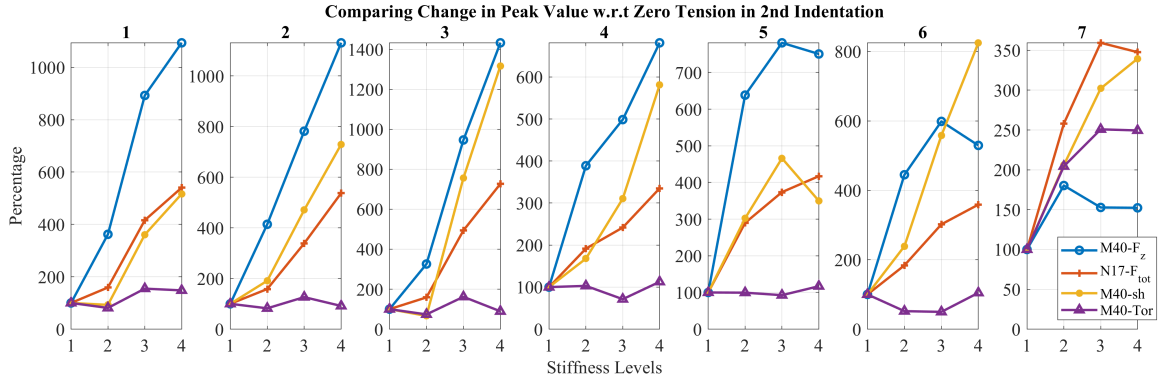

Fig. 5.15 *Percentage of increase peak values of all sensing modalities in different pressure schemes compared to no tension, across four tension levels;* 2^{nd} *Indentation.*

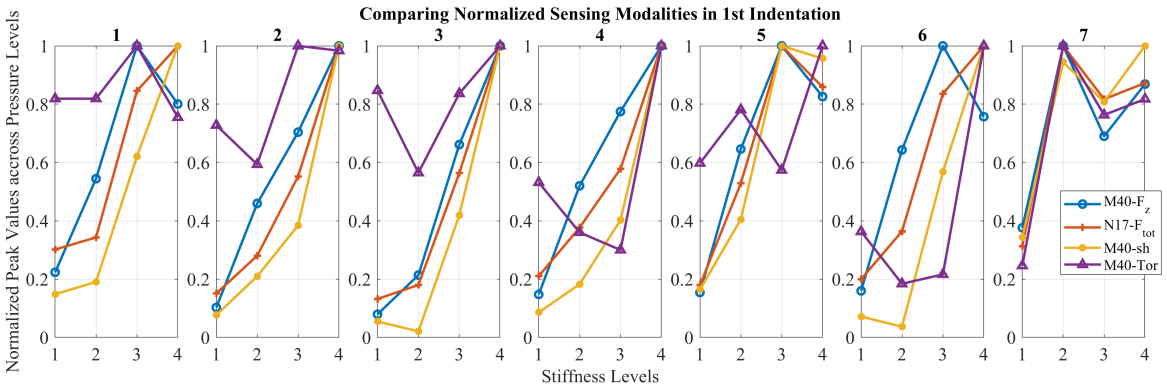

Fig. 5.16 *Normalized peak values of all sensing modalities in different pressure schemes across four tension levels;* 1^{st} *Indentation.*

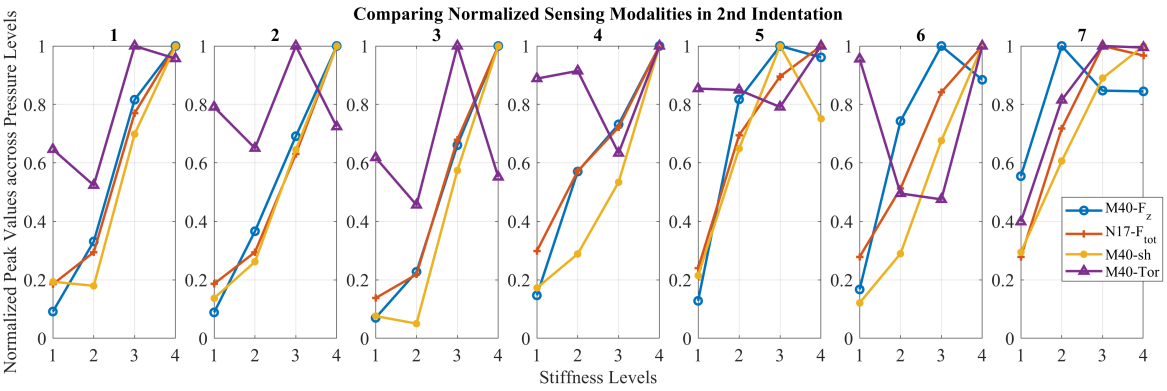

Fig. 5.17 *Normalized peak values of all sensing modalities in different pressure schemes across four tension levels;* 2^{nd} *Indentation.*

The RMS of for each peak signal is calculated as:

$$RMS = \sqrt{\frac{1}{n}\sum x_n^2} \tag{5.3}$$

Where n is the index of the sample and x is the recorded value. In order to quantify the distance between the RMS values of different tension levels, we calculate the Euclidean distance for each sensing modality between any tension level compared to the no-induced tension (denoted as "base tension") separately, as:

$$ED = \sqrt{\sum (RMS_i - RMS_{base})^2} \quad ; \quad i = 1, 2, 3, 4 \tag{5.4}$$

Where i denotes the tension level, and $i = 1$ is the no-induced tension (base tension). The results are plotted in Figure 5.18.

The Euclidean distance between the four tension levels indicates the gain in achieving higher force readings by regulating the internal impedance via the embedded tendons. In general, the sensing modalities display a rising trend as the stiffness increases. Subgraph (c) shows that the base torque readings experience the best gain when the manipulator is pressurized to attain the posture "g" in Figure 5.4, contrary to other modalities. It is also visible that pressure scenario 5 ("e" in Figure 5.4) offers the least change in gaining higher sensing values by increasing the stiffness, across all of the modalities.

B. RMS and Euclidean Distance Between Sensing Modalities

The Euclidean distance of RMS values between sensing modalities is depicted in Figure 5.19. In each case, the left and right subfigure refer to the first and second indentation, receptively. In this cross-analysis, a difference in indentation does not show any inclination towards either of the sensing modalities paired in the graphs.

The distributions in subfigure (a) of Figure 5.19 show a stronger inclination towards the vertical force experienced at the base compared to the shear force at the base. The same tendency toward the base vertical force is witnessed when plotted against the total force recorded by the tip Nano17. However, the RMS distribution between shear force at the base and the tip total force appear to be scattered with an equal distance. It should be noted

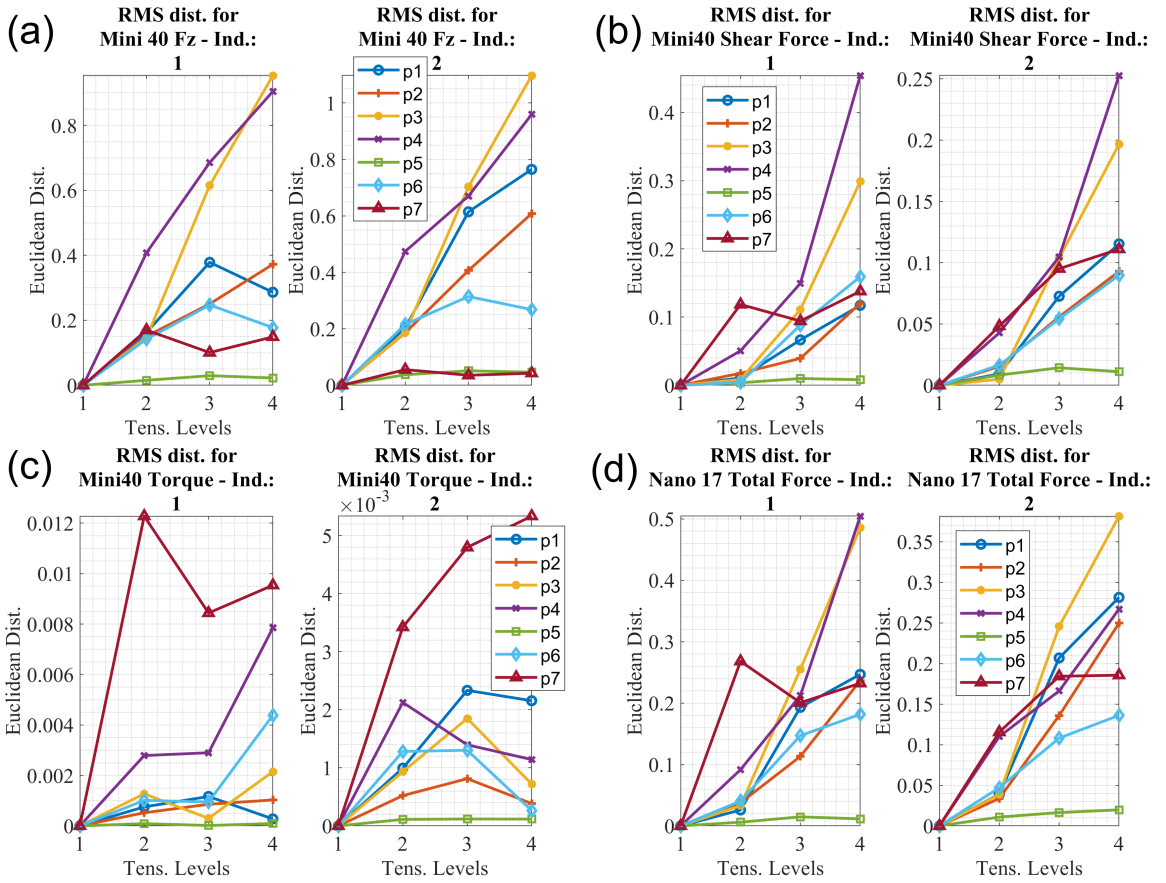

Fig. 5.18 *Euclidean distance of RMS of peak values in all four sensing modalities, in different pressure schemes across four tension levels, and for both indentations.*

that the units and magnitude of the sensing modalities are inherent in these results. If the RMS values are normalized according to:

$$RMS_{normalized} = \frac{RMS}{max(RMS)}, \tag{5.5}$$

the graphs depicted in Figure 5.20 are obtained.

Results demonstrate that on a unified scale, the investigated sensing modalities are in unison with respect to gaining more information due to increasing the internal impedance, apart from the torque values recorded at the base.

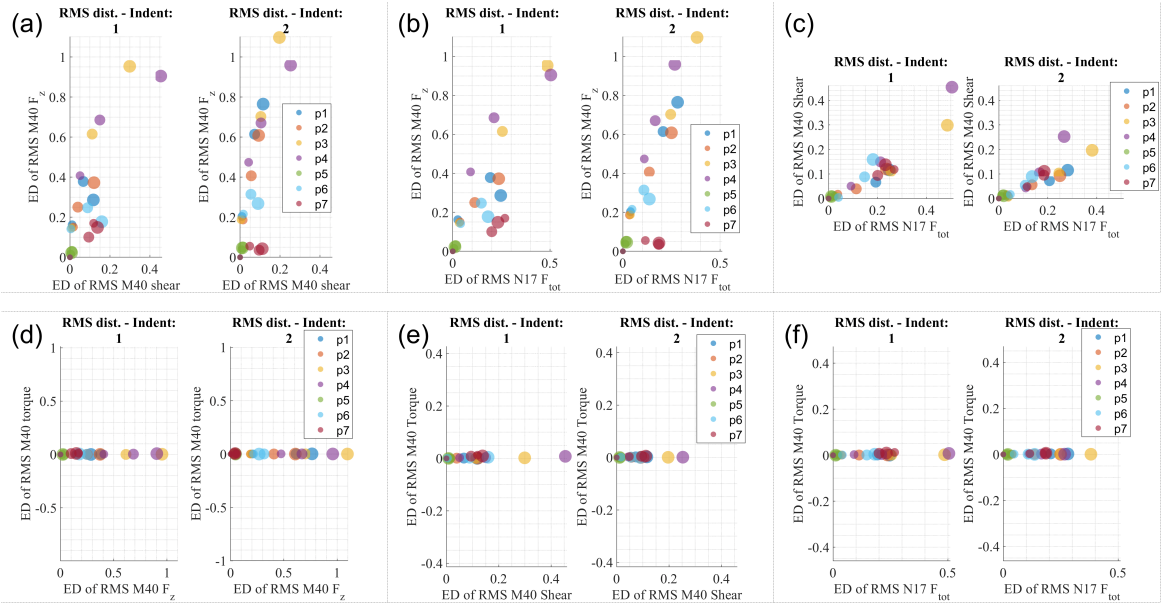

Fig. 5.19 *Euclidean Distance of RMS of peak values between four sensing modalities in different pressure schemes across four tension levels for both indentations.*

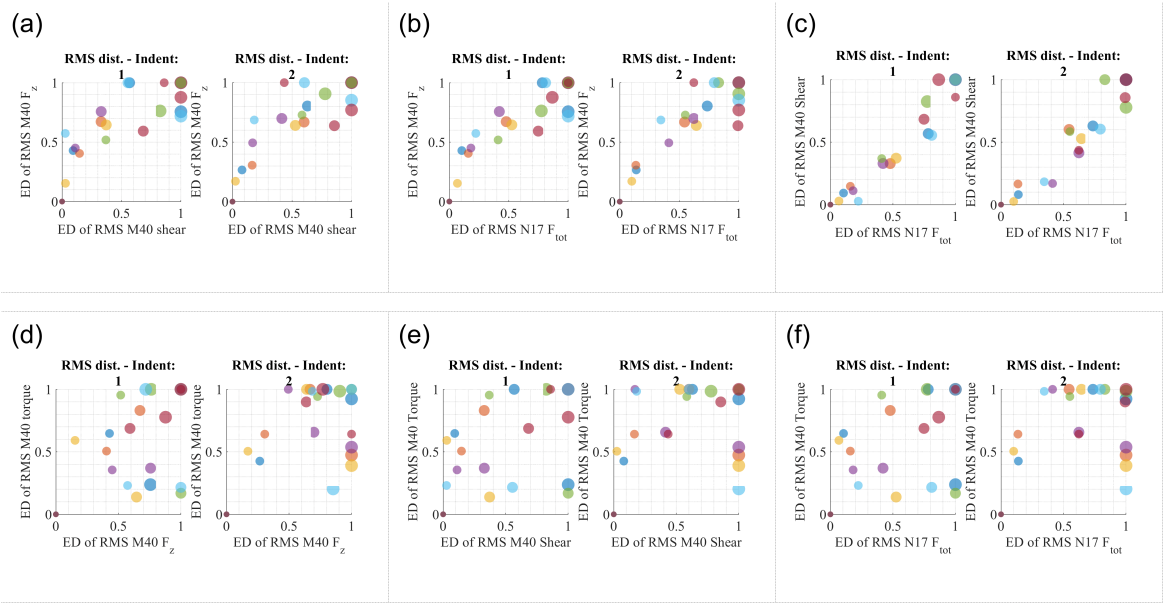

Fig. 5.20 *Euclidean Distance of RMS of peak values, normalized, between the four sensing modalities in different pressure schemes across four tension levels for both indentations.*

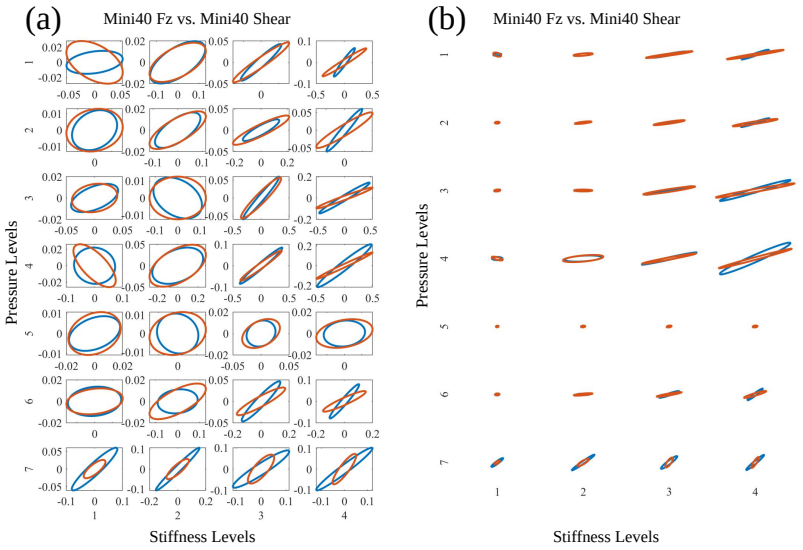

Fig. 5.21 *The covariance ellipse between peak Mini40 Fz and Mini40 Shear. Fig.b depicts equally scaled axes where all y axes are from [-0.3,0.3] and x axes are between [-0.7,0.7]. Blue and red represent 1st and 2nd indentation, respectively.*

5.5.2 Covariance Analysis

We investigate the covariance between each pair of the sensing modalities. Results are shown in Figures 5.21, 5.22, 5.23, 5.24, 5.25, 5.26. In each case, subfigure (a) demonstrates the scaled plots for a better display of the units. Subfigure (b) depicts the same plots but with axes which are equally scaled, with the range mentioned in the caption of each figure. The shape of the ellipsoids represents the eigenvalues of the principal components of each covariance matrix. As seen, the direction of the principal component to a great extent does not change as the manipulator is stiffened in different trials. The angle of the major axis of the ellipse - which corresponding the larger eigenvalue - signifies the relative contribution by each of the paired modalities.

Examining the graphs show that the in general, the distributions along the larger eigenvalue increase with increasing the internal impedance.

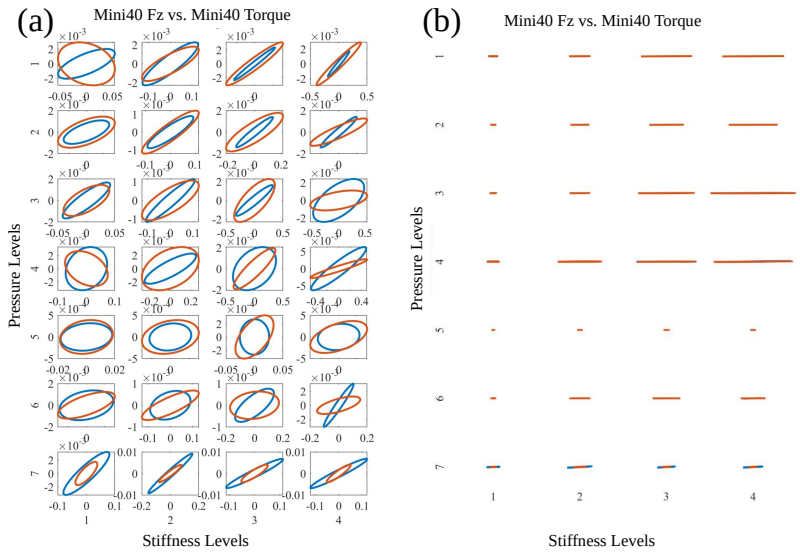

Fig. 5.22 *The covariance ellipse between peak Mini40 Fz and Mini40 torque. Fig.b depicts equally scaled axes where all y axes are from [-0.2,0.2] and x axes are between [-0.8,0.8]. Blue and red represent 1st and 2nd indentation, respectively.*

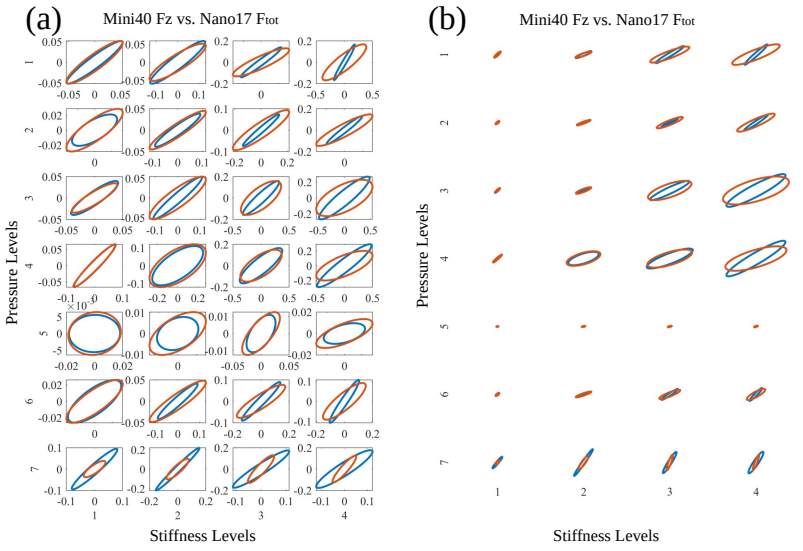

Fig. 5.23 *The covariance ellipse between peak Mini40 Fz and Nano17 Ftot. Fig.b depicts equally scaled axes where all y axes are from [-0.6,0.6] and x axes are between [-0.7,0.7]. Blue and red represent 1st and 2nd indentation, respectively.*

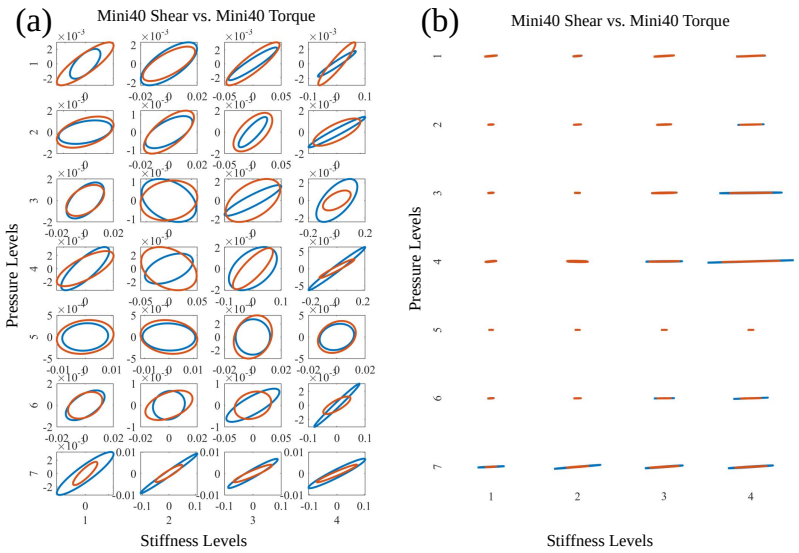

Fig. 5.24 *The covariance ellipse between peak Mini40 shear and Mini40 Torque. Fig.b depicts equally scaled axes where all y axes are from [-0.02,0.02] and x axes are between [-0.5,0.5]. Blue and red represent 1st and 2nd indentation, respectively.*

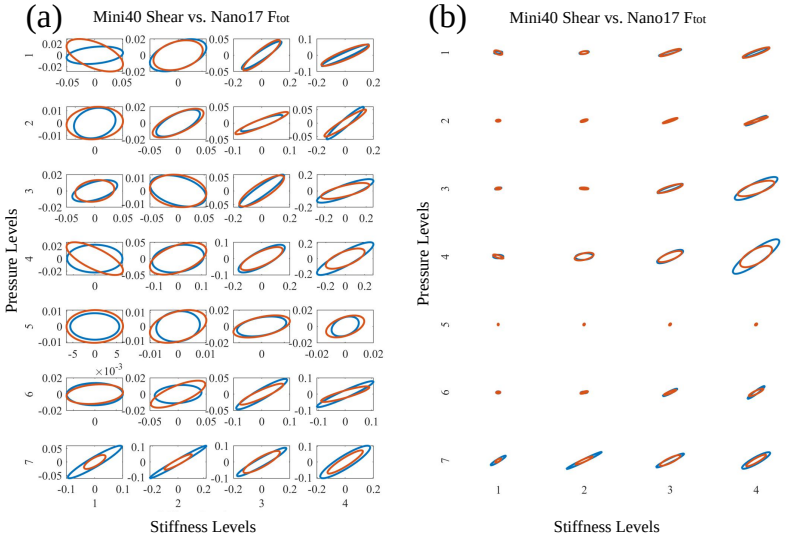

Fig. 5.25 *The covariance ellipse between peak Mini40 shear and Nano17 Ftot. Fig.b depicts equally scaled axes where all y axes are from [-0.25,0.25] and x axes are between [-0.55,0.55]. Blue and red represent 1st and 2nd indentation, respectively.*

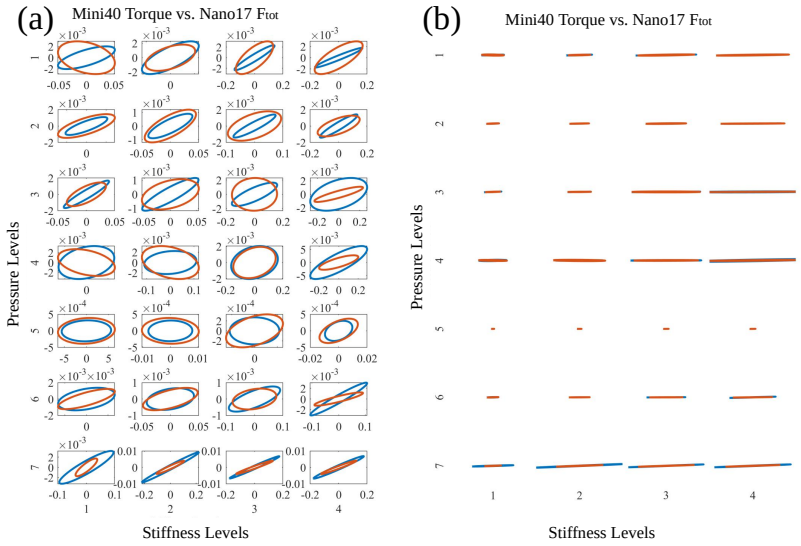

Fig. 5.26 *The covariance ellipse between peak Mini40 torque and Nano17 Ftot. Fig.b depicts equally scaled axes where all y axes are from [-0.02,0.02] and x axes are between [-0.5,0.5]. Blue and red represent 1st and 2nd indentation, respectively.*

5.6 Conclusions

The current study proposed a novel approach in robotic palpation for soft tissues by employing a soft continuum appendage capable of impedance variation. By incorporating two force sensors at either end of the soft appendage, we recorded online sensing data in a similar way that occurs in biological haptic sensing organs by exploiting both tactile and proprioceptive information to explore the environment. Utilising the soft continuum appendage demonstrated the ability to exploit the embodiment in generating sensory information at the base, similar to proprioception in biological organs; hence enabling the removal of tip sensors in such robotic platforms.

Moreover, obtained results suggest that the vertically aligned position of the manipulator yields more magnified values of contact force in detecting an embedded anomaly in a soft tissue, though to an extent were the magnitude of sensed data is not compromised by the extended elastic structure. We also witnessed a relatively low change in the amplitude of the torque felt at the base compared to the other modalities when the stiffness increased, in addition to the point that the “scraping” posture favours the base torque sensing more.

It was also seen that internal stiffening via tendons in general boosted the sensory readings, increasing the proprioceptive vertical force sensed at the base to about 14 times the case without stiffening. Cross-analysis of sensing modalities revealed a more drastic effect of stiffening on the vertical force read at the base in comparison with other investigated modalities. On the other hand, increasing the tip indentation of the soft appendage had no apparent effect on any sensing modality to have more prevalence in amplification compared to the others.

The soft structure actuated by fluidic chambers and tendons deliver the ability to conform to geometrical irregularities within the workspace restrictions, with the following benefits:

1) This morphology allows acquiring haptic data from regions which are hard or even impossible to access using rigid link robots; hence extending the reachable workspace for robotic probing compared to rigid-link system of the same scale;

2) This morphology enables more freedom in posture, hence making it possible to optimize the morphology of the robot to regulate embodied haptic perception in various poses.

The embodiment of the soft continuum appendage enables adaptive behaviour by physical reactions of the body [39] which not only enhances safety concerns but also is capable of removing the need for additional sensory hardware. This "intelligent" behaviour reduces computational effort from the sensorimotor control which encourages service in more complex tasks. Studying multiple sensing modalities offered a unique opportunity in this class of robots as opposed to studies as [44, 45] which only took base torque into consideration. Investigation in cross-modality sensing is indeed beneficial for both natural and artificial contact appendages, as humans modulate both lateral and normal forces during palpation [100, 219]. There still is not a consensus on which elements are the most relevant in haptic sensing [229], with the fallout of undermining the role of tangential forces which in reality contribute significantly in manipulation and sensing deformable and complex objects [27].

The antagonistic nature of the variable impedance resembles muscular activity in a wide range of animals and humans. Various combinations in posture and stiffness helped replicating different morphologies similar to the human finger, therefore coming closer to the notion of the subjective behaviour witnessed when humans explore the properties of an

object [175]. This setting could potentially serve in a learning scheme to generate a data repository for robotic perceptions in other studies. Future work could include taking into account the variation of other parameters such as anomaly depth, geometry, and stiffens, in addition to the physical and geometrical properties of the hosting tissue such as surface friction and stiffness, or considering different invoking parameters such as probing velocity and/or resulting transient dynamical effects.

The findings from this research confirm the role of internal impedance in increasing the sensing gain as claimed in other studies [44], and show that soft robotic palpation can benefit from increased stiffness. However, the paradigm of haptic sensation and the role of morphological control to enhance this perception continues to present many unknown details, which have hindered a comprehensive manifestation of this trait in robotic systems.

Chapter 6

A Fuzzy-based Approach to Online Stiffness Regulation for Safe Human-Robot Interaction

Abstract— *The final chapter of this thesis looks into bringing about "soft robotics" in rigid-link manipulators. The growing presence of robots in industry has intensified the investigation of safe physical human-robot interaction (pHRI) entailing rigid-link robots, giving birth to the notion of collaborative soft robotics. To this end, the methods developed as part of these studies can be categorized into three main branches: active methods (e.g., active impedance control), passive methods (e.g., integrating compliant components in the actuators or in the structure), and a combination of both methods. In this chapter, a novel active approach is presented to address this topic. A fuzzy inference mechanism is employed to generate a decision for regulating the overall stiffness of the robotic arm in the task-space direction(s) along the trajectory that is assumed to lead to a collision between the human and the robot, instead of an overall and equal effect on the stiffness in all Cartesian direction(s). This chapter describes the underlying mathematical theory as well as simulations performed in the Robotic Operating System (ROS) along with experiments conducted using a Baxter robot, showing promising results and great potential for a wide range of applications.*

6.1 Introduction

Qualities such as high degree of precision, repeatability, speed, and ability to conduct repetitive tasks without fatigue, have been the key drivers for robots to be integrated into industrial settings [230]. Traditionally, segregation of the human's and robot's workspaces has been the preferred integration concept, by using physical fences or prohibited zones for human extrance to achieve the required safety [19, 230]. However, a wide range of applications that are at present executed manually could benefit from close collaboration between the robot and the worker [230, 67]. In this regard, however, contact with the robot arm within an unstructured task or with human workers poses a major challenge [57], as standard approaches in industrial robotics are not feasible to be applied for workspace sharing due to safety being compromised [67]. Consequently, the field of industrial robotics is experiencing a paradigm shift from the traditional heavy-duty robot operating in a fenced area separated from the human worker, to robots that work closely with the human, adapt to the movements of the human, and physically interact with them [33, 67]. Hence, an interaction control method is required to ensure that the collaborative forces do not exceed a point of damaging to robot or injuring the operator [231]. Along these lines, multiple approaches have been adopted to realize the concept of Soft Robotics in industrial settings.

One of key parameters in this regard is the manipulator's stiffness, where researchers have offered several of approaches to tackle. These methods could broadly be subdivided into

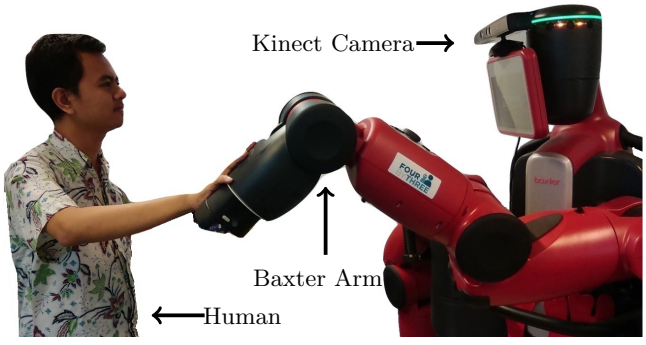

Fig. 6.1 *Human in close proximity of the robot: Experiments utilized the left arm of a Baxter robot and a Kinect camera for tracking.*

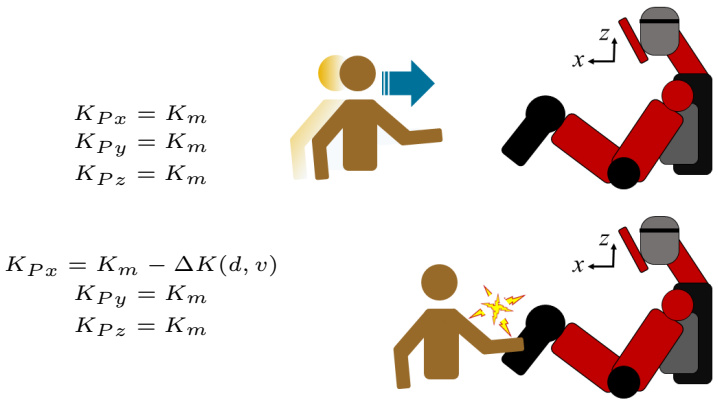

Fig. 6.2 *Example of directional stiffness adjustment: If possible collision between human (left) and robot (right) is detected along the x axis, stiffness is only reduced in that direction by the amount of $\Delta K(d, v)$, and not affecting stiffness along the y and z directions.*

two categories [57]: I) Integration of force/torques sensors in rigid-link robots and applying control at joint level to produce "soft" behavior; i.e. mimicking variable impedance via the controller [11]; and, II) Accommodating active and/or passive compliance in actuators, such as integrating stiffness controllable actuators into lightweight robots to adjust stiffness parameters depending on the required level of accuracy and detection of potential collisions with a human worker. One approach to realize this led to the development of a new class of actuators known as Variable Impedance Actuators (VIA). Inspired by the muscular movement in animals and humans, VIA's control the robot arm by using two motors to control both the equilibrium point of the arm, and its rigidity or compliance. The trend moves towards lightweight robots - examples include the Universal Robots UR5/UR10®, the lightweight robots from KUKA®, FerRobotics®, Franka®, and the dual arm Baxter robot and single arm Sawyer robot from Rethink Robotics®. Sophisticated software tools available for some of these robots are able to monitor the environment. Depending on sensory input, parameters are then adjusted within the robot's setup to best guarantee the worker's safety [34].

There are a variety of laboratory prototypes of different implementations of variable impedance actuators, which have been categorized in [10]. [232] allows rapid stiffness regulation capabilities, AwAS-I and AwAS-II [233] utilize an additional motor to vary the stiffness. A quasi-antagonistic configuration is employed in the DLR QA-Joint [234] where the actuation and stiffness motors enable decoupling those two variables. Within the EU H2020

project FourbyThree, researchers have developed an industrial robot with a new generation of rotary elastic actuators for customized assembly of modular robot arms with different dimensions and degrees of freedom (FourByThree website, http://fourbythree.eu (retrieved on 13.03.2019)).

To avoid or mitigate collisions between robot and human or regulate stiffness during a collaborative task, a variety of sensors can be used to monitor the environment to assist the robot for appropriate reaction, based on their understanding of the level of risk. Stiffness regulation based on available sensory information has been encountered in the literature with Salisbury [235] first introducing the concept in 1980. In [236, 71], a variable stiffness joint model for nonlinear control design was proposed. The advantages of time-varying stiffness control has been the focus in [237, 238]. The research resulted in a static-optimized controller that optimizes the error of the position and force trajectory error metric. An optimal control strategy to allow time-varying torque and stiffness profiles is proposed in [239]. The methodology is able to adjust stiffness leading to a better performance in highly dynamic, explosive tasks utilizing a model-based optimal control. Analytical predictions to optimal control considering velocity maximization has been investigated in [240, 32]. The authors of [11] provide a review on variable impedance actuators as an approach which has received increasing attention recently.

An intuitive approach to achieve safe human-robot collaboration is taking inspiration from natural human-human collaboration. Humans monitor more than one factor in the environment and react accordingly based on their qualitative understanding of the level of risk. We aim to implement an active impedance control algorithm capable of reflecting this qualitative, multi-parameter decision-making behavior similar to humans. Hence, we propose a novel fuzzy-based approach to real-time stiffness regulation in rigid-link robotic manipulators for safe human-robot interaction which could be employed in industrial settings. Dynamic parameters including distance and relative speed between the human and the robot are considered as the inputs to a fuzzy inference mechanism to generate a decision for adjusting the stiffness of the robotic arm in the relevant task space direction(s), in such a way that: A) the stiffness in the irrelevant direction(s) is not affected; and B) change of

stiffness in the relevant task space directions are not equal, but rather proportional to the level of risk along each direction, determined by the algorithm. To the best of our knowledge, this is the first work employing a fuzzy algorithm in adjusting the directional stiffness of the robot to enhance safety in human-robot interaction.

Section 6.2 entails the mathematical description, consisting of the concept of stiffness adjustment and the fuzzy inference mechanism. In section 6.3, the simulations and the experiments are presented. Results are discussed in section 6.4, and finally, conclusions and possible future works are mentioned in section 6.5.

6.2 Mathematical Description

6.2.1 Stiffness Adjustment Concept

For the basic task of controlling the end effector of a robot arm to attain a certain position $\boldsymbol{x}_d \in \mathbb{R}^3$, a control signal $\boldsymbol{\tau}_c \in \mathbb{R}^n$ as a vector containing the torque of each joint can be designed as:

$$\boldsymbol{\tau}_c = -\mathbf{J}^T \mathbf{K}_P (\boldsymbol{x} - \boldsymbol{x}_d) - K_D \mathbf{J}^T \dot{\boldsymbol{x}} + \mathbf{G} \tag{6.1}$$

where $\boldsymbol{x} \in \mathbb{R}^3$ is the current position of the end effector, $\mathbf{G} \in \mathbb{R}^3$ is the gravity compensation term in the Cartesian coordinates, the scalar K_D is the damping coefficient, and $\mathbf{J} \in \mathbb{R}^{3\times n}$ is the Jacobian matrix which maps the joint velocity $\dot{\boldsymbol{q}} \in \mathbb{R}^n$ to the task-space velocity $\dot{\boldsymbol{x}} \in \mathbb{R}^3$ according to:

$$\dot{\boldsymbol{x}} = \mathbf{J}\dot{\boldsymbol{q}} \tag{6.2}$$

For constructing the stiffness matrix $\mathbf{K}_P \in \mathbb{R}^{3\times 3}$, it is noted that the aim is achieving decoupled stiff/compliant behavior in the three Cartesian coordinates. In order to do so, we set this matrix to be diagonal as:

$$\mathbf{K}_P = \begin{bmatrix} K_{Px} & 0 & 0 \\ 0 & K_{Py} & 0 \\ 0 & 0 & K_{Pz} \end{bmatrix} \tag{6.3}$$

The scalars K_{Px}, K_{Py}, and K_{Pz} are the stiffness components for each axis of the task space. This diagonal configuration of $\mathbf{K}_P$ enables adjusting the arm's stiffness independently along the relevant direction(s). In this way the robotic arm can demonstrate directional behaviour.

With $\mathbf{B}(\boldsymbol{q})$ and $\mathbf{C}(\boldsymbol{q}, \dot{\boldsymbol{q}})$ denoting the inertia and Coriolis matrices respectively, and $\boldsymbol{F} \in \mathbb{R}^3$ as the external force vector, the dynamic equation of motion for the manipulator is:

$$\mathbf{B}(\boldsymbol{q})\ddot{\boldsymbol{q}} + \mathbf{C}(\boldsymbol{q}, \dot{\boldsymbol{q}})\dot{\boldsymbol{q}} + \mathbf{G}(\boldsymbol{q}) = \boldsymbol{\tau}_c + \mathbf{J}^T\boldsymbol{F} \tag{6.4}$$

Applying an external force would move the robotic arm to a new equilibrium position. We calculate this new equilibrium position, $\boldsymbol{x}_e$, by substituting the control signal from (6.1) into (6.4), and setting $\ddot{\boldsymbol{q}} = \mathbf{0}$ and $\dot{\boldsymbol{q}} = \mathbf{0}$ to obtain:

$$\boldsymbol{x}_e = \boldsymbol{x}_d + \mathbf{K}_P^{-1}\boldsymbol{F} \tag{6.5}$$

As we can see, the amount that this new equilibrium position $\boldsymbol{x}_e$ deviates from the desired position $\boldsymbol{x}_d$, depends on the stiffness matrix $\mathbf{K}_P$. Hence, changing the entries of this matrix will directly influence the amount of this deviation. In addition, as the entries of this stiffness matrix comprise the spring coefficients in each Cartesian direction, alteration in the values would also directly affect how fast the response of the system would be to return to the desired position $\boldsymbol{x}_d$ when the external force is removed, as referring to equation (6.1) shows the control torque $\boldsymbol{\tau}_c$ to be directly proportional to the stiffness matrix. Higher values in the entries of $\mathbf{K}_P$ would result in a faster response to attain the positional set point, and with a higher overshoot; contrary to lower values which generate a slower response with less overshoot. Moreover, due to the fact that $\mathbf{K}_P$ is a diagonal matrix, the inverse is simply:

$$\mathbf{K}_P^{-1} = \begin{bmatrix} \frac{1}{K_{Px}} & 0 & 0 \\ 0 & \frac{1}{K_{Py}} & 0 \\ 0 & 0 & \frac{1}{K_{Pz}} \end{bmatrix} \tag{6.6}$$

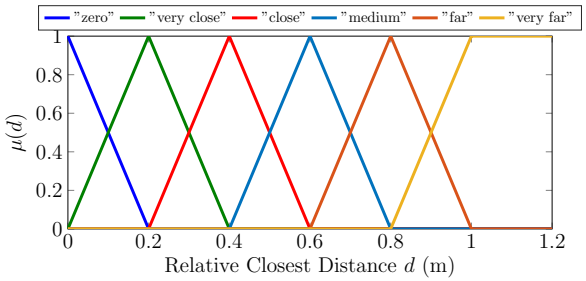

Fig. 6.3 *Fuzzy membership function for categorizing human/robot distance d; from "zero" to "very far (1.2m)".*

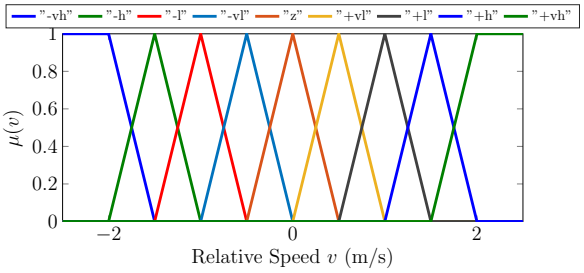

Fig. 6.4 *Fuzzy membership function for categorizing relative human/robot speed v; from "very high distancing" to "very high approaching".*

This implies that the deviation of the end effector's position from equilibrium along each axis is not affected by the stiffness component along other axes, reflecting the importance of setting $\mathbf{K}_P$ as a diagonal matrix.

6.2.2 Fuzzy Inference Mechanism

The role of the fuzzy inference mechanism is to generate an overall stiffness for the robotic arm based on sensory data. Subsequently, this stiffness is projected onto the three Cartesian directions of the task space; and from there, passed on to the low level controller to determine the stiffness of each joint.

Currently the information from both the relative speed v and the closest distance d between the human and the robot are being utilized. The fuzzy sets are chosen as triangular membership functions. The radius of 1 m between the human and the robot is considered as the pertinent distance for stiffness adjustment, and is divided into five zones of "zero", "very close", "close", "medium", "far", and "very far"; as shown in Figure 6.3. The relative speed, defined from -2 m/s to $+2$ m/s, is divided into nine zones: from "-very high" to "+very high",

with the negative and positive signs indicating "approaching" or "distancing", respectively; as shown in Figure 6.4. The overall stiffness is divided into five zones from a minimum of 0 to a maximum of $K_m = 100\,\mathrm{N/m}$ (in one set of trials) or $K_m = 200\,\mathrm{N/m}$ (in another set of trials), as depicted in Figure 6.5. This maximum value is empirically set by taking into account the safety of the human participant in our experiments, yet being sufficiently high to be clearly felt by the human upon contact therefore enabling the demonstration of the main concept discussed herein.

The decision table is constructed as shown in Table 6.1 to calculate the overall stiffness $K_0(d, v)$ for the robotic arm based on the sensory information from the distance d and the relative speed v between the robot and the human. As we can see, the closer the distance is between the human and the robot, the lower the stiffness would be, and vice versa. As for the relative speed, the stiffness will be lower due to higher approaching speed, and vice versa.

This overall stiffness $K_0(d, v)$ needs to projected onto the three Cartesian components of the task space: K_{Px}, K_{Py}, and K_{Pz}. An important aspect of this projection is that: A) the overall stiffness should change only along the necessary direction(s) without affecting the stiffness component(s) in irrelevant direction(s); and B) change of stiffness along relevant directions should each be proportional to the level of risk along each direction, and not necessarily equal to one another. In order to do so, we define a stiffness difference ΔK as:

$$\Delta K(d, v) = K_m - K_0(d, v) \tag{6.7}$$

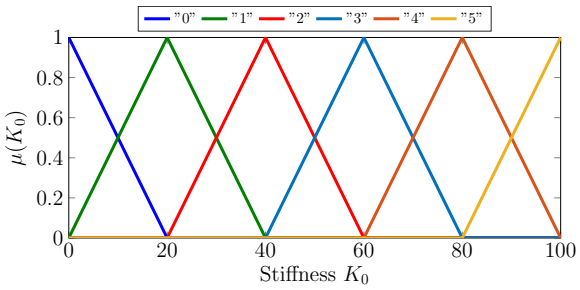

Fig. 6.5 *Fuzzy membership function for categorizing the robot overall stiffness; from minimum stiffness (0) to maximum stiffness (*$100\,\mathrm{N/m}$ *or* $200\,\mathrm{N/m}$ *in different tests).*

Table 6.1 The fuzzy rules for stiffness adjustment based on human-robot distance and relative speed

Fuzzy Rule		Distance					
		Zero	V.C.	C.	M.	F.	V.F.
Relative Speed	-V.H.	0	0	0	1	3	5
	-H.	0	0	0	2	4	5
	-L.	0	0	1	3	4	5
	-V.L.	0	0	1	4	5	5
	Zero	0	1	2	5	5	5
	V.L.	0	1	4	5	5	5
	L.	0	1	4	5	5	5
	H.	0	1	5	5	5	5
	V.H.	0	1	5	5	5	5

For example, when the human is stationary in a far position from the robot along the positive x direction, the stiffness in all directions should be as high as K_m. The human then moves towards the robot along the x direction with speed v, and enters the "monitored" zone at a distance d from the robot. This results in the decrease of stiffness in x direction, K_{Px}, by the amount of $\Delta K(d, v)$ calculated from Equation 6.7, while the stiffness in other directions (namely K_{Py} and K_{Pz}) do not change, as illustrated in Figure 6.2. Extending this one-dimensional example to the more general $\mathbb{R}^3$ space, in a similar manner, should the line of collision be along any arbitrary diagonal path in space, stiffness in all x and y and z directions shall be adjusted continuously, yet each according to a "weighted" decision. In this case, the stiffness change $\Delta K(d, v)$ in each direction is set to be proportional to the relative position along each axis. Denoting the relative position vector between the robot and the human with $\boldsymbol{r}$, we define the stiffness component weight in each Cartesian direction as:

$$w_i(\boldsymbol{r}) = \frac{|\boldsymbol{r}^T \hat{\boldsymbol{u}}_i|}{\sqrt{\boldsymbol{r}^T \boldsymbol{r}}}; \qquad i = x, y, z \tag{6.8}$$

where $\hat{\boldsymbol{u}}_x$, $\hat{\boldsymbol{u}}_y$, and $\hat{\boldsymbol{u}}_z$ are the unit vectors in the global frame of the task space. Hence, the stiffness components in each direction are calculated as:

$$K_{Pi}(d, v, \boldsymbol{r}) = K_m - \Delta K(d, v) w_i(\boldsymbol{r}); \qquad i = x, y, z \tag{6.9}$$

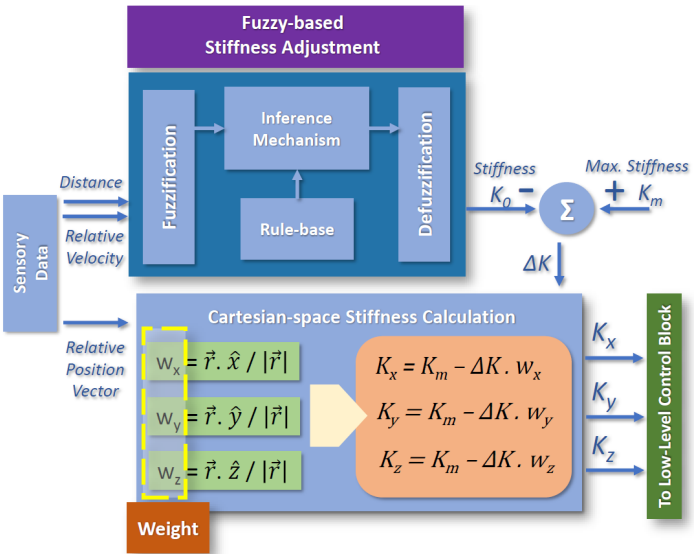

Fig. 6.6 *Calculation flowchart of the overall algorithm.*

The values obtained for K_{Px}, K_{Py}, and K_{Pz} subsequently constitute the stiffness matrix $\mathbf{K}_P$ in (6.3), enabling directional adjustment of the robotic arm's stiffness. A flowchart of the overall algorithm is depicted in Figure 6.6.

6.3 Simulations and Experiments

Referring to the Figure 6.7, the Kinect Camera monitors the position of the human and the robot via ROS TF. This information is fed to the next node via ROS Topic to determine the closest distance, by designating points to the joints of both the human arm and the robot arm. At each instance, the pair of points (one from the human and one from the robot arm) that are the closest, constitute the closest distance. The result is subsequently sent to the nodes for relative speed and the node for fuzzy inferencing, via ROS Topic. The relative speed is calculated via simple numerical differentiation of the data from closest distance. The fuzzy inferencing node uses these values to calculate the desired stiffness matrix, which is sent to the controller via ROS Action.

6.3.1 Simulations

Simulations were performed in ROS and the Gazebo simulator. For this purpose, we utilized the left arm of the Baxter (7 DoF's) as the robotic arm, and a simple 6 DoF manipulator (3 links and all revolute joints) representing a human arm. The Baxter arm is programmed to reach a certain position in space, while the "human" arm approaches it and finally makes contact with the Baxter arm. In the current scenario, the "human" arm moves towards the Baxter arm mainly along the y axis to demonstrate the directional stiffness adjustment. To observe the effectiveness of our proposed algorithm, the simulation was performed in two stages: the first stage, where the stiffness adjustment algorithm is in loop; and the second stage, where the proposed algorithm is deactivated, i.e. the stiffness values are constant. As mentioned before, the relative position between the robot arm and the "human" arm, are calculated by monitoring points assigned to the joints of both the "human" arm and the Baxter arm. The relative speed is calculated via simple numerical differentiation of the data of closest distance. For monitoring the results, the directional stiffness (K_{Px}, K_{Py}, K_{Pz}), relative position $\boldsymbol{r}$, distance d, relative speed v, joint torque $\boldsymbol{\tau}$, and the contact force F were recorded, as shown in Figures 6.8-6.9.

6.3.2 Experimental Protocol

For the experiments, a Kinect camera (Microsoft) placed on the head of the Baxter robot was used to track the movements and positions. Similar to the simulations, the experiments were carried out using the left arm of the Baxter robot. The right arm of the human participant

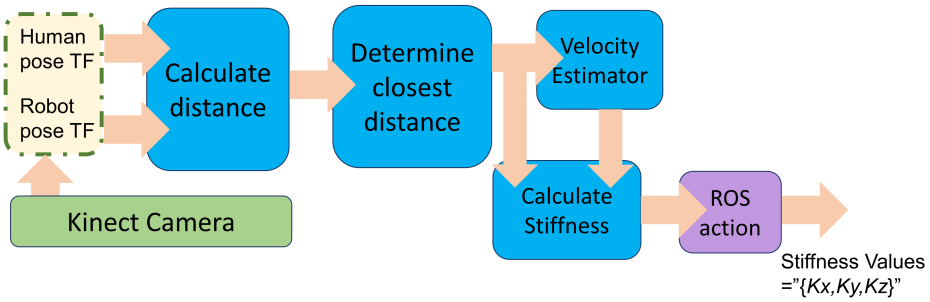

Fig. 6.7 *Flowchart depicting the software implementation.*

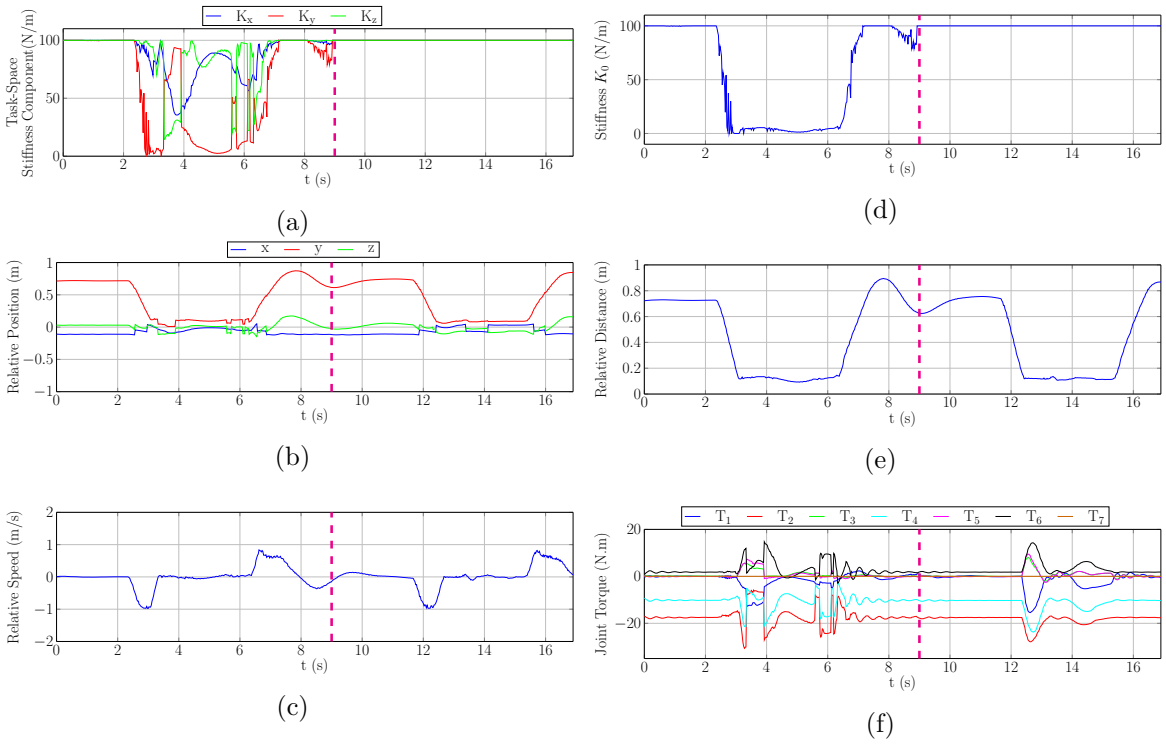

Fig. 6.8 *Simulations: Depicting the change of various parameters in time as the simulated "human" arm approaches and distances from the Baxter arm. The magenta bar indicates the switching point were the stiffness adjustment algorithm is deactivated after that.*

was set as the *active arm*; i.e, tracked by the Kinect, and the distance was again calculated by designating points to the joints (detected by the Kinect) on both the robot arm and the human's *active arm*, and measuring the instantaneous closest pair of points. The joint angles of the robot arm were measured and the arm pose was calculated using forward kinematics. The robot arm was set at an initial pose, while the human approached it from different directions. Three human subjects were involved in two sets of trials. In the first set, maximum

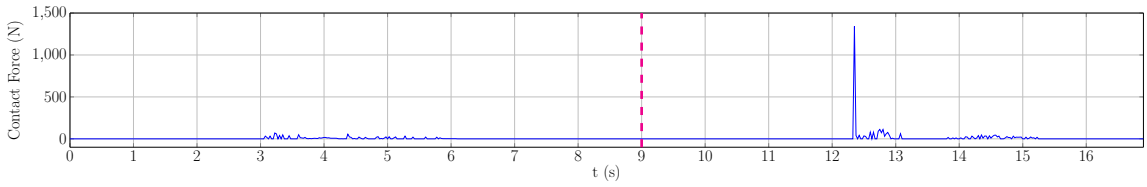

Fig. 6.9 *Simulations: Depicting contact force between simulated "human" arm and Baxter arm, with an activated stiffness adjustment algorithm (left of magenta bar), and without stiffness adjustment (right of magenta bar)*

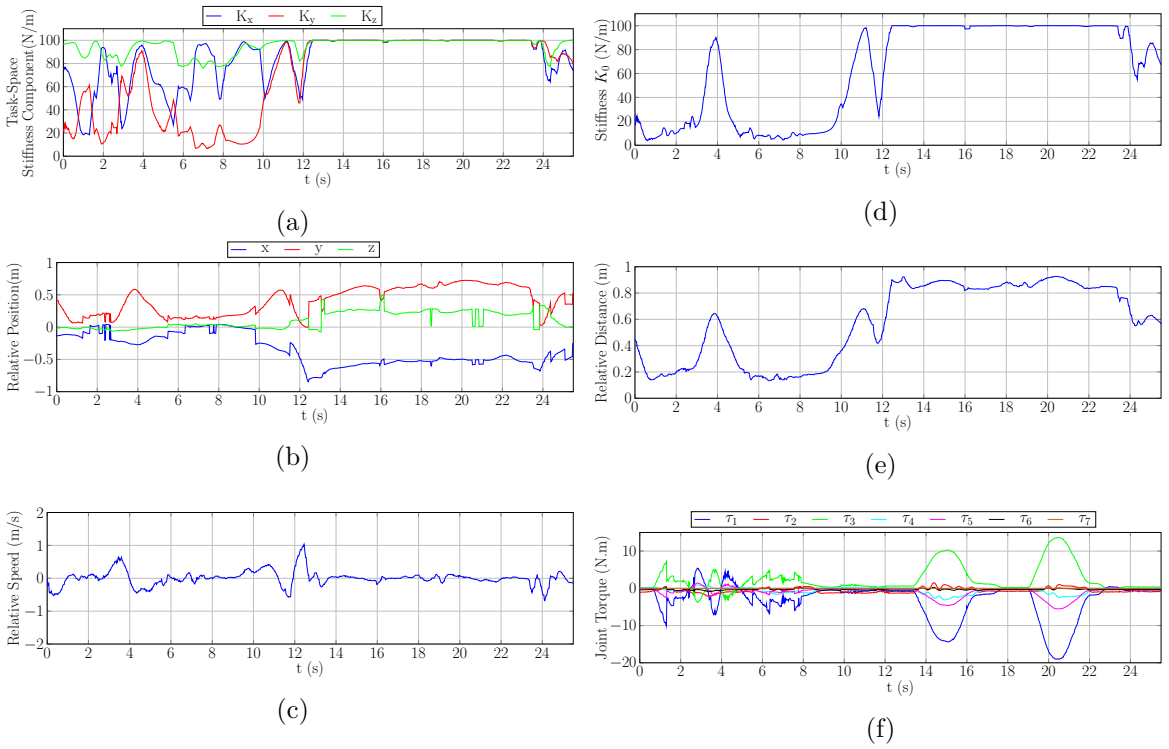

Fig. 6.10 *Experiment Results: Change of various parameters are depicted in time as the human approaches and distances from the Baxter robot. (with, and without the stiffness adjustment algorithm)*

stiffness is set to 100 N/m , and two stages were defined: one with the stiffness adjustment in loop, and the other without stiffness adjustment. The stiffness components (K_{Px}, K_{Py}, K_{Pz}), relative position $\boldsymbol{r}$, distance d, relative speed v, and joint torques $\boldsymbol{\tau}$ were recorded, as depicted in Figure 6.10. A detailed description of this set of trials is included in section 6.4.

In the second set of trials, the maximum stiffness is set to 200 N/m and the stiffness adjustment algorithm is continuously active. The human subjects in turn approach the robot from a random direction while moving back and forth. The results are demonstrated in Figures 6.11-6.12.

6.4 Discussion

The results of the simulations are shown in Figures 6.8-6.9, with the vertical magenta bar indicating switching between the first stage (when the proposed algorithm is running) and the

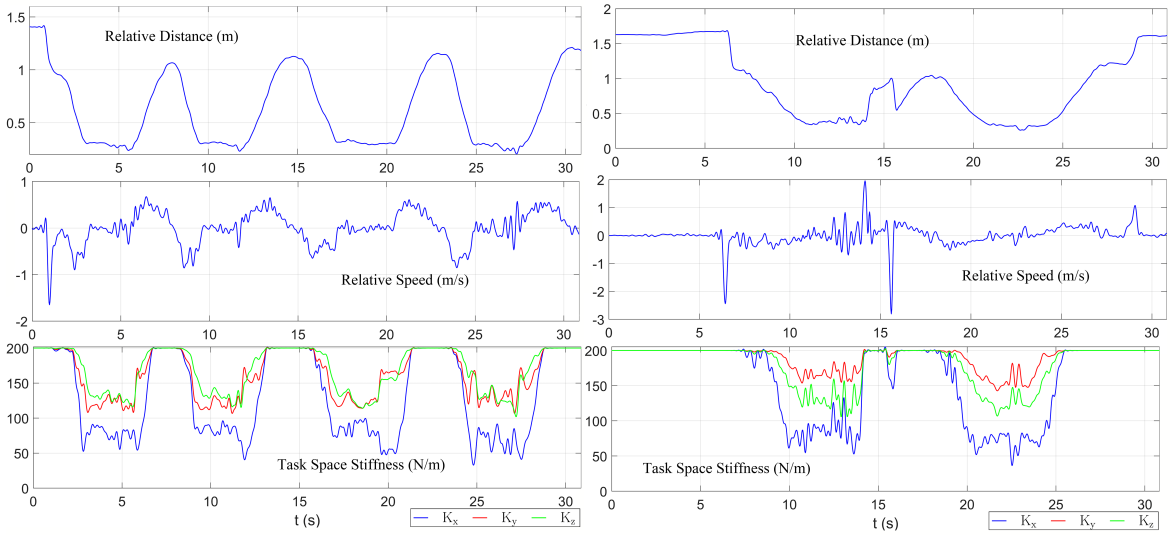

Fig. 6.11 *Trials with human/robot interaction with* $K = 200\,\mathrm{N/m}$.

second stage (stiffness is constant, without adjustment). In the first stage, slightly after $t = 2\,\mathrm{s}$ it could be seen that the "human" approaches the robot (visible from decrease of distance d in Figure 6.8.e along with negative speed v in Figure 6.8.c). The overall stiffness value K_0 decreases until reaching a minimum level where contact occurs, as shown in Figure 6.8.d. Since the human approached the robot along the y direction (as visible from Figure 6.8.b where the y value in red decreases), the stiffness in y direction K_y (red) decreases considerably

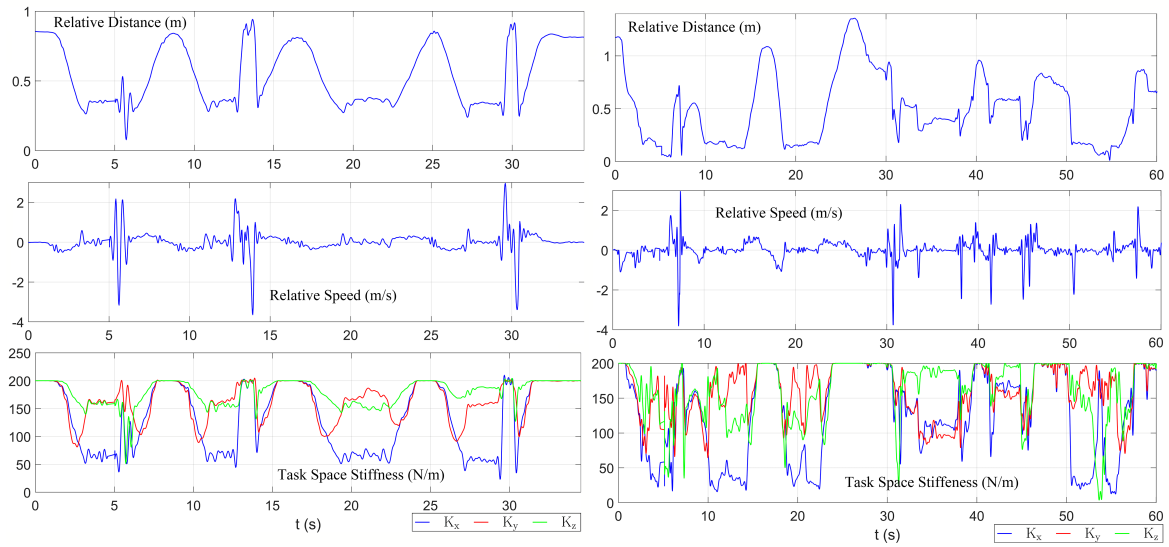

Fig. 6.12 *Trials with human/robot interaction with* $K = 200\,\mathrm{N/m}$.

compared to K_x (blue) and K_z (green) in Figure 6.8.a. As the human starts to move away from the robot slightly after $t = 6\,\mathrm{s}$ (visible from increase of distance d in Figure 6.8.e and positive speed v in Figure 6.8.c), the overall stiffness K_0 (Figure 6.8.d) and the stiffness in y direction (Figure 6.8.a) revert back to the initial high stiffness state. This shows that the fuzzy-based stiffness adjustment mechanism works as intended.

In Figure 6.9 we can observe that the recorded contact force shows a slight disturbance due to a contact at the first stage ($3\,\mathrm{s} < t < 6\,\mathrm{s}$) where the stiffness adjustment is active. The same routine is repeated in the second stage ($t > 9\,\mathrm{s}$) while the "human" is again set to approach the robot from a farther distance, yet due to the inactivity of the stiffness adjustment algorithm, it is observed that the stiffness does not decrease upon the human and robot getting closer, and finally at the contact point, high contact forces are recorded ($12\,\mathrm{s} < t < 13\,\mathrm{s}$). This shows that the proposed algorithm can reduce the produced contact force upon human-robot collision, and thus, significantly improve the safety of the human.

Looking into the results from the experiments, a similar behavior is observed (Figure 6.10). The contact force F is not recorded directly since the absence of local contact force sensors is currently the expected presumption in a comprehensive collaboration [241]. Yet the performance of the proposed algorithm could be advocated for by observing the joint torques (Figure 6.10.f), as we attempt to bring the robot arm to a configuration which is fairly close to its initial pose. This idea could be exploited to promote the notion of "intrinsic force sensing" where the contact forces are not estimated with sensors proximal to the end-effector or the contact points, yet using joint-level information [164].

As the human moves closer to the robot arm during $0\,\mathrm{s} < t < 3\,\mathrm{s}$ and again during $4\,\mathrm{s} < t < 9\,\mathrm{s}$ (as seen in decrease of distance d in Figure 6.10.e and negative speed v in Figure 6.10.c), the overall stiffness value K_0 decreases until reaching a minimum level where contact occurs, as shown in Figure 6.10.d. From $0\,\mathrm{s} < t < 1\,\mathrm{s}$ the human approaches the robot (observed from Figure 6.10.b where the y value in red decreases), causing the stiffness in y direction K_y (red) to decrease considerably compared to K_x (blue) and K_z (green) in Figure 6.10.a. In this period, the human's arm is approaching the robot predominantly from the y direction, while x and z are "almost" constant. Yet the human arm jitters about the

x axis while approaching the robot, and the K_x stiffness component reflects this. Around $t = 2\,\text{s}$, the distance of the arm has begun to increase (viewed in Figure 6.10.e). As the human arm is moving away, again the jitter in the x direction results in a relatively volatile variation of stiffness, since the arm is almost in alignment with the robot's x axis and slight but sudden deviations tend to reflect as the temporal spike viewed in K_x (blue) at $t = 2\,\text{s}$ in Figure 6.10.a. From about $t = 3\,\text{s}$ till $t = 4\,\text{s}$, the distance is increasing (Figure 6.10.e), causing the stiffness components in Figure 6.10.a to increase again. Yet again from about $t = 4\,\text{s}$ till nearly $t = 6\,\text{s}$, the distance decreases in the xy plane with a faster rate in y compared to x, and hence we could see a sharper drop of K_y (red) compared to K_x (blue) in Figure 6.10.a.

Additionally, it is possible to observe how the system acts when running with high stiffness. At $t \approx 13\,\text{s}$ and onwards, the stiffness is high because the *active arm* of the human is far from the robot. At this stage, the robotic arm is pushed with an object made to be undetected by the Kinect camera; with the separate occurrences visible in Figure 6.10.f. as the torques rise in magnitude. As the stiffness adjustment algorithm is not activated, the recorded joint torques are considerably larger (in magnitude) during contact occurrences within this time span ($t > 13\,\text{s}$) compared to when the stiffness adjustment algorithm was active due to contact with the detectable human arm ($t < 9\,\text{s}$). These results illustrate how the robot behaves to be less stiff when the active arm of the human is in close proximity. Also, it is observed that the overall stiffness K_0 (Figure 6.10.d) almost follows the same pattern of the human-robot distance (Figure 6.10.e), which matches our intuitive expectation. In the next set of trials, the maximum stiffness is set to $200\,\text{N/m}$ and the human approaches the distances from the robot, with results shown in Figures 6.11-6.12.

It is noted that the closest distance between the human and robot does not evolve smoothly through time, since it is constantly being measured by observing the closest pair of points (between the Baxter arm and the human arm) during their motion, hence could shift rapidly from one pair of points to another, resulting in the non-smooth profiles of the relative velocity and stiffnesses as seen in the graphs.

6.5 Conclusion

Here, we have presented a novel approach to achieve soft behavior by looking into directional stiffness regulation of a robotic arm for safe human-robot interaction based on fuzzy inference. A Baxter robot has been use to demonstrate the on-line adjustment of the arm stiffness according to the relative position/velocities between the human and the robotic arm received from sensory information.

This research aimed to demonstrate the principles of this approach and its effectiveness. Therefore a number of relevant scenarios have been investigated both in simulations and experiments. The maximum stiffness was chosen to be sufficient for demonstrating the concept of stiffness variation while being clearly noticeable by the human upon contact, and yet be considerate regarding the safety of the human participant during the experiments.

It should be noted that the main focus of this study is the safety of the human. Hence, although directional stiffness adjustment is purposefully introduced to (possibly) reduce the change in the robot's stiffness behavior, yet depending on the nature of the collaborative task and line of collision, stiffness reduction might detrimentally affect the quality of the task at hand, as the safety of the human is much prioritized.

A potential drawback in this study might be the need for initial recognition of the human and robot by the camera, which should seamlessly continue throughout the task. Hence, occlusions of the robot and/or human arm (which is more likely to occur in cluttered work spaces), or unexpected entrance in the camera's field of view, could be problematic and necessitate the use of additional tracking devices. The proposed method here utilizes simultaneous tracking of three points on the human arm w.r.t to three points on the robot arm and evaluates the stiffness based on the closest pair. Due to the nature of the relative motion between the human and robot, this could result in rapid transition between the pair of points calculated to be the closest, and hence volatile stiffness alteration. Furthering this research could incorporate additional measures to ameliorate this effect. In addition, although this research considers the distances and relative velocities between the human and

the robot, yet, the proposed method is not limited to these parameters, and integration of any other available significant indicators is feasible depending on the collaboration.

During collaborative operations with the robot, physical contact may occur at any unspecified point, and both sides might even engage an intentional exchange of forces while carrying out a unified motion engaging the common contact point. To realize such an activity in a controlled manner, the exchanged contact forces need to be estimated regardless of any local force sensing device [241]. This research proposes utilizing the values of the joint torques, which could be pursued in further investigations.

Other possible extensions of this work could consist of setting the whole body of the human to be *active*, i.e. detectable by sensor(s), such that the entire human body will be safer when in contact with the robot. Also, other types of fuzzy membership functions than triangular could be implemented to investigate performance improvement. Finally, it is possible to extend the current method from single-point collision to multi-point collision in future studies.

Chapter 7

Conclusion

Abstract— *This thesis aimed to investigate and exploit certain biological features in the paradigm of Soft Robotics to enhance the performance of artificial agents in close proximity of living organisms, namely humans. This chapter lays out a summary of the current research including the driving motivation, the approach adopted, the principal contributions, and the obtained results. At the end, and outlook on possible future directions to extend this research is presented.*

7.1 Summary

Despite all advancements in the field, current robotic systems do not behave like natural species, hence not suitable for interacting near natural species especially humans. If robotic presence were to extend to real world scenarios engulfed with uncertainties in interaction, a paradigm shift is imperative. A recent trend has emerged which takes inspiration from biological entities to address this problem. This thesis aimed to investigate certain aspects of this bio-inspired paradigm to promote robotic applicability in addition to preserve safe interaction. Namely, attention was given to the role of morphology and its capability as a mechanical-computation mediator between the agent and its surroundings. Regulating internal impedance was identified as a prominent factor in biological operators, along with inherent softness of their body which enables safe and successful interaction with their surroundings.

Taking the concept of "Soft Robotics" as a basis, it was observed that the community defines two classes of robots under this umbrella: 1- displaying compliance through deformable material, and 2- displaying compliant behaviour through control. On these premises, this thesis looked into the common ground between the two sub-domains for a better view of the present challenges in the realm of soft robotics, by utilizing passive and/or active morphological features in each context. Particularly, this research focused on two types for contact: safe haptic exploration, and safe industrial collaboration.

Herein, the following topics were addressed:

1. Comprehensive, accurate and real-time model for complete force and pose estimation of a soft continuum manipulator.

   (a) This thesis introduced a novel analytical approach for real-time modelling and simulation of a finger-like soft continuum appendage, constructed from Silicone and consisting of braided extensors. The proposed model is based on discrete kinematics which employs Cosserat rod theory and the Principle of Virtual Work,

and takes into account bending, shortening, elongation and torsion; yielding complete pose and force estimation along the backbone of the soft manipulator.

(b) Along these lines, elasticity versus hyperelasticity assumptions were studied and the principal stress for braided extensors considering various constrains were developed; which can be used for similar presumptions for hyperelastic design utilizing the neo-Hookean or the Gent model. In addition, the proposed method confirmed that within the operational range of this manipulator (which is categorized as strains less than %50) Hookean assumptions is applicable and demonstrates high accuracy for both position tracking and calculating the force propagation along the backbone, removing the need for hyperelastic analysis. Moreover, principal stresses in braided extensors were derived considering defined boundary conditions in the two investigated hyperelastic models which could be applied for structural design.

2. Improving Soft continuum manipulators' load bearing capacities

(a) An innovative design was introduced to combine fluidic actuation with a tendon-driven mechanism in a shared embodiment of a finger-like soft continuum manipulator. It was shown that dual actuation results in improving the load bearing capacities of the soft robot hence bringing the concept of soft manipulators closer to practical applications.

(b) This design allows to generate variable impedance within a soft robot, a dominant feature in biological counterparts when operating interactively with their environment.

3. Safe and effective haptic perception using soft continuum appendage

(a) This thesis introduced a new approach for haptic perception of soft phantoms by employing the variable impedance soft continuum appendage. Various experiments were carried out as the manipulator was brought into different configurations to explore the interaction behaviour and its effect on anomaly detection represented

by a hard nodule embedded in a soft tissue. The results obtained demonstrate promising capabilities for similar platforms to be used in soft haptics.

(b) Regulating the internal impedance allowed to tune the manipulator's morphological characteristics to tweak information gain. Within this innovative topic, the effect of variable impedance on selected sensing modalities was investigated, along with different probing postures which was enabled by intrinsic pressure activation of the soft-bodied module. Such a setting is not constrained to the non-deformable geometry of conventionally studied rigid links, hence showing closer resemblance to natural operators. The embodiment of the soft appendage allows passive conformation to surfaces under exploration, thus removing the need for constant force/position monitoring.

(c) By incorporating two sensors mounted on the tip and on the base of the soft continuum appendage, the developed manipulator was employed to investigate some features in the relation between sensing modalities in tactile perception and proprioception, with results potentially applicable for robotic palpations strategies as well as opening new doors to understand haptic strategies in biological agents.

4. Safe collaboration with human operator in a shared workspace

(a) A novel approach based on human-like decision making was developed using Fuzzy inferencing to generate variable impedance in a rigid-link robot for mitigating collision with the human co-worker. The develop method benefits from straightforward calculations and easy-to-implement logistics, which could promote safety in industrial settings while extending robotic assistance were required.

7.2 Outlook

The concept of Soft Robotics is still in its infancy and due to several hurdles has not yet been adopted in practical applications and hence its potential is not fully unleashed. Many aspects exist that form the world of soft robotics and are currently witnessing transformative progress,

such as material science and artificial intelligence. Emergence of new computational power has resulted in the promotion of Neural Networks in the form of Deep Learning and Machine Learning. Utilizing these techniques has been proposed in concepts such as bodily aware soft robots [242]. Advancements in material science also has resulted in a new class of soft robots with the capability of altering their damping properties [56]. Combining soft-bodied robots with synthetic biology in fields like tissue engineering promises of many advantages in sensing and dexterity, and has gained recent attention [53]. On the other hand materials incorporated in soft robots as of now are mainly elastomer-based exhibiting similar properties to each other. Yet it seems that practical realization of soft robots depends on advancements in this area to generate and produce material bearing higher resemblance to biological tissue especially muscles.

Another area of prime importance is the field of haptics which as of now still faces many challenges. A proposed avenue to apply soft bodied technologies in haptic sensation has been harnessing morphological computation not only for perception but also for haptic display systems [26]. These challenges and many more require a coherent interdisciplinary approach involving materials science, electro-mechanical design, and modelling, along with insights from biological behaviour in tasks such as grasping and perception.

Inspiration from nature has indeed offered novel technological visions and solutions for the robotic world. However, underlying paradigms of how intelligent behaviour emerges in soft-bodied artificial and natural systems are unknown to a great extent. Such studies have motivated the topic of evolutionary developmental soft robotics (evo-devo-soro) with a different take on bio-inspiration, by replicating the biological processes that forms soft bodied creatures to develop agents which evolve artificially [28]. In this sense, designing robots with biological behaviours are pursued to shed new light on understanding the natural wolrd [243].

References

[1] K. Nakajima, H. Hauser, R. Kang, E. Guglielmino, D. G. Caldwell, and R. Pfeifer, "A soft body as a reservoir: case studies in a dynamic model of octopus-inspired soft robotic arm," *Frontiers in Computational Neuroscience*, vol. 7, no. July, pp. 1–19, 2013.

[2] R. Pfeifer, M. Lungarella, and F. Iida, "Self- Organization, Embodiment, and Biologically Inspired Robotics," *Science Robotics*, vol. 318, no. November, pp. 1088–1093, 2007.

[3] N. Sornkarn, *Morphological Computation in Active Haptic Embodied Perception*. Phd, King's College London, London, UK, 2016.

[4] R. Pfeifer, F. Iida, and M. Lungarella, "Cognition from the bottom up: On biological inspiration, body morphology, and soft materials," *Trends in Cognitive Sciences*, vol. 18, no. 8, pp. 404–413, 2014.

[5] D. Rus and M. T. Tolley, "Design, fabrication and control of soft robots," *Nature*, vol. 521, no. 7553, pp. 467–475, 2015.

[6] M. Cianchetti, T. Ranzani, G. Gerboni, T. Nanayakkara, K. Althoefer, P. Dasgupta, and A. Menciassi, "Soft Robotics Technologies to Address Shortcomings in Today's Minimally Invasive Surgery: The STIFF-FLOP Approach," *Soft Robotics*, vol. 1, no. 2, pp. 122–131, 2014.

[7] T. Ranzani, M. Cianchetti, G. Gerboni, I. DeFalco, and A. Menciassi, "A Soft Modular Manipulator for Minimally Invasive Surgery: Design and Characterization of a Single Module," *IEEE Transactions on Robotics*, vol. 32, no. 1, pp. 187–200, 2016.

[8] M. Cianchetti and C. Laschi, "Pleasant to the Touch: By Emulating Nature, Scientists Hope to Find Innovative New Uses for Soft Robotics in Health-Care Technology," *IEEE Pulse*, vol. 7, no. 3, pp. 34–37, 2016.

[9] J. Shintake, V. Cacucciolo, D. Floreano, and H. Shea, "Soft Robotic Grippers," *Advanced Materials*, vol. 1707035, no. May, 2018.

[10] S. Wolf, G. Grioli, O. Eiberger, W. Friedl, M. Grebenstein, H. Hoppner, E. Burdet, D. G. Caldwell, R. Carloni, M. G. Catalano, D. Lefeber, S. Stramigioli, N. Tsagarakis, M. Van Damme, R. Van Ham, B. Vanderborght, L. C. Visser, A. Bicchi, and A. Albu-Schäffer, "Variable Stiffness Actuators: Review on Design and Components," *IEEE/ASME Transactions on Mechatronics*, vol. 21, no. 5, pp. 2418–2430, 2016.

[11] B. Vanderborght, A. Albu-Schäffer, A. Bicchi, E. Burdet, D. G. Caldwell, R. Carloni, M. G. Catalano, O. Eiberger, W. Friedl, G. Ganesh, M. Garabini, M. Grebenstein, G. Grioli, S. Haddadin, H. Hoppner, A. Jafari, M. Laffranchi, D. Lefeber, F. Petit, S. Stramigioli, N. Tsagarakis, M. Van Damme, R. Van Ham, L. Visser, and S. Wolf,

"Variable impedance actuators: A review," *Robotics and Autonomous Systems*, vol. 61, no. 12, pp. 1601–1614, 2013.

[12] J. Hughes, U. Culha, F. Giardina, F. Guenther, A. Rosendo, and F. Iida, "Soft Manipulators and Grippers: A Review," *Frontiers in Robotics and AI*, vol. 3, no. November, pp. 1–12, 2016.

[13] F. P. Petit, *Analysis and Control of Variable Stiffness Robots*. Phd, ETH Zurich, 2014.

[14] R. M. Füchslin, A. Dzyakanchuk, D. Flumini, H. Hauser, K. J. Hunt, R. H. Luchsinger, B. Reller, S. Scheidegger, and R. Walker, "Morphological Computation and Morphological Control: Steps Toward a Formal Theory and Applications," *Artificial Life*, vol. 19, no. 1, pp. 9–34, 2013.

[15] T. Ziemke, "What's that thing called embodiment?," in *Annual Meeting of the Cognitive Science Society*, (Boston, Massachusetts, USA), pp. 1305–1310, Cognitive Science Society, 2003.

[16] S. G. Nurzaman, U. Culha, L. Brodbeck, L. Wang, and F. Iida, "Active sensing system with in situ adjustable sensor morphology," *PLoS ONE*, vol. 8, no. 12, pp. 1–12, 2013.

[17] J. F. Wilson, D. Li, Z. Chen, and R. T. George, "Flexible robot manipulators and grippers: Relatives of elephant trunks and squid tentacles," in *Robots and Biological Systems: Towards a New Bionics?* (P. Dario, G. Sandini, and P. Aebischer, eds.), (Berlin, Heidelberg), pp. 475–494, Springer Berlin Heidelberg, 1993.

[18] F. Iida, A. Rosendo, S. Nurzaman, C. Laschi, R. Wood, and D. Floreano, "Soft robotics and morphological computation," *IEEE Robotics and Automation Magazine*, vol. 23, no. 3, pp. 28–29, 2016.

[19] N. Pedrocchi, F. Vicentini, M. Malosio, and L. M. Tosatti, "Safe human-robot cooperation in an industrial environment," *International Journal of Advanced Robotic Systems*, vol. 10, no. 27, pp. 1–13, 2013.

[20] R. Pfeifer and G. Gomez, "Morphological computation - Connecting brain, body, and environment," in *Creating Brain-Like Intellligence* (B. Sendhoff, ed.), vol. 5436, pp. 66–83, Berlin, Germany: Springer, 2009.

[21] D. B. Camarillo, C. F. Milne, C. R. Carlson, M. R. Zinn, and J. K. Salisbury, "Mechanics modeling of tendon driven continuum manipulators," *IEEE Transactions on Robotics*, vol. 24, no. 6, pp. 1262–1273, 2008.

[22] R. Pfeifer and J. Bongard, *How the Body Shapes the Way We Think: A New View of Intelligence*. Cambridge, Massachusetts: MIT Press, 1st ed., 2006.

[23] T. Nanayakkara, A. Jiang, M. Del Rocío Armas Fernández, H. Liu, K. Althoefer, and J. Bimbo, "Stable Grip Control on Soft Objects With Time-Varying Stiffness," *IEEE Transactions on Robotics*, vol. 32, no. 3, pp. 626–637, 2016.

[24] J. Rossiter and H. Hauser, "Soft robotics - The next industrial revolution?," *IEEE Robotics and Automation Magazine*, vol. 23, no. 3, pp. 17–20, 2016.

[25] A. Bicchi, J. K. Salisbury, and D. L. Brock, "Contact Sensing from Force Measurements," *The International Journal of Robotics Research*, vol. 12, no. 3, pp. 249–262, 1993.

[26] J. E. Bernth, V. A. Ho, and H. Liu, "Morphological computation in haptic sensation and interaction: from nature to robotics," *Advanced Robotics*, vol. 1864, pp. 1–23, 2018.

[27] A. Llamosi and S. Toussaint, "Measuring Force Intensity and Direction with a Spatially Resolved Soft Sensor for Biomechanics and Robotic Haptic Capability," *Soft Robotics*, vol. "Ahead of Print", pp. 1–10, 2019.

[28] F. Corucci, N. Cheney, S. Kriegman, J. Bongard, and C. Laschi, "Evolutionary Developmental Soft Robotics As a Framework to Study Intelligence and Adaptive Behavior in Animals and Plants," *Frontiers in Robotics and AI*, vol. 4, no. July, pp. Article34(1–7), 2017.

[29] B. Trimmer, "A journal of soft robotics: Why now?," *Soft Robotics*, vol. 1, no. 1, pp. 1–4, 2014.

[30] B. Siciliano and O. Khatib, *Springer Handbook of Robotics*. Switzerland: Springer-Verlag Berlin Heidelberg, 2nd ed., 2016.

[31] M. Garrad, J. Rossiter, and H. Hauser, "Shaping behaviour with adaptive morphology," *IEEE Robotics and Automation Letters (RA-L)*, vol. 3, no. 3, pp. 2056–2062, 2018.

[32] S. Haddadin, M. Weis, S. Wolf, and A. Albu-Schäffer, "Optimal control for maximizing link velocity of robotic variable stiffness joints," in *The International Federation of Automatic Control Milano (IFAC)*, vol. 44, (Milano, Italy), pp. 6863–6871, IFAC Proceedings Volumes, 2011.

[33] A. Albu-Schäffer, O. Eiberger, M. Grebenstein, S. Haddadin, C. Ott, T. Wimböck, S. Wolf, and G. Hirzinger, "Soft robotics," *IEEE Robotics and Automation Magazine*, vol. 15, no. 3, pp. 20–30, 2008.

[34] A. Bicchi and G. Tonietti, "Fast and "soft-arm" tactics," *IEEE Robotics and Automation Magazine*, vol. 11, no. 2, pp. 22–33, 2004.

[35] T. G. Thuruthel, *Machine Learning Approaches for Control of Soft Robots*. Phd, Scuola Superiore Sant'Anna (SSSA), Pisa, Italy, 2018.

[36] R. Kang, E. Guglielmino, L. Zullo, D. T. Branson, I. S. Godage, and D. G. Caldwell, "Embodiment design of soft continuum robots," *Advances in Mechanical Engineering*, vol. 8, no. 4, pp. 1–13, 2016.

[37] F. Iida and S. G. Nurzaman, "Adaptation of sensor morphology: An integrative view of perception from biologically inspired robotics perspective," *Interface Focus*, vol. 6, no. 4, pp. 20160016(2–17), 2016.

[38] C. Della Santina, L. Pallottino, D. Rus, and A. Bicchi, "Exact Task Execution in Highly Under-Actuated Soft Limbs: An Operational Space Based Approach," *IEEE Robotics and Automation Letters (RA-L)*, vol. 4, no. 3, pp. 2508–2515, 2019.

[39] M. Cianchetti, A. Arienti, M. Follador, B. Mazzolai, P. Dario, and C. Laschi, "Design concept and validation of a robotic arm inspired by the octopus," *Materials Science and Engineering C*, vol. 31, no. 6, pp. 1230–1239, 2011.

[40] B. Hochner, "An embodied view of octopus neurobiology," *Current Biology*, vol. 22, no. 20, pp. R887–R892, 2012.

[41] R. Kang, D. T. Branson, T. Zheng, E. Guglielmino, and D. G. Caldwell, "Design, modeling and control of a pneumatically actuated manipulator inspired by biological continuum structures," *Bioinspiration and Biomimetics*, vol. 8, no. 3, 2013.

[42] M. Cianchetti, M. Calisti, L. Margheri, M. Kuba, and C. Laschi, "Bioinspired locomotion and grasping in water: The soft eight-arm OCTOPUS robot," *Bioinspiration and Biomimetics*, vol. 10, no. 3, 2015.

[43] N. Hogan, "Impedance control: An approach to manipulation, part i - theory," *ASME Journal of Dynamic Systems, Measurement, and Control*, vol. 107, no. 1, pp. 1–7, 1985.

[44] N. Sornkarn, M. Howard, and T. Nanayakkara, "Internal impedance control helps information gain in embodied perception," in *IEEE International Conference on Robotics and Automation (ICRA)*, (Hong Kong, China), pp. 6685–6690, IEEE, 2014.

[45] N. Sornkarn and T. Nanayakkara, "The efficacy of interaction behavior and internal stiffness control for embodied information gain in haptic perception," in *IEEE International Conference on Robotics and Automation (ICRA)*, vol. May, (Stockholm, Sweden), pp. 2657–2662, IEEE, 2016.

[46] S. Hurley, "Active perception and perceiving action: The shared circuits model," *Perceptual Experience*, 01 2005.

[47] N. Sornkarn and T. Nanayakkara, "Can a Soft Robotic Probe Use Stiffness Control Like a Human Finger to Improve Efficacy of Haptic Perception?," *IEEE Transactions on Haptics*, vol. 10, no. 2, pp. 183–195, 2017.

[48] S. B. Laughlin, "Energy as a constraint on the coding and processing of sensory information," *Current Opinion in Neurobiology*, vol. 11, no. 4, pp. 475 –480, 2001.

[49] K. Ghazi-Zahedi, C. Langer, and N. Ay, "Morphological computation: Synergy of body and brain," *MDPI Entropy*, vol. 19, no. 9, pp. 1–15, 2017.

[50] R. S. Johansson and Ä. B. Vallbo, "Tactile sensory coding in the glabrous skin of the human hand," *Trends in Neurosciences*, vol. 6, pp. 27 – 32, 1983.

[51] M. Lungarella and O. Sporns, "Mapping information flow in sensorimotor networks," *PLOS Computational Biology*, vol. 2, pp. 1–12, 10 2006.

[52] M. Cianchetti, T. Ranzani, G. Gerboni, I. DeFalco, C. Laschi, and A. Menciassi, "STIFF-FLOP surgical manipulator: Mechanical design and experimental characterization of the single module," in *IEEE/RSJ International Conference on Intelligent Robots and Systems (IROS)*, (Tokyo, Japan), pp. 3576–3581, IEEE, 2013.

[53] S. Coyle, C. Majidi, P. LeDuc, and K. J. Hsia, "Bio-inspired soft robotics: Material selection, actuation, and design," *Extreme Mechanics Letters*, vol. 22, pp. 51–59, 2018.

[54] G. Bao, H. Fang, L. Chen, Y. Wan, F. Xu, Q. Yang, and L. Zhang, "Soft Robotics-Academic Insights and Perspectives Through Bibliometric Analysis," *Soft Robotics*, vol. 5, no. 3, pp. 1–13, 2018.

[55] F. Iida and C. Laschi, "Soft robotics: Challenges and perspectives," *Procedia Computer Science*, vol. 7, pp. 99–102, 2011.

[56] A. Di Lallo, M. G. Catalano, M. Garabini, G. Grioli, M. Gabiccini, and A. Bicchi, "Dynamic Morphological Computation Through Damping Design of Soft Continuum Robots," *Frontiers in Robotics and AI*, vol. 6, no. April, pp. Article23(1–19), 2019.

[57] A. Albu-Schäffer, M. Fischer, G. Schreiber, F. Schoeppe, and G. Hirzinger, "Soft robotics: what Cartesian stiffness can obtain with passively compliant, uncoupled joints?," in *IEEE/RSJ International Conference on Intelligent Robots and Systems (IROS)*, vol. 4, (Sendai, Japan), pp. 3295–3301, IEEE, 2004.

[58] M. Koehler, A. M. Okamura, and C. Duriez, "Stiffness Control of Deformable Robots Using Finite Element Modeling," *IEEE Robotics and Automation Letters (RA-L)*, vol. 4, no. 2, pp. 469–476, 2019.

[59] S. Mintchev and D. Floreano, "Adaptive Morphology," *IEEE Robotics & Automation Magazine*, vol. September, no. 23, pp. 42–54, 2016.

[60] J. Burgner-Kahrs, D. C. Rucker, and H. Choset, "Continuum Robots for Medical Applications: A Survey," *IEEE Transactions on Robotics*, vol. 31, no. 6, pp. 1261–1280, 2015.

[61] C. Laschi, B. Mazzolai, and M. Cianchetti, "Soft robotics: Technologies and systems pushing the boundaries of robot abilities," *Science Robotics*, vol. 1, no. 1, pp. 1–12, 2016.

[62] P. Paoletti, G. Jones, and L. Mahadevan, "Grasping with a soft glove : intrinsic impedance control in pneumatic actuators," *Journal of Royal Society Interface*, vol. 17, pp. 20160867(1–14), 2017.

[63] N. Hogan and S. P. Buerger, "Impedance and Interaction Control," in *Robotics and Automation Handbook* (T. R. Kurfess, ed.), ch. 19, pp. 19.1–19.23, Florida, US: CRC Press, 1st ed., 2005.

[64] N. Hogan, "Mechanical Impedance of Single- and Multi-Articular Systems," in *Multiple Muscle Systems* (J. Winters and S. Woo, eds.), p. 149–164, New York, NY: Springer, 1990.

[65] Hogan, Neville, "On the stability of manipulators performing contact tasks," *IEEE Journal on Robotics and Automation*, vol. 4, no. 6, pp. 677–686, 1988.

[66] R. D. Howe, "Tactile Sensing and Control of Robotic Manipulation," *Journal of Advanced Robotics*, vol. 8, no. 3, pp. 245–261, 1994.

[67] S. Haddadin, A. Albu-Schäffer, and G. Hirzinger, "Requirements for safe robots: Measurements, analysis and new insights," *The International Journal of Robotics Research*, vol. 28, no. 11-12, pp. 1507–1527, 2009.

[68] A. De Luca, A. Albu-Schäffer, S. Haddadin, and G. Hirzinger, "Collision detection and safe reaction with the DLR-III lightweight manipulator arm," in *IEEE/RSJ International Conference on Intelligent Robots and Systems (IROS)*, (Beijing, China), pp. 1623–1630, IEEE, 2006.

[69] F. Petit, W. Friedl, H. Hoppner, and M. Grebenstein, "Analysis and synthesis of the bidirectional antagonistic variable stiffness mechanism," *IEEE/ASME Transactions on Mechatronics*, vol. 20, no. 2, pp. 684–695, 2015.

[70] C. Yang, G. Ganesh, S. Haddadin, S. Parusel, A. Albu-Schäffer, and E. Burdet, "Human-Like Adaptation of Force and Impedance in Stable and Unstable Interactions," *IEEE Transactions on Robotics*, vol. 27, no. 5, pp. 918–930, 2011.

[71] A. DeLuca, F. Flacco, A. Bicchi, and R. Schiavi, "Nonlinear Decoupled Motion-Stiffness Control and Collision Detection / Reaction for the VSA-II Variable Stiffness Device," in *IEEE/RSJ International Conference on Intelligent Robots and Systems (IROS)*, (St. Louis, USA), pp. 5487–5494, IEEE, 2009.

[72] V. C. Müller and M. Hoffmann, "What Is Morphological Computation? On How the Body Contributes to Cognition and Control," *Artificial Life*, vol. 23, 2017.

[73] N. Sornkarn, P. Dasgupta, and T. Nanayakkara, "Morphological computation of haptic perception of a controllable stiffness probe," *PLoS ONE*, vol. 11, no. 6, pp. 1–21, 2016.

[74] J. Back, T. Manwell, R. Karim, K. Rhode, K. Althoefer, and H. Liu, "Catheter contact force estimation from shape detection using a real-time Cosserat rod model," in *IEEE/RSJ International Conference on Intelligent Robots and Systems (IROS)*, (Hamburg, Germany), pp. 2037–2042, IEEE, 2015.

[75] K. Xu and N. Simaan, "An investigation of the intrinsic force sensing capabilities of continuum robots," *IEEE Transactions on Robotics*, vol. 23, no. 3, pp. 576–587, 2008.

[76] K. Xu and N. Simaan, "Intrinsic Wrench Estimation and Its Performance Index for Multisegment Continuum Robots," *IEEE Transactions on Robotics*, vol. 26, no. 3, pp. 555–561, 2010.

[77] R. Blickhan, A. Seyfarth, H. Geyer, S. Grimmer, H. Wagner, and M. Günther, "Intelligence by mechanics," *Philosophical Transactions of the Royal Society A: Mathematical, Physical and Engineering Sciences*, vol. 365, no. 1850, pp. 199–220, 2007.

[78] G. E. Loeb, "Control implications of musculoskeletal mechanics," in *IEEE International Conference of the Engineering in Medicine and Biology Society (EMBC)*, (Montreal, Quebec, Canada), IEEE, 1995.

[79] F. J. Valero-Cuevas, J. Yi, D. Brown, R. V. McNamara, C. Paul, and H. Lipson, "The tendon network of the fingers performs anatomical computation at a macroscopic scale," *IEEE Transactions on Biomedical Engineering*, vol. 54, pp. 1161–1166, June 2007.

[80] L. Lindenroth, C. Duriez, J. Back, K. Rhode, and H. Liu, "Intrinsic force sensing capabilities in compliant robots comprising hydraulic actuation," in *IEEE/RSJ International Conference on Intelligent Robots and Systems (IROS)*, (Vancouver, BC, Canada), pp. 2923–2928, IEEE, 2017.

[81] S. Sadati, *Decentralized Morphological Stiffness Tunable Interface for Continuum Manipulators*. Phd, King's College London, London, UK, 2018.

[82] K. Nakajima, H. Hauser, T. Li, and R. Pfeifer, "Information processing via physical soft body," *Nature Scientific Reports*, vol. 5, pp. 1–11, 2015.

[83] J. C. Gwilliam, Z. Pezzementi, E. Jantho, A. M. Okamura, and S. Hsiao, "Human vs. robotic tactile sensing: Detecting lumps in soft tissue," in *IEEE Haptics Symposium (HAPTICS 2010)*, pp. 21–28, 2010.

[84] L. Blanc, A. Delchambre, and P. Lambert, "Flexible medical devices: Review of controllable stiffness solutions," *Actuators*, vol. 6, no. 3, 2017.

[85] J. Fraś, J. Czarnowski, M. Maciaś, J. Główka, M. Cianchetti, and A. Menciassi, "New STIFF-FLOP module construction idea for improved actuation and sensing," in *IEEE International Conference on Robotics and Automation (ICRA)*, (Seattle, Washington, USA), pp. 2901–2906, IEEE, 2015.

[86] I. DeFalco, M. Cianchetti, and A. Menciassi, "A soft multi-module manipulator with variable stiffness for minimally invasive surgery," *Bioinspiration and Biomimetics*, vol. 12, no. 5, 2017.

[87] A. Shiva, S. H. Sadati, Y. Noh, J. Fraś, A. Ataka, H. Würdemann, H. Hauser, I. D. Walker, T. Nanayakkara, and K. Althoefer, "Elasticity versus hyperelasticity considerations in quasistatic modeling of a soft finger-like robotic appendage for real-time position and force estimation," *Soft Robotics*, vol. 6, no. 2, pp. 228–249.

[88] M. Li, A. Faragasso, J. Konstantinova, V. Aminzadeh, L. D. Seneviratne, P. Dasgupta, and K. Althoefer, "A novel tumor localization method using haptic palpation based on soft tissue probing data," in *IEEE International Conference on Robotics and Automation (ICRA)*, (Hong Kong, China), pp. 4188–4193, 2014.

[89] M. Manti, T. G. Thuruthel, A. Pratesi, E. Falotico, M. Cianchetti, and C. Laschi, "Exploiting Morphology of a Soft Manipulator for Assistive Tasks," in *Springer-Verlag*, vol. 8064, 2011.

[90] M. Manti, A. Pratesi, E. Falotico, M. Cianchetti, and C. Laschi, "Soft assistive robot for personal care of elderly people," in *IEEE International Conference on Biomedical Robotics and Biomechatronics (BioRob)*, (UTown, Singapore), pp. 833–838, IEEE, June 2016.

[91] K. Althoefer, "Antagonistic actuation and stiffness control in soft inflatable robots," *Nature Reviews Materials*, 2018.

[92] M. Runciman, A. Darzi, and G. P. Mylonas, "Soft Robotics in Minimally Invasive Surgery," *Soft Robotics*, vol. "Ahead of Print", pp. 1–21, 2019.

[93] C. Della Santina, D. Lakatos, A. Bicchi, and A. Albu-Schäffer, "Using Nonlinear Normal Modes for Execution of Efficient Cyclic Motions in Soft Using Nonlinear Normal Modes for Execution of Efficient Cyclic Motions in Soft Robots," *CoRR*, vol. abs/1806.0, no. June, pp. 1–17, 2018.

[94] V. Hayward, "Is there a 'plenhaptic' function?," *Philosophical Transactions of the Royal Society B: Biological Sciences*, vol. 366, no. 1581, pp. 3115–3122, 2011.

[95] W. M. Bergmann Tiest and A. M. L. Kappers, "Cues for haptic perception of compliance," *IEEE Transactions on Haptics*, vol. 2, no. 4, pp. 189–199, 2009.

[96] R. S. Dahiya, G. Metta, M. Valle, and G. Sandini, "Tactile Sensing — From Humans to Humanoids," *IEEE Transactions on Robotics*, vol. 26, no. 1, pp. 1–20, 2010.

[97] L. Dupin, V. Hayward, and M. Wexler, "Generalized movement representation in haptic perception.," *Journal of Experimental Psychology: Human Perception and Performance*, vol. 43, no. 3, pp. 581–595, 2017.

[98] J. Paillard and M. Brouchon, "A proprioceptive contribution to the spatial encoding of position cues for ballistic movements," *Brain research*, vol. 71, p. 273—284, May 1974.

[99] S. Luo, J. Bimbo, R. S. Dahiya, and H. Liu, "Robotic tactile perception of object properties: A review," *Mechatronics*, vol. 48, no. August, pp. 54–67, 2017.

[100] J. Konstantinova, G. Cotugno, P. Dasgupta, K. Althoefer, and T. Nanayakkara, "Palpation force modulation strategies to identify hard regions in soft tissue organs," *PLoS ONE*, vol. 12, no. 2, pp. 1–24, 2017.

[101] A. DeGreef, P. Lambert, and A. Delchambre, "Towards flexible medical instruments: Review of flexible fluidic actuators," *Precision Engineering*, vol. 33, no. 4, pp. 311–321, 2009.

[102] R. K. Katzschmann, A. D. Marchese, and D. Rus, "Autonomous Object Manipulation Using a Soft Planar Grasping Manipulator," *Soft Robotics*, vol. 2, no. 4, pp. 155–164, 2015.

[103] L. Wang and F. Iida, "Deformation in Soft-Matter Robotics: A Categorization and Quantitative Characterization," *IEEE Robotics and Automation Magazine*, vol. 22, no. 3, pp. 125–139, 2015.

[104] F. Renda, M. Giorelli, F. Renda, M. Calisti, M. Cianchetti, and C. Laschi, "Dynamic Model of a Multibending Soft Robot Arm Driven by Cables Dynamic Model of a Multibending Soft Robot Arm Driven by Cables," *IEEE Transactions on Robotics*, vol. 30, no. October, pp. 1109–1122, 2014.

[105] M. Wehner, R. L. Truby, D. J. Fitzgerald, B. Mosadegh, G. M. Whitesides, J. A. Lewis, and R. J. Wood, "An integrated design and fabrication strategy for entirely soft, autonomous robots," *Nature Letter*, vol. 536, no. 7617, pp. 451–455, 2016.

[106] M. Eder, F. Hisch, and H. Hauser, "Morphological computation-based control of a modular, pneumatically driven, soft robotic arm," *Advanced Robotics*, vol. 1864, no. December, pp. 1–11, 2017.

[107] Z. Wang, P. Polygerinos, J. T. Overvelde, K. C. Galloway, K. Bertoldi, and C. J. Walsh, "Interaction Forces of Soft Fiber Reinforced Bending Actuators," *IEEE/ASME Transactions on Mechatronics*, vol. 22, no. 2, pp. 717–727, 2017.

[108] T. G. Thuruthel, Y. Ansari, E. Falotico, and C. Laschi, "Control Strategies for Soft Robotic Manipulators: A Survey," *Soft Robotics*, vol. 5, no. 2, pp. 149–163, 2018.

[109] M. Giorelli, F. Renda, M. Calisti, A. Arienti, G. Ferri, and C. Laschi, "Neural Network and Jacobian Method for Solving the Inverse Statics of a Cable-Driven Soft Arm with Nonconstant Curvature," *IEEE Transactions on Robotics*, vol. 31, no. 4, pp. 823–834, 2015.

[110] E. Tatlicioglu, I. D. Walker, and D. M. Dawson, "Dynamic Modelling for Planar Extensible Continuum Robot Manipulators," in *IEEE International Conference on Robotics and Automation (ICRA)*, (Roma, Italy), pp. 1357–1362, IEEE, 2007.

[111] P. Polygerinos, Z. Wang, J. T. Overvelde, K. C. Galloway, R. J. Wood, K. Bertoldi, and C. J. Walsh, "Modeling of Soft Fiber-Reinforced Bending Actuators," *IEEE Transactions on Robotics*, vol. 31, no. 3, pp. 778–789, 2015.

[112] D. B. Camarillo, C. R. Carlson, and J. K. Salisbury, "Configuration tracking for continuum manipulators with coupled tendon drive," *IEEE Transactions on Robotics*, vol. 25, no. 4, pp. 798–808, 2009.

[113] B. A. Jones, R. L. Gray, and K. Turlapati, "Three dimensional statics for continuum robotics," in *IEEE/RSJ International Conference on Intelligent Robots and Systems (IROS)*, (St. Louis, USA), pp. 2659–2664, IEEE, 2009.

[114] T. Mahl, A. E. Mayer, A. Hildebrandt, and O. Sawodny, "A Variable Curvature Modeling Approach for Kinematic Control of Continuum Manipulators," in *American Control Conference (ACC)*, (Washington, DC, USA), pp. 4945–4950, AACC, 2013.

[115] M. Neumann and J. Burgner-Kahrs, "Considerations for follow-the-leader motion of extensible tendon-driven continuum robots," in *IEEE International Conference on Robotics and Automation (ICRA)*, (Stockholm, Sweden), pp. 917–923, IEEE, 2016.

[116] D. C. Rucker and R. J. Webster, "Statics and Dynamics of Continuum Robots With General Tendon Routing and External Loading," *IEEE Transactions on Robotics*, vol. 27, no. 6, pp. 1033–1044, 2011.

[117] G. Chen, M. T. Pham, and T. Redarce, "Sensor-based guidance control of a continuum robot for a semi-autonomous colonoscopy," *Robotics and Autonomous Systems*, vol. 57, no. 6-7, pp. 712–722, 2009.

[118] B. L. Conrad, J. Jung, R. S. Penning, and M. R. Zinn, "Interleaved continuum-rigid manipulation: An augmented approach for robotic minimally-invasive flexible catheter-based procedures," in *IEEE International Conference on Robotics and Automation (ICRA)*, (Karlsruhe, Germany), pp. 718–724, IEEE, 2013.

[119] B. A. Jones and I. D. Walker, "Practical Kinematics for Real-Time Implimentation of Continuum Robots," *IEEE Transactions on Robotics*, vol. 22, no. 6, pp. 1087–1099, 2006.

[120] B. A. Jones and I. D. Walker, "Kinematics for multisection continuum robots," *IEEE Transactions on Robotics*, vol. 22, no. 1, pp. 43–55, 2006.

[121] M. Rolf and J. J. Steil, "Constant curvature continuum kinematics as fast approximate model for the Bionic Handling Assistant," in *IEEE International Conference on Intelligent Robots and Systems (IROS)*, (Vilamoura, Portugal), pp. 3440–3446, IEEE, 2012.

[122] R. J. Webster and B. A. Jones, "Design and Kinematic Modeling of Constant Curvature Continuum Robots: A Review," *The International Journal of Robotics Research*, vol. 29, no. 13, pp. 1661–1683, 2010.

[123] H. Wang, C. Wang, W. Chen, X. Liang, and Y. Liu, "Three-Dimensional Dynamics for Cable-Driven Soft Manipulator," *IEEE/ASME Transactions on Mechatronics*, vol. 22, no. 1, pp. 18–28, 2017.

[124] J. Jung, R. S. Penning, N. J. Ferrier, and M. R. Zinn, "A Modeling Approach for Continuum Robotic Manipulators : Effects of Nonlinear Internal Device Friction," in *IEEE/RSJ International Conference on Intelligent Robots and Systems (IROS)*, (San Francisco, CA, USA), pp. 5139–5146, IEEE, 2011.

[125] D. Trivedi, A. Lotfi, and C. D. Rahn, "Geometrically Exact Models for Soft Robotic Manipulators," *IEEE Transactions on Robotics*, vol. 24, no. 4, pp. 773–780, 2008.

[126] S. Sadati, S. E. Naghibi, A. Shiva, Y. Noh, A. Gupta, I. D. Walker, K. Althoefer, and T. Nanayakkara, "A Geometry Deformation Model for Braided Continuum Manipulators," *Frontiers in Robotics and AI*, vol. 4, no. June, pp. 1–25, 2017.

[127] I. S. Godage, G. A. Medrano-Cerda, D. T. Branson, E. Guglielmino, and D. G. Caldwell, "Dynamics for variable length multisection continuum arms," *The International Journal of Robotics Research*, vol. 35, no. 6, pp. 695–722, 2016.

[128] R. E. Goldman, A. Bajo, and N. Simaan, "Compliant motion control for multisegment continuum robots with actuation force sensing," *IEEE Transactions on Robotics*, vol. 30, no. 4, pp. 890–902, 2014.

[129] F. Renda, M. Cianchetti, H. Abidi, J. Dias, and L. Seneviratne, "Screw-Based Modeling of Soft Manipulators With Tendon and Fluidic Actuation," *Journal of Mechanisms and Robotics*, vol. 9, no. 4, pp. 041012–1 to 041012–8, 2017.

[130] C. Della Santina, R. K. Katzschmann, A. Bicchi, and D. Rus, "Dynamic control of soft robots interacting with the environment," in *IEEE International Conference on Soft Robotics (RoboSoft)*, (Livorno, Italy), pp. 46–53, 2018.

[131] W. S. Rone and P. Ben-Tzvi, "Continuum robot dynamics utilizing the principle of virtual power," *IEEE Transactions on Robotics*, vol. 30, no. 1, pp. 275–287, 2014.

[132] A. D. Marchese and D. Rus, "Design, kinematics, and control of a soft spatial fluidic elastomer manipulator," *The International Journal of Robotics Research*, vol. 35, no. 7, pp. 840–869, 2016.

[133] T. Kato, I. Okumura, S. E. Song, A. J. Golby, and N. Hata, "Tendon-Driven Continuum Robot for Endoscopic Surgery: Preclinical Development and Validation of a Tension Propagation Model," *IEEE/ASME Transactions on Mechatronics*, vol. 20, no. 5, pp. 2252–2263, 2015.

[134] I. S. Godage, D. T. Branson, E. Guglielmino, G. A. Medrano-Cerda, and D. G. Caldwell, "Shape function-based kinematics and dynamics for variable length continuum robotic arms," in *IEEE International Conference on Robotics and Automation (ICRA)*, (Shanghai, China), pp. 452–457, IEEE, 2011.

[135] I. S. Godage, E. Guglielmino, D. T. Branson, G. A. Medrano-Cerda, and D. G. Caldwell, "Novel modal approach for kinematics of multisection continuum arms," in *IEEE/RSJ International Conference on Intelligent Robots and Systems (IROS)*, (San Francisco, CA, USA Novel), pp. 1093–1098, IEEE, 2011.

[136] S. Sadati, S. Naghibi, I. D. Walker, K. Althoefer, and T. Nanayakkara, "Control Space Reduction and Real-Time Accurate Modeling of Continuum Manipulators Using Ritz and Ritz-Galerkin Methods," *IEEE Robotics and Automation Letters*, vol. 3, no. 1, pp. 328–334, 2018.

[137] S. Sadati, S. E. Naghibi, A. Shiva, I. D. Walker, K. Althoefer, and T. Nanayakkara, "Mechanics of Continuum Manipulators, a Comparative Study of Five Methods with Experiments," in *Towards Autonomous Robotic Systems*, vol. 10454, (Surrey, UK), pp. 686–702, Springer International Publishing, 2017.

[138] S. Hasanzadeh and F. Janabi-Sharifi, "An Efficient Static Analysis of Continuum Robots," *ASME Journal of Mechanisms and Robotics*, vol. 6, no. 3, pp. 031011(1–5), 2014.

[139] F. Jiang, H. Zhang, and J. Zhao, "Kinematics and Statics for Soft Continuum Manipulators With Heterogeneous Soft Materials," in *ASME Dynamic Systems and Control Conference (DSCC)*, (Minneapolis, Minnesota, USA), pp. 9909(1–9), ASME, 2016.

[140] Y. Shapiro, K. Gabor, and A. Wolf, "Modeling a Hyperflexible Planar Bending Actuator as an Inextensible Euler–Bernoulli Beam for Use in Flexible Robots," *Soft Robotics*, vol. 2, no. 2, pp. 71–79, 2015.

[141] G. Alici, T. Canty, R. Mutlu, W. Hu, and V. Sencadas, "Modeling and Experimental Evaluation of Bending Behavior of Soft Pneumatic Actuators Made of Discrete Actuation Chambers," *Soft Robotics*, vol. 5, no. 1, pp. 24–35, 2018.

[142] D. C. Rucker and R. J. Webster, "Deflection-Based Force Sensing for Continuum Robots: A Probabalistic Approach," in *IEEE/RSJ International Conference on Intelligent Robots and Systems (IROS)*, (San Francisco, CA, USA), pp. 3764–3769, IEEE, 2011.

[143] J. Fraś, J. Czarnowski, M. Maciaś, and J. Główka, "Static modeling of multisection soft continuum manipulator for stiff-flop project," *Advances in Intelligent Systems and Computing*, vol. 267, pp. 365–375, 2014.

[144] R. Kang, Y. Guo, L. Chen, D. T. Branson, and J. S. Dai, "Design of a Pneumatic Muscle Based Continuum Robot With Embedded Tendons," *IEEE/ASME Transactions on Mechatronics*, vol. 22, no. 2, pp. 751–761, 2017.

[145] M. Dehghani and S. A. A. Moosavian, "Compact modeling of spatial continuum robotic arms towards real-time control," *Advanced Robotics*, vol. 28, no. 1, pp. 15–26, 2014.

[146] V. Falkenhahn, T. Mahl, A. Hildebrandt, and O. Sawodny, "Dynamic Modeling of Bellows-Actuated Continuum Robots Using the Euler – Lagrange Formalism," *IEEE Transactions on Robotics*, vol. 31, no. 6, pp. 1483–1496, 2015.

[147] E. Amanov, J. Granna, and J. Burgner-kahrs, "Toward Improving Path Following Motion: Hybrid Continuum Robot Design," in *IEEE International Conference on Robotics and Automation (ICRA)*, (Singapore), pp. 4666–4672, IEEE, 2017.

[148] L. S. Cowan and I. D. Walker, "The importance of continuous and discrete elements in continuum robots," *International Journal of Advanced Robotic Systems*, vol. 10, pp. 1–13, 2013.

[149] N. Giri and I. D. Walker, "Three module lumped element model of a continuum arm section," in *IEEE/RSJ International Conference on Intelligent Robots and Systems (IROS)*, (San Francisco, CA, USA), pp. 4060–4065, IEEE, 2011.

[150] I. S. Godage, R. Wirz, I. D. Walker, and R. J. Webster, "Accurate and Efficient Dynamics for Variable-Length Continuum Arms: A Center of Gravity Approach," *Soft Robotics*, vol. 2, no. 3, pp. 96–106, 2015.

[151] C. Duriez and T. M. Bieze, "Soft Robot Modeling, Simulation and Control in Real-Time," in *Soft Robotics: Trends, Applications and Challenges. Biosystems & Biorobotics* (C. Laschi, J. Rossiter, F. Iida, M. Cianchetti, and L. Margheri, eds.), vol. 17, pp. 103–109, Switzerland: Springer, Cham, 1st ed., 2017.

[152] T. M. Bieze, F. Largilliere, A. Kruszewski, Z. Zhang, R. Merzouki, and C. Duriez, "Finite Element Method-Based Kinematics and Closed-Loop Control of Soft, Continuum Manipulators," *Soft Robotics*, vol. 5, no. 3, pp. 348–364, 2018.

[153] M. Gazzola, L. H. Dudte, A. G. McCormick, and L. Mahadevan, "Forward and inverse problems in the mechanics of soft filaments," *Royal Society Open Science*, vol. 5, no. 6, pp. 171628(1–35), 2018.

[154] C. Duriez, "Control of elastic soft robots based on real-time finite element method," in *IEEE International Conference on Robotics and Automation (ICRA)*, (Karlsruhe, Germany), pp. 3982–3987, IEEE, 2013.

[155] B. He, Z. Wang, Q. Li, H. Xie, and R. Shen, "An analytic method for the kinematics and dynamics of a multiple-backbone continuum robot," *International Journal of Advanced Robotic Systems*, vol. 10, pp. 1–13, 2013.

[156] J. Lock, G. Laing, M. Mahvash, and P. E. Dupont, "Quasistatic modeling of concentric tube robots with external loads," in *IEEE/RSJ International Conference on Intelligent Robots and Systems (IROS)*, (Taipei, Taiwan), pp. 2325–2332, IEEE, 2010.

[157] V. Vitiello, S.-L. Lee, T. P. Cundy, and G. Z. Yang, "Emerging Robotic Platforms for Minimally Invasive Surgery," *IEEE Reviews in Biomedical Engineering*, vol. 6, no. 3, pp. 111–126, 2013.

[158] A. Bajo, R. B. Pickens, S. D. Herrell, and N. Simaan, "Constrained motion control of multisegment continuum robots for transurethral bladder resection and surveillance," in *IEEE International Conference on Robotics and Automation (ICRA)*, (Karlsruhe, Germany), pp. 5837–5842, IEEE, 2013.

[159] A. C. Dometios, X. S. Papageorgiou, A. Arvanitakis, C. S. Tzafestas, and P. Maragos, "Real-Time Dynamical Trajectory Tracking Using Online Point-Cloud Data : Towards a User Adaptive Assistive Bath Robot," in *IEEE/RSJ International Conference on Intelligent Robots and Systems (IROS)*, (Vancouver, BC, Canada), pp. 5031–5036, IEEE, 2017.

[160] A. Bajo and N. Simaan, "Hybrid motion/force control of multi-backbone continuum robots," *The International Journal of Robotics Research*, vol. 35, no. 4, pp. 422–434, 2016.

[161] I. S. Godage, T. Nanayakkara, and D. G. Caldwell, "Locomotion with continuum limbs," in *IEEE International Conference on Intelligent Robots and Systems (IROS)*, (Vilamoura, Algarve, Portugal), pp. 293–298, IEEE, 2012.

[162] M. Calisti, M. Giorelli, G. Levy, B. Mazzolai, B. Hochner, C. Laschi, and P. Dario, "An octopus-bioinspired solution to movement and manipulation for soft robots," *Bioinspiration and Biomimetics*, vol. 6, no. 3, p. 036002 (10pp), 2011.

[163] I. Tunay, "Spatial continuum models of rods undergoing large deformation and inflation," *IEEE Transactions on Robotics*, vol. 29, no. 2, pp. 297–307, 2013.

[164] K. Xu and N. Simaan, "Analytic Formulation for Kinematics, Statics, and Shape Restoration of Multibackbone Continuum Robots Via Elliptic Integrals," *ASME Journal of Mechanisms and Robotics*, vol. 2, no. 1, pp. 011006(1–13), 2010.

[165] J. Back, L. Lindenroth, R. Karim, K. Althoefer, and K. Rhode, "New Kinematic Multi-Section Model for Catheter Contact Force Estimation and Steering," in *IEEE/RSJ International Conference on Intelligent Robots and Systems (IROS)*, (Daejeon, Korea), pp. 2122–2127, IEEE, 2016.

[166] S. Kim, C. Laschi, and B. Trimmer, "Soft robotics: A bioinspired evolution in robotics," *Trends in Biotechnology*, vol. 31, no. 5, pp. 287–294, 2013.

[167] P. Polygerinos, N. Correll, S. A. Morin, B. Mosadegh, C. D. Onal, K. Petersen, M. Cianchetti, M. T. Tolley, and R. F. Shepherd, "Soft Robotics: Review of Fluid-Driven Intrinsically Soft Devices; Manufacturing, Sensing, Control, and Applications in Human-Robot Interaction," *Advanced Engineering Materials*, vol. 19, no. 12, pp. 1–22 (1700016), 2017.

[168] W. Liu and C. D. Rahn, "Fiber-Reinforced Membrane Models of McKibben Actuators," *ASME Journal of Applied Mechanics*, vol. 70, no. 6, pp. 853–859, 2003.

[169] Y. Akamatsu, T. Nakamura, and Y. Kusaka, "Development of a soft manipulator with flexible joints using smart fluid and pneumatics cushion for collision with human," in *IEEE/ASME International Conference on Advanced Intelligent Mechatronics (AIM)*, (Tokyo, Japan), pp. 1–6, IEEE, 2007.

[170] A. Shiva, A. Stilli, Y. Noh, A. Faragasso, I. DeFalco, G. Gerboni, M. Cianchetti, A. Menciassi, K. Althoefer, and H. A. Wurdemann, "Tendon-Based Stiffening for a Pneumatically Actuated Soft Manipulator," *IEEE Robotics and Automation Letters*, vol. 1, pp. 632–637, July 2016.

[171] A. N. Gent, *Engineering with Rubber - How to Design Rubber Components*. München, Germany: Carl Hanser Verlag, 3rd ed., 2012.

[172] G. Puglisi and G. Saccomandi, "The Gent model for rubber-like materials: An appraisal for an ingenious and simple idea," *International Journal of Non-Linear Mechanics*, vol. 68, pp. 17–24, 2015.

[173] C. O. Horgan, "The remarkable Gent constitutive model for hyperelastic materials," *International Journal of Non-Linear Mechanics*, vol. 68, pp. 9–16, 2015.

[174] M. A. Hopcroft, W. D. Nix, and T. W. Kenny, "What is the Young's Modulus of Silicone?," *Journal of Microelctromechanical Systems*, vol. 19, no. 2, pp. 229–238, 2010.

[175] J. Konstantinova, A. Jiang, K. Althoefer, P. Dasgupta, and T. Nanayakkara, "Implementation of tactile sensing for palpation in robot-assisted minimally invasive surgery: A review," *IEEE Sensors Journal*, vol. 14, no. 8, pp. 2490–2501, 2014.

[176] M. Li, J. Konstantinova, G. Xu, B. He, V. Aminzadeh, J. Xie, H. A. Wurdemann, and K. Althoefer, "Evaluation of stiffness feedback for hard nodule identification on a phantom silicone model," *PLoS ONE*, vol. 12, no. 3, pp. 1–18, 2017.

[177] N. Herzig, P. Maiolino, F. Iida, and T. Nanayakkara, "A Variable Stiffness Robotic Probe for Soft Tissue Palpation," *IEEE Robotics and Automation Letters (RA-L)*, vol. 3, no. 2, pp. 1168–1175, 2018.

[178] R. E. Goldman, A. Bajo, and N. Simaan, "Algorithms for autonomous exploration and estimation in compliant environments," *Robotica*, vol. 31, no. 1, pp. 71–87, 2013.

[179] S. Sanan, N. Simaan, H. Choset, A. Bajo, and S. Tully, "Simultaneous Compliance and Registration Estimation for Robotic Surgery," in *Robotics: Science and Systems (RSS)*, (Berkeley, CA, USA), RSS foundation, 2014.

[180] C. Shi, X. Luo, P. Qi, T. Li, S. Song, Z. Najdovski, T. Fukuda, and H. Ren, "Shape sensing techniques for continuum robots in minimally invasive surgery: A survey," *IEEE Transactions on Biomedical Engineering*, vol. 64, no. 8, pp. 1665–1678, 2017.

[181] J. Konstantinova, H. Wurdemann, A. Shafti, A. Shiva, and K. Althoefer, eds., *Soft and Stiffness-controllable Robotics Solutions for Minimally Invasive Surgery: The STIFF-FLOP Approach*. Gistrup, Denmark: River Publishers, 1st ed., 2018.

[182] J. Barbič, *Real-time Reduced Large-Deformation Models and Distributed Contact for Computer Graphics and Haptics*. Phd, Carnegie Mellon University, Pittsburgh, PA, USA, 2007.

[183] T. Bretl and Z. McCarthy, "Quasi-static manipulation of a Kirchhoff elastic rod based on a geometric analysis of equilibrium configurations," *The International Journal of Robotics Research*, vol. 33, no. 1, pp. 48–68, 2014.

[184] R. Takano, H. Mochiyama, and N. Takesue, "Real-time shape estimation of Kirchhoff elastic rod based on force/torque sensor," in *IEEE International Conference on Robotics and Automation (ICRA)*, (Singapore), pp. 2508–2515, IEEE, 2017.

[185] C. B. Black, J. Till, and D. C. Rucker, "Parallel Continuum Robots: Modeling, Analysis, and Actuation-Based Force Sensing," *IEEE Transactions on Robotics*, vol. 34, no. 1, pp. 29–47, 2018.

[186] J. Konstantinova, G. Cotugno, P. Dasgupta, K. Althoefer, and T. Nanayakkara, "Autonomous robotic palpation of soft tissue using the modulation of applied force," in *IEEE RAS/EMBS International Conference on Biomedical Robotics and Biomechatronics (BioRob)*, (UTown, Singapore), pp. 323–328, IEEE, 2016.

[187] I. B. Wanninayake, L. D. Seneviratne, and K. Althoefer, "Estimation of tissue stiffness using a prototype of air-float stiffness probe," in *IEEE International Conference on Robotics and Automation (ICRA)*, (Hong Kong, China), pp. 1426–1431, IEEE, 2014.

[188] E. Ayvali, R. A. Srivatsan, L. Wang, R. Roy, N. Simaan, and H. Choset, "Using Bayesian Optimization to Guide Probing of a Flexible Environment for Simultaneous Registration and Stiffness Mapping," in *IEEE International Conference on Robotics and Automation (ICRA)*, (Stockholm, Sweden), pp. 931–936, IEEE, 2016.

[189] D. C. Rucker, "Integrating Rotations Using Nonunit Quaternions," *IEEE Robotics and Automation Letters (RA-L)*, vol. 3, no. 4, pp. 2979–2986, 2018.

[190] B. Balachandran and E. B. Magreb, *Vibrations*. Canada: Cengage Learning, 2nd ed., 2009.

[191] C. Duriez and T. M. Bieze, "Soft Robot Modeling, Simulation and Control in Real-Time," in *Soft Robotics: Trends, Applications and Challenges. Biosystems & Biorobotics* (C. Laschi, J. Rossiter, F. Iida, M. Cianchetti, and L. Margheri, eds.), vol. 17, pp. 103–109, Switzerland: Springer, Cham, 1st ed., 2017.

[192] R. Buckingham, "Snake arm robots," *Industrial Robot: the international journal of robotics research and application*, vol. 29, no. 3, pp. 242–245, 2002.

[193] R. Cieslak and A. Morecki, "Elephant trunk type elastic manipulator - a tool for bulk and liquid type materials transportation," *Robotica*, vol. 17, pp. 11–16, 1999.

[194] I. D. Walker, D. M. Dawson, T. Flash, F. W. Grasso, R. T. Hanlon, B. Hochner, W. M. Kier, C. C. Pagano, C. D. Rahn, and Q. M. Zhang, "Continuum robot arms inspired by cephalopods," in *Unmanned Ground Vehicle Technology VII*, vol. 5804 of *procspie*, pp. 303–314, may 2005.

[195] C. Laschi, M. Cianchetti, B. Mazzolai, L. Margheri, M. Follador, and P. Dario, "Soft Robot Arm Inspired by the Octopus," *Advanced Robotics*, vol. 26, no. 7, pp. 709–727, 2012.

[196] I. A. Gravagne, C. D. Rahn, and I. D. Walker, "Large deflection dynamics and control for planar continuum robots," *IEEE/ASME Transactions on Mechatronics*, vol. 8, no. 2, pp. 299–307, 2003.

[197] W. McMahan, B. A. Jones, and I. D. Walker, "Design and implementation of a multi-section continuum robot: Air-octor," in *IEEE/RSJ International Conference on Intelligent Robots and Systems (IROS)*, pp. 3345–3352, 2005.

[198] H. Yamashita, A. Iimura, E. Aoki, T. Suzuki, T. Nakazawa, E. Kobayashi, H. Hashizume, I. Sakuma, and T. Doh, "Development of endoscopic forceps manipulator using multi-slider linkage mechanisms," in *1st Asian Symposium on Computer Aided Surgery - Robotic and Image guided Surgery*, (Ibaraki, Japan), 2005.

[199] R. Roy, L. Wang, and N. Simaan, "Investigation of effects of dynamics on intrinsic wrench sensing in continuum robots," in *IEEE International Conference on Robotics and Automation (ICRA)*, (Stockholm, Sweden), pp. 2052–2059, IEEE, 2016.

[200] A. Jiang, T. Aste, P. Dasgupta, K. Althoefer, and T. Nanayakkara, "Granular jamming with hydraulic control," in *ASME 2013 International Design Engineering Technical Conferences and Computers and Information in Engineering Conference*, vol. 6A: 37th Mechanisms and Robotics Conference, p. V06AT07A021, 2013.

[201] T. Ranzani, G. Gerboni, M. Cianchetti, and A. Menciassi, "A bioinspired soft manipulator for minimally invasive surgery," *Bioinspiration and Biomimetics*, vol. 10, no. 3, pp. 1–14, 2015.

[202] S. Sareh, A. Jiang, A. Faragasso, Y. Noh, T. Nanayakkara, P. Dasgupta, L. Seneviratne, H. Wurdemann, and K. Althoefer, "Bio-inspired tactile sensor sleeve for surgical soft manipulators," in *IEEE International Conference on Robotics and Automation (ICRA)*, (Hong Kong, China), pp. 1454–1459, IEEE, 2014.

[203] M. Li, T. Ranzani, S. Sareh, L. D. Seneviratne, P. Dasgupta, H. A. Wurdemann, and K. Althoefer, "Multi-fingered haptic palpation utilizing granular jamming stiffness feedback actuators," *Smart Materials and Structures*, vol. 23, no. 9, pp. 095007 (1–12), 2014.

[204] D. Caldwell, G. Medrano-Cerda, and M. Goodwin, "Control of pneumatic muscle actuators," *IEEE Control Systems*, vol. 15, 1995.

[205] A. Jiang, G. Xynogalas, P. Dasgupta, K. Althoefer, and T. Nanayakkara, "Design of a variable stiffness flexible manipulator with composite granular jamming and membrane coupling," in *IEEE/RSJ International Conference on Intelligent Robots and Systems (IROS)*, (Vilamoura, Algarve, Portugal), pp. 2922–2927, IEEE, 2012.

[206] Y. Kim, S. Cheng, S. Kim, and K. Iagnemma, "Design of a tubular snake-like manipulator with stiffening capability by layer jamming," in *IEEE/RSJ International Conference on Intelligent Robots and Systems (IROS)*, (Vilamoura, Algarve, Portugal), pp. 4251–4256, IEEE, 2012.

[207] S. Sadati, S. E. Naghibi, K. Althoefer, and T. Nanayakkara, "Toward a low hysteresis helical scale Jamming interface inspired by teleost fish scale morphology and arrangement," in *IEEE International Conference on Soft Robotics (RoboSoft)*, (Livorno, Italy), pp. 455–460, IEEE, 2018.

[208] G. Mcknight, R. Doty, A. Keefe, G. Herrera, and C. Henry, "Segmented reinforcement variable stiffness materials for reconfigurable surfaces," *Journal of Intelligent Material Systems and Structures*, vol. 21, no. 17, pp. 1783–1793, 2010.

[209] N. G. Cheng, A. Gopinath, L. Wang, K. Iagnemma, and A. E. Hosoi, "Thermally tunable, self-healing composites for soft robotic applications," *Macromolecular Materials and Engineering*, vol. 299, no. 11, pp. 1279–1284, 2014.

[210] W. Shan, S. Diller, A. Tutcuoglu, and C. Majidi, "Rigidity-tuning conductive elastomer," *Smart Materials and Structures*, vol. 24, p. 065001, may 2015.

[211] J. R. Capadona, K. Shanmuganathan, D. J. Tyler, S. J. Rowan, and C. Weder, "Stimuli-responsive polymer nanocomposites inspired by the sea cucumber dermis," *Science*, vol. 319, no. 5868, pp. 1370–1374, 2008.

[212] F. Maghooa, A. Stilli, Y. Noh, K. Althoefer, and H. A. Wurdemann, "Tendon and pressure actuation for a bio-inspired manipulator based on an antagonistic principle," in *IEEE International Conference on Robotics and Automation (ICRA)*, (Seattle, Washington, USA), pp. 2556–2561, 2015.

[213] M. Kier and M. Stella, "The arrangement and function of octopus arm musculature and connective tissue," *Journal of Morphology*, vol. 268 (10), pp. 831–843, 2007.

[214] S. Neppalli, B. Jones, W. McMahan, V. Chitrakaran, I. Walker, M. Pritts, M. Csencsits, C. Rahn, and M. Grissom, "Octarm - a soft robotic manipulator," in *IEEE/RSJ International Conference on Intelligent Robots and Systems (IROS)*, (San Diego, CA, USA), pp. 2569–2569, Oct 2007.

[215] A. Jiang, E. Secco, H. Wurdemann, T. Nanayakkara, P. Dasgupta, and K. Athoefer, "Stiffness-controllable octopus-like robot arm for minimally invasive surgery," in *3rd Joint Workshop on New Technologies for Computer/Robot Assisted Surgery (CRAS)*, (Verona, Italy), 2013.

[216] E. Stengrard and R. Van Den Berg, "Imperfect Bayesian inference in visual perception," *PLoS Computational Biology*, vol. 15, no. 4, pp. 1–27, 2018.

[217] T. R. Coles, D. Meglan, and N. W. John, "The Role of Haptics in Medical Training Simulators: A Survey of the State of the Art," *IEEE Transactions on Haptics*, vol. 4, no. 1, pp. 51–66, 2011.

[218] G. Cotugno, K. Althoefer, and T. Nanayakkara, "The Role of the Thumb: Study of Finger Motion in Grasping and Reachability Space in Human and Robotic Hands," *IEEE Transactions on Systems, Man, and Cybernetics: Systems*, vol. 47, no. 7, pp. 1061–1070, 2017.

[219] J. Konstantinova, M. Li, V. Aminzadeh, P. Dasgupta, K. Althoefer, and T. Nanayakkara, "Force-velocity modulation strategies for soft tissue examination," in *IEEE/RSJ International Conference on Intelligent Robots and Systems (IROS)*, pp. 1998–2003, 2013.

[220] P. Chalasani, L. Wang, R. Yasin, N. Simaan, R. H. Taylor, and M. Kobilarov, "Concurrent Nonparametric Estimation of Organ Geometry and Tissue Stiffness Using Continuous Adaptive Palpation," in *IEEE International Conference on Robotics and Automation (ICRA)*, (Stockholm, Sweden), pp. 4164–4171, IEEE, 2016.

[221] H. Liu, D. Noonan, B. Challacombe, P. Dasgupta, L. D. Seneviratne, and K. Althoefer, "Rolling Mechanical Imaging for Tissue Abnormality Localization During Minimally Invasive Surgery," *IEEE Transactions on Biomedical Engineering*, vol. 57, no. 2, pp. 404–414, 2010.

[222] P. Puangmali, K. Althoefer, L. D. Seneviratne, D. Murphy, and P. Dasgupta, "State-of-the-art in force and tactile sensing for minimally invasive surgery," *IEEE Sensors Journal*, vol. 8, no. 4, pp. 371–380, 2008.

[223] A. A. Stanley and A. M. Okamura, "Controllable Surface Haptics via Particle Jamming and Pneumatics," *IEEE Transactions on Haptics*, vol. 8, no. 1, pp. 20–30, 2015.

[224] J. Konstantinova, M. Li, G. Mehra, P. Dasgupta, K. Althoefer, and T. Nanayakkara, "Behavioral characteristics of manual palpation to localize hard nodules in soft tissues," *IEEE Transactions on Biomedical Engineering*, vol. 61, no. 6, pp. 1651–1659, 2014.

[225] C. Pacchierotti, D. Prattichizzo, and K. J. Kuchenbecker, "Cutaneous feedback of fingertip deformation and vibration for palpation in robotic surgery," *IEEE Transactions on Biomedical Engineering*, vol. 63, no. 2, pp. 278–287, 2016.

[226] J. Konstantinova, M. Li, V. Aminzadeh, K. Althoefer, T. Nanayakkara, and P. Dasgupta, "Evaluating manual palpation trajectory patterns in tele-manipulation for soft tissue examination," in *IEEE International Conference on Systems, Man, and Cybernetics (SMC)*, (Manchester, United Kingdom), pp. 4190–4195, IEEE, 2013.

[227] T. Helps and J. Rossiter, "Proprioceptive Flexible Fluidic Actuators Using Conductive Working Fluids," *Soft Robotics*, vol. 5, no. 2, pp. 175–189, 2018.

[228] K. Horch, S. Meek, T. G. Taylor, and D. T. Hutchinson, "Object discrimination with an artificial hand using electrical stimulation of peripheral tactile and proprioceptive pathways with intrafascicular electrodes," *IEEE Transactions on Neural Systems and Rehabilitation Engineering*, vol. 19, pp. 483–489, Oct 2011.

[229] J. Platkiewicz, H. Lipson, and V. Hayward, "Haptic Edge Detection Through Shear," *Nature Scientific Reports*, vol. 6, no. November 2015, pp. 1–10, 2016.

[230] O. Khatib, A. Casal, K. Yokoi, O. Brock, and K. Chang, "Robots in Human Environments: Basic Autonomous Capabilities," *The International Journal of Robotics Research*, vol. 18, no. 7, pp. 684–696, 1999.

[231] J. de Gea and F. Kirchner, "Modelling and Simulation of Robot Arm Interaction Forces Using Impedance Control," in *The International Federation of Automatic Control (IFAC)*, (Seoul, Korea), pp. 15589–15594, IFAC Proceedings Volumes, 2008.

[232] R. Schiavi, G. Grioli, S. Sen, and A. Bicchi, "VSA-II: a novel prototype of variable stiffness actuator for safe and performing robots interacting with humans," in *IEEE International Conference on Robotics and Automation (ICRA)*, pp. 2171–2176, May 2008.

[233] A. Jafari, N. G. Tsagarakis, and D. G. Caldwell, "A novel intrinsically energy efficient actuator with adjustable stiffness (AwAS)," *IEEE/ASME Transactions on Mechatronics*, vol. 18, no. 1, pp. 355–365, 2013.

[234] O. Eiberger, S. Haddadin, M. Weis, A. Albu-Schäffer, and G. Hirzinger, "On joint design with intrinsic variable compliance: Derivation of the DLR QA-joint," in *IEEE International Conference on Robotics and Automation (ICRA)*, (Anchorage, Alaska, USA), pp. 1687–1694, IEEE, 2010.

[235] J. K. Salisbury, "Active stiffness control of a manipulator in cartesian coordinates," in *19th IEEE Conference on Decision and Control including the Symposium on Adaptive Processes*, pp. 95–100, Dec 1980.

[236] A. Albu-Schäffer, S. Wolf, O. Eiberger, S. Haddadin, F. P. Petit, and M. Chalon, "Dynamic modelling and control of variable stiffness actuators," in *IEEE International Conference on Robotics and Automation (ICRA)*, (Anchorage, Alaska, USA), pp. 2155–2162, IEEE, 2010.

[237] M. Matinfar and K. Hashtrudi-Zaad, "Optimization-based robot compliance control: Geometric and linear quadratic approaches," *The International Journal of Robotics Research*, vol. 24, no. 8, pp. 645–656, 2005.

[238] D. Mitrovic, S. Klanke, and S. Vijayakumar, "Learning impedance control of antagonistic systems based on stochastic optimization principles," *The International Journal of Robotics Research*, vol. 30, no. 5, pp. 556–573, 2011.

[239] D. J. Braun, M. Howard, and S. Vijayakumar, "Exploiting Variable Stiffness in Explosive Movement Tasks," in *Robotics: Science and Systems (RSS)*, (Los Angeles, CA, USA), RSS Foundation, 2011.

[240] M. Garabini, A. Passaglia, F. Belo, P. Salaris, and A. Bicchi, "Optimality principles in stiffness control: The VSA hammer," in *IEEE International Conference on Robotics and Automation (ICRA)*, (San Francisco, CA, USA), pp. 3341–3346, IEEE, 2011.

[241] E. Magrini and A. DeLuca, "Hybrid Force / Velocity Control for Physical Human-Robot Collaboration Tasks," in *IEEE/RSJ International Conference on Intelligent Robots and Systems (IROS)*, (Daejeon, Korea), pp. 857–863, IEEE, 2016.

[242] G. Soter, A. Conn, H. Hauser, and J. Rossiter, "Bodily aware soft robots: integration of proprioceptive and exteroceptive sensors," in *IEEE International Conference on Robotics and Automation (ICRA)*, (Brisbane, Australia), pp. 2448–2453, IEEE, 2018.

[243] T. G. Thuruthel, E. Falotico, F. Renda, T. Flash, and C. Laschi, "Emergence of behavior through morphology: A case study on an octopus inspired manipulator," *Bioinspiration & Biomimetics*, vol. (In Press), pp. 2–12, 2019.